ABSTRACT

Title of Document:	ENGINEERING THIN FILMS OF MAGNETIC ALLOYS AND SEMICONDUCTOR OXIDES AT THE NANOSCALE Ting Xie, Doctor of Philosophy, 2016
Directed By:	Professor R.D. Gomez Department of Electrical and Computer Engineering Professor Thomas E. Murphy Department of Electrical and Computer Engineering

The thesis aims to exploit properties of thin films for applications such as spintronics, UV detection and gas sensing. Nanoscale thin films devices have myriad advantages and compatibility with Si-based integrated circuits processes. Two distinct classes of material systems are investigated, namely ferromagnetic thin films and semiconductor oxides. To aid the designing of devices, the surface properties of the thin films were investigated by using electron and photon characterization techniques including Auger electron spectroscopy (AES), X-ray photoelectron spectroscopy (XPS), grazing incidence X-ray diffraction (GIXRD), and energy-dispersive X-ray spectroscopy (EDS). These are complemented by nanometer resolved local proximal probes such as atomic force microscopy (AFM), magnetic force microscopy (MFM), electric force

microscopy (EFM), and scanning tunneling microscopy to elucidate the interplay between stoichiometry, morphology, chemical states, crystallization, magnetism, optical transparency, and electronic properties.

Specifically, I studied the effect of annealing on the surface stoichiometry of the CoFeB/Cu system by *in-situ* AES and discovered that magnetic nanoparticles with controllable areal density can be produced. This is a good alternative for producing nanoparticles using a maskless process. Additionally, I studied the behavior of magnetic domain walls of the low coercivity alloy CoFeB patterned nanowires. MFM measurement with the in-plane magnetic field showed that, compared to their permalloy counterparts, CoFeB nanowires require a much smaller magnetization switching field , making them promising for low-power-consumption domain wall motion based devices. With oxides, I studied CuO nanoparticles on SnO_2 based UV photodetectors (PDs), and discovered that they promote the responsivity by facilitating charge transfer with the formed nanoheterojunctions. I also demonstrated UV PDs with spectrally tunable photoresponse with the bandgap engineered ZnMgO. The bandgap of the alloyed ZnMgO thin films was tailored by varying the Mg contents and AES was demonstrated as a surface scientific approach to assess the alloying of ZnMgO. With gas sensors, I discovered the rf-sputtered anatase-TiO_2 thin films for a selective and sensitive NO_2 detection at room temperature, under UV illumination. The implementation of UV enhances the responsivity, response and recovery rate of the TiO_2 sensor towards NO_2 significantly. Evident from the high resolution XPS and AFM studies, the surface contamination and morphology of the thin films degrade the gas sensing response. I also demonstrated that surface additive metal nanoparticles on thin

films can improve the response and the selectivity of oxide based sensors. I employed nanometer-scale scanning probe microscopy to study a novel gas senor scheme consisting of gallium nitride (GaN) nanowires with functionalizing oxides layer. The results suggested that AFM together with EFM is capable of discriminating low-conductive materials at the nanoscale, providing a nondestructive method to quantitatively relate sensing response to the surface morphology.

ENGINEERING THIN FILMS OF MAGNETIC ALLOYS AND SEMICONDUCOTR OXIDES AT THE NANOSCALE

By

Ting Xie

Dissertation submitted to the Faculty of the Graduate School of the
University of Maryland, College Park, in partial fulfillment
of the requirements for the degree of
Doctor of Philosophy
2016

Advisory Committee:
Professor R.D. Gomez, Chair/Advisor
Professor Thomas Murphy, Co-Advisor
Dr. Abhishek Motayed
Dr. Albert Davydov
Professor Martin Peckerar
Professor Lourdes Salamanca-Riba (Dean's Representative)

Preface

This dissertation contains 7 chapters. Most of the results discuss in chapters 5 to 7 have been published and presented in peer-referred journals and conferences. Here I listed all the related publications chapter wise.

Chapter 5: Control of morphology, magnetic and composition properties of CoFeB thin films

-**T. Xie** and R.D. Gomez, "Maskless formation of magnetic nanoparticles by annealing continuous CoFeB/Cu bilayer thin films," IEEE Transactions on Magnetics, 51(11), 1-4, 2015.

-**T. Xie** and R.D. Gomez, "Mask-less fabrication of areal density tunable magnetic nanoparticles with annealing of CoFeB/Cu bilayer thin film: Utilizing grain boundary diffusion," IEEE International Magnetics Conference, Beijing, China, 2015.

Chapter 6: Wide-bandgap Semiconductor oxides based high-performing ultraviolet photodetectors

-**T. Xie**, D. Romero and R.D. Gomez, "Surface compositions of atomic layer deposited Zn1-xMgxO thin films studied using Auger electron spectroscopy," Journal of Vacuum Science and Technology A, 33(5), 05E110, 2015.

-**T. Xie***, G. Liu*, B. Wen, J.Y. Ha, N.V. Nguyen, A. Motayed and R. Debnath, "Tunable ultraviolet photoresponse in solution-processed p-n junction photodiodes based on transition metal oxides," ACS Applied Materials and Interfaces, 7(18), 9600-9667, 2015.

* Authors contribute equally.

-**T. Xie***, R. Hasan*, B. Qiu*, E. Arinze, N. Nguyen, A. Motayed, S. Thon and R. Debnath,"High-performing visible-blind photodetectors based on SnO2/CuO nanoheterojunctions," Applied Physics Letters, 2015.

-R. Hasan*, **T. Xie***, S. C. Barron, G. Liu, N. Nguyen, A. Motayed, M. Rao and R. Debnath, "Self-powered heterojunction ultraviolet photodetectors fabricated on plastic substrates," APL Materials, 3(10), 106101, 2015.

-R. Debnath, **T. Xie**, B. Wen,W. Li, J.Y. Ha, N. Sullivan, N. Nguyen and A. Motayed, "A solution-processed high-efficiency p-NiO/n-ZnO heterojunction photodetector," RSC Advances, 5(19), 14646-14652, 2015.

Chapter 7: UV-assisted operation of semiconductor oxides based gas sensors at room-temperature

-**T. Xie**, N. Sullivan, K. Steffens, B. Wen, G. Liu, R. Debnath, A. Davydov, R.D. Gomez and A. Motayed, "UV-assisted NO2 sensing at room-temperature using rf-sputtered TiO2 thin-film," Journal of Alloys and Compounds, 653, 255-259, 2015.

-**T. Xie**, B. Wen, G. Liu, S. Guo, A. Motayed, T.E. Murphy and R.D. Gomez, "Imaging TiO_2 nanoparticles on GaN nanowires with electrostatic force microscopy," American Physical Society March Meeting, Baltimore, MD, USA, 2016.

-**T. Xie**, A. Rani, B. Wen, A. Castillo, B. Thomson, R. Debnath, T.E. Murphy, R.D. Gomez and A. Motayed, "The effects of surface conditions of TiO_2 thin film on the UV-assisted gas sensing response at room temperature," 43rd International Conference on Metallurgical Coatings and Thin Films, San Diego, CA, USA, 2016.

* Authors contribute equally.

-G. Liu, B. Wen **T. Xie**, A. Castillo, J.Y. Ha, N. Sullivan, R. Debnath, A. Davydov, M. Peckerar and A. Motayed, "Top-down approach for fabrication of horizontally-aligned gallium nitride nanowire arrays," Microelectronic Engineering, 142, 58-63, 2015.

Dedication

To my my parents, Jianjun Chen and Heping Xie,

for their endless support and caring to my life,

to my son, Lucas Xie, for inspiring me towards a brighter future,

and to beloved wife, Shunqin Chen, for being there with me.

Acknowledgements

It is my great pleasure and fortune to meet and collaborate with many remarkable people during my work towards to the Doctoral degree. Without their guidance, support and contributions, I would not be able to end the dissertation as a sole author. It is now my pleasure to express my gratitude to all of them.

I would like to thank Professor R.D. Gomez for his endless support to me, my family and my research. I thank him for leading me to the fascinating world of research with his continual encouragement and guidance. He always made himself available as a mentor and a friend to give me advice and suggestions. This thesis would never be initiated without him. I express my sincere gratitude to Professor Thomas Murphy and Dr. Abhishek Motayed for introducing me to the fruitful research of semiconductor oxides. It is their invaluable insight and inspiration that guide me to the correct direction for solutions. I thank Dr. Albert Davydov for his numerous support and suggestions for my research at the National Institute of Standards and Technology (NIST), which made the project possible.

I would also thank to the dissertation committee members Professor Martin Peckerar and Professor Lourdes Salamanca-Riba for their time and efforts to evaluate this dissertation.

I am very grateful to all my friends and colleagues at Laboratory for Physical Science (LPS) and NIST for their support towards my work. Special thanks go to Dr. Charles Krafft, Dr. Michael Dreyer, Dr. Danilo Romero and Jin-seock Ma at LPS for their education and help to build up my experimental skillset at the very beginning stage of

my research. My sincerely gratitude goes to Dr. Ratan Debnath at NIST for his enlightening suggestions to my research and many opportunities for collaboration. My appreciation goes to Md Rezaul Hasan, Dr. Kristen Steffens, Dr. Cindi Dennis, Dr. Serigy Krylyuk and Dr. Jong-yong Ha for helping me with various things at NIST. I also thank to my fellows at N5 sensors, Inc, Dr. Baomei Wen, Dr. Guannan Liu, Nichole Sullivan, Audie Castillo and Brian Thomson for proving me enjoyable working environment and offering me help in many aspects.

My deepest gratitude goes to my beloved wife Shunqin Chen for being at my side all these years to support me and inspire me. Her encouragement is invaluable for me in difficult times. I am thankful to my parents Jianjun Chen and Heping Xie for their unconditional endless support for my study and my life.

Table of Contents

List of Tables

List of Figures

1. Chapter 1: Introduction

1.1. Motivation

1.1.1. CoFeB based spintronics

CoFeB has attracted significant attention for spintronics application in the past decade [1-6] due to its low coercivity, high spin polarization, low anisotropy, and high resistivity. These attributions are ideal in spintronics which relies on two fundamental discoveries: the giant magnetoresistance (GMR) effect [7, 8] and the tunneling magnetoresistance (TMR) effects [9, 10].

Giant magnetoresistance (GMR) is a property of certain multilayers of ferromagnetic/non-ferromagnetic metal (spacer)/ferromagnetic known as spin valves. The electrical resistance of a spin valve changes significantly depending on the magnetic alignment of the layers, which can be controlled by external magnetic field. The phenomenon is caused by the selective scattering of electrons with minority/majority spin polarization between the polarizing source and detector layers. Therefore, the ferromagnetic material with very high spin polarization and very low coercivity, such as CoFeB, is well suited for building sensitive GMR spin valves [11-13].

Since the spacer layer of spin valves is also metallic, the intrinsic resistance of a GMR based device is low. This is in contrast with a TMR based magnetic tunnel junction (MTJ), which is similar to a spin valve except that the spacer layer is insulating. The magnetization of ferromagnetic layers of a MTJ can be controlled by applying an external magnetic field. Depending on relative orientations of ferromagnetic layers in a MTJ, the tunneling current through the insulating layer changes dramatically. Recently, ultrahigh TMR has been achieved in MTJs consisting of CoFeB/MgO system, with record ratios of 603 % and 120 % for planar and perpendicular schemes, respectively [14, 15]. Beyond the widespread use in MTJs, CoFeB is also favorable for controlled domain wall motion devices due to its high spin polarization and low crystalline anisotropy [1, 11].

A domain wall (DW) is an interface between two distinct magnetic domains. The movement of DW or equivalently the switching of local magnetization can be accomplished with spin-polarized current [16, 17] and external magnetic field [18, 19]. The reversal of magnetization with spin-polarized current is induced by the spin-torque-transfer (STT) effect, which was predicted by Slonczewski [20] and Berger [21]. STT originates from the spin-dependent scattering of electrons that is opposite to spin-polarization process [22]. This effect is exploited in nanowires patterned with ferromagnetic materials and controlled domain wall motion devices have been realized [17, 19, 23]. This concept has been suggested for the next generation stable non-volatile magnetoresistance random access memory (MRAM) with high bit density, long lifetime, and low power consumption [18, 19, 22, 23]. Low power switching is particularly important to reduce heat in high frequency operation. To further lower the

energy requirement in a magnetization switching, the domain wall pinning strength that is proportional to the Gilbert damping constant must be diminished [24]. The amorphous nature and the low damping constant [25-27] of CoFeB (0.006) makes it suitable for applications in low switching power DW motion devices.

1.1.2. Nanoscale magnetic islands for biomedical devices

Nanoscale magnetic islands have been employed extensively in high-density magnetic recording media in the past [28]. In recent years, magnetic particles have also been exploited for various biomedical uses according to therapeutic effects evident from the enhancement of bacterial biofilms growth in the presence of moderate applied magnetic field [29-31]. These findings open up the intriguing potential of using embedded or surface coated submicron magnetic islands as components of implantable alternative therapy devices. For such applications, owing to the non-planar geometries of implantable medical devices, the conventional lithography process for forming nanoscale islands is extremely challenging. To circumvent the impracticality in this and other applications, an alternative approach to form nanoscale magnetic islands from continuous CoFeB and copper thin films is introduced in this thesis. The goal is to develop a technique without the need of masks and other lithography steps to fabricate nanoscale magnetic islands, and to understand and control their geometry and areal density. The interest is to understand the diffusion of the Co and Fe magnetic species concomitant with the crystallization of the copper. The copper grains create nanometer size voids that are presumably filled with CoFe, creating a distribution of nanometer sized clusters in a matrix of Cu. We are interested in determining if the stoichiometry of the original film is preserved during diffusion since the technologically important

properties-low coercivity and high spin polarization of $Co_{1-x}Fe_x$ alloy manifests itself only over a narrow range of x. We are also interested in studying how the resulting nanoparticle size and distribution can be controlled by a judicious choice of bilayer film thickness and annealing conditions.

1.1.3. Semiconductor oxide based UV photodetectors

high-performance PD is generally designed to meet the high *5S* standards, i.e. *sensitivity*, *signal-to-noise ratio*, *spectral selectivity*, *speed* and *stability* [32], as well as to achieve linear photoresponse with respect to the incident light power [33]. The priority of the above performance factors for a UV PD design depends significantly on the specific applications, for instance, a fast response time can be the primary requirement in UV imaging, in which fast signal acquisition is a necessary [33].

Conventional UV PDs based on well-established Si photodiode, pyroelectric device, vacuum tube, and charge coupled device are currently the mainstream in the market [34]. However, the narrow bandgap (1.1 eV, infrared) of Si requires extra costly high pass optical filters and phosphors to tune the Si-based PDs to the appropriate spectral ranges and block the long wavelength response, which poses challenges to achieve new generation of UV detection system with miniature size, high energy-efficiency and low-cost [32, 33]. To overcome the limitation inherent from the narrow bandgap of Si, UV PDs consisted of wide-bandgap materials, such as GaN, SiC, and wide-bandgap semiconductor oxides, have recently emerged and developed rapidly [35-42]. The use of semiconductor oxides in UV PDs mainly rely on their intrinsic properties, including optical transparency in the near-UV and visible spectra, low impact to environment, and thermal stability. UV PDs constructed with semiconductor oxides have been

explored mainly in the structures of photoconductor, metal-semiconductor-metal, Schottky barrier, *p-i-n* junction and *p-n* junction, as illustrated in the Figure 1.2.1. Table 1.1 summarizes physical properties of several semiconductor oxides that have been demonstrated in UV PDs applications.

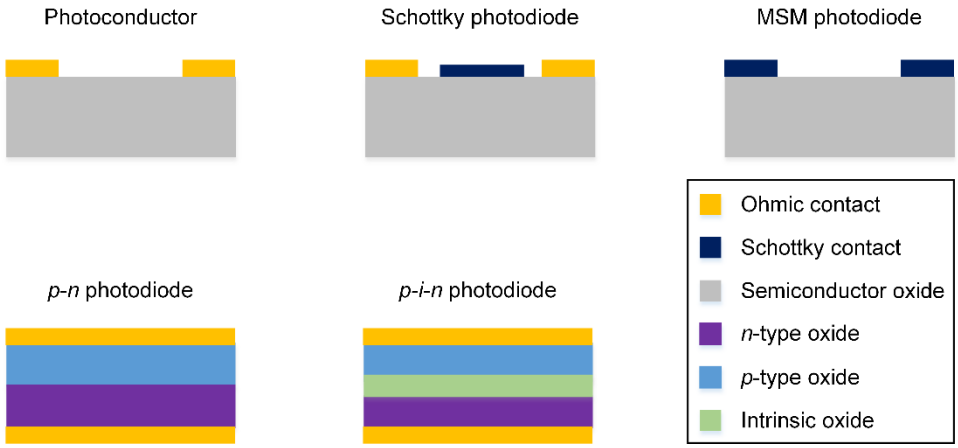

Figure 1.2.1 Schematic structures of demonstrated semiconductor oxide based UV photodetectors.

Table 1.1 Properties of several semiconductor oxides for UV PDs applications.

Semiconductor oxides	Crystal structures	Carrier type	Bandgap/eV
SnO_2	Tetragonal	n	3.6-4 (direct), 2.6 (indirect)
ZnO	Hexagonal	n	3.37
NiO	Octahedral	p	3.6
In_2O_3	Cubic	n	3.6 (direct), 2.5 (indirect)
CeO_2	Cubic	n	3.2

1.1.4. Emerging applications of semiconductor oxides in gas sensors

Gas sensor technology has developed at a remarkable pace over the last few decades. Gas sensors have become an indispensable element for applications ranging from toxic

gas detection to industrial monitoring. Though numerous gas sensors based on various techniques and materials are now commercially available, research efforts are being continuously directed towards the development of next-generation miniaturized gas sensors with ultra-low power consumption [43]. Among the widespread materials for gas sensing applications, solid state semiconductor oxides (SCOs) distinguish themselves over other competitors because they possess distinctive electrical properties that are often highly sensitive to chemical environmental changes and moreover they are compatible with modern microelectronics process and thus allow for miniaturization and low-cost fabrication [44, 45]. Because of these properties, semiconductor oxides have been widely investigated to find new functionalities of chemiresistivity [46]. Various gas sensors based on TiO_2, SnO_2, ZnO, CuO, WO_3, CoO and many others has been demonstrated with high selectively and sensitivity towards the numerous gas species, including hydrogen (H_2), carbon monoxide (CO), carbon dioxide (CO_2), nitrogen oxide (NO), nitrogen dioxide (NO_2), Hydrogen sulfide (H_2S), ammonia (NH_3), methanol (CH_4), Benzene (C_6H_6), Hydrogen cyanide (HCN) and many others [47-54]. In many of these gas sensors, the functional oxides oxidize the analyte gases fully or partially. The primary gas detection technique relays on the change in the electrical resistance of the of semiconductor oxides. When being exposed to gas species, the sensing oxides oxidize the analyte gases fully or partially, modulating the oxygen concentration on the surface and consequently altering the electrical resistance of the material [44, 46, 55].

The development of semiconductor oxide based gas sensors is tightly in parallel with the advances in microelectronics. Therefore, current semiconductor oxide based gas

sensors have been exploited and investigated mainly in the conventional pellet, thick and thin film structures, which are high compatibility with modern electronic fabrication technologies [55]. In addition to bulk and thin-film sensors, the use of nanoforms of semiconductor oxides as gas sensors has drawn considerable attention recently [55-58]. The basic nanoforms employed for gas sensing applications include nanoparticles, nanowires, nanotubes, and nanobelts [55]. The higher surface to volume ratio and smaller grain size of the oxides in the nanoforms has been shown to improve the sensitivity of gas sensors [45, 55].

Owning to the large interaction energy required for the chemisorption [59], semiconductor oxides based gas sensors are usually operated at elevated temperature. However, at high operating-temperature, sensors suffer from the degradation of material and structure due to coalescence of grains [60]. In the last decade, UV-assisted gas senting has attracted considerable attention because of the enhanced chemical gas response under UV illumination. UV-assisted gas sensing of semiconductor oxide based sensor could potentially be employed at room temperature [59, 61-66], which not only prolongs the sensor lifetime, but also reduces power consumption [67]. Moreover, low temperature gas detection also allows for the operation of sensors in hazardous (e.g., flammable or explosive) environments. For instance, situations where the working ambient atmosphere contains concentrations higher than the lower explosion limit (LEL). Moreover, room temperature operation of gas sensors enables the integration of gas sensors with Si-based integrated circuits and a completely eliminates heating elements.

1.2. Scope and goals of the thesis research

This thesis aims to investigate the magnetism of CoFeB and demonstrate the applications of semiconductor oxides in gas sensors and UV photodetectors. The dissertation research was conducted within a coherent framework of engineering solid-state thin films at the nanoscale.

This dissertation is divided into seven chapters. Chapter 2 reviews the relevant fundamental basics of ferromagnetism and the concept of domain walls, as well as the properties of CoFeB alloys. Chapter 3 overviews the development of gas sensors and UV photodetectors. This chapter also provides the theoretical basis for semiconductor oxide-based gas sensors and UV photodetectors. Chapter 4 describes several thin film and nanostructure characterization methods, namely Auger electron spectroscopy (AES), magnetic force microscopy (MFM), X-ray photoelectron spectroscopy (XPS), X-ray diffraction (XRD) and Tauc's plot, which are used to characterize the materials under consideration.

Chapter 5 investigates the magnetism of CoFeB nanostructures by addressing following three questions, namely, 1. what are the surface compositions of annealed CoFeB/Cu films under different conditions? 2. What is the role of under-layer thickness, under-layer material and annealing temperature in determining the areal density and size of formed submicron magnetic islands in a CoFeB/Metal bilayer film? 3. What is minimum external magnetic field needed to move a domain wall in a CoFeB nanowire? The chapter is organized into three sub-chapters to answer the questions. In Chapter 5.1, CoFeB/Cu bilayer films were prepared with various thicknesses and substrates using different physical vapor deposition (PVD) techniques, and annealed

the films at different temperatures under UHV condition. A series of Auger electron spectroscopy measurements were performed on the prepared films to conclude the annealing effects on surface compositions of CoFeB/Cu films. Chapter 5.2 reports a novel yet simple mask-less method for fabricating monodispersed nanoscale magnetic islands by annealing continuous CoFeB/Cu bilayer films. The surface composition at various stages of preparation was determined by *in situ* Auger electron spectroscopy, along with scanning electron microscopy (SEM), high-resolution atomic and magnetic force microscopy. The composition of the magnetic clusters was established by energy dispersive x-ray spectroscopy (EDS). The results indicate that annealing drives the diffusion of the coalesced Co and Fe into the Cu under-layer, causing them to aggregate into submicron islands at the Cu grain boundaries. Meanwhile, the areal density of the islands was found to be strongly dependent on the Cu thickness and annealing temperature, while the size of magnetic particles was only weakly dependent. This feature allows me to control the distribution of monosized magnetic islands. In Chapter 5.3, CoFeB nanowires were fabricated with e-beam lithography and examined with MFM to demonstrate the formation of head-to-head or tail-to-tail DWs. An in-situ MFM scanning with applied in-plane magnetic field was also performed to show the DW motion in CoFeB nanowire with moderate external field.

Chapter 6 describes the application of wide-bandgap semiconductor oxides in high-performing ultraviolet (UV) photodetectors (PDs). Chapter 6.1 reports the significant performance enhancement of SnO_2 thin film UV PDs through incorporation of CuO/SnO_2 *p-n* nanoscale heterojunctions. The self-assembled nanoheterojunctions were formed by sputtering Cu clusters that oxidize in ambient to form CuO on SnO_2

thin films. The morphology, the distribution of nanoparticles, and the optical properties of the CuO/SnO_2 heterostructured thin films were investigated The performance improvements were attributed to enhanced UV absorption, demonstrated both experimentally and using optical simulations, and electron transfer facilitated by the nanoheterojunctions. The peak responsivity of the PDs at a bias of 0.2 V improved from 1.9 A/W in a SnO_2-only device to 10.3 A/W after CuO deposition. The wavelength-dependent photocurrent-to-dark current ratio was estimated to be ~ 592 for the CuO/SnO_2 PD at 290 nm at the incident light power of 6.9 μW. In Chapter 6.2, solution-processed p-n heterojunction photodiodes have been fabricated based on p-type NiO and ternary n-type $Zn_{1-x}Mg_xO$ (x = 0 – 0.1). Composition related structural, electrical, and optical properties are also investigated for all the films. The bandgap of $Zn_{1-x}Mg_xO$ films can be tuned between 3.24 eV to 3.49 eV by increasing Mg content. The fabricated highly visible-blind p-n junction photodiodes show excellent rectification ratio along with good photoresponse and quantum efficiency under UV illumination. With an applied reverse bias of 1 V and depending on the value of x, the maximum responsivity and detectivity of the devices varies between (0.22 - 0.4) A/W and (0.17 - 2.2) × 10^{12} $cm.\sqrt{Hz}/W$, respectively. The photodetectors show excellent UV-to-visible rejection ratio. Compositional non-uniformity has been observed locally in the alloyed films with x = 0.1, which is manifested in photoresponse and x-ray analysis data. Chapter 6.3 presents Auger electron spectroscopy (AES) studies of $Zn_{1-x}Mg_xO$ films grown by interrupted atomic-layer deposition (ALD) techniques. The films were fabricated by alternating ALD deposition of ZnO and MgO layers up to 1000 cycles. $Zn_{1-x}Mg_xO$ films with progressively decreasing Mg/Zn ratios (Mg/Zn =

1/1, 1/2, 1/3, 1/4, 1/5, 1/6, 1/9 and 2/8, 3/12, 4/16, and 5/20) were fabricated for this study. The AES results exhibit an abrupt drop of Mg composition on the ZMO surface when the Mg/Zn < 1/3. Additionally, the surface composition ratios of O to Mg, O to Zn and Mg to Zn were estimated with known Auger sensitivity factors. The results indicate that Mg ions diffuse into the bulk, forming $Zn_{1-x}Mg_xO$ alloys.

Chapter 7 demonstrates TiO_2 based, chemiresistive gas sensors which operate at room temperature under ultraviolet (UV) illumination. In Chapter 7.1, rf-sputter deposited and post-annealed TiO_2 thin films were characterized by atomic force microscopy, X-ray photoelectron spectroscopy, and X-ray diffraction to obtain surface morphology, chemical state, and crystal structure, respectively. UV-vis absorption spectroscopy and Tauc's plots show the optical properties of the TiO_2 films. Under UV illumination, the NO_2 sensing performance of the TiO_2 films shows a reversible change in resistance at room-temperature. The observed change in electrical resistivity can be explained by the modulation of surface-adsorbed oxygen. This work is the first demonstration of a facile TiO_2 sensor for NO_2 analyte that operates at room-temperature under UV illumination. Moreover, the sensitivity of the TiO_2 sensors can be further enhanced by adding foreign receptors such as Ag and Au nanoparticles (NPs). The morphology of deposited metal NPs were studied by AFM. Furthermore, the fabrication process of the TiO_2 based NO_2 sensors was optimized to achieve higher sensitivity and the effect of carbon contamination on sensing performance was studied by XPS. Chapter 7.2 covers the demonstration of using electrostatic force microscopy (EFM) in combination with atomic force microscopy (AFM) as a non-destructive technique for morphological characterization of the dispersed TiO_2 NPs on GaN NWs. A tip-surface capacitor model

was proposed to discuss the applicability of this method to other material systems. The TiO_2 and TiO_2-Pt functionalized GaN nanowires have also been as sensors for NO_2 and H_2, respectively.

2. Chapter 2: Ferromagnetism of the CoFeB alloy

2.1. Energy and Domain Theory of Ferromagnetism

Magnetic domains and their transient regions domain walls were firstly introduced by Pierre Weiss in the early 20th century [68]. These concepts allow people to understand ferromagnetism in terms of the alignment of magnetic moments. Within past few decades, the development of magnetic imaging techniques, including magnetic force microcopy (MFM) and Kerr microscopy, enable the exploration of magnetic domains formed in nanoscale ferromagnetic structures. The formation of magnetic domains results from the lowering of total energy of the system. The main types of energy are magnetostatic, exchange, magnetocrystalline, and Zeeman.

Magnetostatic energy arises from the interaction of magnetic dipoles. To understand this type of energy, we need to introduce the concept of demagnetizing field in a magnetic system. The discontinuity of magnetization on surface induces magnetic charges which leads to the demagnetizing field through a dipole interaction inside the magnetized body. The field H_d is proportional to the magnetization $\vec{M}$ and is and shape-dependent. For a shape of sphere, the field is related to magnetization by a demagnetization factor N, given by,

$$\overrightarrow{\boldsymbol{H_d}} = -N\overrightarrow{\boldsymbol{M}} \qquad (2\text{-}1)$$

Therefore, the corresponding magnetostatic energy density can be expressed as

$$e_{ms} = -\frac{1}{2}\overrightarrow{\boldsymbol{H_d}} \cdot \overrightarrow{\boldsymbol{M}} = -\frac{1}{2}NM^2 \quad (2\text{-}2)$$

The exchange energy is induced by the strong interaction of two adjacent spins,

$$e_{ex} = -2J_e\overrightarrow{\boldsymbol{S_i}} \cdot \overrightarrow{\boldsymbol{S_j}} \quad (2\text{-}3)$$

where J_e is the exchange integral, $\boldsymbol{S_i}$ and $\boldsymbol{S_j}$ are spin vectors. The polarity of the exchange integral J_e depends on the crystal structure. The exchange energy is minimized when electron spins are parallel and anti-parallel, which corresponds to ferromagnetism and anti-ferromagnetism respectively.

Magnetocrystalline energy usually results from the spin-orbit coupling. The energy depends on the anisotropy of the magnetization alignment in preferred crystal directions. Two typical types of anisotropy are uniaxial and cubic whose energy density is given by the following equations [69],

$$e_{ani}^{Uniaxial} = K_{u1}\sin^2\theta + K_{u2}\sin^4\theta + \cdots \quad (2\text{-}4)$$

$$e_{ani}^{cubic} = K_1(\alpha_1^2\alpha_2^2 + \alpha_1^2\alpha_3^2 + \alpha_3^2\alpha_2^2) + K_2\alpha_1^2\alpha_2^2\alpha_3^2 \quad (2\text{-}5)$$

where K_{u1} and K_{u2} are the anisotropy constants for uniaxial symmetry system, and $\theta = 0$ is the direction in parallel to the axis of symmetry. K_1 and K_2 are the anisotropy constants for cubic system and α_1, α_2 and α_3 are the magnetization of x, y and z axis respectively.

Zeeman energy represents the interaction between the applied external field and the magnetic moments of the electronic spins. It is given by,

$$e_z = -\overrightarrow{\boldsymbol{H_{ext}}} \cdot \overrightarrow{\boldsymbol{M}} \quad (2\text{-}6)$$

where e_z is at its minimum when the magnetization aligns with the applied external field.

2.2. Magnetic domain walls

2.2.1. Bloch wall

A Bloch wall, named after the physicist F. Bloch, represents a thin magnetization transition region at the boundary between magnetic domains. Within the Bloch wall, the magnetization rotates transverse to the plane of domains, as shown in the Figure 2.1(a). The Bloch wall can therefore be considered as a thin magnetic slice with high exchange energy. Thus, in the absence of applied field or strain, Bloch walls typically appear in bulk magnetic materials whose thickness is remarkably larger than the width of the domain walls.

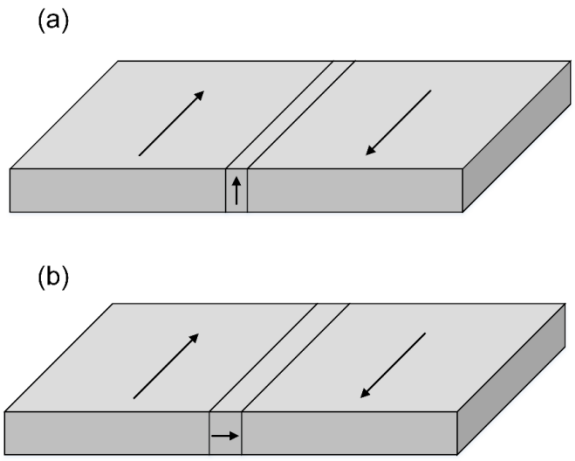

Figure 2.1 Domain wall configurations of (a) Bloch wall and (b) Néel wall.

2.2.2. Néel wall

In the contrast to Bloch walls, Néel walls dominate in thin magnetic films. Firstly studied by the French physicist L. Néel, a Néel wall is an in-plane magnetization transition region between magnetic domains that minimizes the magnetostatic dipole

interaction between poles at thin film surfaces [70]. Within the Néel wall region, the magnetization rotates continuously from the direction of the first domain to the second in the plane of domain walls. Figure 2.1(b) shows the magnetization configuration of a typical Néel wall.

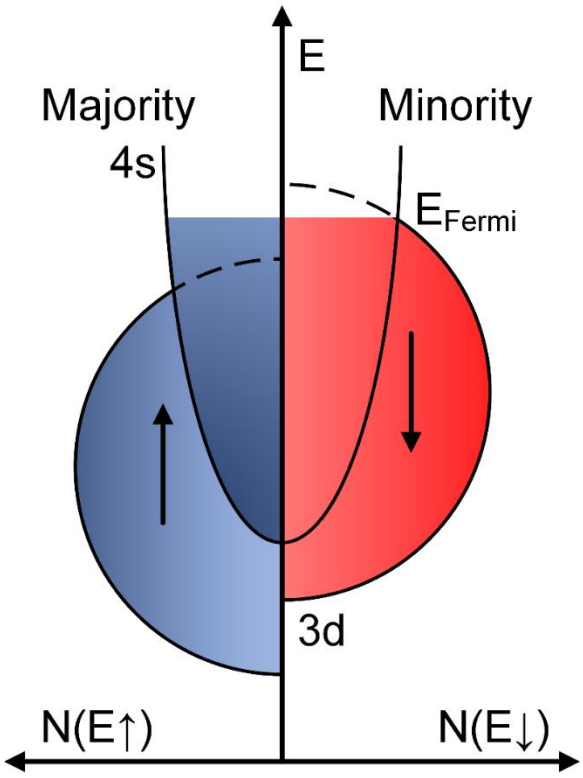

Figure 2.2 Energy band structure of ferromagnetic metals.

2.3. Properties of CoFeB alloy

The conduction band of CoFeB consists of partially filled 3d and fully filled 4s electron energy bands. A typical band structure of ferromagnetic metals, such as Fe, Co, and Ni, is shown in Figure 2.2. The Figure shows a parabolic 4s band and an asymmetric 3d band with Zeeman energy induced energy shift in spin-up and spin down electrons. In the given example of a spin polarized ferromagnetic material, the majority conduction

electron is spin-up and the minority is spin-down. The minority electrons experience more scattering due to many empty states in the spin-down 3d band, which leads to a high spin-down resistance. Consequently, the two types of electrons, spin-up and spin-down, transport through the ferromagnetic material independently and form two parallel conduction channels. Therefore, the total conductivity and resistivity of a ferromagnetic can be derived as,

$$\sigma_T = \sigma_\uparrow + \sigma_\downarrow \tag{2-7}$$

$$\rho_T = \frac{\rho_\uparrow \rho_\downarrow}{\rho_\uparrow + \rho_\downarrow} \tag{2-8}$$

where σ_T, $\sigma_\uparrow$, and $\sigma_\downarrow$ is the total, spin-up and spin-down conductivity, respectively; and ρ_T, $\rho_\uparrow$, and $\rho_\downarrow$ is the total, spin-up and spin-down resisitivity, respectively. The imbalance of density of electronic states (DOS) at the Fermi level leads to the spin polarization (P) of CoFeB with the following definition,

$$P = \frac{N(E_{F\uparrow}) - N(E_{F\downarrow})}{N(E_{F\uparrow}) + N(E_{F\downarrow})} \tag{2-9}$$

where $N(E_{F\uparrow})$ and $N(E_{F\uparrow})$ are the density of electronic states with spin-up and spin-down electrons at the Fermi level, respectively. According to results obtained from point-contact Andreev reflection measurement, the spin polarization of amorphous CoFeB can reach 65% which is much higher than Co and Fe [1]. Besides the high spin polarization, CoFeB also has several advantages including low coercivity, low anisotropy and high resistivity [25, 71, 72].

3. Chapter 3: Overview of UV photodetectors and gas sensors

3.1. UV photodetectors

3.1.1. History and development of UV photodetectors

UV radiation was firstly discovered and studied by J. W. Ritter in the earlier 19 century. The discovery, followed with many other investigations at that time, revealed that UV light is identical to visible emission except for the shorter wavelength. UV light spans the wavelength range from 10 nm to 400 nm in the electromagnetic radiation spectrum. UV light is typically divided into the following four regions: UVA with light wavelength from 315 nm – 400 nm, UVB with light wavelength from 280 nm – 315 nm, UVC with light wavelength from 100 nm – 280 nm, and extreme UV (EUV) with light wavelength from 10 nm – 121 nm [73]. As atmospheric ozone absorbs solar light below 280 nm in wavelength and visible light spans from 400 nm to 700 nm, UV PDs are identified as solar-blind and visible-blind, which response to light wavelength below 280 nm and 400 nm respectively, based on their spectral selectivity [32]. UV light is an energetic ionization radiation that can activate many chemical processes and cause severe problems, such as skin cancer to human-beings. Moreover, the detection of UV can find its applications in chemical and biological analysis, flame detection, digital imaging, missile plume detection, and optical communication [74]. Therefore, the development of high-performance UV PD is of significant importance.

A wide variety of techniques have been demonstrated and accomplished for UV detection, including photomultiplier (PMT), thermal detector, charge-coupled device (CCD), and Si-based photodiode. Photomultiplier tubes, in which a UV-sensitive photocathode ejects an electron upon UV illumination, has high gain and signal-to-noise ratio, but restricted by its bulky and fragile structure [75]. Similar drawbacks also restrict the utility of thermal UV detectors (pyrometer and bolometer) which are frequently used for calibration purpose. Thermal devices are also generally slow and wavelength-independent [75]. On the contrary, solid state device based UV PDs, such as CCD and Si-based photodiodes, are usually light-weight and energy-efficient. Due to the well-established technology and relative low-cost, Si-based UV enhanced photodiodes currently dominate the market [34]. The Si UV PDs are commonly configured as p-n junction photodiodes and charge-inversion photodiodes (similar to metal-oxide semiconductor structures) [76, 77]. However, limitations inherited from the intrinsic properties of Si exist in this type of UV PD. First of all, external optical filters are essential to block the visible and infrared photons, eliminating the long-wavelength response of the UV PD due to the narrow bandgap (1.1eV) of Si. Otherwise, the UV PD will be overwhelmed with the noise response from visible and IR signals. For instance, the spectral irradiance power over 1 cm^2 of visible and IR light under AM 1.5 condition is more than 0.1 W, which is in the same magnitude of order as a commercially available high output power UV LED. Additionally, the exposure to radiation which is much higher than the bandgap has been shown to degrade the silicon in long time operation [75]. Furthermore, SiO_2 passivation layer typically deposited on

the front surface of Si photodiodes absorbs UV radiation, thereby reducing the external quantum efficiency and it also degrading the quality of the coating over time [75].

3.1.2. Semiconductor oxide based UV photodetectors

To surmount many of the limitations listed above, a new generation of semiconductor-based UV PDs employing wide-bandgap semiconductors has been developed. Among the demonstrated wide-bandgap materials used for UV PDs, semiconductor oxides, represented by ZnO (and its alloy ZnMgO) and SnO_2, are particularly favored because of their visible-blindness, low dislocation density [78], high-energy radiation resistance,[79] chemical and thermal stability [80], for UV detection. Thus, semiconductor oxides are the potential candidates for the next generation of UV PDs.

Figure 1.2.1 illustrates 5 different configurations that have been used for UV photodetection: photoconductor, Schottky, MSM, *p-n*, and *p-i-n* photodiodes. Each structure has its uniqueness of advantages in the UV PD application. The photoconductor consists of two ohmic contacts on semiconductors. This type of UV PD is essentially a radiation-sensitive resistor. In general, Schottky and MSM photodiodes have the common advantages of low-temperature process, fabrication simplicity, low-noise, and high response speed [34]. The *p-n* junctions are the most common and well-studied structure for UV detection. UV photodiodes are typically more sensitive but slow, due to the low carrier diffusion velocity, in response to incident light than Schottky photodiodes [34].

Several frequently used and important figures of merit of semiconductor oxide based UV PDs are enumerated below:

i. External quantum efficiency η is the ratio of the number of collected carriers to the number of incident photons, namely, yield of photocurrent per incident photon. It describes the coupling ability of the detector to the light radiation. The efficiency is defined as

$$\eta = \frac{I_{ph}/q}{\Phi_{in}} \tag{3-1}$$

where I_{ph} is the collected photocurrent, q is the electron charge, and Φ_{in} is the flux of incident photons.

ii. Photoresponsivity R_{ph} is determined by the external quantum efficiency η. It measures the input-output gain of a detector system. For photodetectors, it is usually defined as output photocurrent per input optical power at a specific wavelength,

$$R_{ph} = \frac{I_{ph}}{P_{in}} = \eta \frac{q\lambda}{hc} \tag{3-2}$$

Where I_{ph}, P_{in}, η, q, λ, h, and c are the collected photocurrent, the incident light power, the external quantum efficiency, the electron charge, the wavelength, Planck's constant, and the light velocity, respectively.

iii. Detectivity D^* is the parameter that evaluates the noise performance of a photodetector using the following expression (assuming that the dark current dominate the noise),

$$D^* = \frac{R_{ph}}{\sqrt{2qI_{dark}}} \tag{3-3}$$

Where $R_{ph,}$ q and I_{dark} are measured responsivity under light illumination, the electron charge, and current measured in dark, respectively.

iv. Cutoff wavelength λ_c is closely related to the bandgap E_g of a semiconductor used in the PDs. The incident photon energy should be larger than the bandgap to excite electron-hole pairs and consequently trigger the effective photoresponse. Therefore the cutoff wavelength is defined as the following,

$$\lambda_c(nm) = \frac{hc}{E_g} = \frac{1240}{E_g\,(eV)} \tag{3-4}$$

Where h, c and Eg are Planck's constant, the light velocity and bandgap of semiconductor. However, photoresponse yielded by incident photons with lower energy is also observed frequently, which is due to the defects of the semiconductors.

v. UV-to-visible rejection ratio $R_{UV\text{-}vis}$ quantifies the ratio of the photoresponse in the UV regime to the visible light regime. It is usually defined with the expression,

$$\mathrm{R_{UV-vis}} = \frac{R_{ph}(UV)}{R_{400nm}} \tag{3-5}$$

Where $R_{ph}(UV)$ and R_{400nm} are the measured photoresponsivities at a specific wavelength in UV regime and 400 nm, respectively. A high UV-to-visible ratio is always desirable for the photodetector since it shows very weak response to the solar visible spectrum and thus no filter is required.

3.2. Chemical gas sensors

3.2.1. History and development of gas sensors

A gas sensor is a device that can produce a physical or observable signal that reflects the concentration of a certain gas species. Different types of gas sensors have been

proposed and developed to meet the requirements for toxic gas monitoring and industrial sensing purposes. This overview gives a brief introduction to the most widely used types of chemical gas sensor and then focuses on the fundamental aspects of semiconductor oxide functionalized gas sensors.

The majority of gas sensors were introduced into the market in 1960s or later [43]. In general, gas sensors operate based on the combining functions of chemical reception and signal transduction. Chemical reception is characterized as the interactions of gas analyte with sensor (receptor) through adsorption, reaction, and electrochemical reaction while signal transduction transforms the affected physical properties (heat, mass, dimension, and resistance) into measurable electrical or optical signals through properly selected materials and designed structures [43]. The presence of gas receptor and signal transducer in one device scheme is the key factor in constructing a gas sensor. For instance, in a quartz crystal microbalance based HCN sensor, a CoO adsorbent serves as a gas receptor for the HCN analyte, and the resonant frequency of the quartz oscillator shifts because of the mass change, thereby forming the transducer. [81]. By following this principle, gas sensors based on semiconductors (oxides and Si), solid electrolytes, piezoelectric crystal, catalytic combustion, and optical fiber have been introduced and demonstrated [43]. Table 3.1 summaries above mentioned types of gas sensors.

Table 3.1 Various types of chemical gas sensors.

Type	Device structure	Responding signal
Si	Pd gate MOSFET	Threshold voltage
Semiconductor oxides	Pellet, film, nano-form	Resistance
Solid electrolyte	Gas cell	EMF
Piezoelectric crystal	Microbalance resonator	Resonant frequency
Catalytic combustion	Catalyst bead with Pt coil	Resistance
Optical fiber	Waveguide	Light absorption

3.2.2. Semiconductor oxides based chemiresistive gas sensors

The implementation of semiconductor oxides into gas sensing applications was initially inspired by the observation of oxide-gas reactions by Heiland [82], Bielanski *et al* [83], and Seiyama *et al* [84]. In 1962, Taguchi demonstrated a sintered SnO_2 based gas sensor and employed the sensor in a gas leakage alarm system [43, 85]. Since then, the uses of semiconducting oxides as gas sensors has drawn extensive attention in the sensor research community. However, due to the complex nature of the crystalline grains involved in a semiconductor oxide based gas sensor, the basic gas sensing mechanism is not yet totally understood [43].

In principle, semiconductor oxide based gas sensors are combinations of three basic factors, namely, receptor, transducer and utility [86]. The receptor function is related to the surface properties of the semiconductor oxides. It considers the ability of interactions between the oxide surfaces to the gas species. During the reception process, surface adsorbed oxygen on semiconductor oxides plays an important role in reacting with the exposed gas species. The adsorbed oxygen on semiconductor are ionized into

O_2^-, O^-, O^{2-} forms by gaining electrons from the surface of the semiconductor [46]. The ionization process of oxygen depends on the operational temperature. In general, O_2^-, O^-, O^{2-} forms dominate in the temperature regions < 150 °C, 150 °C to 400 °C and > 400 °C, respectively [87]. According to experimental results, the receptor function of a certain oxide can be further magnified by the loading of specific foreign receptors such as noble metals, acidic or basic oxides [43].

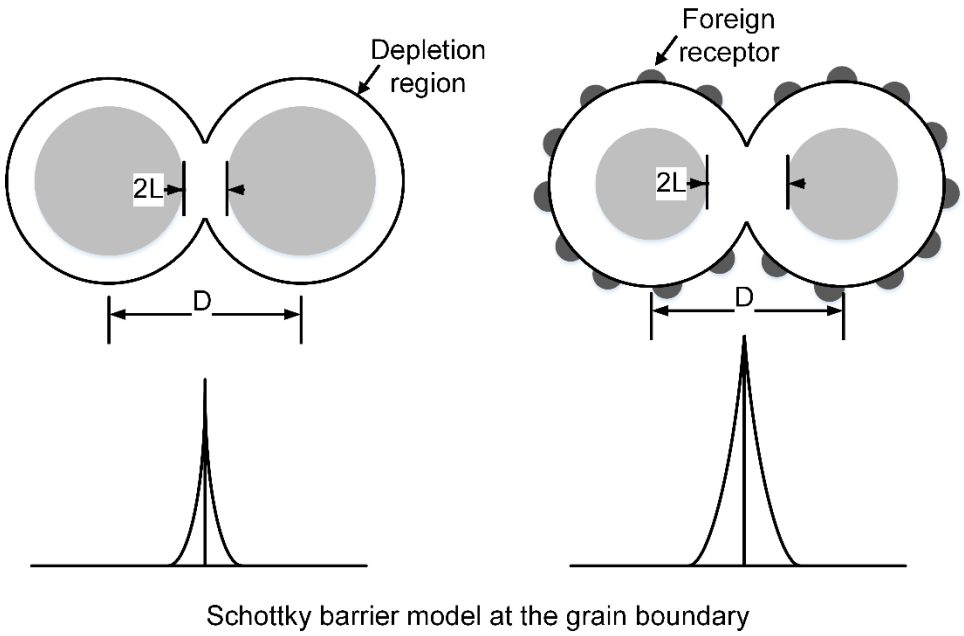

Figure 3.1 Schematic diagram of Schottky barrier model for transducer function [86].

Transducer function basically transforms the concentration change of surface adsorbed oxygen into a measurable electrical signal. The transducer function is strongly related to the grain size *D* and the depth of depletion region *L* of the sensing element [55]. A double Schottky barrier model proposed by Yamazoe is widely accepted to explain the transportation of electrons through the grain boundaries as shown in Figure 3.1 [86].

According to the model, the resistance of the sensor changes with the variation of the barrier height which is affected by the depth of the depletion region *L*. This model can also explain the precipitous enhancement of the sensing response when grain size $D \leq 2L$ [55]. Moreover, the model is in good agreement with the effects of foreign receptors on the sensing properties [43].

The utility factor concerns the diffusion of gas analyte into the bulk grains of the sensor. This factor is determined by two competing kinetic effects of the gas analyte: reaction and diffusion. If a gas analyte reacts acutely with the oxide surface, it is mostly adsorbed in a shallow region and thus cannot diffuse deeper into the bulk, leaving the rest of the sensor unutilized [86]. Based on an analysis performed on a SnO_2 thin film device [88], the depth profile of the gas concentration is determined by the magnitude of a non-dimensional factor *m* as descried by the following equation set [86],

$$\frac{C}{C_s} = \frac{cosh((1-x/L)m)}{cosh\, m} \tag{3-6}$$

$$m = L(k/D_k)^{1/2} \tag{3-7}$$

$$D_k = (4r/3)(2RT/\pi M)^{1/2} \tag{3-8}$$

Where *C* is the gas concentration within the oxide film bulk, C_s is the gas concentration on surface of the oxide film, *x* is the distance from the surface, *L* is the thickness of film, *k* is the rate of surface reaction, D_k is Knudsen diffusion coefficient, *r* is pore radius, *R* is gas constant (8.3144 J/mol K), *T* is temperature in K, and *M* is gas molecular weight. If *m* is smaller than 1, more than 30% of gas analyte can reach the bottom of the thin film. Convsersely, when m becomes large, the penetration depth decreases drastically. The relation of depth profile of gas concertation with respect to *m* is

depicted in Figure 3.2. The reaction–diffusion equation of gas diffusion dynamic is also in consistent with the well-known volcano-shaped correlation between resistance and ambient temperature [43].

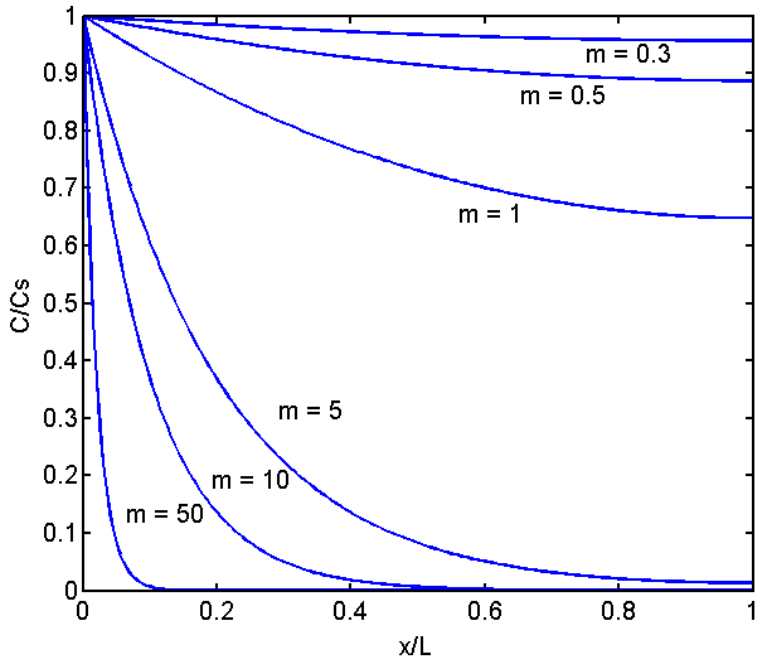

Figure 3.2 Gas concentration profile within a thin film type chemiresitive sensor.

Based on the type of majority carrier, semiconductor oxides can be characterized as *n* or *p* types. The origin of mobile carriers in semiconductor oxides comes mostly from doped aliovalent cations and oxygen nonstoichiometry [89, 90]. The fundamental mechanism governing the gas sensing of an *n* or *p* type semiconductor oxide differs in the following aspects [46]: (1) the surface adsorbed oxygen anions induced electron depletion region and hole accumulation region in n-type or p-type semiconductor oxides, respectively; (2) conduction path through cores (serial type) or boundaries

(parallel type) of the grains in n-type or p-type semiconductor oxides, respectively. The schematic illustrations of the difference are depicted in Figure 3.3.

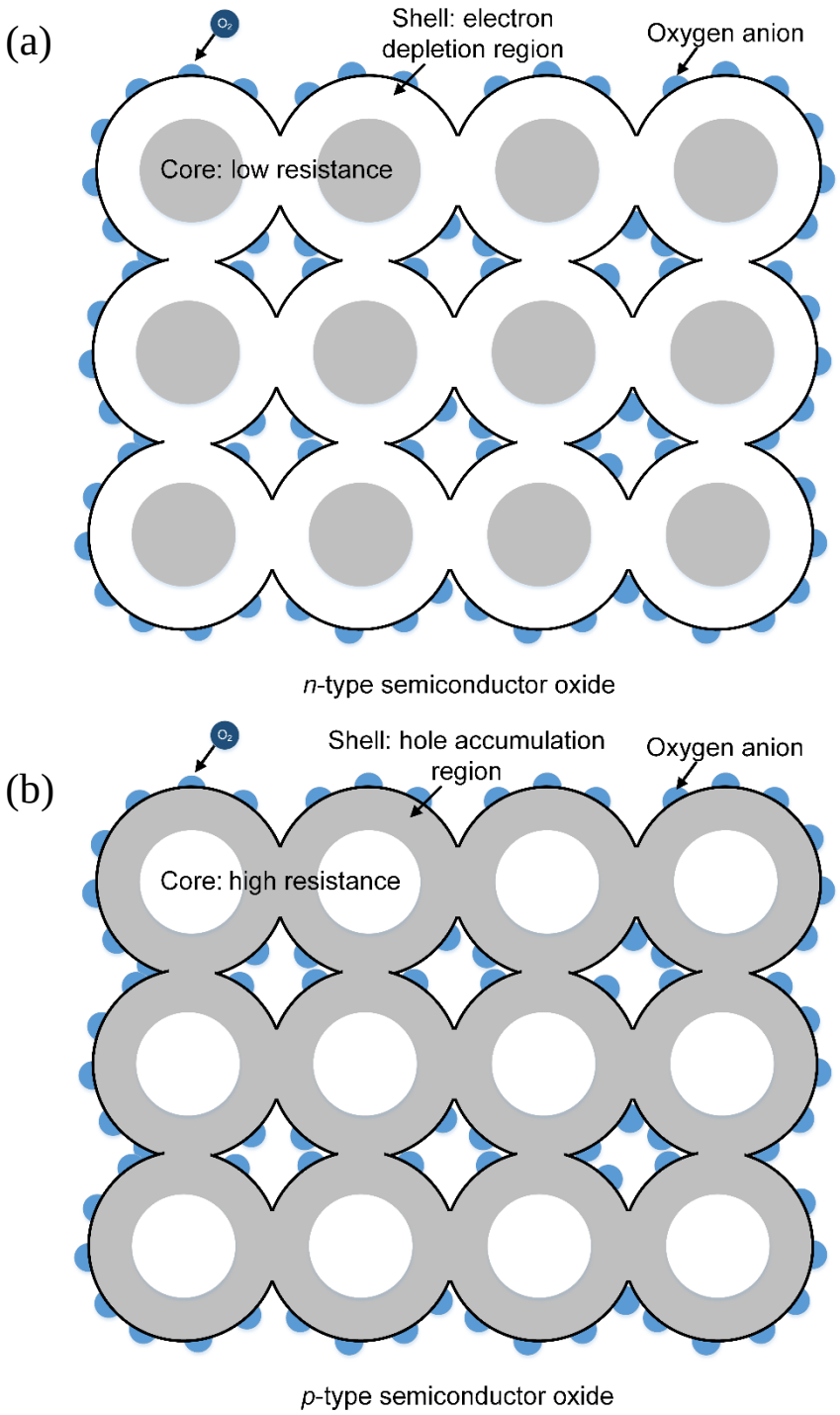

Figure 3.3 schematic diagram of the adsorbed oxygen anions with induced electron carrier distributions in (a) *n*-type and (b) *p*-type semiconductor oxide networks.

Also, the number of adsorbed oxygen anions on *n*-type or *p*-type differs markedly according to results measured from 16 semiconductor oxides using temperature-programmable desorption techniques [91]. In general, the transition metal oxides with multi-valency states, such as Fe_2O_3 and NiO, have large amount of adsorbed oxygen, which is caused by the low stability of oxides associated with redox reactions [46]. The type of gas analyte, reducing or oxidative, also poses distinct response on the semiconductor oxides sensors. For the case of n-type oxides, when reducing gas such as H_2, CO, NH_3 and H_2S is exposed to the surface of sensors, electrons are transferred into adsorbed oxygen anions, reducing the thickness of depletion region and thus the resistance. On the contrary, when oxidizing gas like NO_2 is adsorbed on oxide, more ionosorption oxygen anions will form on surface, increasing the depletion region and consequently the conductivity of sensor. The exposure of reducing and oxidative gases to *p*-type oxides will lead opposite effects on the change of resistance as indicated in the Figure 3.4.

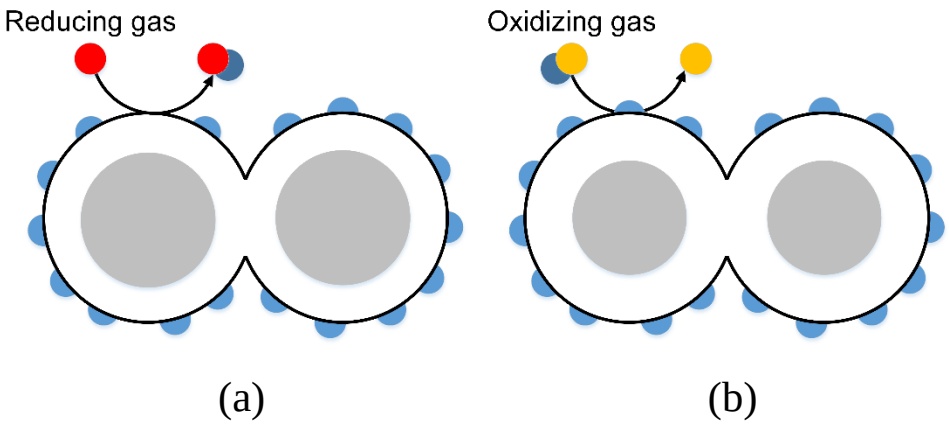

Figure 3.4 Gas sensing responses of *n*-type semiconductor oxides to (a) reducing and (b) oxidizing gas analytes.

4. Chapter 4: Overview of characterization techniques for thin films and nanostructures

4.1. Auger electron spectroscopy

The Auger process was first introduced by Pierre Auger in 1925 to explain a radiationless transition of x-ray excited ions [92]. Auger electron emission process starts with core shell ionization, resulting from bombardment of sample surface with sufficiently energetic electrons, ions, or x-ray [93]. The ionized core shell causes an outer shell electron to fill the vacancy and as demanded by conservation of energy, simultaneously emitting an Auger electron with a characteristic kinetic energy instead of a photon in the case in an x-ray photoelectron spectroscopy process [94]. The two types of relaxation processes are sketched in Figure 4.1.

By convention, Auger transitions are identified by the energy levels involved. A XY_IY_{III} Auger transition denotes that the ionized shell is X, a Y_I shell electron jumps into vacancy and a Y_{III} shell electron is emitted as an Auger electron. For simplicity, such Auger transition is denoted as XYY. Generally speaking, the number of possible Auger transitions increasing with heavier elements as they have larger number of energy levels [5]. Auger electron and x-ray photon yield of different transitions as a function of atomic number is illustrated in Figure 4.2.

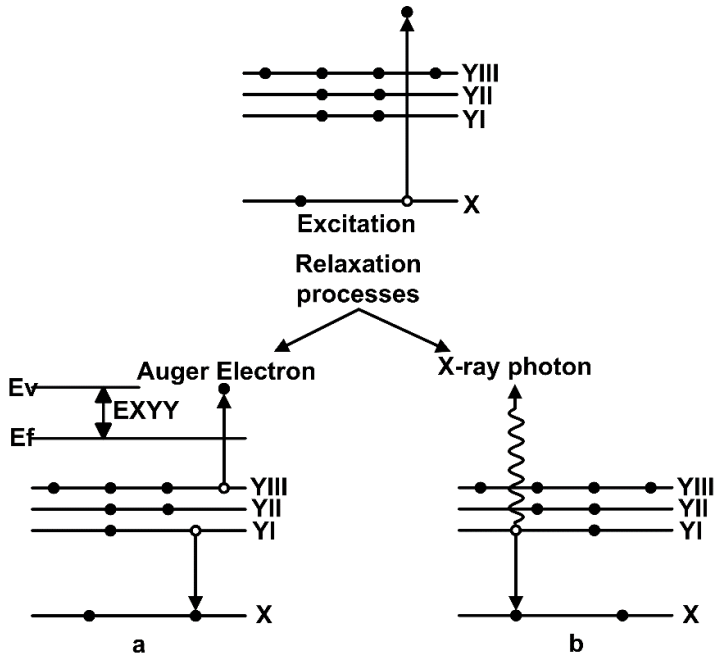

Figure 4.1 Schematic diagrams of (a) Auger electron emission and (b) X-ray photon emission process of ionized atom [93, 94].

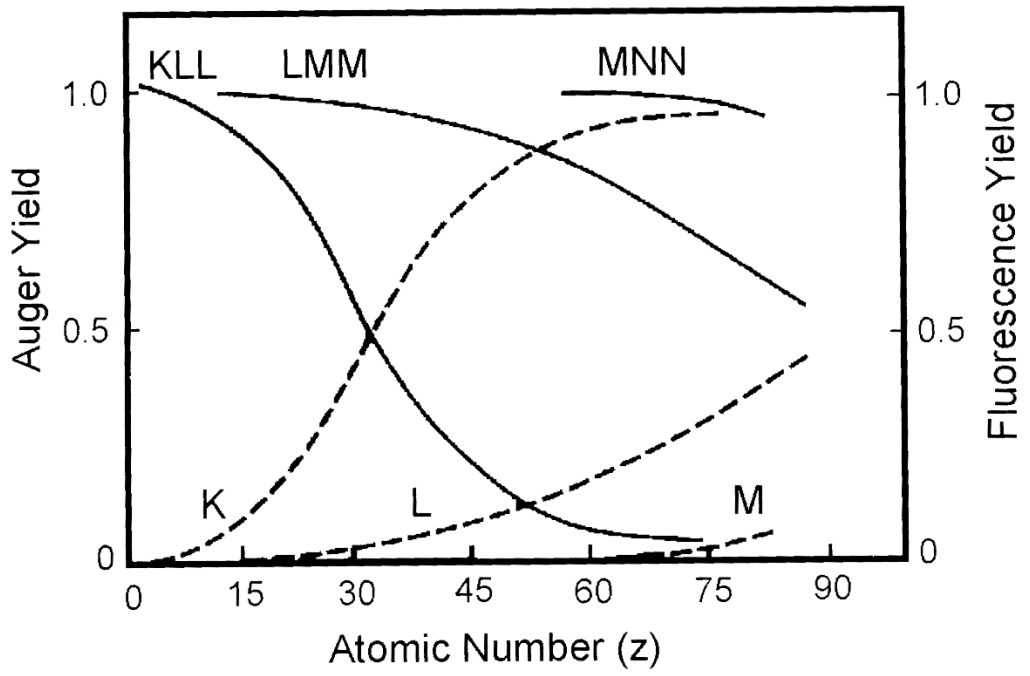

Figure 4.2 Auger electron and x-ray photon yield of different transitions as a function of atomic number. Reprinted from Childs et al. [93].

The characterization kinetic energy associated with an ABC Auger transition can be calculated by the following equation[95]:

$$E_{ABC}(Z) = E_A(Z) - E_B(Z) - E_C(Z) - \phi \qquad (4\text{-}1)$$

Where E_A is the binding energy of energy level A for the neutral atom whose atomic number is Z and ϕ is the work function. E_B and E_C are the binding energies for B or C levels after atom ionization. One approximate expression of E_B and E_C is [95]:

$$E_i = \frac{E_i(Z) + E_i(Z+1)}{2} \qquad (4\text{-}2)$$

Where E_i is binding energy of i-level and i can be either B or C. Coghlan and Clausing used this approximation to tabulate comprehensive Auger electron energies [96].

Conventional Auger electron spectroscopy represents the signal intensity of $dN(\mathrm{E})/\mathrm{d}E$ of the backscattered electrons to minimize the influence of large continuous background electron density from the emitted secondary electrons and back scattered primary electrons[97]. The elements that comprise a material or device is identified by its Auger peak positions and its peak to peak magnitude represents its composition on surface [97]. In our case, the primary incident e-beam energy was set at 3k eV. Relative Auger sensitivity factors (S_x) for different elements of incident e-beam at 3k eV are available in open resource [98].

4.2. Magnetic Force Microscopy

Magnetic force microscopy is a widely used technique to characterize the localized surface magnetism due to its high lateral resolution, capability with AFM instrument and easy sample preparation procedure [99]. MFM utilizes pre-magnetized scanning

probes to interact with the long distance stray field from a sample. The bright and dark contrast in the MFM images roughly corresponds to magnetic charges or divergence of magnetization [100]. The spatial resolution of the MFM measurement is related to the distance from probe to the sample surface [28].

A commercially available AFM instrument combined with MFM tool is available from Digital Instruments (now a division of Bruker). It combines the so called tapping mode AFM and lift-mode MFM to image surface morphology and magnetism simultaneously. Figure 4.3 is a schematic diagram to show its operation principle.

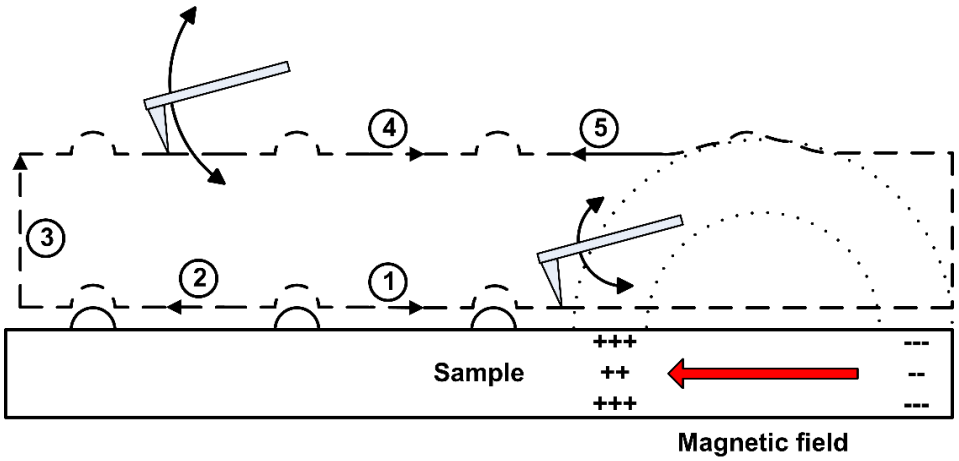

Figure 4.3 Schematic diagram of MFM lift-mode principles [101].

A thorough scanning process starts from a tapping mode AFM scan indicated as step 1 and 2 in Figure 4.3. Before loading the probe to the surface, the pre-magnetized probe is oscillated by piezoelectric material at the resonant frequency of the probe with amplitude ~ 2 V. The amplitude is detected by exploiting a photo-detector to measure the intensity of a laser beam, which is reflected from the tip of a probe. During AFM

scans in both trace and retrace directions, the information about surface topologies is acquired and stored for further application. At the end of AFM retrace, the tip is lift up to a preset lift scan height in step 3. Then the tip is forced to follow the stored topography profiles to trace and retrace the surface while recording the magnetic-induced shift in the resonant frequency of the probe. The magnetic influence will shift the resonant frequency of the probe with an amount of Δf which is proportional to vertical gradient of the magnetic force on the tip [101]. Such force gradient can be related to the magnetostatic energy $\bar{m} \cdot \bar{B}$ in an ideal magnetic dipole model with the following equation [102],

$$\frac{\partial F_z}{\partial z} = m_x \frac{\partial^2 B_x}{\partial z^2} + m_y \frac{\partial^2 B_y}{\partial z^2} + m_z \frac{\partial^2 B_z}{\partial z^2} \qquad (4\text{-}3)$$

Where m is the effective magnetic moment of the probe and B is magnetic flux. In practice, the probe is pre-magnetized in z direction, i.e. normal to the surface[100]. So only the third term on right hand side of Eq. 4.3 is effective under this situation, which simplifies the interoperation of scanned MFM image. Figure 4.4 shows the diagram of the setup for AFM and MFM measurements.

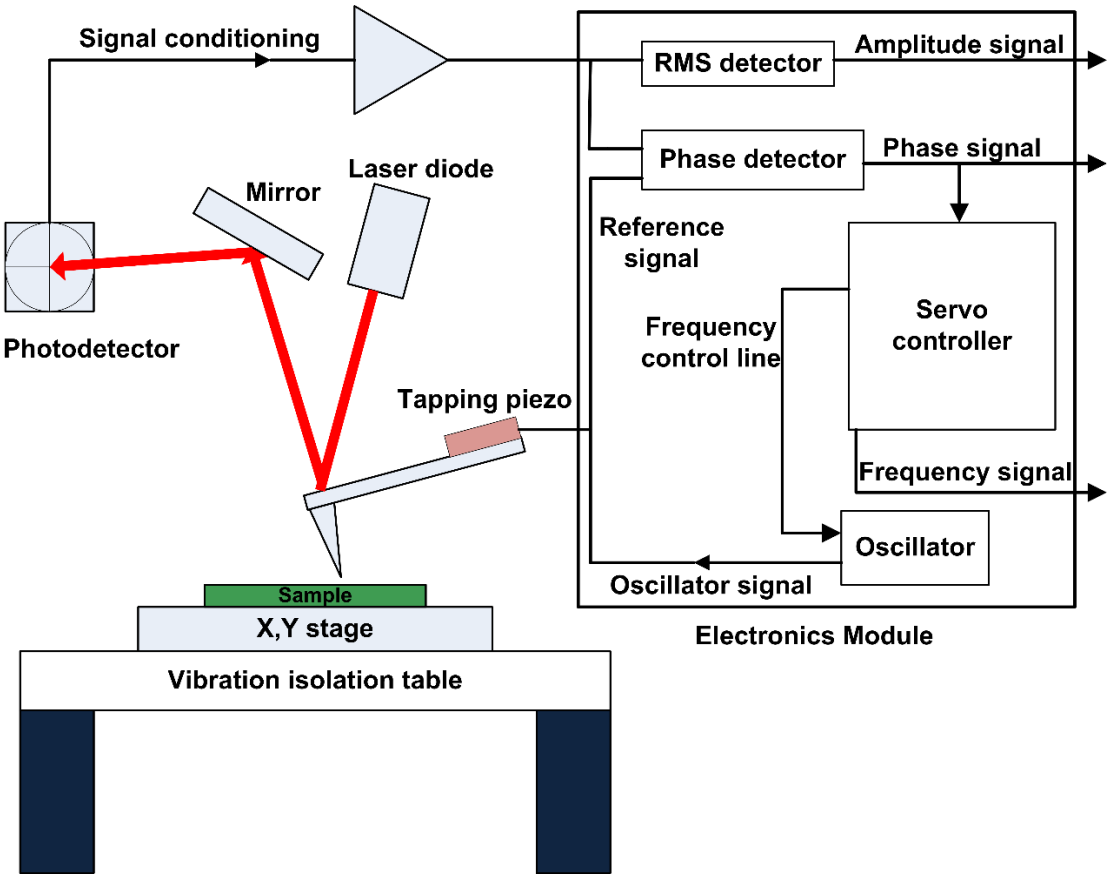

Figure 4.4 Schematic diagram of a multi-mode AFM and MFM microscope measurement system [101].

4.3. X-ray photoelectron spectroscopy

X-ray photoelectron spectroscopy (XPS) is a frequently used surface chemistry analyzing technique. In principle, XPS is capable in measuring elemental composition, chemical state and electronic state of materials. Figure 4.5 shows the schematic of a XPS instrument, depicting the basic mechanism behind XPS. X-ray photons with specific energy impinges the solid surface to excite the core level electrons emitting from the top 1-10 nm of the analyzed area. The ejected electrons are then energetically filtered by the hemispherical analyzer before collected by the detector. Since the

electronic states in atoms are quantized, the resulting photoelectron spectrum exhibits discrete peaks, over a range of electron binding energies, with characteristic electronic structures of the excited atoms. In principle, except for hydrogen, all the elements on surface can be identified and quantified by the energies and intensities of the photoelectron peaks, respectively. However, the chemical environment of the detected atoms may cause energy shifts in the spectrum, adding difficulties to interpret data accurately but providing valuable information of the surface.

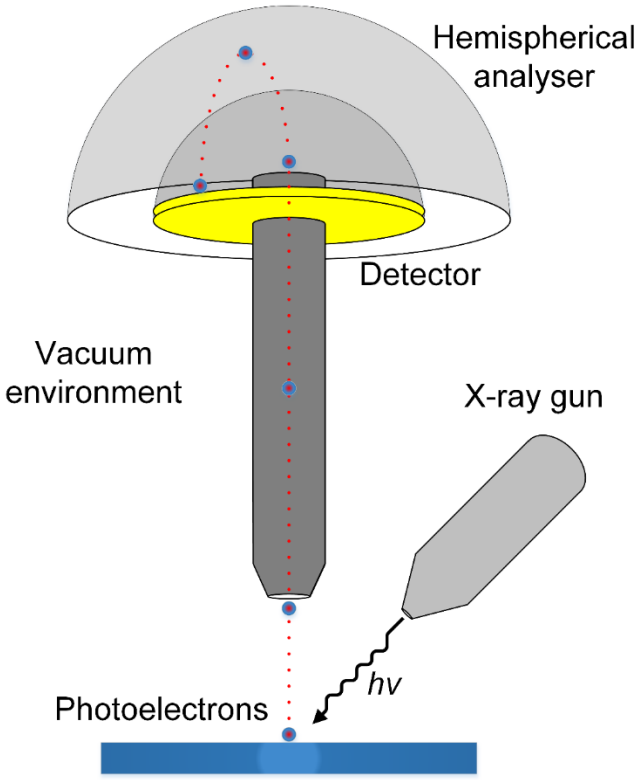

Figure 4.5 Schematic diagram of XPS measurement [103].

4.4. X-ray diffraction

X-ray diffraction (XRD) is a non-destructive analytical technique primarily used for phase identification of crystalline materials. The x-rays are generated by a cathode ray tube, in which a target material is excited using an electron beam. The x-ray is then monochromatically filtered, concentrated and focused onto the sample. The x-ray diffraction peaks result from constructive interference of the monochromatic beam of x-rays and a crystalline sample at specific angles. The angular pattern of diffracted x-ray is collected by while rotating the sample. The interpretation of x-ray diffraction patterns is based on Bragg's law ($n\lambda = 2d\sin\theta$) as shown in Figure 4.6a, which describes the relationship of the wavelength of the incident x-rays to the diffraction angle and the lattice spacing between the planes of atoms [104]. By comparison of diffraction patterns with standard reference, the phase identification of a material is achieved. Consequently, the x-ray diffraction patterns act as the fingerprint that reveals the atomic constituents of a material. For thin film applications, the conventional XRD θ/2θ scanning method generally produces weak signal from the film and intense signal from the substrate due to the deep penetration of incident X-rays. Therefore, it is widespread in thin film XRD characterization to perform a 2θ scan at a fixed grazing incidence (known as GIXRD) to minimize the signal contribution from substrate. The incidence angle α is fixed typically between 0.25^{0} to 3^{0}, exceeding the critical angle for total reflection. Figure 4.6b illustrates the grazing incidence diffraction geometry.

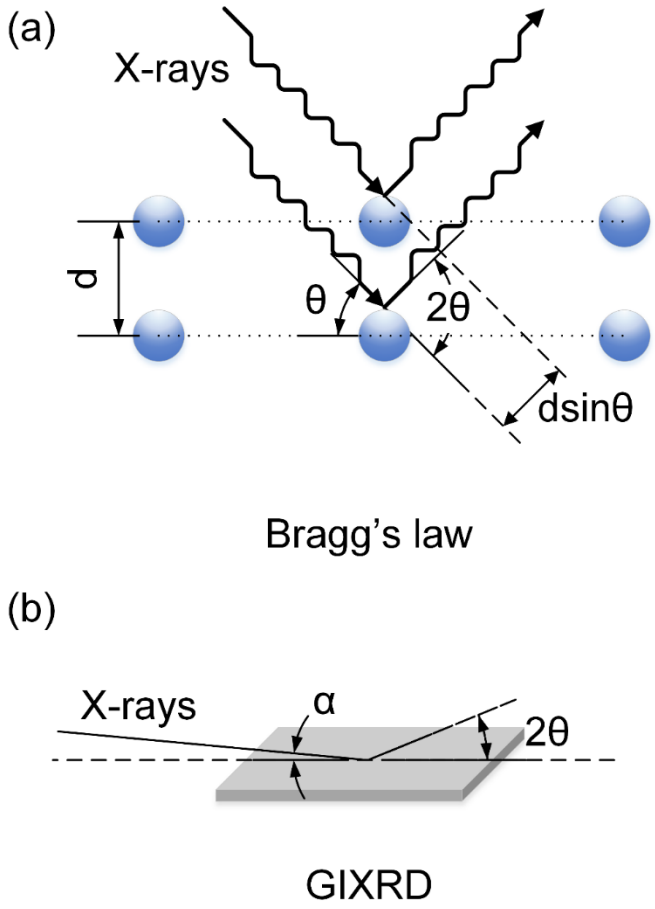

Figure 4.6 Diagram of (a) Bragg's Law at 2θ deviation angle and (b) Illustration of grazing incidence XRD at incidence angle α. The beam is diffracted in the plane of the surface of the sample by the angle 2θ.

4.5. Tauc's plot

Optical absorption measurement is a technique to characterize optical properties of amorphous semiconductor thin films. By examining how the absorption typically depends upon the photon energy, one can often deduce the electronic transition parameters of the material [105]. Several approaches, namely the Tauc [106], Tauc-Lorentz [107], and Forouhi-Bloomer [108]models, have been introduced and widely accepted. Among all the applicable models, the Tauc model is the most widespread

approach to determine the optical band gap energy in semiconductors [105]. The Tauc model is derived based on the approximate parabolic dependence of the absorption coefficient α with respect to photon energy, near the band edge of many semiconductors [106]. By following the Tauc's approach, the optical band gap energy *Eg* can be derived from extrapolating of the linear region in the curve of $(\alpha h\nu)^{1/2}$ as a function of hν with zero. More generally, the absorption coefficient generally obeys the following empirical relation [109]:

$$\alpha h\nu = \beta\left(h\nu - E_g\right)^r \tag{4-4}$$

Where β^{-1} is the band edge parameter and r is a number that denotes the nature of electronic transition. For allowed indirect transitions, r = 2; for forbidden indirect transitions, r = 3; for allowed direct transitions, r = ½; and for forbidden indirect transitions, r = 3/2 [110]. The absorption coefficient α can be decided from ellipsometry measurement or derived from absorbance spectrum with the following equation [111]:

$$\alpha = 2.303\frac{A}{d} \tag{4-5}$$

Where A is the absorbance data obtained from the spectrum and d is the thickness of the film.

5. Chapter 5: Control of morphology, magnetic and composition properties of CoFeB thin films

5.1. Investigation of annealing effect on surface elemental information of CoFeB thin film with Cu under-layer

5.1.1. Introduction

The CoFeB/Cu system has been extensively used to enhance the performance in GMR based spin valves [71, 112-119]. Among the available magnetic materials, the CoFeB is ideally suited as the spin polarized layer in the GMR based spin valve, owing to its high spin polarization and low crystalline anisotropy [1, 11]. In this application, Cu is widely used as a non-magnetic spacer layer to decouple the source and detector layers. Cu is also favored for head read sensor of HDD industry [120] due to its low cost and widespread use as interconnects in the semiconductor industry. Therefore, CoFeB/Cu bilayer structure is a ubiquitous ingredient in GMR based spin valves.

It is well accepted that the GMR effect originates from spin-dependent scattering and thus interface plays a crucial role in determining the performance of a GMR structure [121]. Therefore, it is important to know how the CoFeB/Cu interface reacts to elevated temperature. At present, there is a very limited knowledge about the changes in the

surface characteristics of a CoFeB/Cu bilayer as a function of fabrication parameters such as thickness of the bilayer as well as thermal annealing.

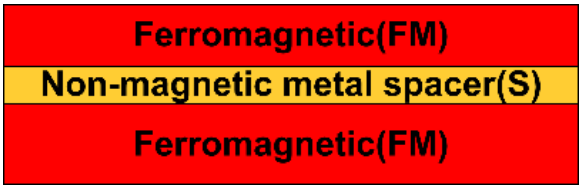

Figure 5.1 Diagrammatic structure of a GMR effect based spin valve.

The diffusion and segregation behavior of Cu with the presence of CoFeB may lead plausible solutions to improve the performance of GMR based spin. As it has already been proved that GMR can be tailored by engineering the thickness of the Cu layer in a CoFeB\CoFeB\Cu\FeMn spin valve [71]. The key role that a spacer layer's thickness plays in a spin valve structure is well realized. Diffusion of substrate Cu onto CoFeB surface after annealing will shrink the distance between two separated magnetic layers, enhancing the magnetic coupling strength. Therefore a higher external magnetic field is needed to flip the magnetization of the free layer, lowering the sensitivity of the spin valve. It is also well established that capping layers on a thin CoFeB film has effects on its magnetic properties such as dead layer, saturation magnetization and anisotropy field [122, 123]. Thus a judiciously chosen capping layer is crucial in enhancing the performance of spin valves [124, 125]. Conversely, the unexpected diffusion and segregation of substrate Cu after annealing process could alter the composition of the CoFeB/capping layer interface. Such change will lead unexpected variation in GMR performance of the spin valve. Lastly, the coercivity of a crystallized magnetic film is generally influenced by interface defects [71]. Hence, the diffusion and segregation of

Cu may cause more surface defects of the CoFeB thin film, which in turn increases the coercivity of the CoFeB film and degrades the sensitivity as well. Researchers have already shown similar behavior of Cu diffusion and segregation on NiFe surface in a Cu/NiFe/FeMn bilayer structure and the behavior results a lower exchange-bias field between NiFe and FeMn layers [126, 127].

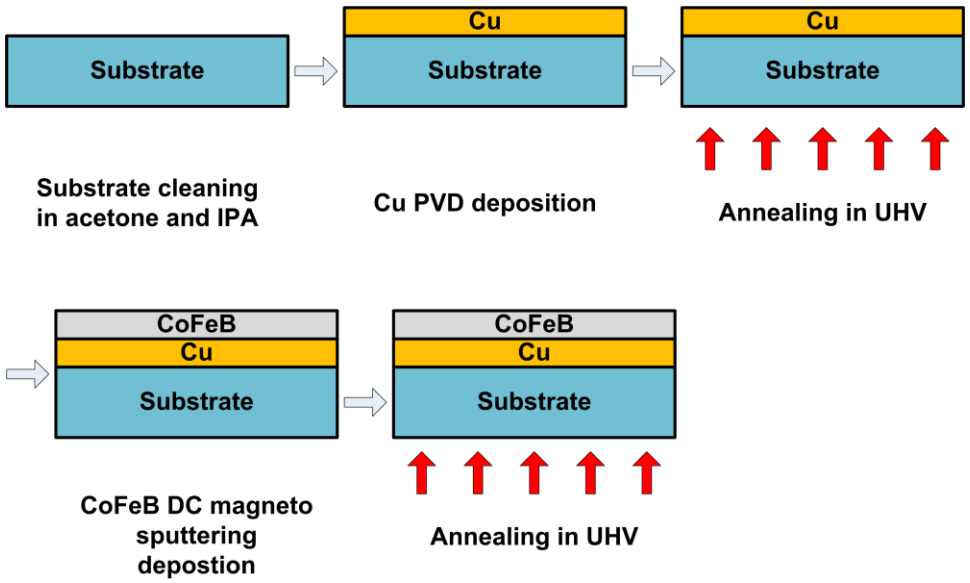

Figure 5.2 Process flow of sample preparation for the investigation of CoFeB/Cu bilayer diffusion.

5.1.2. Experimental details

To investigate the compositional information of CoFeB with Cu under-layer after annealing, different substrates (MgO and Si with thermal oxide) and different Cu PVD deposition techniques (DC sputtering and e-beam evaporation) were used to compare the diffusion properties of CoFeB into Cu substrate. CoFeB films were deposited by DC sputtering from a $Co_{60}Fe_{20}B_{20}$ target. All the film depositions were conducted under a base pressure of 2.5×10^{-6} Torr. The film thickness was determined by deposition time.

For extreme thick Cu films ~280 nm, the thickness was also measured by a Tencor profilometer. After every film deposition process, the samples were annealed around a constant temperature at ~550 °C for hours. A calibrated Mikron IR thermometer focused on sample surface measured the annealing temperatures. The sample preparation procedure is depicted in Figure 5.2.

Auger electron spectroscopy (AES) technique can be used to examine the annealing effect on the surface composition changes of a CoFeB/Cu bilayer. AES is a widely used and well established technique to obtain surface elemental information [128]. It is very surface-sensitive for nearly all elements, especially for lighter ones as experiments had already revealed the fact that L-transition of Auger electron yield dominates over x-ray emission until the atomic number is larger than 50 [94]. Also, the fact that the emitted Auger electrons can be collected at a wide range of angles leads to less constraints of the analyzer and sampling position [129]. Conventionally, Auger electron spectroscopy shows the signal of $\frac{d\mathrm{N}(E)}{dE}$ to diminish the influence of large continuous background electron density which is due to emitted secondary electrons and back scattered primary electrons [97]. Element is identified by its Auger peak positions and its peak to peak magnitude represents concentration on surface [93, 97]. Since the size of the primary e-beam is around 1 cm^2, the AES data represents an average signal of the surface. Data were obtained with a LEED/Auger spectrometer under UHV conditions. The Omicron surface analytical system used in this work consists of a tungsten electron beam gun, SPECTLEED optics, control units with integrated lock-in amplifier/oscillator and a computer workstation. The electron beam incident energy can be set as high as 3.5 keV.

The four-grid SPECTLEED Optics is used as a retarding field analyzer (RFA) in this system. The retarding voltage is applied to the grids to filter the electrons below certain energy and the passing electrons are detected at the LEED screen. A schematic diagram of the system is shown is Figure 5.3. The incident e-beam energy was set at 3 keV in this experiment. Tabulated relative Auger sensitivity focused factors (S_x) for different elements of incident e-beam at 3 keV is available in open resource [98].

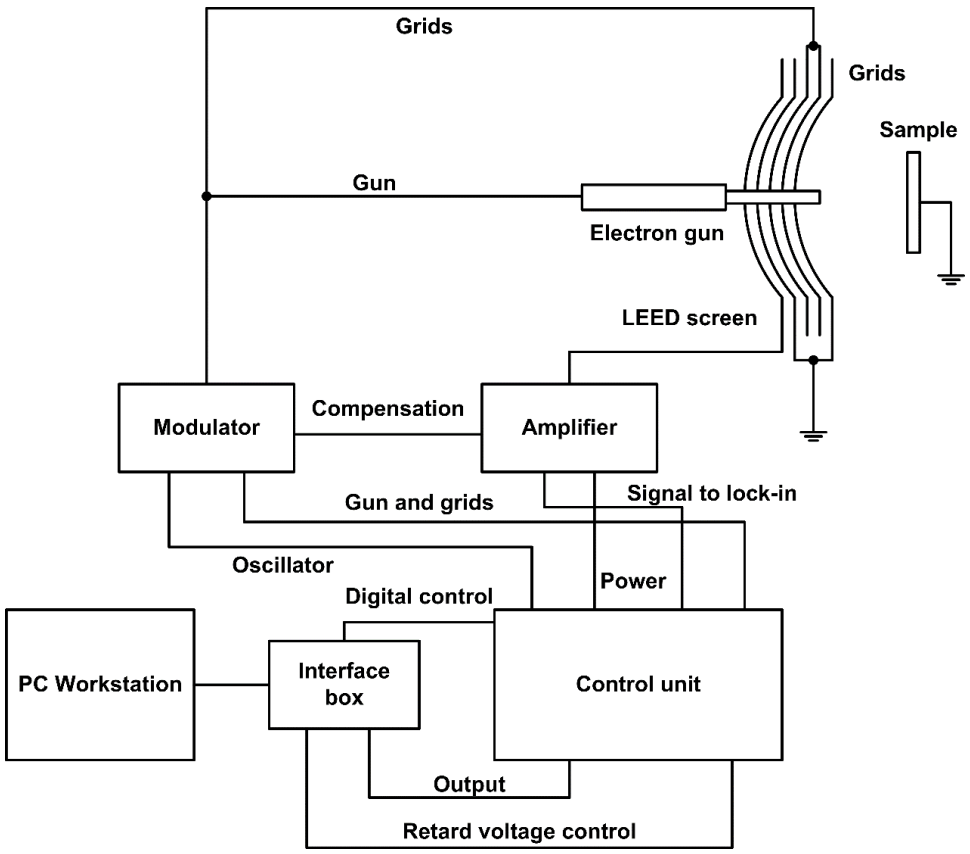

Figure 5.3 Schematic diagram of a LEED/Auger spectrometer system with a four-grid RFA [130].

While exact quantitative interpretation of an Auger electron spectroscopy remains a challenge, simple equations with accuracy can be used to calculate surface composition

[97]. The ratio of two chemical elements' compositions on surface can be estimated using the following equation [97],

$$R_Y^X = \frac{I_X / S_X}{I_Y / S_Y} \tag{5-1}$$

Where I_x stands for the absolute peak-to-peak value of chemical element X obtained from Auger electron spectroscopy. S_x is relative Auger yield and sensitivity factor of element X. Auger relative sensitivity factors for interested elements at primary e-beam of 3 keV kinetic energy are listed in Table 5.1.

Table 5.1 Auger relative sensitivity factors for B of KLL transition, Cu, Co and Fe of LMM transitions.

S_B(KLL)	S_S(LMM)	S_{Cu}(LMM)	S_{Co}(LMM)	S_{Fe}(LMM)
1.2	0.93	0.23	0.32	0.35

5.1.3. Results and discussion

AES plots were obtained after Cu and CoFeB depositions as well as annealed CoFeB/Cu bilayer to compare the annealing effect on surface elemental compositions at two distinct kinetic energy ranges (30~75 eV and 80~950 eV). Because of large number of secondary electrons collected at low energy range, AES measurement parameters such as sensitivity, time constant and oscillation amplitude for lower kinetic energy range (30~75 eV) are not directly comparable to those collected at the other ranges. Auger electron peaks are identified with reference to standard AES spectrum handbook [97]. Being neighbors in the periodic table, LMM the Fe peaks overlap with

some of the LMM Co peaks so they cannot be used to identify Fe. In the lower energy range, MNN Fe and MNN Co peaks differ by a few eV and are clearly distinct to identify Fe.

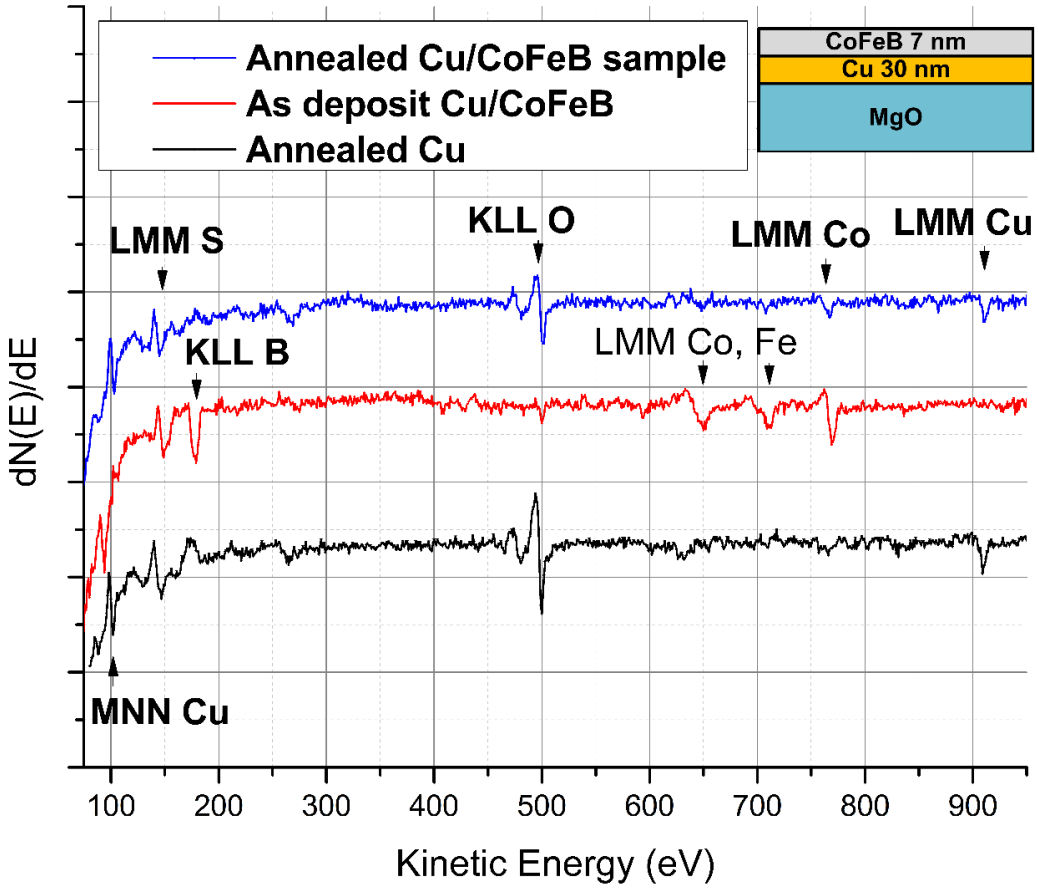

Figure 5.4 AES plots of annealed DC sputtered Cu film (black line), as-deposited and annealed (510 °C, one hour) CoFeB/Cu bilayers (red line, blue line) on a dddMgO substrate. The Auger peaks were identified with element name associated Auger electron transition, such as LMM Cu, KLL O etc.

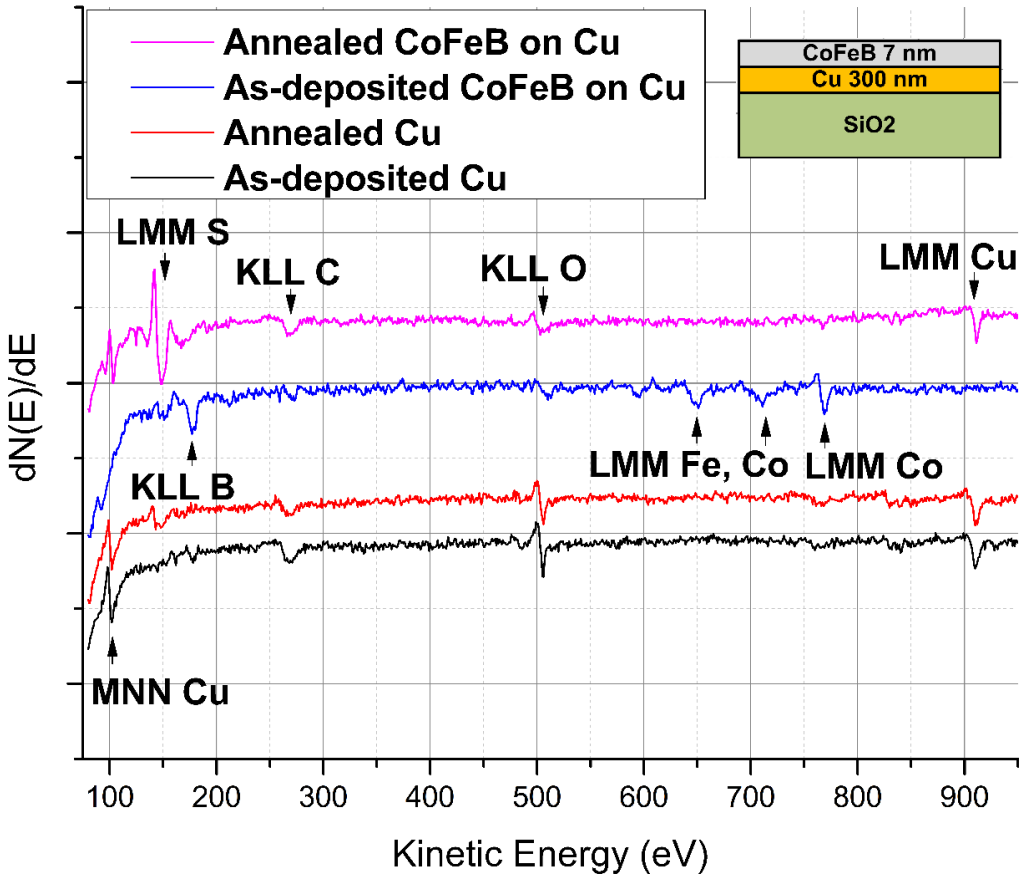

Figure 5.5 AES plots of as-deposit and annealed e-beam evaporated Cu film (Magenta line, black line), as-deposit CoFeB/Cu bilayers (red line) and annealed (580 °C, 2 hours) bilayers (blue line) on SiO2.

Figure 5.4 and Figure 5.5 show the AES plots of as-deposited and annealed Cu and CoFeB/Cu bilayers. The Auger spectra of the as-deposited CoFeB/Cu only show Co, Fe or B peaks which indicates full coverage of the deposited CoFeB thin film over the Cu substrate at the a thickness more than the mean free path of the AES electrons. After the annealing process, Cu Auger peaks appear on the surface of the CoFeB/Cu bilayers in both samples regardless differences in substrates, Cu deposition techniques and Cu layer thicknesses. At the same time, the Co Auger peaks become less intense, while Fe and B peaks have become negligible. The AES data of annealed CoFeB/Cu samples

show a direct evidence of surface CoFeB into the Cu substrate and such behavior persists regardless of substrates, Cu deposition methods and thicknesses.

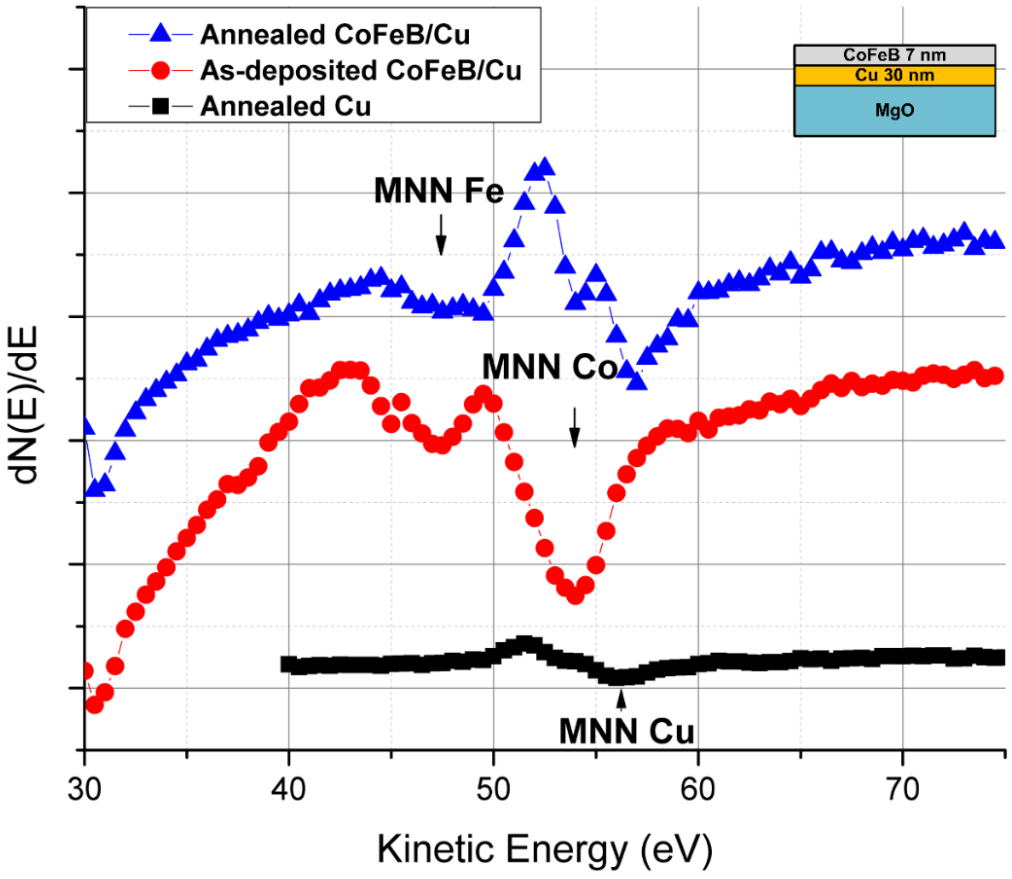

Figure 5.6 AES plots of the same sample in Figure 5.4 at a lower kinetic energy range.

Along with the appearance of Cu peaks, sulfur also shows up in the AES spectra for the annealed CoFeB/Cu samples. This is not surprising because sulfur is a common impurity in Cu and similar S segregating behavior has been observed by others [131]. The segregation of sulfur on surface is bolstered by low energy range AES date in Figure 5.6 and Figure 5.7 as well. A clear shift of MNN transition Cu Auger peaks towards higher energy can be obtained for the annealed sample. This shift implies a

change of chemical environment around Cu and thus a possible formation of copper sulfur compounds on the surface.

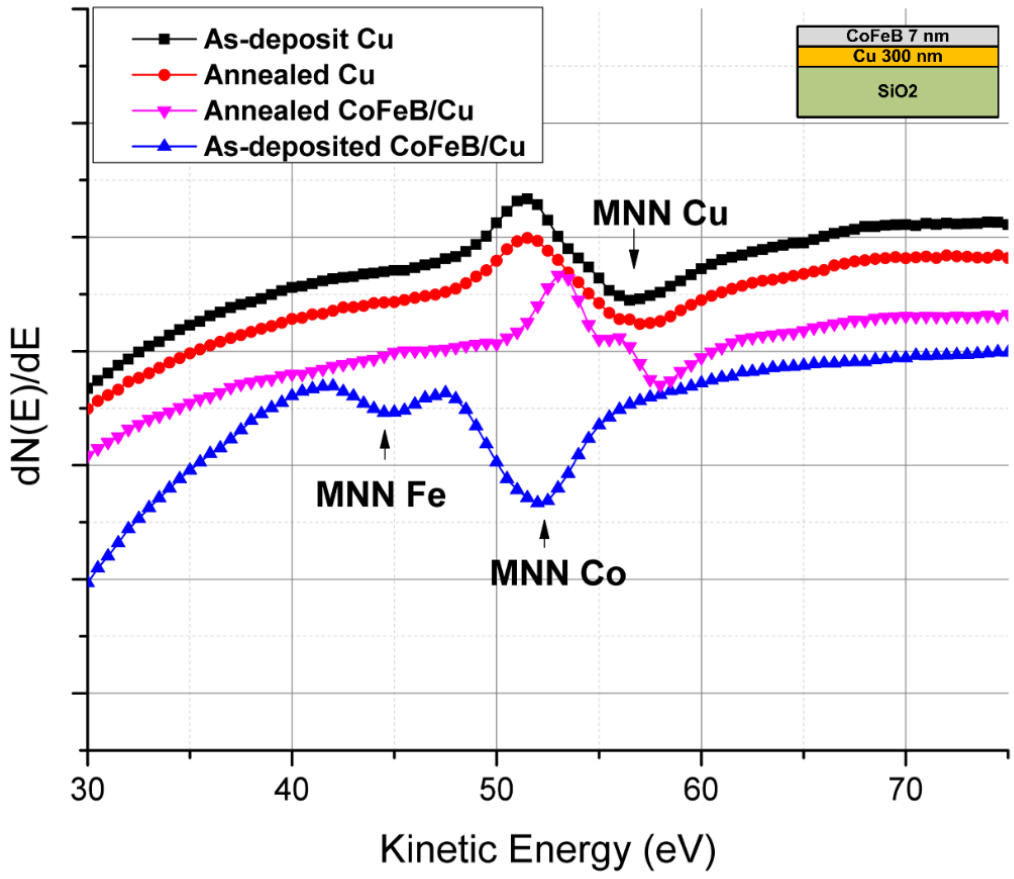

Figure 5.7 AES plots of the same sample in Figure 5.5 at a lower kinetic energy range.

The ratio of Cu and S compositions on surface can be estimated with Eq. 5.1 and AES data from Figure 5.5 and Figure 5.6 for two samples. The calculated results are listed in Table 5.2. The difference in Cu to S ratio may arise from the different targets used during Cu depositions and the difference in annealing processes. Nevertheless, the difference does not affect the diffusion behavior of CoFeB into the bulk Cu, which is

of crucial importance to the performance of GMR device. After the annealing processes, the intensities of Co, Fe are too small to be clearly distinguished from noise to calculate their ratios to Cu.

Table 5.2 Surface composition ratios of Cu, sulfur, oxygen and carbon for annealed CoFeB/Cu bilayers.

Element At. %	CoFeB/Cu /MgO	CoFeB/Cu /SiO_2
Cu	28	42
S	11	22
O	58	32
C	3	3

5.1.4. Conclusions

In summary, Auger electron spectroscopy reveals that at the annealing temperature of 550 °C, CoFeB/Cu bilayer films do not retain their distinct layers. Instead, Co, Fe, B diffuses into the Cu underlayer while S segregates on the surface. These findings motivated us to examine the surface morphology of the annealed multilayer, during which we observed the formation the magnetic nanoparticles from continuous films.

5.2. Formation of areal density controllable magnetic nanoparticles by annealing continuous CoFeB/Cu bilayer thin films

5.2.1. Introduction

Conventional submicron or nanoscale magnetic islands fabrication usually involves lithography techniques such as e-beam lithography or nanoimprinting [132-134]. However, it is extremely difficult and prohibitively expensive to perform top-down

lithography technique on a non-planar surface due to the nature of focusing e-beam or light. Other techniques such as scanning probe voltage pulse deposition technique may be capable to produce magnetic islands on non-planar substrates by applying a negative voltage pulse to a pre-coated tip with magnetic material [135]. However, this method is slow and can only be used for small area, owing to the limited scanning area [133]. Moreover, it requires tremendous focusing steps on a non-planar surface. Another potential candidate to fabricate magnetic islands on non-planar substrate is to ion implant magnetic material into substrate and then to form magnetic islands by post annealing [99, 136]. In such method, the high energy distributed to the surface with ion implantation process may cause severe damage and the post-annealing temperature needs to be high[99] (> 800~1000 ^{0}C) in order dto drive the formation of magnetic islands on surface.

To circumvent the impracticality of the aforementioned techniques, we introduce an approach to form submicron magnetic islands from continuous CoFeB and copper thin films. This is an offshoot of our annealing studies to drive the magnetic species into the bulk Cu underlayer. We report evidence that the magnetic islands form at the copper grain boundaries and their density can be tuned by varying the thickness of Cu.

5.2.2. Experimental details

The starting samples were prepared from a bilayer comprised of 7 nm CoFeB film with 280 nm or 3 nm Cu underlayer, on a SiO_2 substrate. The thickness of the CoFeB film was chosen based on two competing factors. On the one hand, a very thick film will significantly lengthen the annealing time required to deplete the Co and Fe from

surface. On the other hand, if the film were too thin, i.e., less than the electron mean free path, Auger electrons from the Cu underlayer will be detected in the pre-annealed case. This would have made it difficult to clarify the diffusion of CoFe into the Cu upon annealing. The Cu underlayer was e-beam evaporated onto the SiO_2 substrate under a base pressure of 2×10^{-6} Torr, while CoFeB was DC magneto sputtered from $Co_{60}Fe_{20}B_{20}$. The thickness of the Cu layer was monitored by a crystal quartz microbalance during deposition, while the thickness of the CoFeB film was established by deposition time from a pre-calibrated rate. After CoFeB film deposition, the sample was annealed at 500 °C inside the UHV ($<10^{-8}$ Torr) analysis chamber for several hours. Annealing at higher temperatures to drive the diffusion faster was not an option because the diffusion mechanism is different for temperatures >> 500 °C [121]. The sample temperature was measured using a Mikron IR thermometer focused on sample surface. The surface was analyzed by Auger electron spectroscopy (AES) before and after the annealing process. After establishing the average surface characteristics from AES, AFM and MFM scans were performed to probe the surface locally. Images of the surface morphology and magnetic structure with a low magnetic moment tips were simultaneously acquired. We further verified the chemical composition of specific regions of a few samples using SEM with EDS.

5.2.3. Results and discussion

A. Effect of Annealing on Surface Compositions

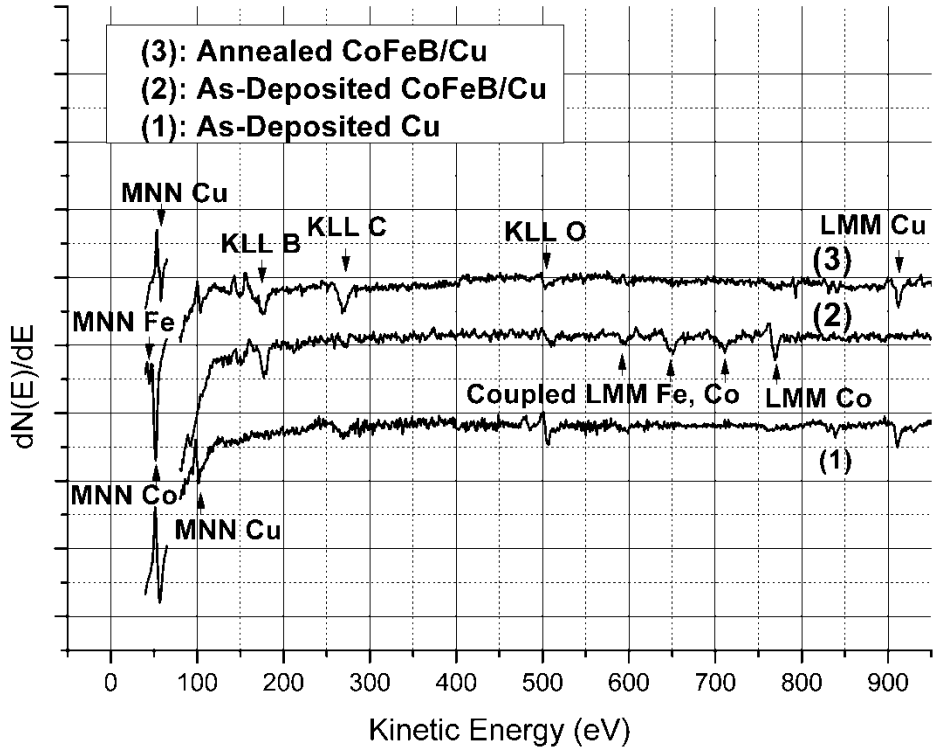

Figure 5.8 AES plots: (3) annealed / (2) as-deposited CoFeB on 280 nm Cu under-layer, and (1) as-deposited Cu on SiO2 substrates. The kinetic energy ranged from 35 to 65 eV and 80 to 950 eV. The Auger peaks were identified with element names associated with corresponding Auger electron transition, such as LMM Cu, MNN Cu etc.

The comparison of surface elemental information of annealed/as-deposited CoFeB with Cu under-layer and as-deposited Cu by AES measurements at two distinct kinetic energy ranges (35~65 eV and 80~950 eV) is depicted in Figure 5.8. Because of the large number of secondary electrons collected at low energy range, AES measurement parameters such as sensitivity, time constant and oscillation amplitude for lower kinetic energy range (35~65 eV) are different, and therefore direct comparison of signal intensities from two ranges is not applicable. The size of electron beam used in this experiment is around 1 cm in diameter so that the AES data represents an average over this area.

The Figure shows the AES spectra at various preparation steps for a given sample. The chronology of the surface preparation is described by the AES spectrum from bottom to top. Spectrum (1) corresponds to Cu on SiO_2, Spectrum (2) represents the as-deposited CoFeB on Cu, and Spectrum (3) shows the case after annealing at 500 °C for 2 hours. Auger electron peaks in Figure 5.8 are identified with reference to standard AES spectra [93, 97]. Spectrum (1) shows Cu, along with oxygen at 506 eV and a slight C peak at 270 eV. C contamination is fairly common in the sample, presumably due to the outgassing of chamber walls from the high heat of the e-beam evaporator. Similarly oxygen contamination may have resulted from oxidation when transferring sample from the e-beam Cu evaporator to the Omicron Analytical system. Nevertheless, we assume that these contaminants will not play significant role in surface diffusion. Spectrum (2) shows clearly the LMM 769 eV cobalt peak with perhaps some contributions for Fe. Being neighbors in the periodic table, LMM Fe peaks overlap with some LMM Co peaks so they cannot be used to identify Fe. We then use the lower energy range (<65 eV) in which the MNN Fe and MNN Co peaks differ by a few eV and are clearly distinct. Cu disappears completely after 7 nm deposition of CoFeB without annealing. The spectrum reveals that the surface is completely covered by CoFeB at a thickness greater than the mean free path of the Auger electrons from copper. The persistence of the oxygen peak, albeit diminished, may come from oxygen diffusion. Spectrum (3) is the case after annealing. It shows the reemergence of sharp Cu peaks along with carbon, and concomitant with the disappearance of the Co and Fe peaks. This suggests that Cu displaces the Co and Fe on the surface, with a likely scenario that the Co and Fe atoms diffuse into the bulk at elevated temperature.

However, the B peak is only slightly attenuated after annealing, suggesting that B remains on the surface. This result is in agreement with reports by several publications that show the annealing process out diffuses B from CoFe matrix, affecting the distribution of B in annealed CoFeB thin film [137-139]. It is also worth noting that B has an extremely high Auger relative sensitivity factor (S_B(KLL) = 1.2, S_{Cu}(LMM) = 0.23, S_{Co}(LMM) = 0.32, S_{Fe}(LMM) = 0.35) [98], so that Boron is preferentially detected.

In order to analyze the relative concentrations, we measure the peak intensities and compare them against reference standards. While exact quantitative interpretation of an Auger electron spectroscopy remains a challenge, simple equations with accuracy can be used to calculate surface composition [97]. The ratio of two chemical elements' compositions on surface can be estimated using the equation 5-1 [97],

where I_x stands for the absolute peak-to-peak value of chemical element X obtained from Auger electron spectroscopy. S_x is the relative sensitivity factor of element X. With Eq. 5.2 and above sensitivity values, the calculated composition ratio of B to Cu on surface after annealing is 0.13. The noise level of AES spectrum defines the upper limit of Co and Fe composition ratio to Cu on surface after annealing. Using the listed sensitivity factor and Eq. (1) with measured standard deviation of the noise signal, for the given AES spectrum $R_{Cu}^{Co} \leq 0.11$ and $R_{Cu}^{Fe} \leq 0.10$. This suggests that the remaining concentrations of Co and Fe at the surface are at most 11% and 10% respectively. This corroborates the results of the magnetic and topographic images presented below.

B. Effect of Annealing on Morphology and Magnetic Structure

Having established the compositions, Figure 5.9 illustrates the change of surface topography and the formation of magnetic islands from the as-deposited to the annealed case. The left set represents the surface topography taken by AFM in tapping mode and the right column shows the corresponding MFM images. MFM utilizes a pre-magnetized scanning probe to interact with the long range stray field from the sample. The bright and dark contrast in the MFM images roughly corresponds to magnetic charges or divergence of magnetization [100]. The resolution of the MFM measurement is determined by the distance of the probe to the surface [28], which in this experiment is about 40 nm. The granularity of Cu deposited on Si substrate prior to annealing is depicted in Figure 5.9a. The as-deposited Cu form grains with size around 60 nm (inset of Figure 5.9a).

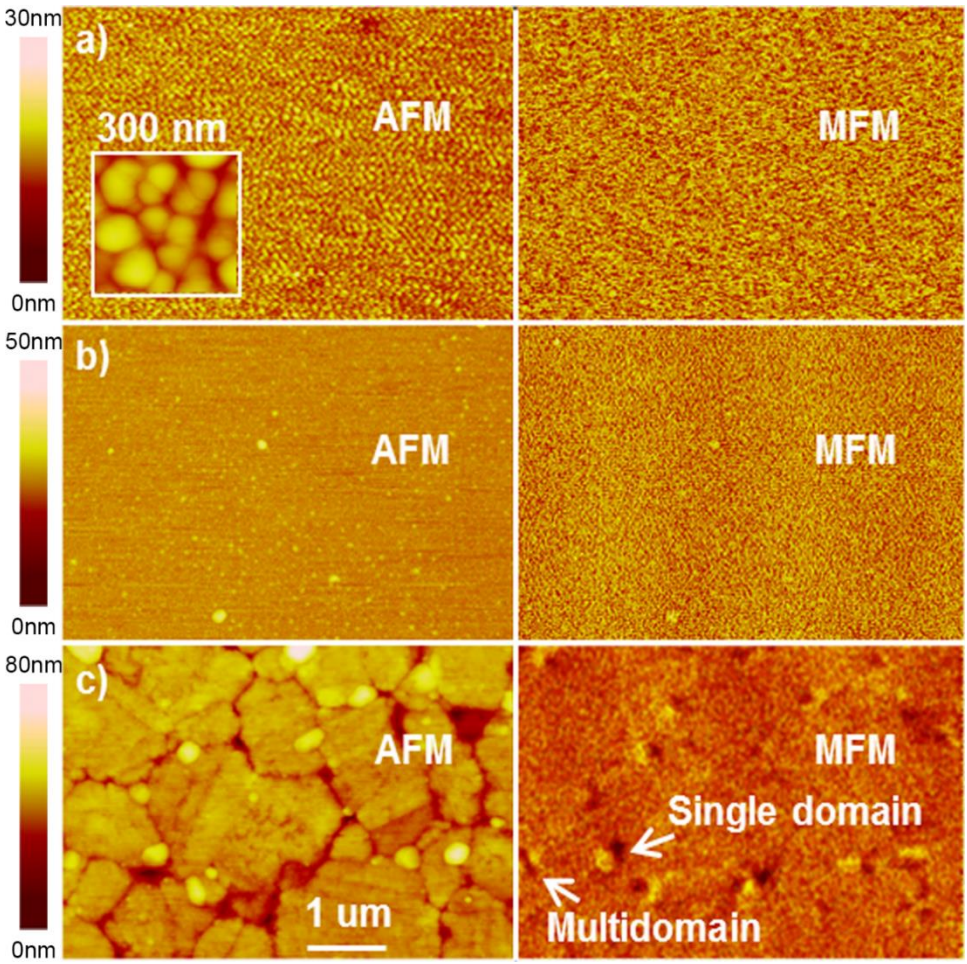

Figure 5.9 Simultaneously acquired AFM (left) and MFM (right) images of (a) as-deposited Cu on SiO_2 substrates, (b) as-deposited CoFeB with Cu under-layer, and (c) annealed CoFeB with 280nm thick Cu under-layer. Inset: as-deposited Cu. Brightness and contrast were adjusted to highlight magnetic features.

As expected, the corresponding MFM image of as deposited Cu in Figure 5.9a shows no magnetic feature. Upon deposition of CoFeB, the surface becomes relatively smooth. The AFM image in Figure 5.9b is evidence that the as-deposited CoFeB on Cu form an amorphous film. The few sharp asperities which break up the otherwise completely featureless surface are probably from contamination during deposition. Furthermore, despite having a magnetic coating, the corresponding MFM in Figure 5.9b manifests no features as well, except the topographic contamination that filters

through the MFM image. The tip-sample distance governs the resolution and sensitivity of the MFM. And the fact that the asperities show up in the MFM indicates that the tip is very close to the surface and the MFM should be able to detect very weak fields. Thus we conclude that 7 nm thin amorphous CoFeB film does not produce detectable magnetic charges. (This is in contrast with our previous findings that as-deposited 15nm and thicker CoFeB films show rich surface structures [2].) But after annealing, the surface changes drastically in both surface topography and magnetic features. Figure 5.9c shows the formation of large polycrystalline grains in which smaller isolated islands are incorporated at the various sites at the grain boundaries. It turns out that these small islands are in fact magnetic, as shown in Figure 5.9c. We observe that some of them are single domain which is characterized by a single bright/dark contrast pair, while others are multi-domain islands [28]. Interestingly, the magnetic islands fall within a relatively narrow range of size distribution.

To establish the stoichiometry of the islands we examined a representative annealed sample using SEM with EDS on an annealed sample. The EDS spectra were obtained at specific spots on the sample and the findings are summarized in Figure 5.10. Spectrum 8 was obtained from a boxed area encompassing a magnetic particle. Spectrum 9 was from a fixed point at the center of the particle and Spectrum 10 was obtained from an area on the background away from the particle. These are indicated in the inset SEM image. (We note that the labeling of the spectra was defined by the EDS software and the labels 8-10 carry no specific relevance.) The spectra taken on the islands clearly show the presence of the magnetic species, while that taken at the background does not.

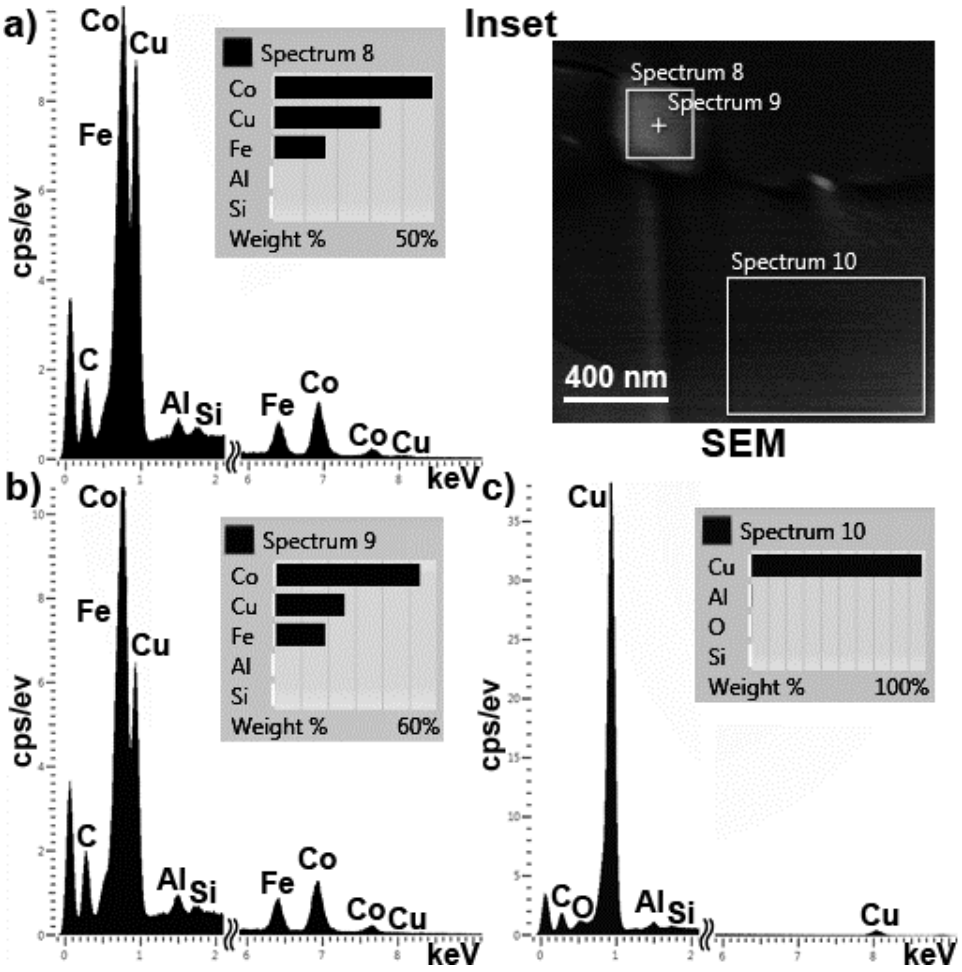

Figure 5.10 EDS spectra: (a) spectrum 8 was obtained from the corresponding boxed area in the inset, (b) spectrum 9 was obtained from the fixed point in the inset, and (c) spectrum 10 was obtained from corresponding boxed area in the inset. Inset: SEM image of annealed CoFeB/Cu bilayer.

We also calculated the apparent concentration based on the intensity profiles and the results are summarized in Table 5.3. Interestingly, the data indicate that the ratio of Fe/Co is 0.34 (4.84/14.2) and 0.36 (5.24/14.56) for Spectra 8 and 9 respectively. These values are very close to the starting ratio of 1:3 in the original target alloy $Co_{60}Fe_{20}B_{20}$. This therefore suggests that the magnetic species diffuse together, maintaining their alloy composition. Moreover, since there are no detectable traces of Fe and Co on the

background, we conclude that these species have completely migrated and are confined at the Cu grain boundaries.

Table 5.3 Apparent concentrations of Co, Fe and Cu obtained from EDS spectra.

Apparent concentration	Co	Fe	Cu
Spectrum 8	14.2	4.84	3.92
Spectrum 9	14.56	5.24	2.69
Spectrum 10	None	None	17.73

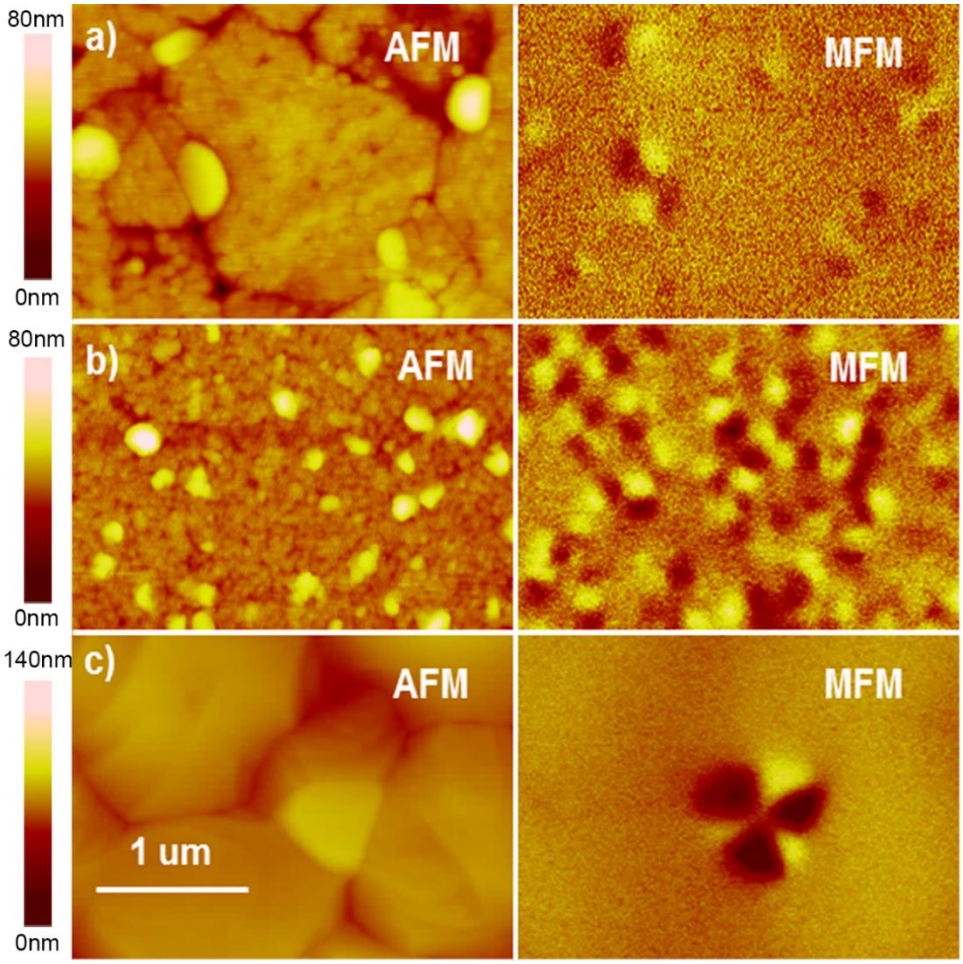

Figure 5.11 Simultaneously acquired AFM (left) and MFM (right) images of a) CoFeB on 280 nm Cu annealed at 500 ° C, b) CoFeB on 3 nm Cu annealed at 500 °C, and c) CoFeB on 280 nm Cu annealed at 620 °C. Brightness and contrast were adjusted to highlight magnetic features.

Finally, we consider the effect of Cu underlayer thickness and the annealing temperature. Comparison of Figure 5.11a and b show that for the same annealing temperature, the thicker (280 nm) Cu under-layer produces less areal density of magnetic nanoparticles compared to the thinner (3 nm) Cu underlayer. Similarly, the comparison of Figure 5.11a and c shows that the increased annealing temperature causes larger Cu grains to grow and thus, lower density of nanoparticles.

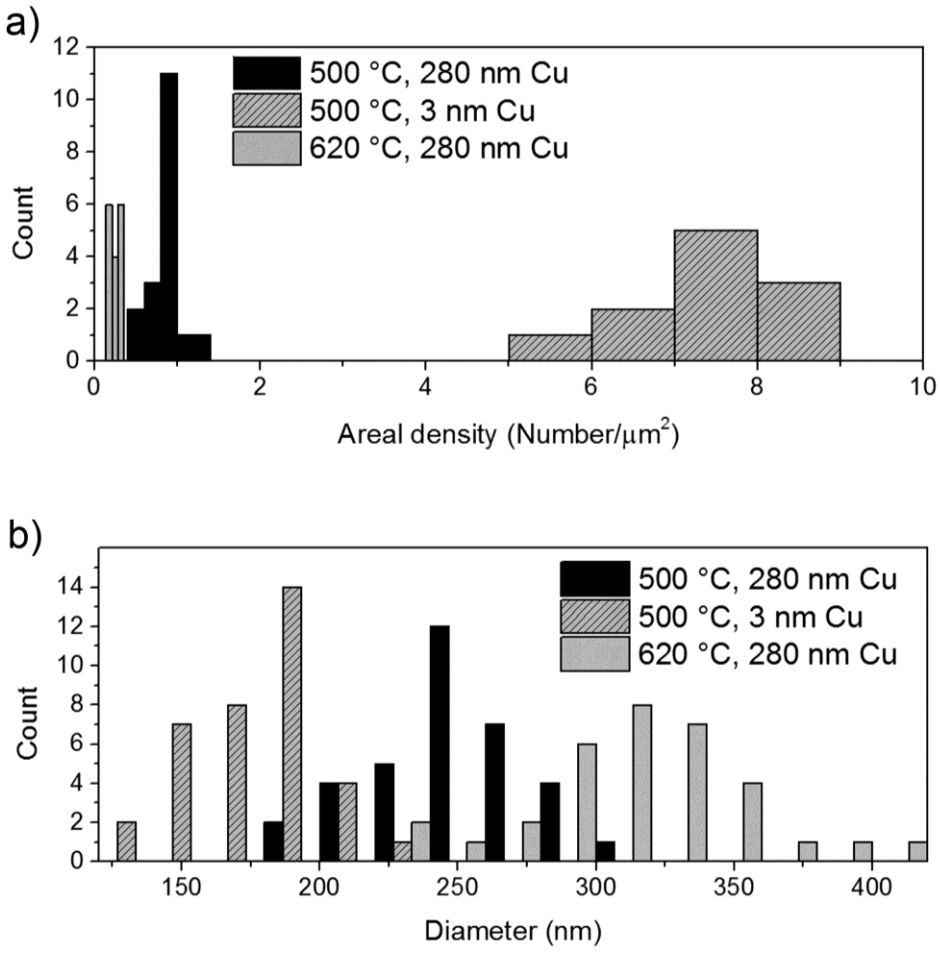

Figure 5.12 Histograms of a) particle size and b) areal density distribution according to the different under-layer Cu thickness and annealing temperatures indicated in the labels.

Figure 5.12 shows the histograms of the size and the areal density of the formed islands under different conditions. A rudimentary statistical analysis of many scans shows that at 500 °C annealing temperature, the areal density is roughly 0.82±0.58 per square micron for thick Cu underlayer and 7.68±0.83 for the thin Cu underlayer. The size of magnetic particle is about 256 nm±36 nm for the thick underlayer, compared with 187nm±44 nm for the thin case. In other words, while the density of magnetic particles varied by a factor of 8, the particle size varied by less than 60% in over two orders of magnitude difference in Cu underlayer thickness. This suggests that the underlayer thickness strongly affects the particle areal density but only weakly affects the particle size. Other studies have shown that 540 °C is a critical temperature below which Co and Fe preferentially diffuse to the grain boundary and above the constituent magnetic ions interdiffuse with under-layer Cu [121]. Thus, fewer nanoparticles are expected after annealing at 620°C than 500°C. Comparison of Figure 5.11a and c indeed shows marked difference due to difference annealing temperatures. Statistical analysis of many similar images give 0.24+/-0.13 per square micron density with 300 nm for the sample annealed at 620 °C.

5.2.4. Conclusions

In this work, we report a novel method for producing magnetic submicron islands from bilayer films of CoFeB/Cu. Annealing drives the diffusion of Co and Fe, and the concomitant growth of Cu islands, which forces the accumulation of cobalt and iron at the grain boundary sites. Co and Fe migrate together while preserving their alloy composition in forming magnetic islands. At 500 °C and below, the size is relatively

constant and varying the thickness of CoFeB underlayer and annealing temperature can control the areal density.

5.3. Controlled domain wall motion device in CoFeB nanowires

5.3.1. Introduction

The recent development of controlled domain wall motion devices is a promising technology for the next generation nonvolatile magnetic race-track device or MRAM, in which the digital information is stored in the domain walls [17, 140]. The evolving MRAM with high performance and reliability has demonstrated an alternative approach to Si-based RAM to achieve high bit density and low power consumption [19]. Domain wall motion (DWM) can be triggered by external applied magnetic field and spin-polarized current which is theoretically predicted by Berger and experimentally demonstrated in thin films and nanowires structures [16, 17, 21, 25]. Compared to continuous films, nanowire structures with magnetic domain trapping sites can offer significant higher storage density (bits per area). Information stored in DWM devices can be extracted by GMR and TMR readers [17, 25, 115, 141, 142]. Prior experimental work has shown that the use of CoFeB instead of widely employed Py in spintronics devices can greatly reduce the magnetic domain wall pinning strength [25]. In this work, we fabricated CoFeB based nanowires with domain wall pinning sites and demonstrated the controlled domain wall motion with moderate external field.

5.3.2. Experimental details

The CoFeB nanowire was patterned through e-beam lithography followed by a standard lift-off process. To assist the lift-off process, a double layer photoresist technique is employed in the fabrication process. The two layers of photoresist used in this experiment are PMMA 495A and PMMA 950, which are widely used high-resolution positive e-beam lithography photoresists. The numbers after PMMA stand for the molecular weight of the polymer. As lighter molecule dissolves faster, the under-layer PMMA 495A creates an undercut below the PMMA 950 layer , which facilitates lift-off. The developer used for the process was MIBK/IPA (1:3). The design of the CoFeB nanowire structure is shown in Figure 5.13. The pattern is a strip with notches that act a domain wall trapping sites. The nano-constriction notches have been shown to work well as pinning sites for domain walls [17, 19].

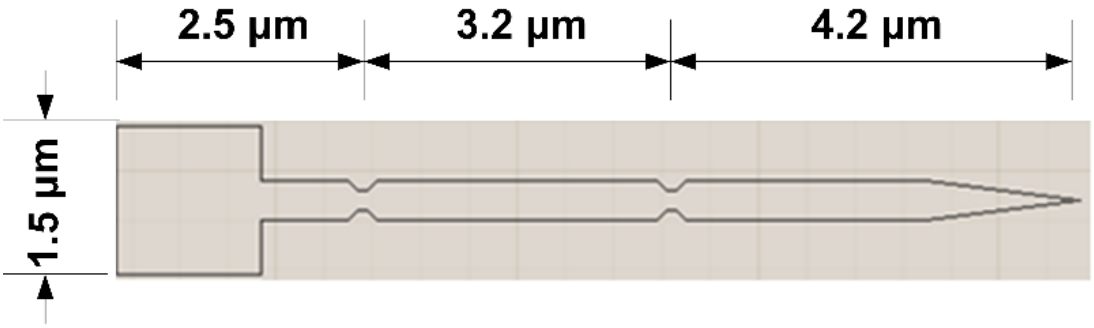

Figure 5.13 Design of the controlled domain wall motion device based on CoFeB nanowire.

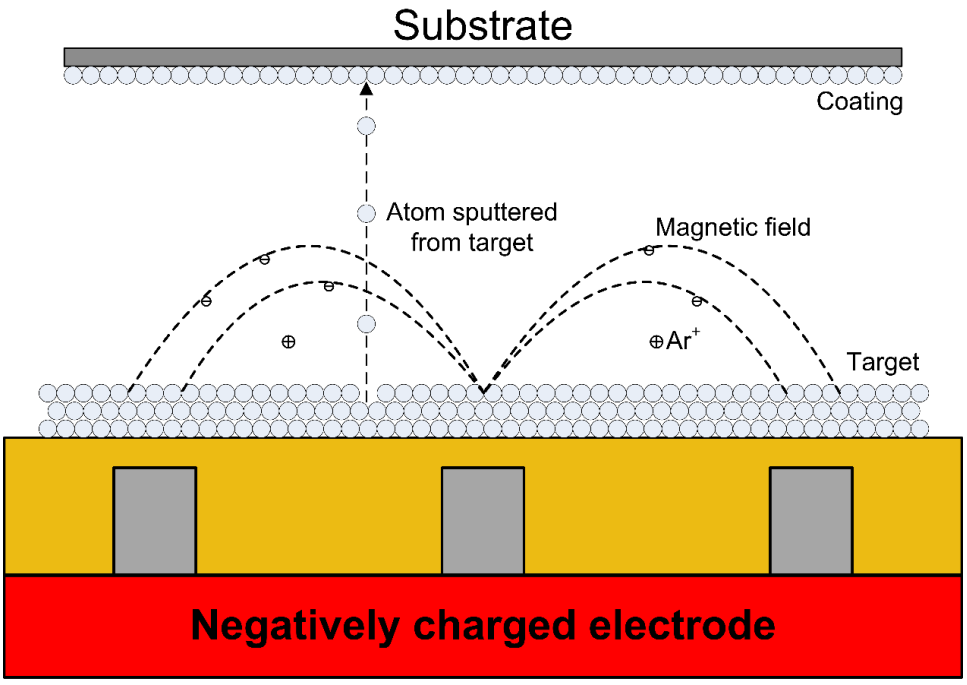

Figure 5.14 Schematic diagram of DC magneto sputtering process.

CoFeB was deposited on Si substrate by DC magnetron sputtering in a UHV chamber. The base pressure of the chamber was maintained at 10^{-9} Torr. Before the magnetron sputtering, pure argon gas was introduced into the UHV chamber to maintain a sputtering pressure of 6.1 mTorr. During the sputtering, Ar was ionized by the electrical field, creating plasma to bombard the CoFeB target**.** Different from the acceleration of ions directly towards the cathode in a basic DC sputtering process, the existence of the strong magnetic field near the target surface in the magnetron sputtering process leads to electrons travelling along the magnetic flux lines. Thus, the plasma is confined to the magnetic field, reducing the heating and structural damage of the substrate caused by ion bombardment. Meanwhile, the electrons trapped in the magnetic field enhances the probability of ionizing a neutral argon gas molecule, increasing in the number of available ions and enhancing the sputtering and depositing rate. The schematic diagram

of the magnetron sputtering process is shown in Figure 5.14. The applied sputtering power is 69 W. The deposition rate of CoFeB for the system we used was calibrated to be 1 Å/sec. The CoFeB deposition time was set to be 7 min, corresponding to a roughly 42 nm thick film. Figure 5.15 shows the process flow of the fabrication process.

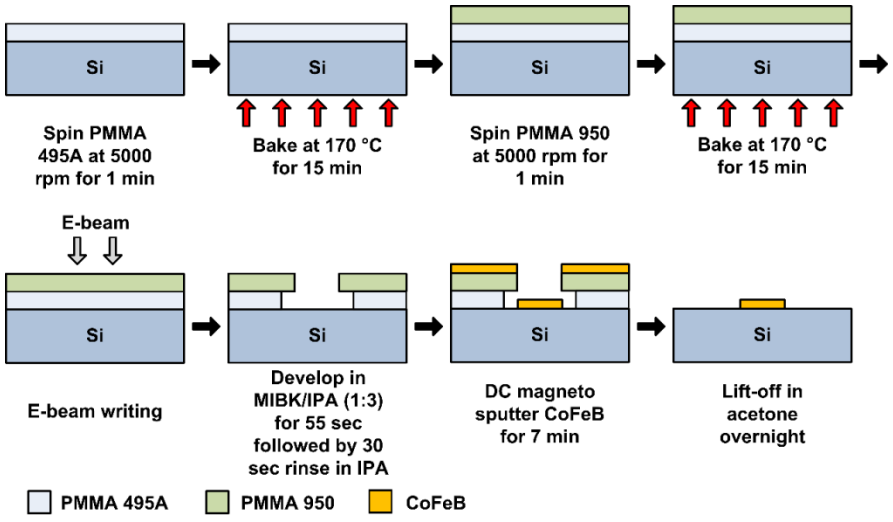

Figure 5.15 Fabrication process flow of the controlled domain wall motion device based on CoFeB nanowires

Apart from the lithography of CoFeB thin film, the hysteresis loop of a deposited continuous film was characterized by vibrating samples magnetometer (VSM). In a VSM measurement, the sample was placed inside a uniform magnetic field and then physically vibrated at a high frequency. The change of magnetic flux due to the sample vibration induced voltage across a nearby coil. The created voltage was proportional to the magnetic moment or equivalently the total magnetization of the vibrating sample, independent on the applied quasi-static magnetic field.

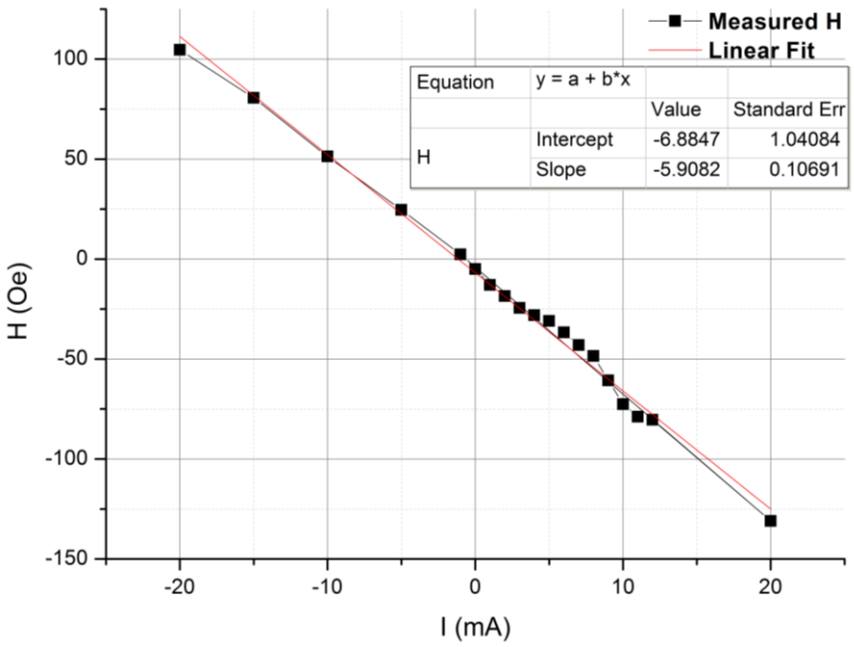

Figure 5.16 Plot of Magnetic field intensity with respect to input current for the C shape electromagnet.

After sample preparation, the CoFeB nanowire was characterized by AFM and MFM without and with applied in plane magnetic field. The in-plane magnetic field is generated from a C shape electromagnet. The sample was placed in between the gap of the electromagnetic which sits on the X,Y stage while scanning. The electromagnet was calibrated with a Lakeshore gauss meter. The relation of the input current I with the generated magnetic field intensity H was plotted in Figure 5.16. The linear relation between I and H was expected as the magnetic field generated in the gap can be derived from the following equation [143],

$$H_{gap} = N \cdot I / L_{gap} \qquad (2.1)$$

Where L_{gap} is the gap spacing and N is the number of coils. The slope for the H-I plot analyzed from a linear fitting algorithm is calculated about -5.9. H field with none input

current is -6.9 Oe which is due to the remanence of Permalloy core used in the C shape electromagnet.

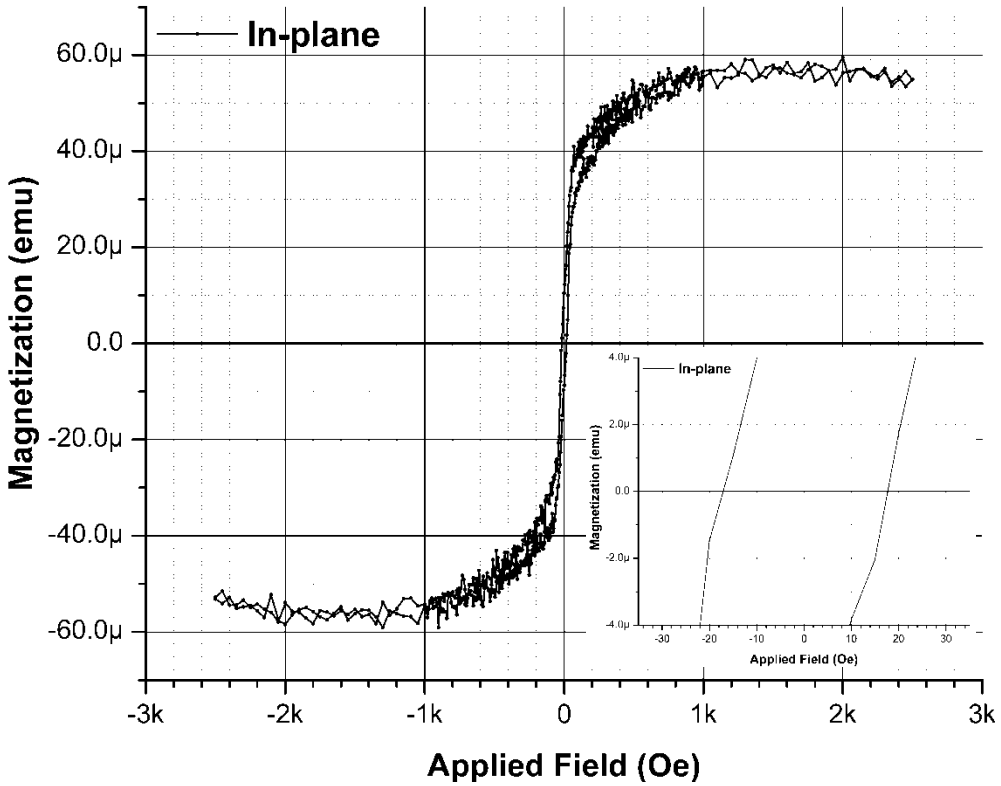

Figure 5.17 Measured hysteresis loop of sputtered CoFeB thin film. Inset: zoom in near zero applied field.

5.3.3. Results and discussion

Figure 5.17 shows the measured hysteresis loop of the deposited CoFeB thin film. From the Figure, a coercivity field of 19 Oe can be identified for the prepared CoFeB film. The obtained magnitude of coercivity matches closely with reported data of CoFeB [144], indicating a soft ferromagnetism of the prepared CoFeB.

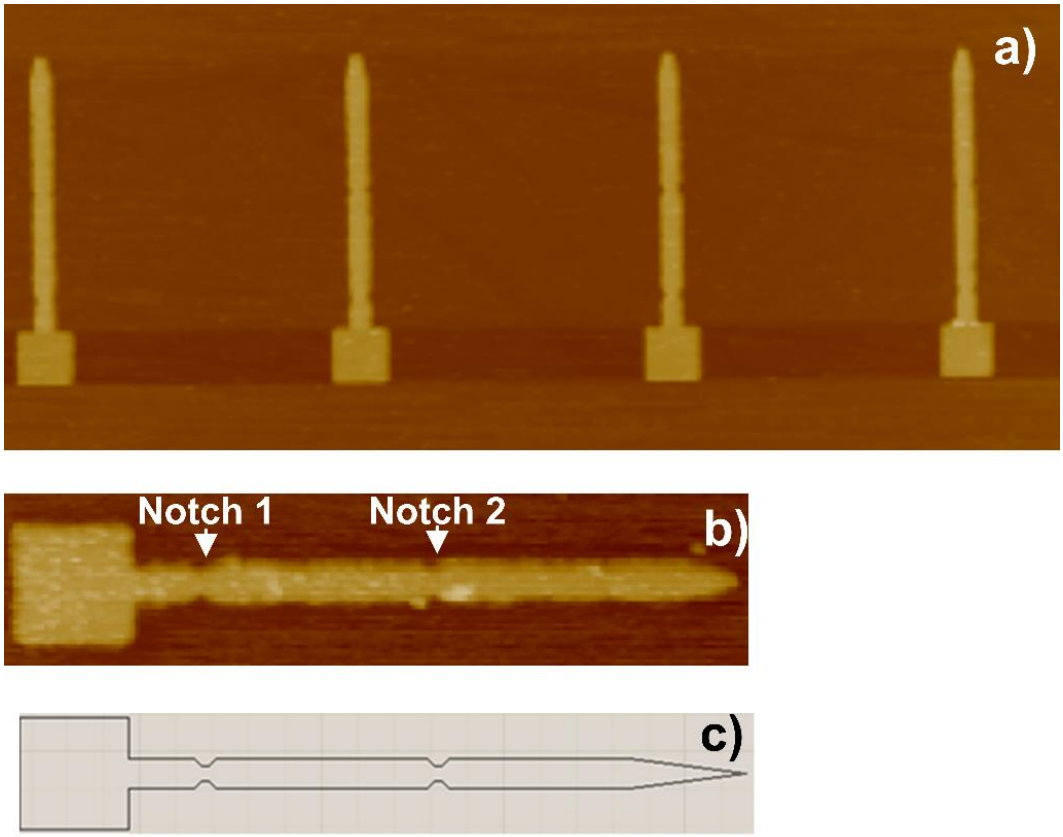

Figure 5.18 AFM images of patterned CoFeB nanowires a) set of four nanowires. b) zoom-in AFM image of a nanowire with comparison to pattern design in c).

Figure 5.18a shows the AFM images of a set of patterned CoFeB nanowires. The designed nano-constrictions notches of domain walls can be identified in the images. The identical structure of the fabricated single nanowire and the original design is evident from the comparison of the AFM image of Figure 5.18b and CAD drawing of Figure 5.18c.

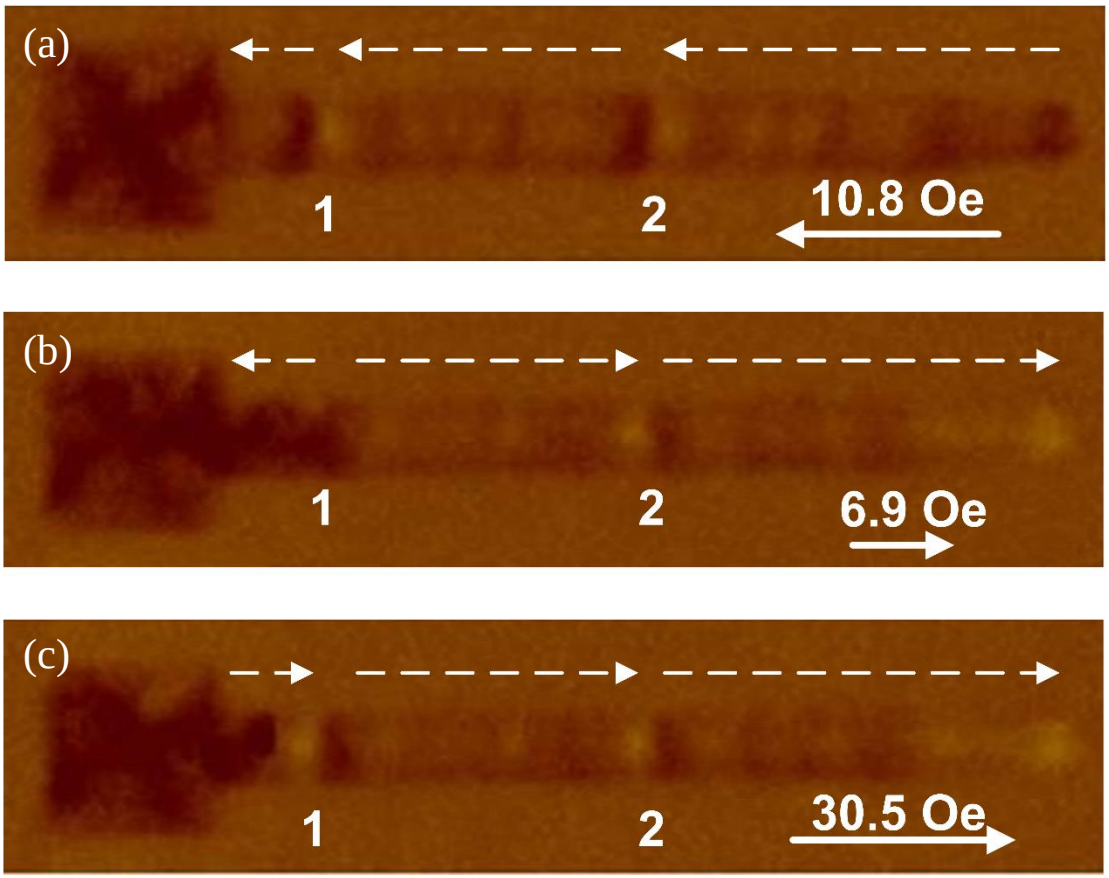

Figure 5.19 MFM images of patterned CoFeB nanowires with applied magnetic field. The magnetization directions of segments are presented by the dash lines while the solid line presents the direction of applied external field. Magnitudes of applied external field are typed on the solid lines.

Magnetic properties of the patterned CoFeB nanowires were investigated with MFM under the applied in-plane magnetic field. Figure 5.19 shows the captured MFM images of the CoFeB nanowire under various magnitudes of the applied field. Two notches in the nanowire are labeled from the left to the right as 1 and 2, respectively. Figure 5.19a shows the two bright/dark contrast spots in the notch 1 and 2 under a 10.8 Oe magnetic field pointing left. The two contrast spots stand for two head-to-tail domain walls at the nano-constriction sites. This configuration of domain walls is the result of the allied magnetization of the three segments which are separated by the two notches. The

direction of the magnetization of each segment is indicated by the dashed line with arrow. After applying a small magnetic field of 6.9 Oe towards the right, as indicated in Figure 5.19b, a tail-to-tail domain wall is pinned in notch 1. The formation of the tail-to-tail domain wall originates from the flipping of magnetization, from left to the right, in the two longer nanowire segments due to the applied field. Figure 5.19 shows the case when the magnetic field is raised high enough so that the magnetization of all three segments are aligned in parallel. Summarized from many times of experiments, we concluded a 22 Oe switching field for the CoFeB based nanowires, which is much smaller than in Py based devices [17].

5.3.4. Conclusions

Evident from the MFM measurement with in-plane magnetic field, the fabricated CoFeB nanowires are able to trap domain walls at the pining sites, namely the notches. Magnetization switching field for the CoFeB nanowires are measured to be much lower than the Permalloy based nanowires, promising a much reduced switching energy for the CoFeB based controlled domain wall motion device.

6. Chapter 6: Wide-bandgap Semiconductor oxide based high-performing ultraviolet photodetectors

6.1. High-performing visible-blind photodetectors based on SnO_2/CuO nanoheterojunctions

6.1.1. Introduction

Transparent oxide semiconductors (TOSs) have attracted considerable attention in recent years, due to their versatile applications including transparent thin-film transistors, gas sensors, and optoelectronics [54, 145-147]. Visible-blind ultraviolet (UV) photodetectors (PDs) are of particular interest, owing to their broad application in digital imaging, missile plume detection, optical communications, and biomedical sensing [36, 38, 41, 148]. Due to its wide bandgap and corresponding transparency in in the visible light region, SnO_2 has been shown to be promising for visible-blind UV photodiodes [149-151].

Typical *n*-SnO_2 PDs work as photoconductors with electrons as the majority carriers. In a photoconductor, absorption of photons with energy larger than the bandgap energy generates free carriers, leading to an increase in conductivity for a period known as the persistence time. The device conducts a single carrier type, and the persistence time can be lengthened by trapping of the non-conducting carrier type, leading to

photoconductive gain and quantum efficiency exceeding 100%. At a specific operation bias, the photocurrent is measured as the response of the PD, which can be used to calculate the EQE (external quantum efficiency) and responsivity of the device. Current SnO_2 thin-film PD technology is limited by low responsivity, especially at longer UV wavelengths [152]. Beside the continuous efforts in improving the crystal quality of SnO_2 and approaching the one-dimension SnO_2 nanostructures to achieve a better responsivity [153-155], a new approach by employing *pn* heterojunctions to further enhance the light absorption and consequently the performance of SnO_2 based UV PDs is proposed.

Benefitting from the matching band alignment, intrinsic *p*-CuO and *n*-SnO_2 have been demonstrated in forming well-behaved *pn*-heterojunctions [47, 156], making them promising candidates for optoelectronic applications. Here, we build thin-film SnO_2 PDs using a novel, facile, and scalable approach to fabricate nanoscale *p*-*n* heterojunctions with enhanced light absorption in the active material to improve the performance of UV PDs.

Our simplified PD device fabrication method consists of using *rf*-sputtering to deposit SnO_2 thin films and Cu nanoparticle (NP) clusters. The top layer of Cu NPs oxidizes in ambient to form CuO NP clusters, and the primary role of these clusters is to enhance absorption at the longer wavelength edge of the UV response in the PDs. We used finite-difference time-domain (FDTD) simulations to model the light absorption in devices with and without the CuO NPs and achieved good agreement with the experimental absorption spectra. Our electrical measurements indicated that the

inclusion of the CuO NPs improved the responsivity of the PDs more than 5 fold compared to SnO_2-only devices.

6.1.2. Experimental details

The SnO_2 thin films were rf-sputtered to sapphire substrates using a Denton Vacuum Discovery 550 sputtering system. The base pressure was kept at or below 6.7 x 10^{-4} Pa (5 x 10^{-6} Torr) and the substrate temperature was maintained at 325 ^{0}C to yield uniform films. During the reactive sputtering process, a mixture gas of Ar and O_2 was introduced at the rates of 20 standard cubic centimeters per minute (sccm) and 30 sccm, respectively. The thickness of deposited SnO_2 was estimated to be 95 nm ± 2 nm by a J. A. Woollam M2000 ellipsometer.

The CuO on SnO_2 was deposited by rf-sputtering of Cu at room temperature for few minutes. After deposition and exposure to ambient conditions, the Cu was mostly (> 95 %) oxidized to CuO state, which was later confirmed by the X-ray photoelectron spectroscopy (XPS). The Cu was deposited through a shadow mask to form square-shape clusters rather than continuous films on the SnO_2 surface. The size of the Cu clusters was 200 µm x 200 µm and they were 200 µm apart from each other. Interdigitated electrodes (IDEs) were then e-beam evaporated through a shadow mask with the Ti/Al/Ti/Au stack. No optimization of the fabrication process was performed. Figure 6.1 shows a device schematic of the entire structure.

The surface morphology of the SnO_2 and SnO_2-CuO films was imaged by Bruker Dimension FastScan atomic force microscopy (AFM). X-ray photoelectron spectroscopy (XPS) measurements confirmed the chemical status of prepared SnO_2-

CuO films. XPS curve-fitting and analysis was performed using CasaXPS software. The binding energy scale of the spectrum was calibrated to the hydrocarbon peak at 284.8 eV. The absorption spectrum and absorption coefficient (α) of the SnO_2 films and SnO_2-CuO films were studied using Ocean optics QE65000 spectrometer and J. A. Woollam M2000 ellipsometer, respectively.

Responsivities of the SnO_2 and SnO_2-CuO PDs were measured at various biased voltages under a spectrally filtered light source. The measurement, calibrated using a NIST-calibrated silicon photodiode, had a total uncertainty of ± 5 % (fractional). The UV photocurrent response of the PDs was recorded for a voltage range of 0 to 1.2 V at the illumination wavelength of 290 nm.

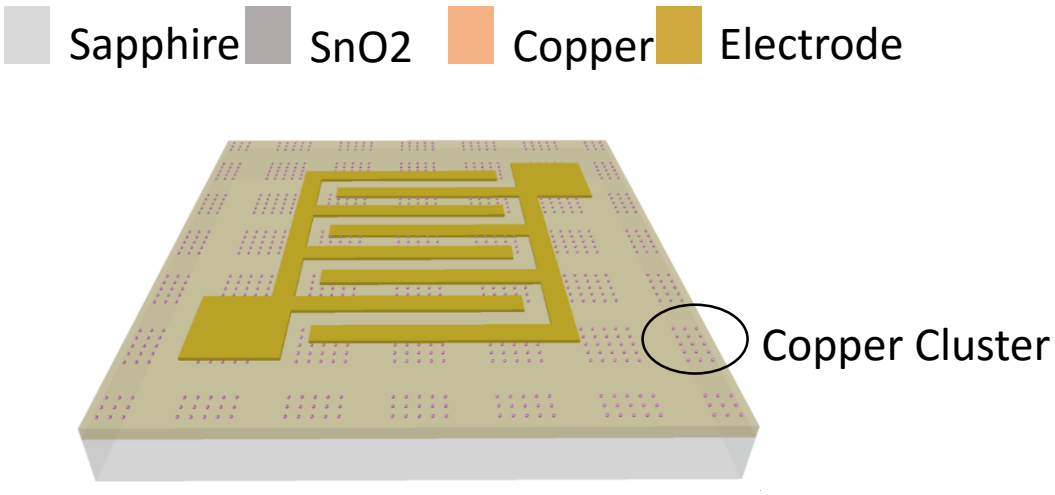

Figure 6.1 Schematic diagram of the fabricated device. Dimensions are not to scale.

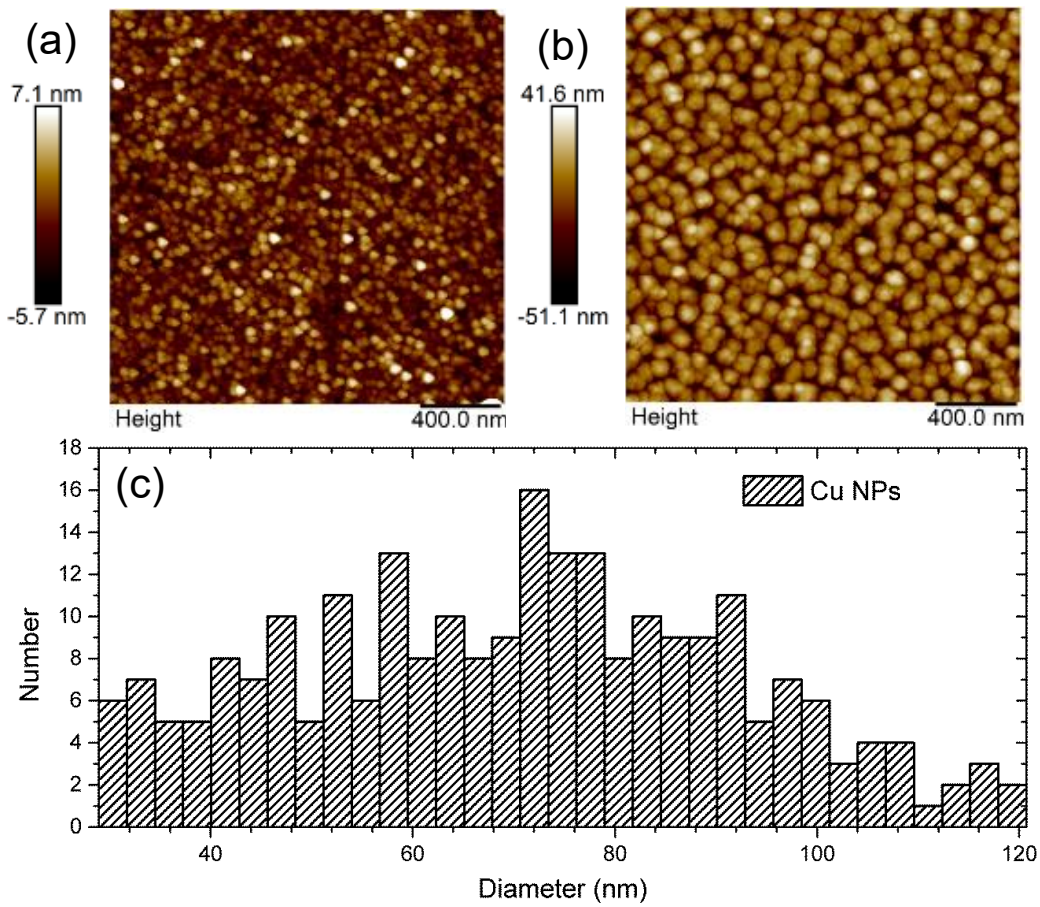

Figure 6.2 (a) and (b) AFM images of SnO_2, and CuO cluster, respectively. (c) Histogram of the size of the deposited CuO NPs.

6.1.3. Results and discussion

Figure 6.2 shows the high resolution AFM images obtained from the CuO cluster, and SnO_2, respectively. The measured root mean square (rms) surface roughness of the SnO_2 film is 1.8 nm and the value increases to 13.8 nm with the presence of fully covered CuO NPs. The grain sizes of the SnO_2 and CuO nanoclusters are estimated as 32.9±13 nm and 74.6±25 nm, respectively. Rudimentary statistical analysis was performed to generate the histogram, as presented in Figure 6.2d, shows an average

density of 65 /um^2 and height of 45 nm for the CuO NPs. The estimated parameters are applied in the FDTD optical simulations.

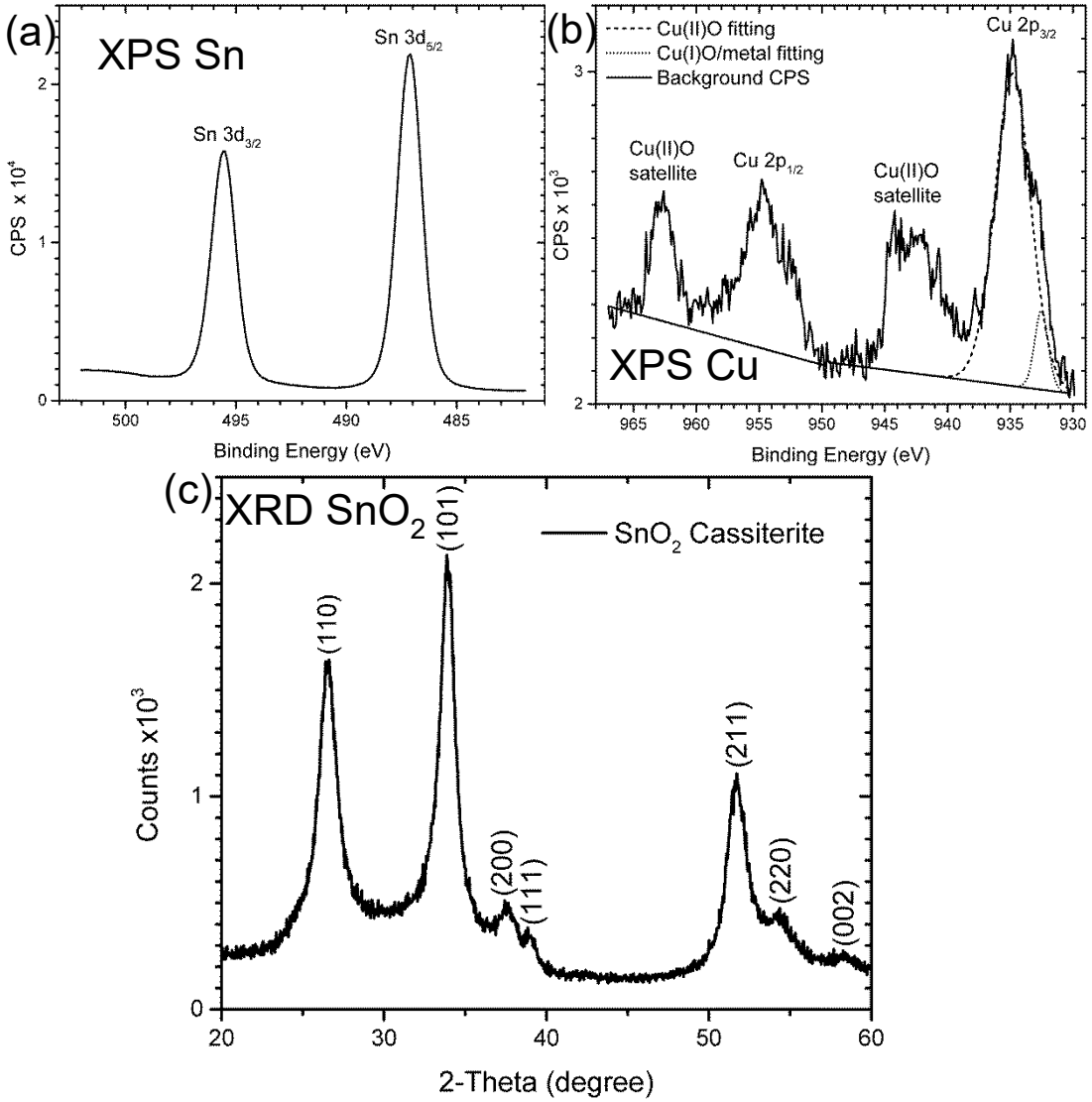

Figure 6.3 XPS spectra of (a) the Sn 3d and (b) the Cu 2p regions of a SnO_2-CuO film, and (c) 2θ XRD patterns of the deposited SnO_2 thin film.

High resolution XPS spectra of Sn 3d and Cu 2p regions of SnO_2-CuO film are shown in Figure 6.3a and b, respectively. As shown in Figure 6.3a, Sn 3d 5/2 peak appears at binding energy of 487.1 ev with a satellite peak characteristic of Sn 3d 3/2 at 495.5 ev, which is consistent with other reported XPS data of SnO_2 [157]. The spectrum of Cu

2p region shows combination states of the Cu elements by referring to published reports [158-160]. Estimated by curve-fitting of the peaks, 95% Cu elements are in the Cu(II)O form and the other 5 % are either in the Cu(I)O or metal form. Therefore, almost all deposited Cu NPs are oxidized into CuO. Since the unintentionally doped CuO and SnO_2 typically shows *p*-type and *n*-type semiconductivity respectively, we therefore conclude that the deposited CuO forms *pn* heterojunction with the underlying SnO_2. Figure 6.3c shows XRD patterns of the prepared 96 nm SnO_2 film on a sapphire substrate. All the diffraction peaks in the XRD spectra are exclusively assigned to the cassiterite phase of SnO_2.

The optical absorbance spectra of the SnO_2 and SnO_2-CuO films are shown in Figure 6.4b. The absorbance (A) quantifies the attenuation of the transmitted light power with the following equation,

$$A = -\log T \tag{6-1}$$

where T is the measured transmittance of the material. A significant enhancement in the light absorption over the wavelength range of 250 nm to 475 nm is observed in the film decorated with CuO NPs compared to the bare SnO_2 film. To verify the enhancement mechanism associated with the addition of the CuO NP clusters, we used FDTD simulations to calculate the optical properties of a 100 nm thick SnO_2 film with and without CuO nanoclusters on top. The CuO NP clusters were modeled as elliptic paraboloids with heights of 45 nm and diameters of 75 nm. The CuO NPs were randomly distributed on the SnO_2 film with an average surface density of 65 μm^{-2}. The size and average density values of the NPs were based on AFM measurements of the real devices. The simulated structure is shown in Figure 6.4a. Refractive indices (*n, k*

values) for the SnO_2 film were obtained from ellipsometry measurements, and reported values were used for the refractive indices (*n, k* values) for the CuO [161] and sapphire substrate [162]. A broadband (200 nm – 1000 nm) plane wave incident from the nanocluster side of the device was used as the excitation source for the simulations.

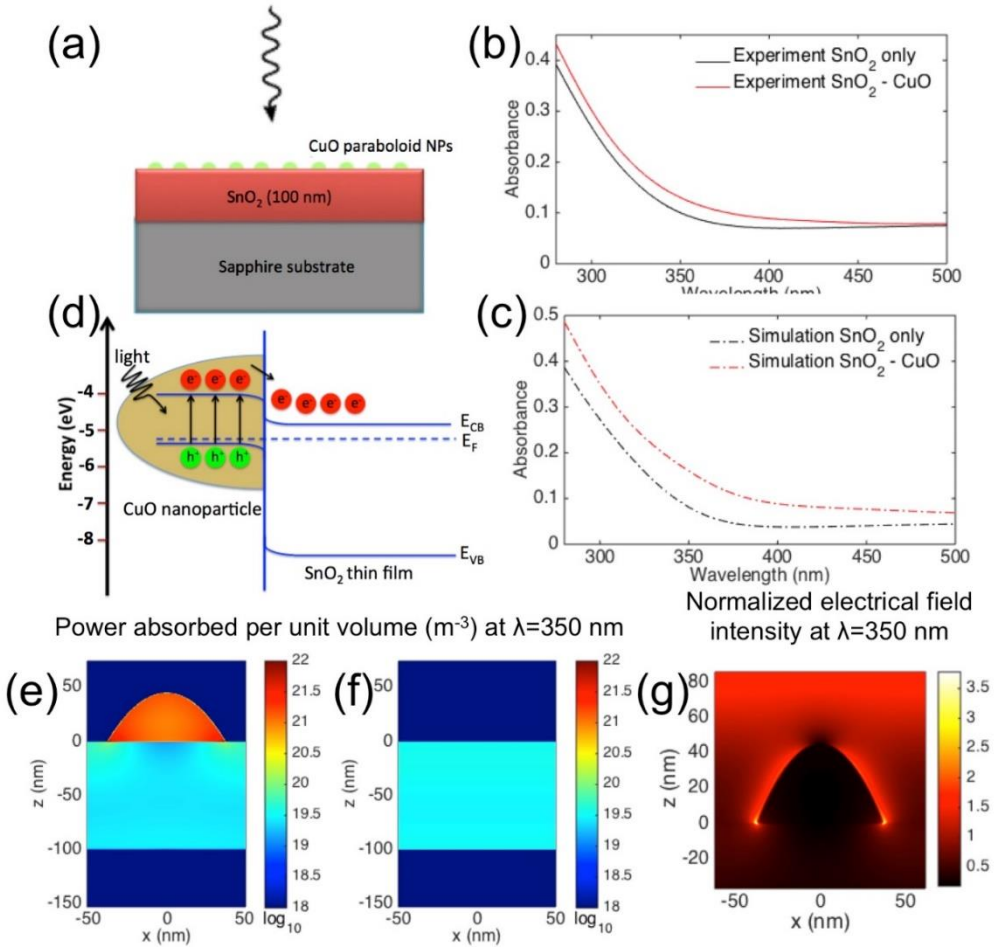

Figure 6.4 (a) Diagram of the setup for the FDTD simulations. A SnO_2 film thickness of 100 nm was used for the simulations with and without CuO NPs. (b) Measured and (c) FDTD simulated absorption spectra of the SnO_2 and SnO_2-CuO films. (d) Schematic band diagram illustrating the hypothesized electron transfer process in the CuO-SnO_2 nanoheterojunctions under irradiation. (e) Spatial cross-section of simulated power absorbed per unit volume at λ = 350 nm in a single CuO NP on a SnO_2 film and (f) in a bare SnO_2 film. (g) Spatial cross-section of simulated normalized electrical field intensity at λ = 350 nm for a single CuO NP on a SnO_2 film.

Figure 6.4b and c show the experimental and simulated absorption spectra for the SnO_2 films with and without CuO NP clusters. The simulated and measured spectra show qualitative agreement in the effect of the CuO NPs on the increase in absorbance across all wavelengths in the plotted range, the apparent red shift of the absorption onset, and the change in shape of the absorbance curve. Differences in quantitative agreement can be attributed to inhomogeneity in the NP size and density distributions, and uncertainty in the SnO_2 film thickness in the real devices.

The simulated spatial absorption profiles for a single CuO NP on a SnO_2 film and a bare SnO_2 film at a wavelength of 350 nm are plotted in Figure 6.4e and f. The normalized electrical field intensity at a wavelength 350 nm is plotted in Figure 6.4g. There is an enhancement of the local electrical field intensity around the NP and strong associated absorption within the NP. We attribute the enhanced absorption in the composite devices to this effect. Our aim was to use this increase in absorption without relying on an increase in SnO_2 film thickness to improve the responsivity of the SnO_2-based photodetectors.

A schematic band diagram for the SnO_2/CuO *pn*-nanoheterojunctions is depicted in Figure 6.4d using energy levels reported for *p*-CuO [163] and *n*-SnO_2 [164]. The nanoheterojunction structure takes advantage of the intense absorption in the CuO NPs to transfer a high density of photogenerated electrons from the *p*-CuO NPs to the *n*-SnO_2 film, while the transfer of holes is hindered by the energy barrier at the junction. The smaller bandgap of CuO (1.35 eV) [163] results in increased absorption at the red edge of the UV spectrum, and the *pn*-heterojunction nature of the CuO/SnO_2 interface facilitates charge transfer upon illumination to increase the responsivity of the

photodetector. Electrons injected into the conduction band of SnO_2 from the CuO increase the free majority carrier density in the photoconductive material, which could lead to a significant increase in photocurrent in the PD. Although the bandgap of CuO is small, the nanoscale structure of the CuO particles are predicted to allow the films to remain "visible-blind" due to poor in-coupling and low absorption in structures that are much smaller than the visible and infrared material photon absorption lengths.

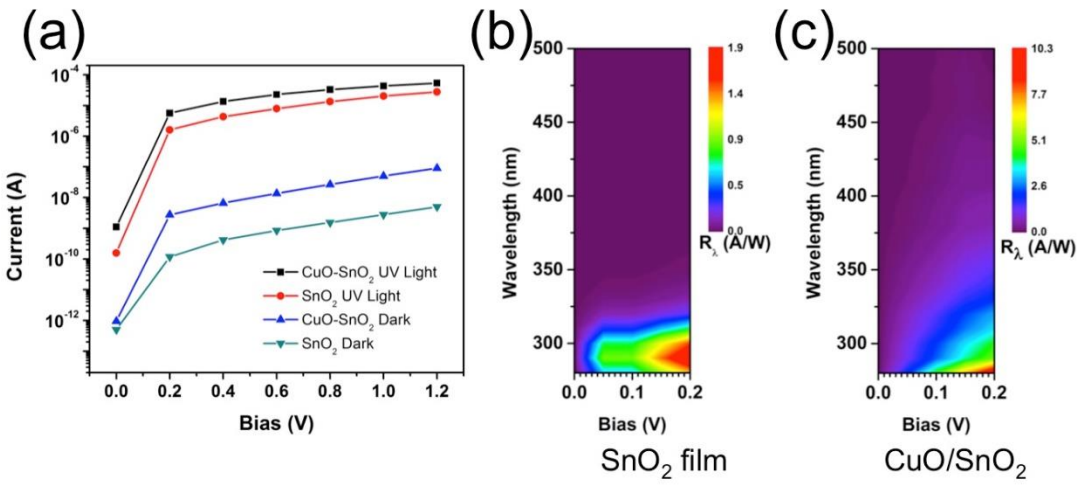

Figure 6.5 (a) ON/OFF I-V curves for SnO_2-only and CuO/SnO_2 PDs under UV illumination at a wavelength of 290 nm. (b) Responsivity as a function of bias and wavelength for SnO_2 and (c) SnO_2-CuO thin film photodetecors.

Typical I-V characteristics of the SnO_2-only and CuO-SnO_2 devices measured in the dark and under UV-illumination are shown in Figure 6.5a. The photocurrent generated in the PD with CuO NPs was almost double that of the SnO_2-only device under 290 nm wavelength illumination for all tested biases. The measured dark current for the CuO-SnO_2 PD was also larger than that of the SnO_2-only device, indicating that the conductivity of the CuO-SnO_2 composite film was larger than that of the SnO_2-only film.

To quantify the performance of the PDs, we used the photocurrent-to-dark current ratio, defined as:

$$Photocurrent - to - dark\ current\ ratio = \frac{I_{UV} - I_{dark}}{I_{dark}} \qquad (6\text{-}2)$$

where I_{UV} is the current under UV illumination, and I_{dark} is the dark current at the same voltage. The CuO-SnO_2 PDs exhibited a PF of ~ 592 at 1.2 V under 290 nm illumination.

Responsivities of the SnO_2 and SnO_2-CuO PDs were measured at various bias voltages under a spectrally filtered light source. The measurements, calibrated using a standard NIST silicon photodiode, were associated with a total uncertainty of ± 5 % (fractional). In order to obtain stable and reliable data, the photocurrent at each wavelength was measured with a delay of 180 seconds with respect to the illumination. The need for stable photocurrent operation precluded higher resolution measurements of the PD response time.

The UV photocurrent response of the PDs was recorded over a voltage range of 0 V to 1.2 V at an illumination wavelength of 290 nm, as shown in Figure 6.5a. In addition to light current enhancements, the dark current also increases after the SnO_2 surface is covered with the CuO NPs, despite the assumed formation of a depletion layer. This increase can be attributed to several potential mechanisms. The small amount of Cu(I)O or Cu metal visible in the XPS spectrum could lead to an increase in the dark current which could be ameliorated in future iterations by including a controlled oxidation step in the fabrication process. Additionally, the presence of defects close to the

nanojunction interface could reduce carrier lifetimes, potentially act as dopants, and facilitate leakage paths, contributing to an increase in device dark current.

Figure 6.5b and c illustrate the spectral responsivity of the SnO_2 devices with and without CuO NPs in the low bias regime. The SnO_2-only PDs reached a maximum responsivity of 1.9 A/W at 0.2 V bias under 290 nm illumination, while the devices with CuO NP clusters exhibited a responsivity of 10.3 A/W at 0.2 V bias under 280 nm illumination. The incorporation of the CuO NPs resulted in a greater than 5 fold improvement of the responsivity. Additionally, the SnO_2-only PD response had a sharp cutoff at around 320 nm in wavelength, whereas the SnO_2-CuO PDs displayed some response out to 340 nm in wavelength at low bias. The broadening of the spectral detection range can be attributed to the drastic enhancement of light absorption and charge transfer facilitated by the SnO_2-CuO nanoheterojunctions in the UVA spectral region. Although the responsivity of these devices is lower than that of PDs based on one-dimensional structures [148, 153], it is competitive with thin-film based UV PDs made from other traditional semiconductor materials [32]. Additionally, this method produces robust structures without complex fabrication processes that operate at low bias, making it suitable for practical applications.

6.1.4. Conclusions

In summary, we have demonstrated high responsivity visible-blind UV PDs based on sputtered SnO_2-CuO nanoheterojunction films. We investigated the properties of the films using AFM and XPS measurements, confirming that the sputtered Cu forms self-assembled nanoparticle clusters that are composed primarily of Cu(II)O after air exposure. The peak responsivity reached a value of 10.3 A/W at a low bias of 0.2 V in

the CuO-SnO_2 devices, representing a five-fold increase over the highest responsivity achieved in devices without CuO NPs. The performance enhancement is attributed to the intense local absorption of the CuO NPs and the charge transfer facilitated by the CuO-SnO *pn* nanoheterojunction structures. Our approach of utilizing CuO-based *pn* nanoheterojunctions to enhance the efficiency of visible-blind SnO_2 photodiodes represents a viable path for building UV optoelectronic devices based on cost-effective materials.

6.2. Tunable ultraviolet photoresponse in solution-processed p-n junction photodiodes based on transition metal oxides

6.2.1. Introduction

The application of semiconductor oxides in UV PDs benefits from their wide-bandgaps in UV spectra, low environmental impacts, thermal stability, and feasibility of constructing bandgap-aligned *p-n* heterojunctions [165]. Among various demonstrated semiconductor oxides employed in *p-n* heterojunction based UV PDs, NiO and ZnO, which are intrinsically *p*- and *n*-type semiconductor oxides respectively, are particularly favored due to their advantageous electrical and optical properties [165-169]. from the II-VI semiconductor ZnO has a direct band gap of 3.3 eV and an exciton binding energy of 60 meV, has and has been employed for applications in optoelectronic devices [170]. Moreover, the bandgap can be engineered between 3.3 eV (ZnO) and 7.8 eV (MgO) by formation of $Zn_{1-x}Mg_xO$ (ZMO) alloys [171, 172]. The alloyed ZMO maintains high optical transparency to visible wavelengths, which is important for transparent optoelectronic applications [169]. Additionally, low

dislocation density during heteroepitaxy [173], high-energy radiation resistance [79], and chemical stability [80] distinguish ZnO (and ZMO) from other wide band gap semiconductors such as GaN (and its alloy $Al_xGa_{1-x}N$), ZnSe, and SiC. Moreover, ZnO is also biocompatible and thus can be utilized in biomedical applications directly [174, 175].

For UV PD applications, ZMO has been primarily realized either as a photoconductor [176] or a Schottky photodiode [177, 178]. In most scenarios, ZMO films have been prepared via prohibitively expensive and sophisticated deposition techniques, such as pulsed laser deposition (PLD) [172, 179], sputtering [172, 180], chemical vapor deposition (CVD) [181], and molecular beam epitaxy (MBE) [182, 183] and they all require energy intensive, high vacuum deposition process. Metal-semiconductor-metal (MSM) and Schottky barrier PDs have their own advantages such as simple planar structure, no UV absorption by metal contact as well low stray capacitance for the former and fabrication simplicity, high speed and absence of high-temperature diffusion processes for the later, *p-n* junction detectors have even more advantages over them, viz. low or zero bias currents, high impedance, larger built in voltage than a Schottky diode made with the same semiconductor as well as low saturation current. In contrast to the well-documented performance of p-NiO/n-ZnO heterojunctions for UV PD applications [35, 165, 184], there have been comparably few reports on homojunction $Zn_{1-x}Mg_xO$ [185, 186], but p-n heterojunctions made with other non-Zn based oxides are lacking using sol-gel method.

In this work, we have successfully fabricated semiconductor oxide UV PDs comprised of solution-processed p-NiO and n-$Zn_{1-x}Mg_xO$ (x = 0 - 0.1) layers on conductive

fluorine-doped tin oxide (FTO) covered glass substrates. The devices show prominent UV photoresponse that can be tuned by adjusting the Mg contents, consistent with the bandgap of alloyed ZnO. For higher Mg content ($x > 0.1$), compositional non-uniformity has been observed over the film which is being manifested in the device optical properties.

6.2.2. Experimental details

The schematic structure of fabricated PDs is illustrated in Figure 6.6a. The FTO/glass substrates were first cleaned with acetone and isopropanol in an ultrasonic bath and subsequently rinsed with deionized water, and finally dried with N_2 gas. For fabrication of UV PDs, NiO precursor was spin-coated on the substrates and the film was immediately dried at 300 °C for several minutes on a hot plate in a fumehood. The procedure was repeated multiple times in order to reach film thickness of 250 nm to 300 nm. Similar procedure was repeated for $Zn_{1-x}Mg_xO$ to achieve ≈ 100 nm to 120 nm thick film. Finally, the bilayer films were annealed at 400 °C for 20 min in air. Ultrathin Ti (10 nm)/Au (3 nm) top contacts were deposited by electron-beam evaporation at a rate of ≈ (0.5 - 1) Å/s through a metal stencil mask having an array of circular openings of 3 mm afterwards. The detailed preparation procedure of oxide precursors is described in the Appendix A.1.

The surface morphology and cross-sectional structure of the PDs were examined using Bruker Dimension FastScan atomic force microscope (AFM) and Hitachi-4700 high resolution scanning electron microscopy (SEM) equipped with energy dispersive X-ray spectrometry (EDS). Cross-sectional images were taken from freshly cleaved

samples after coating them with carbon to avoid charging effects. Structural characterization of the oxide films was conducted using X-ray diffraction (XRD). Vacuum ultraviolet variable angle ellipsometry (VUV-VASE) measurements were performed to determine the dielectric functions of the films from which optical band gaps were extracted by employing Tauc plots [187].

The performance of the devices were characterized for current-voltage (I-V) and external quantum efficiency (EQE) using a spectrally filtered light source and illuminated through Ti/Au contacts during the measurement. The light source was spectrally filtered to deliver monochromatic light from 250 nm to 2400 nm with up to 0.7 nm resolution. Prior to each device measurement, the light source had been switched on for 20 min to ensure power stability. 13 mm in diameter was estimated for the size of exposed area. The EQE system was calibrated using a NIST-calibrated silicon photodiode. A total uncertainty of ± 5 % (fractional) is associated with measured EQE under AM1.5 illumination.

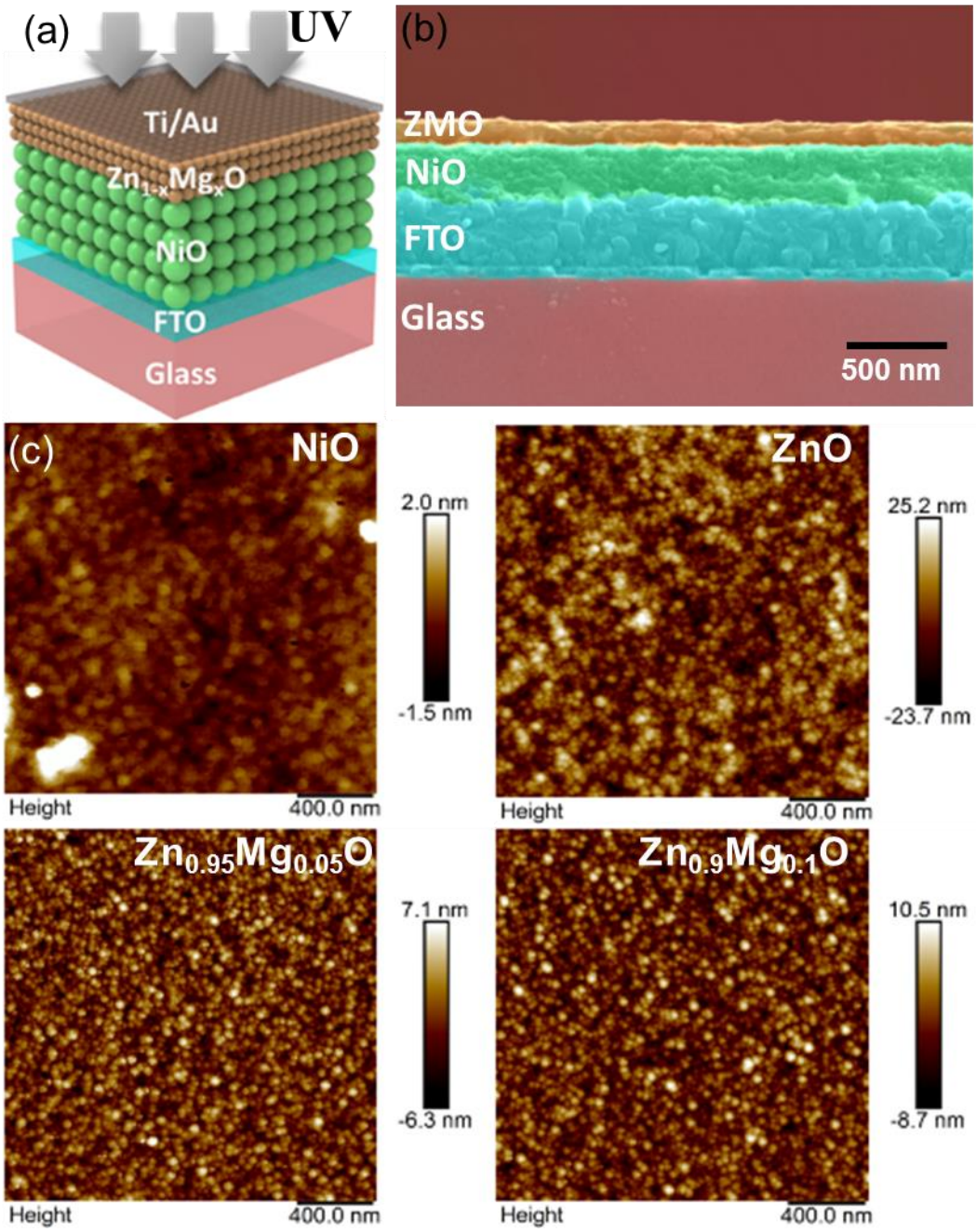

Figure 6.6 NiO/$Zn_{1-x}Mg_xO$ heterojunction PD: (a) Schematic of the device showing metal oxides along with FTO and Ti/Au metal contacts, (b) Cross-sectional SEM (false color) image of an actual device with x = 0.05. (c) AFM images of all the oxides spin coated on silicon substrates after annealing them at 450 ^{o}C for 20 min in air.

6.2.3. Results and discussion

Figure 6.6b is the cross-sectional SEM image obtained from a fabricated PD. The SEM image clearly shows the multilayer structure that is consisted of glass, FTO, NiO and $Zn_{0.95}Mg_{0.05}O$ while the top metal contact layer is too thin to be identified at this magnification. The thicknesses of spin-coated NiO and $Zn_{0.95}Mg_{0.05}O$ can be confirmed to be 300 and 80 nm respectively from the image. Those numbers are consistent with the pre-calibrated process recipe. The sharp interface between NiO and $Zn_{0.95}Mg_{0.05}O$ indicates smooth surfaces of fabricated films, which is further verified by AFM results illustrated in Figure 6.6c. From the high-resolution AFM images of spin-coated and later annealed thin films, clear information of grains can be gleaned at the first sight. The granularity of $Zn_{1-x}Mg_xO$ (x = 0.05, 0.1) films is comparable to the grain size of ZnO film with a typical diameter ranges from 20 to 25 nm. The resemblance in granularity of ZMO and ZnO films originates from the similarity of the ionic radii of Zn^{2+} and Mg^{2+}. However, $Zn_{1-x}Mg_xO$ (x = 0.05, 0.1) films exhibit much smooth surfaces when compared to ZnO film. The calculated root mean square (R_q) of $Zn_{1-x}Mg_xO$ (x = 0, 0.05, 0.1) are 7.15, 2.02, and 2.63 nm, respectively. Distinct from ZnO and ZMO films, NiO film possesses a larger gain size, roughly around 40 nm, with a much diminished surface roughness value, 0.45 nm in terms of R_q. The low surface roughness and small granularity of engineered NiO and ZMO films make them suitable for fabricating abrupt heterojunctions.

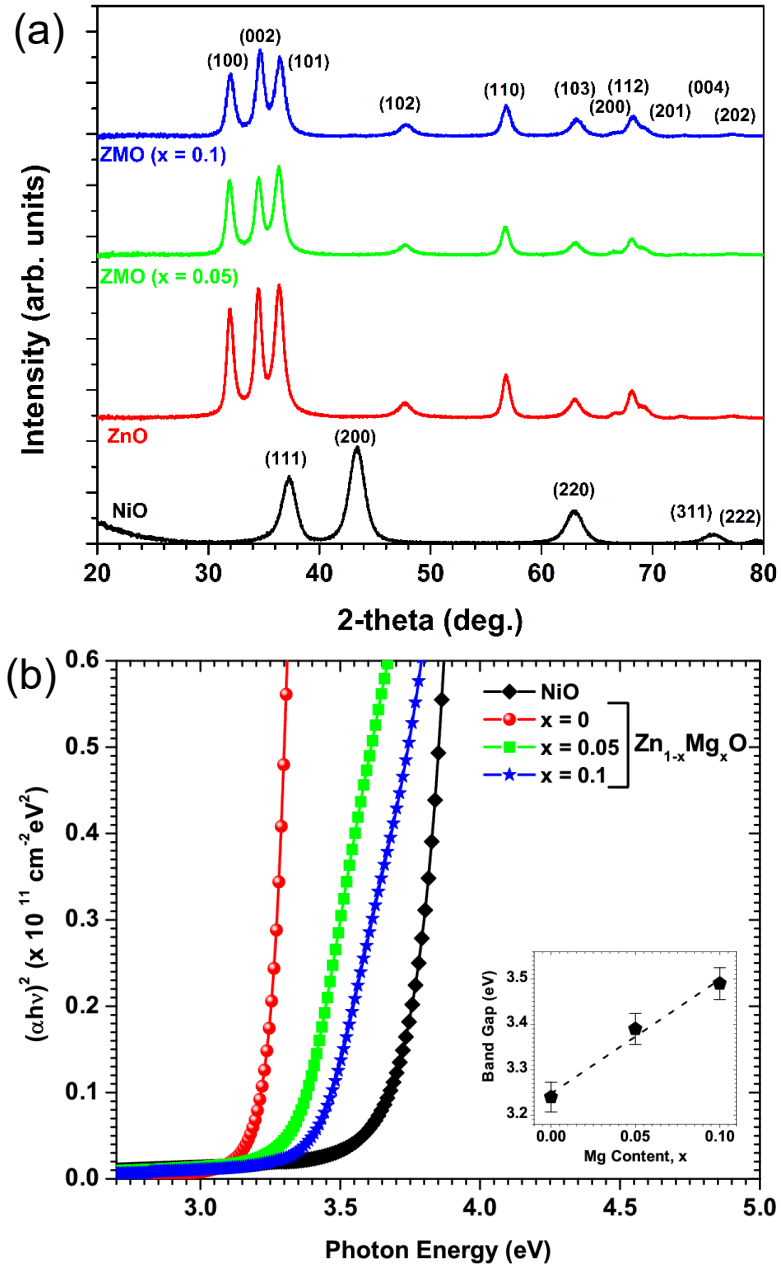

Figure 6.7 (a) XRD scans showing diffraction peaks coming from cubic and hexagonal structures of NiO and $Zn_{1-x}Mg_xO$, respectively. XRD measurements confirm the formation of metal oxides as well as no MgO phase for the alloyed sample. (b) Estimation of the direct energy band gap of all the oxides from ellipsometry measurements (Tauc plot). The inset shows the linear fit of the measured band gap as a function of Mg content.

Figure 6.7a is the XRD patterns of prepared NiO and $Zn_{1-x}Mg_xO$ (x = 0, 0.05, 0.1) films. By referring to standard reference, all detected diffraction peaks are identified as

cubic NiO (JCPDS-78-0643) or hexagonal ZnO structure (JCPDS 36-1451) accordingly. The broad diffraction peaks are in agreement with the polycrystalline nature and the small grain size of processed thin films. A subtle but systematic shifting of ZnO (002) towards higher diffraction angle with an increase in Mg content is identified with a dash line superimposed onto Figure 6.7a. This observation is attributed to the slightly lower ionic radii of Mg^{2+} dopant, consistent with results reported elsewhere [170]. Owing to the small amount of Mg additive into ZnO, no segregation of MgO is found from XRD data. Figure 6.7b is a Tauc plot of NiO and $Zn_{1-x}Mg_xO$ (x = 0, 0.05, 0.1) that relates the absorption coefficient α which is measured with ellipsometry with photon energy $h\nu$. Tauc plot is a widely used technique to characterize optical band gap of semiconductor thin film, through which band gap is derived from extrapolating of the linear region in the curve of $(\alpha h\nu)^{1/r}$ as a function of $h\nu$ with zero, whereas r = 1/2 in this case denotes the allowed direct transitions [109]. The inset of Figure 6.7b displays the deduced optical band gaps, 3.24 eV, 3.38 eV, 3.49 eV of alloyed $Zn_{1-x}Mg_xO$ with different Mg contents x = 0, 0.05, 0.1, respectively while 3.68 eV is found for NiO. The results indicate that all film prepared with our sol-gel method are suitable for UV PDs as they are highly transparent in the visible light range.

In order to understand the optical absorption and bandgap energy of NiO and $Zn_{1-x}Mg_xO$, absorption coefficients (α) are calculated from the dielectric functions of the thin films using ellipsometry. The optical band gap (E_g) is then derived from the Tauc plot which is a linear relationship of $(\alpha h\nu)^2$ vs. photon energy where $h\nu$ is the photon energy (Figure 6.7b). E_g is deduced from a linear fit to the near band gap spectral region and found to be ≈ 3.72 eV for NiO. For $Zn_{1-x}Mg_xO$ films, there is a gradual blue shift

of the fundamental absorption edges with the increase of Mg concentration. The value increases linearly from 3.24 eV for x = 0 to 3.49 eV for x =0.1 which can be fitted with an equation: $E_g = 3.248 + 1.25.x$. It must be noted here that for x = 0.1, the tauc plot shows another linear regime at lower energy (below 3.7 eV) in addition to the one used for linear fitting and this may indicate some composition variation across the sample as will be discussed later on. Although the ionic radii of Mg^{2+} ions (0.57 Å) is almost equal to that of Zn^{2+} ions (0.60 Å) [188], one may expect a wide range of solubility of Mg in ZnO. The thermodynamic solubility limit of Mg in ZnO is only 4% [189], although the solid solubility of MgO in ZnO for thin films has been reported 33 mol% as deposited by PLD [172] and 43% as deposited by MBE [190]. Sol–gel method is based on equilibrium growth conditions and thus the solubility is influenced by the starting precursors, solvents, temperature etc. as opposed to other non-equilibrium growth. The compositional fluctuations in solution-processed $Zn_{1-x}Mg_xO$ systems have also been reported for nominal [191-193] to higher [194] Mg content and our data also indicate some possible compositional variation for x = 0.1. In any case, all the films are highly transparent in the visible range making them suitable for UV PDs.

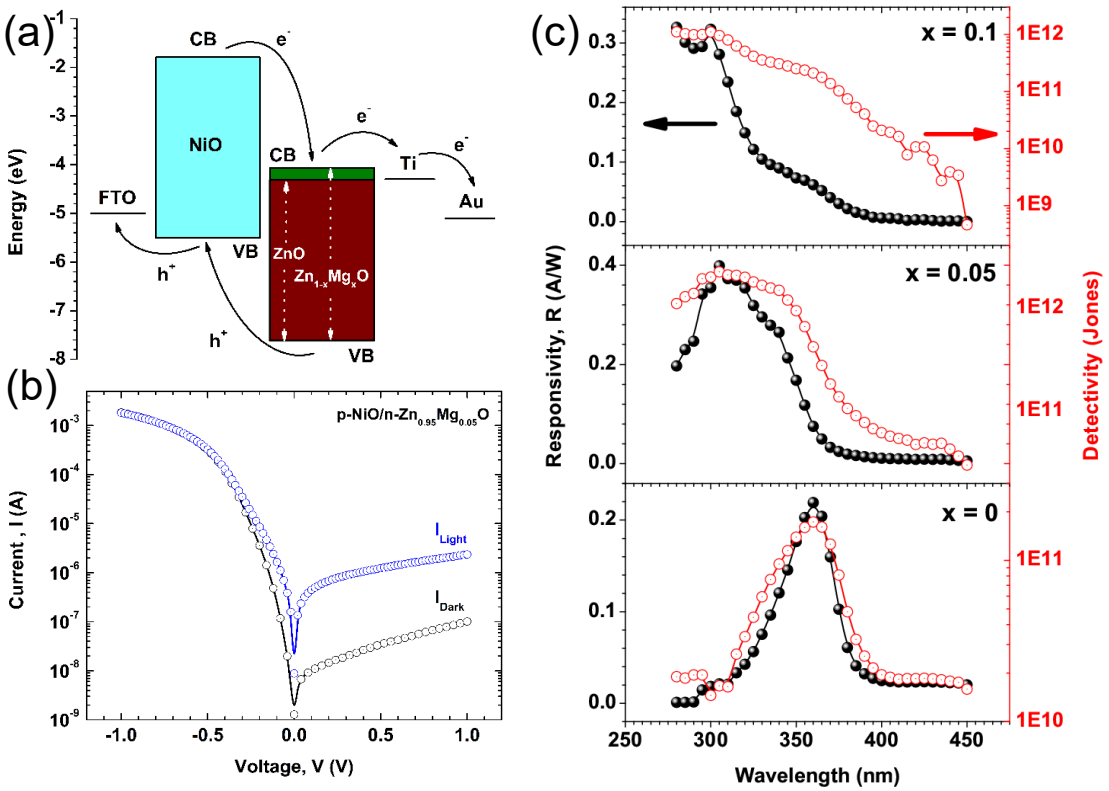

Figure 6.8 (a) Energy levels of various components in the PDs. The conduction band (CB) of $Zn_{1-x}Mg_xO$ changes with Mg content whereas valence band (VB) position remains the same. Photogenerated electrons and holes move to their respective contact. (b) Current-voltage (I-V) plot of the p-NiO/n-$Zn_{0.95}Mg_{0.05}O$ heterojunction diode in dark and UV illumination at 335 nm with 1.2 μW power. The rectifying nature of the diode as well as the photoresponse are evident from the I-V data. (c) Responsivity and detectivity of all the devices at 1 V reverse bias.

The energy levels of various components of the PD are shown in Figure 6.8a, where $Zn_{1-x}Mg_xO$ is depicted as a tunable bandgap system due to different Mg content of x. Based on the reported data, incorporation of Mg^{2+} into ZnO leads to the modifications of conduction band (CB) edge of the ternary oxide whereas the valence band (VB) edge remains unchanged [195]. Thus CB edge values change within ~ 0.25 eV as the corresponding bandgap of $Zn_{1-x}Mg_xO$ vary from 3.24 eV to 3.49 eV with an increase in Mg content (x = 0 - 0.1). Under UV illumination, the photogenerated electrons are transported through the $Zn_{1-x}Mg_xO$ layer to the Ti/Au cathode and the holes are

transported from NiO to FTO anode. Based on the band-edge energy offsets, NiO/ $Zn_{1-x}Mg_xO$ layers form a type-II heterojunction (Figure 6.8a). The built-in field as well as the "*intrinsic*" energy gradient at the type-II interface enables spatial separation of electrons and holes. The current-voltage characteristics of the heterojunction diodes reveals the anticipated rectifying behavior in the dark and exhibits an excellent rectification ratio of ≈ 18500 at ± 1 V (Figure 6.8b). Under UV illumination, current enhancement is observed under reverse bias due to the photogenerated carriers. It is worthwhile to mention here that the current density of the devices decreases after Mg alloying due to the increase in resistivity. ZnO is a n-type material and the higher doping density is attributed to the interstitial zinc and/or oxygen vacancy [196]. By incorporating Mg into ZnO, the oxygen vacancies are suppressed which reduces the carrier density in the film. Hence, dark current decreases from 100 nA to 18 nA at a reverse bias of 1 V when the Mg content increases.

The spectral response of the PD is measured by scaling the measured photocurrent with that of a Si photodetector, given nominally identical illumination under applied reverse bias. The typical responsivity and the detectivity of NiO/$Zn_{1-x}Mg_xO$ devices under a reverse bias 1 V are shown in Figure 6.8c in the spectral range from 280 to 500 nm. For ZnO (x = 0), the peak response occurs at 360 nm with the responsivity of ≈ 0.22 A/W. The -3dB cut-off edge is close to the absorption edge of ZnO. The photoresponse moves to the higher energy in $Zn_{1-x}Mg_xO$ alloy films consistent with the increase of bandgap. For $Zn_{1-x}Mg_xO$ with Mg content of x = 0.05, the maximum responsivity reaches to ~ 0.4 A/W at 310 nm and there is no discernible responsivity for photons below 360 nm consistent with its bandgap (Figure 6.8b and Figure 6.10b). In case of x

= 0.1, the responsivity reaches to ~ 0.32 A/W at 300 nm. However, the device shows a sharp decrease of the photoresponse at 340 nm close to the bandgap of NiO and then slowly decreases above 350 nm which is the absorption edge of $Zn_{1-x}Mg_xO$ (x = 0.1). The responsivity further goes beyond its band gap and this indicates that there is a possible composition fluctuation across the sample.

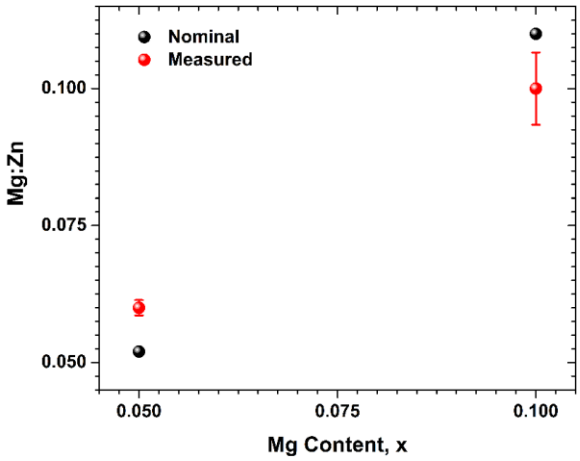

Figure 6.9 Nominal and experimentally measured Mg:Zn ratio with Mg content (x) in $Zn_{1-x}Mg_xO$ thin films. Spectra have been collected at random locations of the samples.

In order to verify this, EDS analysis has been performed for the compositional analyses of Mg and Zn in all the samples. The values are plotted as a function of nominal Mg content (*x*) and compared with the measured Mg:Zn values as shown in Figure 6.9. Experimental Mg:Zn ratio shows less deviation from its nominal value for Mg content of x = 0.05 despite the and thereafter deviates significantly for x = 0.1. Hence, these data suggest a local compositional non-uniformity for higher Mg content which is beyond the thermodynamic solubility limit in an equilibrium system like this. Furthermore, it is possible that Mg may incorporate into NiO during annealing and this is likely to change the bandgap of NiO,[197] which could explain the photoresponse of the alloyed samples. Investigating such effects are beyond the scope of this thesis. On

the other hand, the sample shows the maximum detectivity of (0.17 - 2.2) × 10^{12} Jones depending on the composition. Overall, the data clearly show that one can tune the response of photodiode simply by tuning the bandgap of one constituent materials in the system.

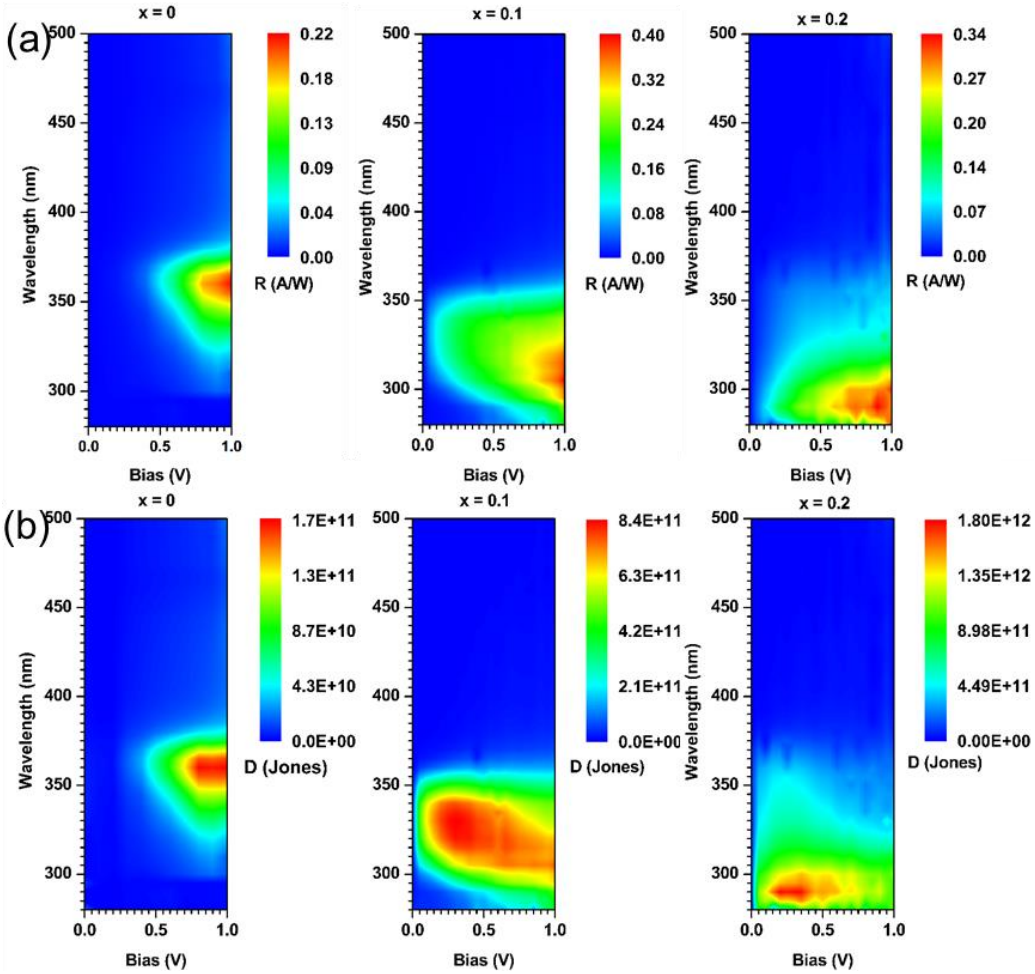

Figure 6.10 Device performance of NiO/$Zn_{1-x}Mg_xO$ heterojunctions with various Mg content, x as a function of applied reverse bias: (a) responsivity, R_λ and (b) detectivity.

The advantages of operating a photodiode under zero or low bias voltage are the low dark current, low noise level, and large dynamic range. In addition, a low operating voltage will allow one to take advantage of the large differential resistance near zero

bias, leading to large directivities. Thus, the devices were further measured below 1 V to assess the performance shown in Figure 6.10. When the devices were tested in photovoltaic mode (i.e., under zero bias), the flow of photocurrent out of the device is restricted. Hence the responsivity is very low particularly for NiO/ZnO devices (maximum value is ~ 0.34 mA/W at 340 nm). For x = 0.05, it is ~ 1.4 mA/W; the detectivity is ~ 6.76×10^{10} Jones, both at 340 nm.

When the bias is increased across the device, there is no appreciable response from NiO/ZnO device below 0.5 V (Figure 6.11a). But for the alloyed samples, the strong response is detected under the same bias. ZnO is intrinsically an n-type semiconductor with high carrier concentration, thus at equilibrium, higher doping levels result in smaller depletion widths [198] and lower quantum yields, since the minority carrier (i.e. holes for ZnO) diffusion lengths are very short in these materials [199]. Upon illumination, the minority carrier current increases, mostly from electron-hole pairs generated within the depletion region. The collection is very inefficient in the quasi-neutral region (part of the device beyond the depletion region) due to the small minority carrier diffusion length and thus recombination can take place. For Mg alloyed devices, the resistivity increases i.e., the doping density decreases with the increase of Mg content. Thus the depletion width on $Zn_{1-x}Mg_xO$ side increases. Hence, NiO/$Zn_{1-x}Mg_xO$ (x = 0.05, 0.1) heterostructure diode shows better photoresponse as compared to ZnO at the same low bias as the minority carriers in the sample are swept out by the large electric despite having short diffusion length. The responsivity of the devices almost saturates at high bias indicating carrier mobility saturation or sweep-out effect yielding a saturation of the current.

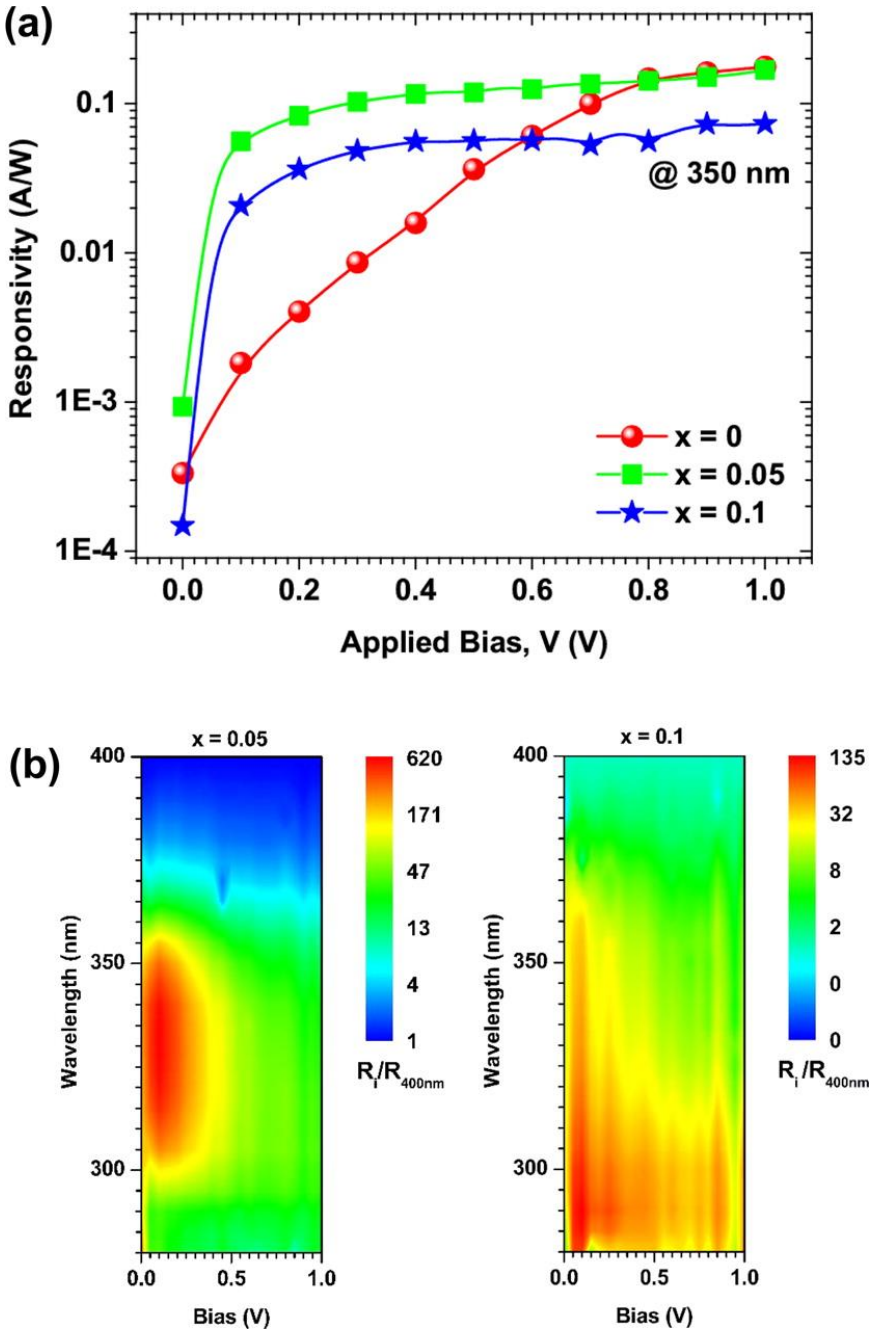

Figure 6.11 (a) NiO/Zn1–*x*Mg*x*O heterojunction device response at 350 nm as a function of applied bias. (b) UV–visible rejection ratio (*R*i/*R*400 nm) for Mg content of $x = 0.05$ and 0.1 in which $i = (280–400)$ nm.

The heterojunction devices also exhibit good UV-selective sensitivity with excellent UV-to-visible rejection ratio ($R_i/R_{400nm}, i = 280 - 400\ nm$) calculated from the responsivity at i^{th} wavelength in the UV regime divided by the responsivity at 400 nm and this gives the rejection ratio for each wavelength. The maximum rejection ratio of

over 600 has been achieved for $Zn_{1-x}Mg_xO$ with x = 0.05, but it is lower for x = 0.1 (Figure 6.11b).

Table 6.1 Performance matrix of various $Zn_{1-x}Mg_xO$ based PDs reported in the literature.

Material	Configuration	Growth	Bias (V)	$Max.R_\lambda$ (A/W)	Ref.
$Zn_{0.38}Mg_{0.62}O$	MSM	MBE	10	1.664	[200]
$Zn_{0.5}Mg_{0.5}O$	p-n	MBE	2	$6m$	[201]
$Zn_{0.53}Mg_{0.47}O$	MSM	Sputtering	5	$10.6m$	[202]
$Zn_{0.66}Mg_{0.34}O$	MSM	PLD	10	0.8	[186]
$Zn_{0.66}Mg_{0.34}O$	MSM	PLD	5	1200	[176]
$Zn_{0.76}Mg_{0.24}O$	p-n	MBE	9	$0.4m$	[185]
$Zn_{0.8}Mg_{0.2}O$	MSM	Sputtering	3	0.02	[203]
$Zn_{0.82}Mg_{0.18}O$	Schottky	CVD	1.5	32	[204]
NiO-ZnO	p-n	Sol-gel	1	0.28	[35]
NiO-ZnO	p-n	Sol-gel	1	10.2	[205]
NiO-$Zn_{1-x}Mg_xO$	**p-n**	Sol-gel	**1**	$\mathbf{0.22 - 0.4}$	**This work**

6.2.4. Conclusions

In summary, simple, cost-effective solution-processed p-n heterojunction UV photodetectors have been conveniently fabricated on FTO/glass substrates by spin-coating method using wide-band gap NiO and $Zn_{1-x}Mg_xO$. Sol-gel $Zn_{1-x}Mg_xO$ thin films show hexagonal wurtzite type of crystalline structure and no significant change of grain morphology for all the films studied. The fabricated heterojunction photodiode exhibits very low dark current under reverse bias with excellent rectification. The PDs have shown tunable photoresponse with superior responsivity and detectivity in the UV

regime. Compositional non-uniformity has also been observed for high Mg content. Considering the advantages of solution-processable fabrication, the devices have potential for use in low cost, large-area UV PD applications.

6.3. Surface compositions of atomic layer deposited $Zn_{1-x}Mg_xO$ thin films studied using Auger electron spectroscopy

6.3.1. Introduction

The incorporation of solid solution of MgO, another II-VI material that has band gap of 7.8 eV, into ZnO has allowed band-gap engineering in alloyed compound $Zn_{1-x}Mg_xO$ (ZMO) [206]. Tailoring the band gap by adjusting the mixture ratio of MgO to ZnO is well established by numerous reports [171, 180, 207-209]. The alloyed ZMO remains optically transparent to visible wavelengths. Additionally, low growth temperature, high radiation hardness and stable chemical property of ZnO (and ZMO) distinguish itself from other wide band gap semiconductors such as GaN or ZnSe [80].

The crystal structure of ZnO is hexagonal with a = 3.24 Å and c = 5.20 Å while MgO is cubic with a = 4.24. Based on the phase diagram, the solid solubility of MgO in ZnO is merely 4 mol. % due to their entirely different crystal structures [210]. However, owing to the similarity of the ionic radii of Mg^{2+} and Zn^{2+}, it was hypothesized and later confirmed that up to 50 mol. % of MgO doped ZnO metastable thin film can be deposited by sputtering a single $Zn_{1-x}Mg_xO$ (ZMO) target [180, 207]. However, MgO and ZnO phases separate after post-annealing treatment of ZMO thin film prepared by such sputtering technique [180, 207]. To circumvent the problem of phase segregation

in sputtered films, alternative fabrication processes, namely, sequential cycling of alternate MgO/ZnO layers were introduced. Multilayer ZMO grown via pulsed laser deposition was found to be thermally stable [171]. X-ray diffraction (XRD) studies indicate that Mg and Zn form alloys on these films [180, 207]. However, XRD is sensitive to the bulk and does not provide information about the surface composition. It is therefore unclear if the ions form alloys or remain atomically distinct on the surface. To answer this question, we utilized Auger electron spectroscopy (AES) under ultra-high vacuum (UHV) condition to investigate surface compositions of cycled MgO/ZnO multilayer thin films prepared by atomic layer deposition (ALD). Among all the thin film deposition methods, ALD has become a mainstream process in metal oxide deposition, owing to its advantage of producing conformal layers even on rough surfaces [211, 212]. AES is a widely used and well established technique to obtain surface elemental information [128]. Briefly, AES is performed by creating core level holes on a sample from collisions with incident electron beam. The vacancy is filled by a transition of an electron from a higher energy level and the simultaneous ejection of another electron to conserve the energy. The energy of emitted electrons is directly related to the energy levels of the sample, and serves to identify specific elements on the surface. The process is highly surface sensitive since only those electrons within only a few atomic layers on the surface can be detected due to the short mean free path of Auger electrons [93]. A specific element is identified by its Auger peak positions and the peak-to-peak magnitude is proportional to its elemental concentration on surface [93, 97]. We present overwhelming evidence based on AES analysis, that

indicate that Mg in as-deposited MgO diffuses into ZnO under layer and forms an alloy of $Zn_{1-x}Mg_xO$ during the ALD fabrication process.

6.3.2. Experimental details

The Mg composition of the $Zn_{1-x}Mg_xO$ thin-films was defined by an ALD supercycle consisting of n [ZnO] cycles interrupted by a single [MgO] cycle where n was varied between 1 and 9. The details of ALD precursors are described in the Appendix A.2. For each composition, the number of supercycles was repeated m times such that $m \times (n+1) = 1000$. Films with different numbers of *m*-[MgO]/*n*-[ZnO] layers (1/4, 2/8, 3/12, 4/16, and 5/20) in a film stack were prepared. We also prepared pure MgO and ZnO films using same ALD deposition process as references for further studies. After growth, the ZMO films were maintained inside an inert N_2 atmosphere. Spectroscopic ellipsometry was used to estimate the thickness of the films. The obtained average rate per ALD cycle for ZnO and MgO is 1.6 Å and 1.0 Å, respectively. The thickness of prepared films ranges from 1000 Å to 1750 Å. The bulk crystal structure and optical bandgap of the films were probed using x-ray diffraction (XRD) and ultraviolet-visible spectroscopy (UV-Vis), respectively. The surface morphology of the films were examined by Atomic Force Microscopy (AFM).

The samples were transferred from ALD to AES chambers within few hours and then kept under ultra-high vacuum (UHV) condition (base pressure < 10^{-9} torr) to outgas surface contamination such as water vapor for several hours before AES measurement. Contamination was inevitable due to the ambient exposure of the samples during the transfer process. However, the AES spectra obtained in our experiment showed clear peaks of Zn, Mg and O. Therefore, it is not likely that surface contamination had

influenced our conclusion that Mg ions diffuse into ZnO underlayer. The AES study of the ZMO thin films were performed in an Omicron Analytical system under UHV conditions. A retarding field analyzer was utilized to filter and collect emitted Auger electrons. AES spectra were obtained in two kinetic energy ranges. One started from 450 eV to 1200 eV and the other ranged from 25 eV to 80 eV. The chosen kinetic energy covered the Auger peak positions of MNN/LMM Zn, KLL O, and LMM/KLL Mg. The low kinetic energy range (25 eV to 80 eV) was severely influenced by the collected secondary electrons so that AES experimental parameters such as oscillation amplitude, sensitivity, and lock-in time constant were adjusted differently for the two ranges. Therefore, a direct comparison of signal intensities from different kinetic ranges is impossible. Lastly, the spot size of incident electron beam was around 1 cm^2, so that the AES results represent an averaged signal across the exposed area.

6.3.3. Results and discussion

Figure 6.12a illustrates the schematic diagram of a $Zn_{0.75}Mg_{0.25}O$ (Mg/Zn =1/3) thin film. Fig. 1b and 1c show the surface morphology of $Zn_{0.5}Mg_{0.5}O$ (Mg/Zn = 1/1) and $Zn_{0.66}Mg_{0.33}O$ (Mg/Zn = 1:2), respectively. The high-resolution AFM images, shown in Figure 6.12b and c, reveal relatively smooth surfaces and small grain sizes of the ALD fabricated multilayer thin films. The estimated root mean square (Rq) surface roughness is 2.75 nm and 3.42 nm for $Zn_{0.5}Mg_{0.5}O$ and $Zn_{0.66}Mg_{0.33}O$, respectively. The grain sizes of the two fabricated ZMO films are very close, both ranging from 40 nm to 50 nm. The similarity of the surface granularities of the ZMO films originates from the resemblance of the Mg^{2+} and Zn^{2+} ions.

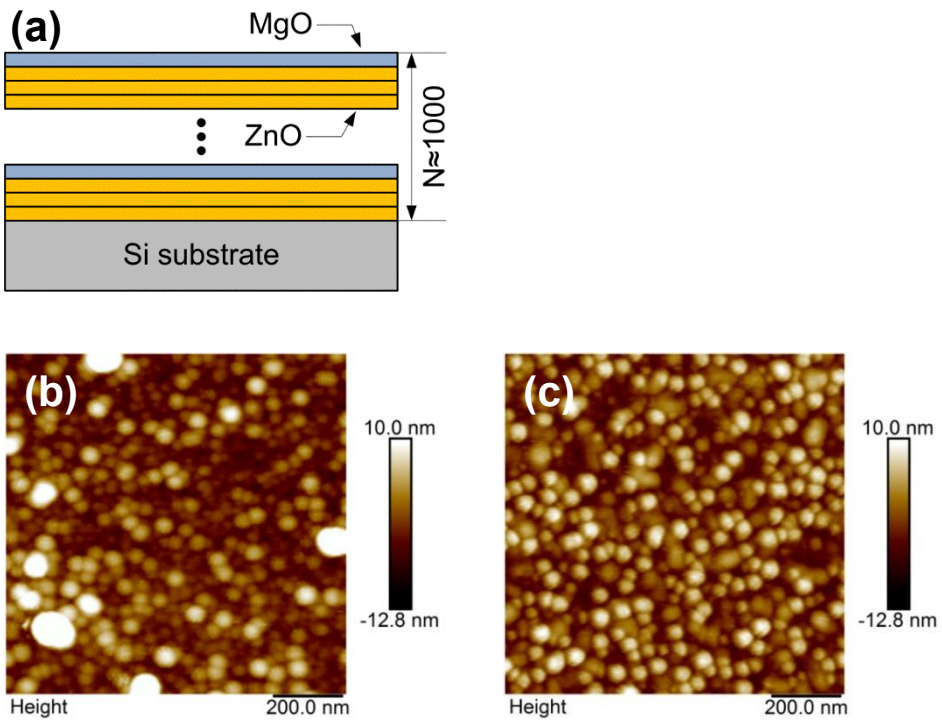

Figure 6.12 (a) schematic diagram of a $Zn_{0.75}Mg_{0.25}O$ (Mg/Zn =1/3) thin film, and AFM images of (b) $Zn_{0.5}Mg_{0.5}O$ (Mg/Zn = 1/1) and (c) $Zn_{0.66}Mg_{0.33}O$ (Mg/Zn = 1/2).

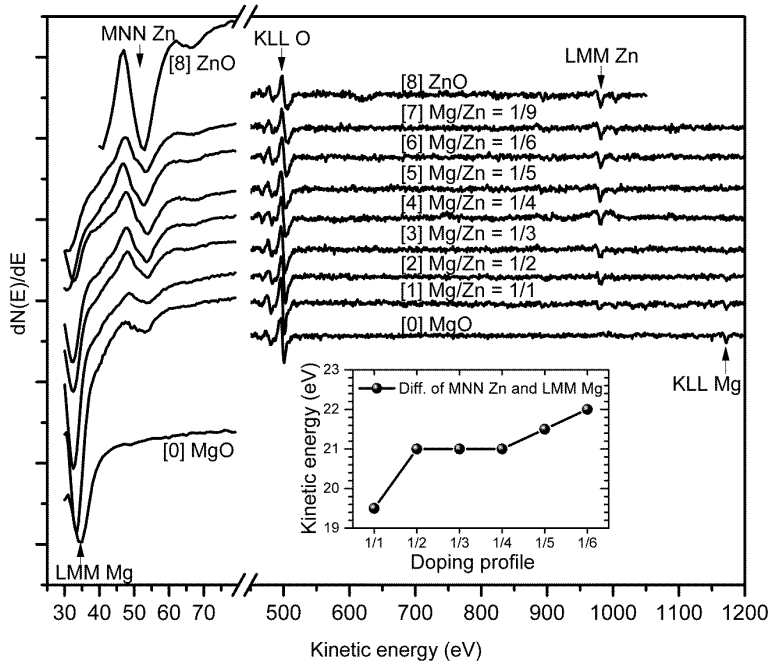

Figure 6.13 AES spectra of MgO film, ZnO film and $Zn_{1-x}Mg_xO$ films with Mg/Zn ratio 1/1 to 1/6 and 1/9. Inset: Differences in AES peak positions of MNN Zn and LMM Mg transitions with respect to various Mg content.

Figure 6.13 shows the AES spectra of undoped MgO, undoped ZnO, and $Zn_{1-x}Mg_xO$ films (Mg/Zn = 1/1, 1/2, 1/3, 1/4, 1/5, 1/6, and 1/9) prepared using the ALD technique. In the figure, spectrum 0 corresponds to the data from the undoped MgO sample while spectrum 8 is from the undoped ZnO film. Spectra 1 to 6 sequenced from bottom to top were obtained from the $Zn_{1-x}Mg_xO$ thin films with the ratios of Mg to Zn from 1:1 to 1:6, respectively and 1:9 for Spectrum 7. The detected Auger peaks of each film are labeled in the figure. From the spectra, we observe that all AES spectra of ZMO films show LMM Zn Auger peak at 981 eV, albeit peaks diminish with increased Mg content. By contrast the KLL Mg peak at 1172 eV drops precipitously as Mg content decrease. Indeed, when the Mg/Zn ratio falls below 1/3, the KLL Mg peak becomes too weak to be distinguished from noise level. Given the fact that the MgO is the topmost layer in all films and that Auger electrons are excited and collected only within a few atomic layers under surface [93], the disappearance of KLL Mg peaks strongly suggest that the deposited Mg atoms on the surface of ZMO films diffuse into the ZnO underlayer during fabrication. The diffusion of Mg from the surface is also bolstered by the results shown in the inset, which shows the difference in Auger peak positions of LMM Mg and MNN Zn collected at low energy spectra. As the Mg content decreases from spectrum 1 (Mg/Zn = 1/1) to spectrum 6 (Mg/Zn = 1/6), the difference in kinetic energies of the LMM Mg and MNN Zn Auger electrons increases monotonically from 19.5 eV to 22 eV. The expanded difference is an evidence for the chemical environment changing of Mg ions, suggesting that Mg ions diffuse into ZnO bulk and form alloy with Zn during ALD fabrication.

In order to further verify the diffusion of Mg ions into bulk, we studied another set of samples with the same Mg/Zn ratio of 1/4 ($Zn_{0.8}Mg_{0.2}O$) but with increasing numbers of MgO/ZnO ALD layers (1/4, 2/8, 3/12, 4/16, and 5/20) in a repeated film stack. Figure 6.14 shows the AES spectra collected from these samples. Spectrum 0 is the data obtained from undoped MgO sample while data from undoped ZnO film is labelled as spectrum 6. Spectrum 1 to 5 corresponds to 1 to5 MgO layers in a repeated film stack, respectively. Notice again that AES is surface sensitive. With the increased amount of Mg from more layers on the top, one would expect to observe Mg AES peak. However, the absence of all KLL Mg Auger peaks of $Zn_{0.8}Mg_{0.2}O$ films at 1172 eV manifests the deficiency of Mg on the surface, indicating the diffusion of Mg ions into ZnO underlayer. The difference of the collected MNN Zn and LMM Mg Auger electrons fluctuates within only ± 1 eV, as shown in the inset, indicating that the chemical environment of the ions is more or less similar in all the $Zn_{0.8}Mg_{0.2}O$ films. This is expected for films with the same Mg/Zn ratio since the concentration rather than the number of layers governs the diffusion.

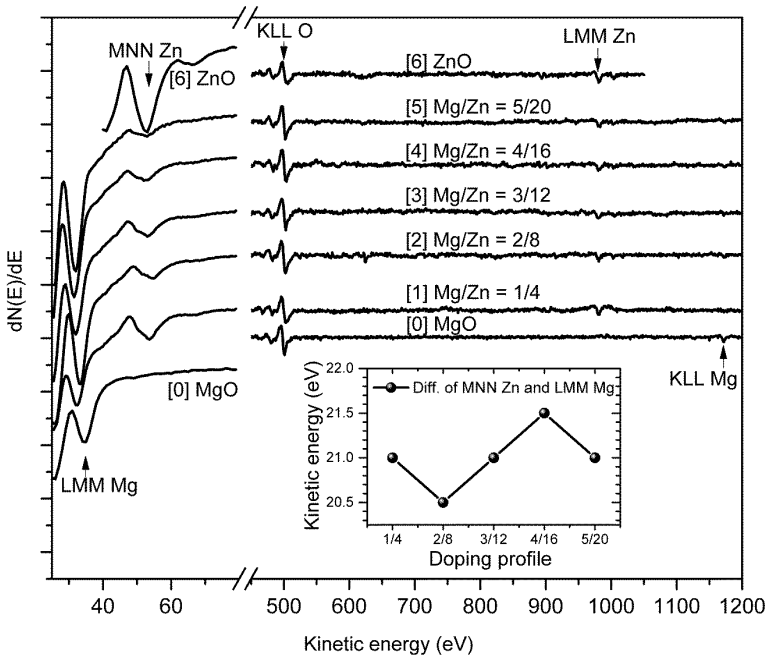

Figure 6.14 AES spectra of MgO film, ZnO film, and Zn0.8Mg0.2O films (Mg/Zn ratio 1/4) with Mg/Zn layers from 1/4 to 5/20. Inset: Differences in AES peak positions of MNN Zn and LMM Mg transitions with respect to various Mg content.

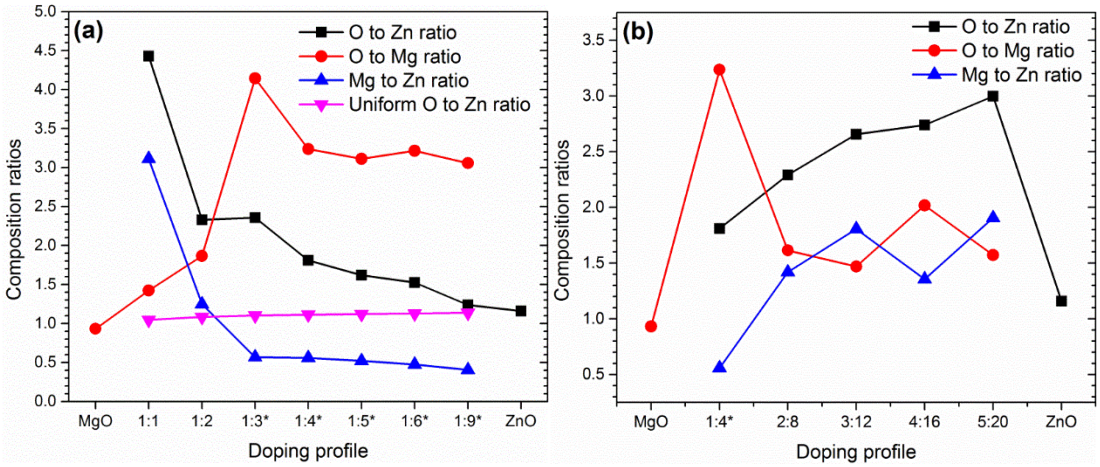

Figure 6.15 Calculated composition ratios of O to Zn ($R^{O}_{Zn}R^{O}_{Zn}$), O to Mg (R^{O}_{Mg}), Mg to Zn (R^{Mg}_{Zn},) and uniform O to Zn (R^{O}_{Zn}(uniform)) ratios for (a) Figure 6.13 and (b) Figure 6.14. The composition ratios labeled with steroid were calculated using standard deviation of noise signal ranging from 1155 eV to 1185 eV.

To further understand the atom distribution on the surface, we calculate the surface compositions of the ZMO films with equation 5-1. Values of Auger sensitivity factors for different elements have been tabulated and published in open source [98]. With the obtained peak-to-peak values of KLL O and LMM Zn Auger peaks from spectra in Figure 6.13 and Figure 6.14 and S_O(KLL) = 0.28 and S_{Zn}(LMM) = 0.17[98], the ratios of surface composition of O to Zn (R_{Zn}^{O}) can be calculated for ZnO film and ZMO films. Similarly, R_{Mg}^{O} as well as R_{Zn}^{Mg}, of MgO film and $Zn_{1-x}Mg_xO$ (Mg/Zn = 1/1 and 1/2) films can be estimated from the KLL O and KLL Mg AES peaks with S_{Mg}(KLL) = 0.06 [98]. Since KLL Mg peaks are indistinguishable from noise level of AES spectra of ZMO (Mg/Zn < 1/3) films, surface composition of Mg on those films cannot be calculated. However, by replacing the peak-to-peak intensity of KLL Mg with the standard deviation of noise from 1155 eV to 1185 eV of the corresponding AES spectrum, we can estimate the upper limit of surface Mg compositions of these films. R_{Zn}^{O}(uniform) is a proposed ideal value that denotes the scenario in which O and Zn ions are uniformly distributed in the ZMO films. It is defined by the following equation,

$$R_{Zn}^{O}(\text{uniform}) = R \cdot R_{Mg}^{O}(\text{MgO}) + (1-R)R_{Zn}^{O}(\text{ZnO}) \qquad (6\text{-}3)$$

where R_{Mg}^{O}(MgO) is the calculated O to Mg ratio of MgO film and R_{Zn}^{O}(ZnO) is the ratio of O to Zn calculated from AES data of ZnO film. R is the ratio of Mg/Zn in the ZMO film. All calculated composition ratios are presented in Figure 6.15. From this analysis, we glean two conclusions. First, the values of R_{Mg}^{O} in Figure 6.15a agree with the qualitative observation from Figure 6.13 that the concentration of Mg ions on the surface decreases precipitously below the Mg/Zn ratio of 1/3. Note here that the actual compositions of Mg ion for $Zn_{1-x}Mg_xO$ (Mg/Zn < 1/3) films are even less that the

correspondent R^{O}_{Mg}. So that the disappearance of Mg Auger peak in the spectra is not because of the low LMM Mg sensitivity factor. Secondly, R^{O}_{Zn} shows the exponential decay towards the ZnO end, which is due to the attenuation of MgO overlayer with the decreasing amount of Mg. The result indicates that the depletion of Mg causes the surface to be oxygen rich. This conclusion is also supported by the fact that R^{O}_{Zn} for ZMO films is higher than the ideal R^{O}_{Zn}(uniform). Similar clues can also be gleaned from Fig 4b. Despite a sharp decrease from 1/4 to 2/8 of Mg/Zn samples, the rest values of R^{O}_{Mg} are relatively constant and more than 50% higher than the R^{O}_{Mg} for MgO film (spectrum 0). The excessive amount of oxygen is due to the diffusion of Mg rather than the Auger electrons from ZnO that filter through the MgO overlayer. Because otherwise, the values of R^{O}_{Mg} with respected to the increased MgO layer in the film stack should decrease monotonically due to the attenuation effect. Therefore, we conclude that Mg diffuses into underlayer of ZMO films, leaving the extra amount of oxygen on surface.

We performed XRD measurements as well to supplement bulk information of the prepared films to our surface analysis results. Figure 6.16a shows the results. In the Figure, the XRD data of the films for Zn/Mg > 2 reveal the (100), (002), and (101) diffraction peaks that are characteristic of the ZnO hexagonal wurtzite structure. For Zn/Mg = 1, the 2θ position of the (100) and (101) peaks are shifted to lower and higher values, respectively. A weak but characteristic peak associated with the (200) plane of the MgO face-centered cubic structure is observed only in the pure MgO film. The absence of the (200) MgO peak in the ZMO films suggests no segregation of MgO in

the multilayer films. The effect on the optical bandgap (E_g) as the ZnO/MgO ratio is varied is displayed in Figure 6.16b. We estimate E_g using a linear fit of the absorbance near optical band edge. The results are presented in the inset which shows the increase in E_g with higher Mg content of the film. Both the XRD and optical bandgap results strongly indicate the incorporation of Mg into the ZnO lattice.

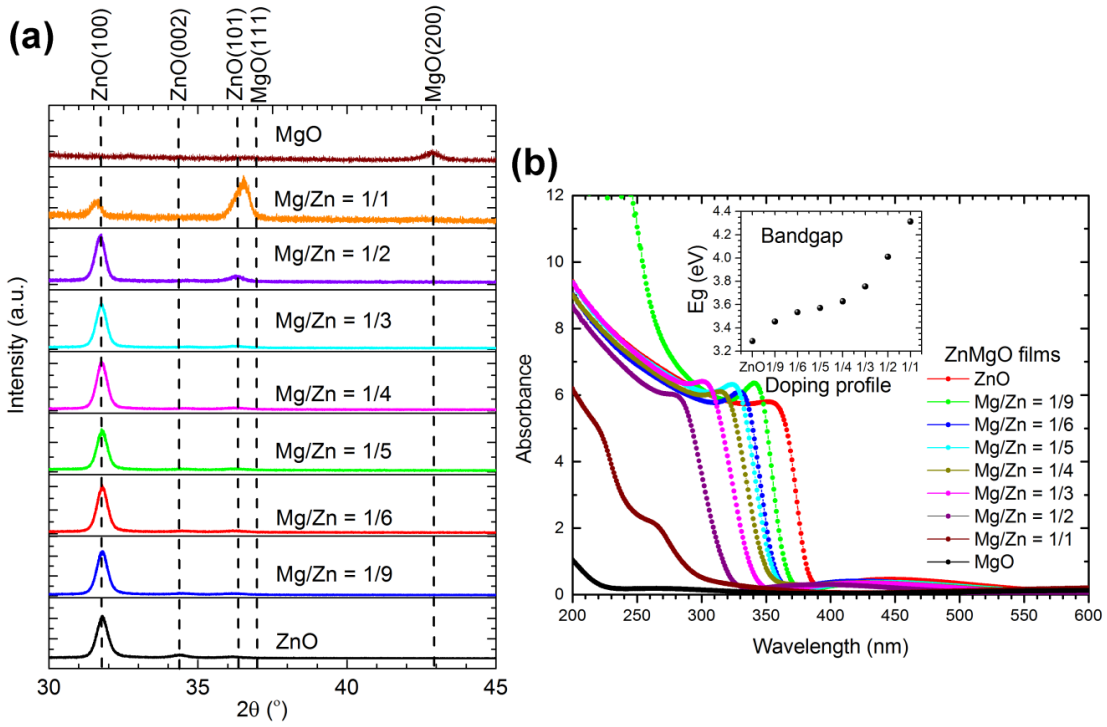

Figure 6.16 (a) Dependence of bulk crystal structure of the thin films on the Zn/Mg ratio from x-ray diffraction. (b) Optical absorption of the films as function of composition. The inset shows the increase in the optical band gap with higher Mg content of the film.

6.3.4. Conclusions

We performed AES on the interrupted ALD fabricated $Zn_{1-x}Mg_xO$ films and analyzed the spectra to obtain the surface compositions. Our results indicate that Mg ions diffuse into ZnO underlayer during the low temperature (150 °C) process while oxygen from

MgO remains on surface, forming $Zn_{1-x}Mg_xO$ alloy. The result is in agreement with the observations from XRD measurement and absorbance spectra. The surface study using AES, but not limited to AES only, provides an approach from surface science to demonstrate the alloying of alternating cycled $Zn_{1-x}Mg_xO$ thin films. Technically, any surface elemental analytical tools, such as AES, Rutherford backscattering spectroscopy, X-ray photoelectron spectroscopy, and secondary ion mass spectrometry can be employed to assess the diffusion of Mg ions on surface in the ZMO films. Moreover, multilayer thin films that are not applicable for bulk analytical techniques can benefit from this surface analytic technique to obtain alloying information from surface compositions.

7. Chapter 7: UV-assisted operation of semiconductor oxides based gas sensors at room-temperature

7.1. Chemiresistive NO_2 sensor based on TiO_2 thin films

7.1.1. Introduction

Nitrogen dioxide (NO_2) pollution has become a critical global issue in recent years. NO_2 is a toxic gas and a major cause of acid rain and photochemical smog. The source of NO_2 mainly arises from the fossil fuels, automobile engines, and industrial plants [65]. The demand for controlling and monitoring NO_2 has driven the gas sensor research community to detect a range of NO_2 concentrations from about 100 nmol mol^{-1} (ppb) in ambient atmosphere [213] to hundreds of µmols mol^{-1} (ppm) in various industries [214, 215].

Solid-state semiconductor oxides have drawn continuous attention for the last few decades, as they promise miniature and low-cost sensors with capability of detecting numerous gas species and many other optoelectronic applications [35, 44, 209, 216]. Among the studied oxide semiconductors, titanium dioxide (TiO_2) stands out owing to its extraordinary chemical stability, resistance to harsh atmospheric conditions [217], and low production cost. TiO_2, a wide-bandgap and intrinsically n-type semiconductor, has been extensively investigated as a NO_2 gas sensor [53, 58, 217-220]. The sensing

mechanism governing the n-type oxide semiconductors is the concentration of surface-adsorbed oxygen modulated by reducing or oxidizing analyte gases, which consequently transduces the conductivity of the sensor. Thus, the exposure of TiO_2 films to reducing gases such as H_2 and CO increases its conductance while oxidizing gases like NO_2 do the opposite [217]. However, the poor conductivity of intrinsic TiO_2 poses a challenge for realizing oxidative gas sensors [58, 217, 219]. To overcome the shortage, one approach to boost the conductivity of TiO_2 is the addition of dopants such as Cr [217], Al [220], and Nb [218]. Alternatively, ultraviolet (UV) illumination can be used to induce the photoconductivity of TiO_2 and thereby enhances the sensing performance of TiO_2 based sensors. Additionally, UV-assisted chemical sensing opens up the intriguing potential of gas detection at room-temperature for sensors based on wide-bandgap oxides [61, 64, 65, 221].

In this work, we demonstrate the use of rf-sputtered anatase-TiO_2 thin-films for NO_2 detection. The fabricated sensors operate at room-temperature under UV illumination and thus fill the application gap of existing TiO_2 based gas sensors. The measured response of the device exhibits a broad NO_2 detection range from 100 ppm to 500 ppm. The fabricated sensors show no response to gases such as CO or CO_2 even at the concentration of 1000 ppm, indicating a good selectivity of the fabricated sensor. A detailed list of sensing responses to gas analytes is attached in the Appendix B.

7.1.2. Experimental details

The TiO_2 thin films were prepared by radio frequency (rf) sputtering of a 99.9% pure TiO_2 target (Kurt. J. Lesker) using a Denton Vacuum Discovery 550 sputtering system. Rf-sputtering is a most utilized low-cost method to produce uniform and dense TiO_2

thin films [222] and compatible with microelectronics fabrication processing. The base pressure was kept at or below 2.7×10^{-4} Pa (2×10^{-6} Torr) and the substrate temperature was set at 325 ^{0}C to enhance the uniformity of the deposited films. 50 standard cubic centimeters per minute (sccm) Ar gas and 300 W rf-sputtering power were maintained during the process to yield a deposition rate of 2.4 nm/min. For sensor applications, 12 nm TiO_2 films were deposited onto 5 mm × 5 mm sapphire substrates using the above recipe. Interdigitated contacts were e-beam evaporated through a shadow mask using the Ti (40 nm)\Al (100 nm)\Ti (40 nm)\Au (40 nm) stack. The samples were then thermally annealed in Ar environment for 30 s at 700 ^{0}C to form good Ohmic contacts on TiO_2 films.

The surface morphology of the TiO_2 thin-film was examined with Bruker Dimension FastScan atomic force microscopy (AFM) under tapping mode. The small (7 nm) radius of the loaded AFM tip ensures enhanced lateral resolution of obtained scans. The chemical state of prepared TiO_2 thin-films was confirmed by X-ray photoelectron spectroscopy (XPS). XPS analysis was performed using a Kratos Analytical Axis-Ultra DLD X-ray Photoelectron Spectrometer with a monochromated Al Kα source (150 W) and a nominal analysis area of 300 μm × 700 μm. Low resolution survey scans (160 eV pass energy, 0.5 eV step size) were taken at 0^0 and 45^0 to the surface normal. In addition, high resolution scans (20 eV pass energy, 0.1 eV step size) were measured at 0^0 and 45^0 to the surface normal for C 1s, O 1s, N 1s, Ti 2p, Al 2p and Al 2s. XPS curve-fitting and analysis was performed using CasaXPS software (v. 2.3.26, Pre-rel 1.4). The binding energy scale was calibrated to the C 1s C*-C peak at 284.5 eV. The optical absorbance and absorption coefficient (α) of the TiO_2 films vs. wavelength were

characterized using an Ocean optics QE65000 spectrometer and J. A. Woollam M2000 ellipsometer, respectively. Structural characterization of the oxide film was conducted by X-ray diffraction (XRD) using a Rigaku SmartLab system. To obtain a reasonable signal-to-noise ratio in the XRD scans, a thicker (50 nm) TiO_2 film was deposited under identical conditions onto a large (3-inch) boron-doped Si wafer.

The gas sensing performance of the fabricated sensor was investigated at room-temperature in a custom-built apparatus. A gaseous mixture of NO_2 and breathing air was introduced into the sensing apparatus. Mass flow controllers independently tuned the flow rate of each component, determining the composition of the mixed gas. The sensors were biased with a constant 5 V supply and currents were measured by a National Instrument PCI DAQ system. A 365 nm light emitting diode provided the UV illumination to the sensor. The output power of the UV source was maintained at 469 μW over 1 cm^2 exposure area with less than 0.5% variation, as verified with a Newport power meter.

7.1.3. Results and discussion

A. Analysis of TiO_2 films

A schematic diagram of the proposed sensor is illustrated in Figure 7.1a. The surface morphology of a prepared 10 nm TiO_2 thin-film on sapphire substrate is shown in Figure 7.1b and c. The AFM image shows the relatively smooth surface as well as small grain size of the TiO_2 thin-film. The estimated root mean square roughness (Rq) is roughly 0.42 nm while the grain size of annealed TiO_2 films was estimated to be in the range of 15 nm to 18 nm.

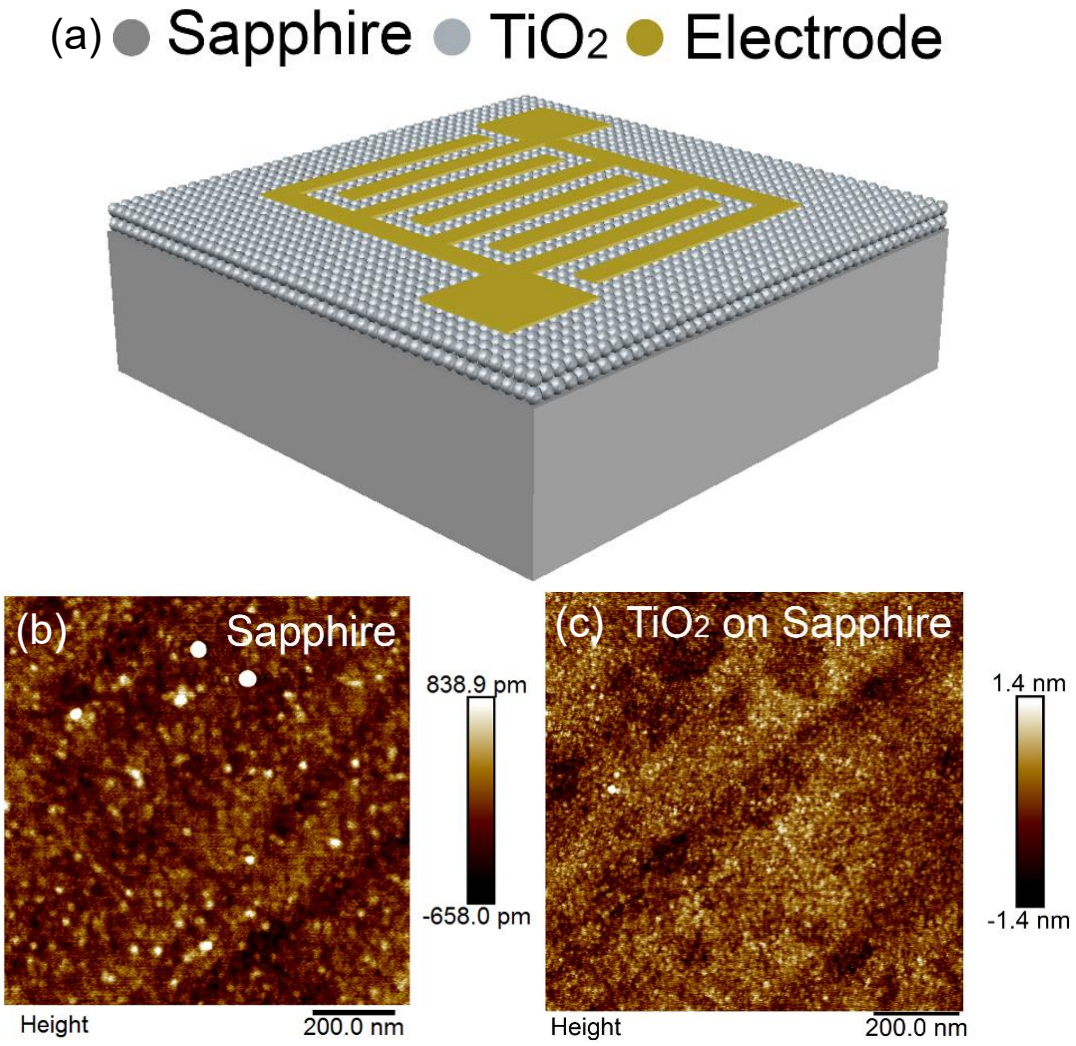

Figure 7.1 Fabricated TiO_2 thin-film device: (a) Schematic of the device showing TiO_2 along with sapphire substrate and Ti/Al/Ti/Au contacts. AFM images of (b) sapphire substrate and (c) TiO_2 coated sample after annealing at 700 ^{0}C in Ar ambient for 30 s.

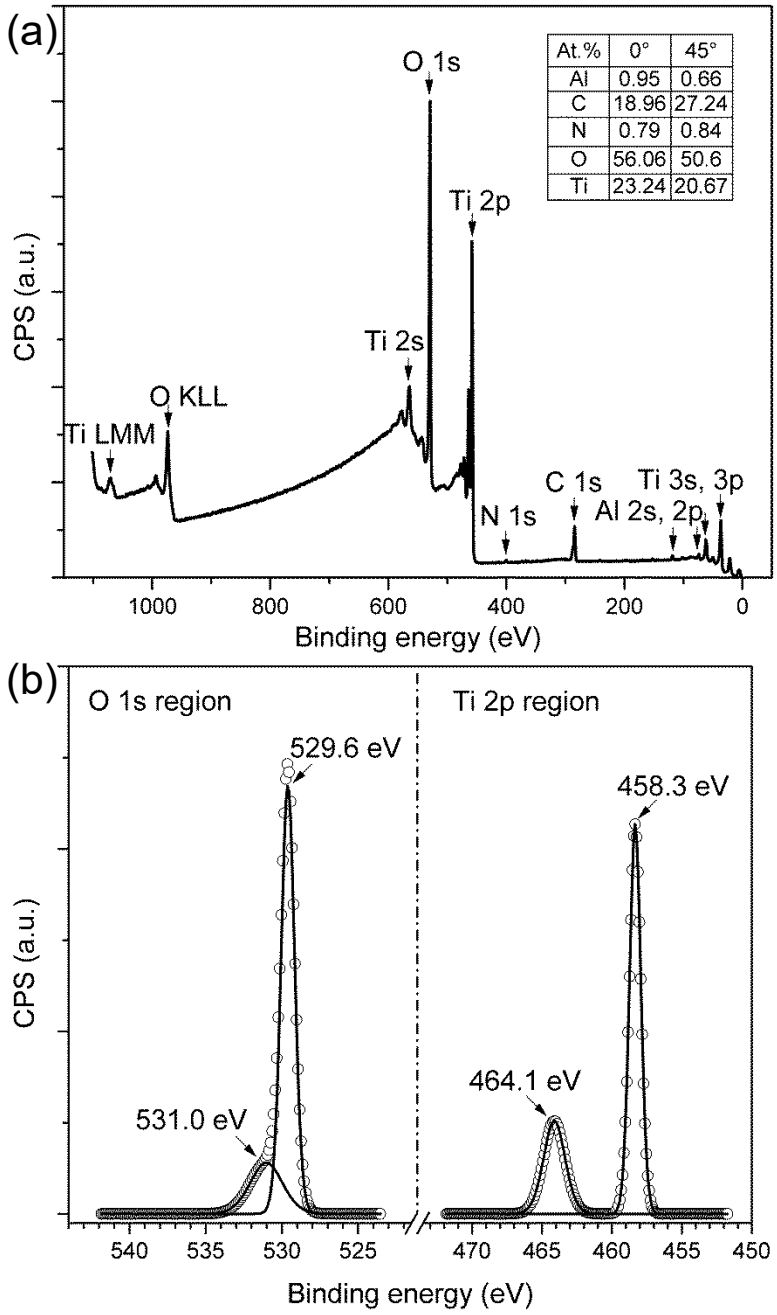

Figure 7.2 XPS spectra of the prepared TiO_2 thin-film: (a) Full spectrum survey scan collected at 0^0 to the surface normal. The inset shows the calculated surface compositions from XPS survey scans performed at both 0^0 and 45^0 to the surface normal. (b) High resolution scans of O 1s and Ti 2p regions. The solid lines represent the deconvoluted peaks from collected signals (denoted by open circles).

Figure 7.2a shows a full spectrum XPS survey scan of a prepared TiO_2/sapphire sample collected at 0^0 to the surface normal. The peak intensities are normalized by the Kratos

relative sensitivity factors provided by CasaXPS. The inset of Figure 7.2a lists the calculated surface compositions from XPS survey scans collected at both 0^0 and 45^0 to the surface normal. All peaks in the XPS spectra are attributed to the sputter-deposited TiO_2 or the sapphire substrate except for C and negligible amount of N. The relative increase in C atomic percentage observed at 45^o indicates that the species arises from the surface contamination. The intensity of photoelectrons escaping from the sample will be attenuated as they pass through an overlayer. As the collection angle is increased, the collected electrons pass through the overlayer at an angle, therefore traversing a greater distance through the overlayer and experiencing greater attenuation due to the overlayer than they would at a collection angle of 0^o. Therefore, photoelectron signals arising from superficial contamination will show a relative increase, whereas those signals arising from elements beneath a surface contamination layer will show a relative decrease, as observed for Al, Ti and O. Therefore, C appears to be superficial adventitious contamination, presumably due to exposure of the sample to the ambient environment after deposition, rather than from a contaminated sputtering process that affects the lattice structure of TiO_2. This corroborates the XRD results presented below. Thus, the emergence of C is regarded as harmless to the fabricated device. Figure 7.2b shows high resolution, deconvoluted XPS scans of the Ti 2p and O 1s regions. A typical Ti 2p doublet peaks centered at 458.3 eV and 464.1 eV verifies the presence of TiO_2 (Ti^{4+}) while the main O 1s peak at 529.6 eV is assigned to lattice oxygen from TiO_2, and the side peak at higher binding energy is attributed to surface hydroxylation [223, 224].

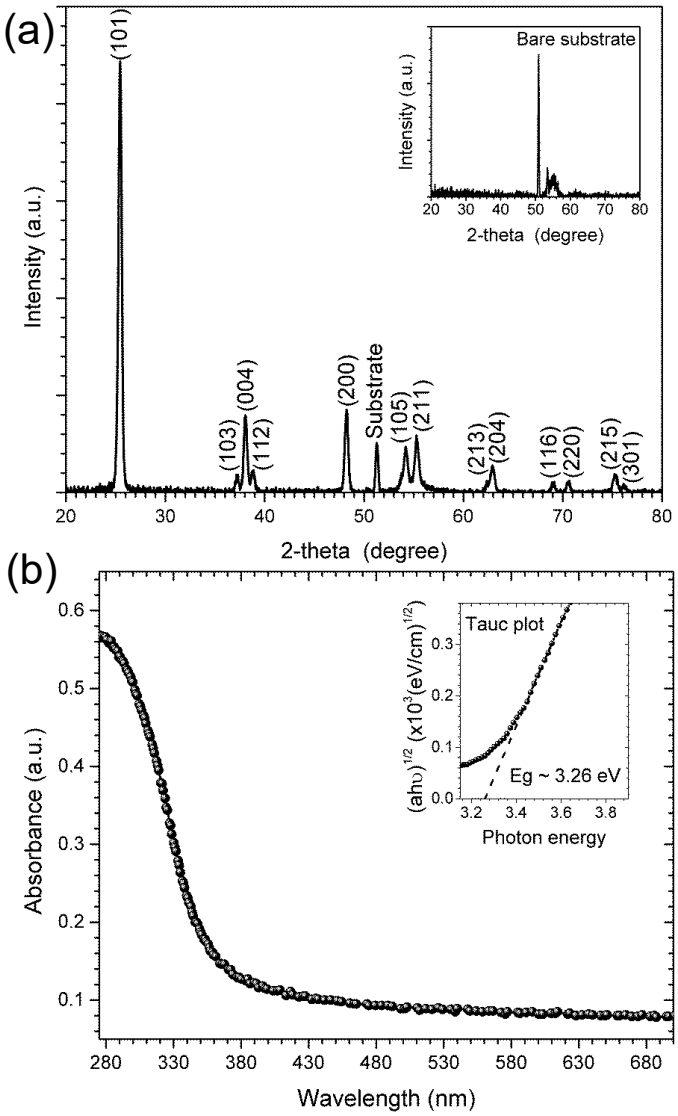

Figure 7.3 (a) XRD patterns of 50 nm TiO_2 coated Si showing diffraction peaks arising exclusively from anatase phase of prepared TiO_2 and Si substrate. The inset confirms the diffraction peaks of the Si substrate. (b) Obtained absorbance spectrum of the prepared TiO_2 thin-film from UV to visible light regions. The inset shows the estimation of the indirect optical band gap of TiO_2 using Tauc plot.

Figure 7.3a shows XRD patterns of the prepared 50 nm TiO_2 film on a 3-inch Si substrate. We use the large Si substrate instead of small sapphire pieces as large surface area of TiO_2 yields better signal-to-noise ratio in our XRD measurement. Results by other groups show that for rf-sputtered TiO_2, the nature of substrate has very limited

influence on the crystal structure of the deposited film [51]. The inset shows the XRD diffraction peaks obtained from a bare substrate. All the diffraction peaks in Figure 7.3a are assigned to the anatase phase. No rutile phase is observed in the XRD patterns. Thus, the XRD data indicates that the prepared TiO_2 film is a polycrystalline anatase phase, which is likely due to the low deposition temperature (< 400 °C) [225] and the low annealing temperature (< 900 °C) [226]. Figure 7.3b shows the UV-vis absorbance of the prepared TiO_2 film in the 275 nm to 700 nm wavelength range. A sharp decrease of the film absorbance in the visible region ($\lambda > 400$ nm) shows a high transparency of the film in the visible region. The inset of Figure 7.3b shows the Tauc plot. By following Tauc's approach as discussed in Chapter 4, the estimated optical bandgap of the prepared TiO_2 is 3.26 eV, in good agreement with reported anatase values [225].

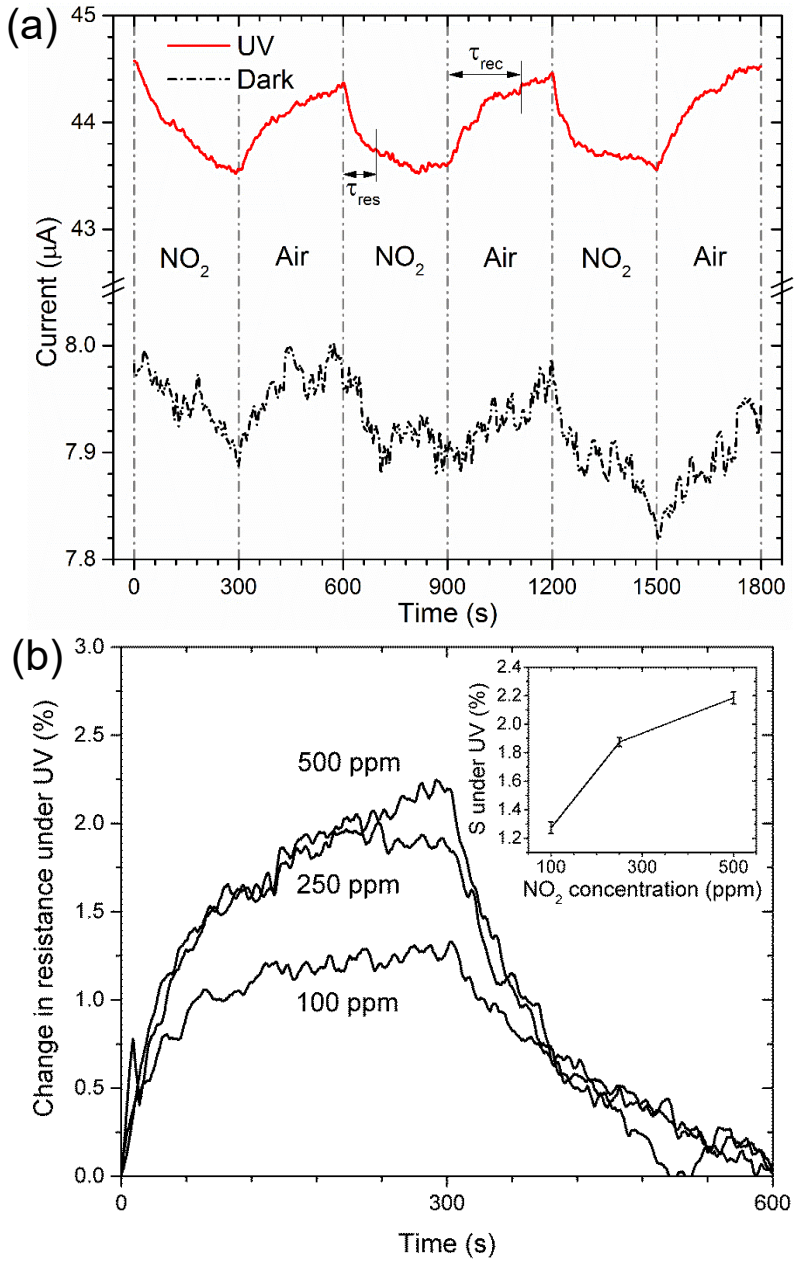

Figure 7.4 Dynamic responses of the TiO_2 based sensor exposed to: (a) 250 ppm NO_2 mixed with breathing air under UV illumination and dark. (b) Comparison of NO_2 response under UV at mixture of 100 ppm, 250 ppm, and 500 ppm with breathing air. The inset shows the measured responses under UV as a function of NO_2 concentrations with uncertainty.

B. Sensing performance

Figure 7.4a shows the room-temperature dynamic responses of the TiO_2 sensors exposed to 250 ppm NO_2 under UV illumination and in dark conditions. For both UV on and off conditions, the sensors are subjected to 250 ppm NO_2 exposure for 5 min followed by 5 min exposure to breathing air. Under UV illumination, the current level of the sensor increases roughly 5.5 times over the dark condition. Compared to the small and noisy gas response in the dark, the sensor demonstrates reversible and distinct NO_2 chemiresistive response under UV illumination. Moreover, unlike shifting of the baseline current observed in the dark operation, the TiO_2 sensor maintains constant baseline current after three gas exposure cycles under UV illumination. Notably, this stable baseline current is essential for sensing applications. The response of the TiO_2 sensor is defined as the relative change in resistance in presence of the analyte,

$$S = \frac{R_g - R_o}{R_o} \qquad (7\text{-}1)$$

where R_g and R_o are measured resistances of the sensor with NO_2 and air flow, respectively. The calculated responses with and without UV illumination are 2.4% and 1.6%, respectively. When exposed to NO_2, the response time (τ_{res}) is defined as the time taken by the sensor current to reach 80% of the response (I_0 - I_f), where I_0 stands for the current measured in air and I_f is the steady current in the presence of the analyte. While the recovery time (τ_{rec}) represents the time required for the sensor to recover to 20% of the response with air flow. The τ_{res} = 100 s and τ_{rec} = 210 s are observed for sensing operation under UV as marked in Fig. 4a. Due to the noisy signal, the corresponding response and recovery time for the dark case are difficult to estimate accurately. Figure 7.4b shows the responses of the sensor to different NO_2

concentrations under UV illumination at room-temperature. The response is tested for NO_2 concentrations ranging from 100 ppm to 500 ppm. The response reaches saturation at high concentration under UV illumination. Such wide sensing range makes the TiO_2 film suitable for industrial NO_2 sensor applications.

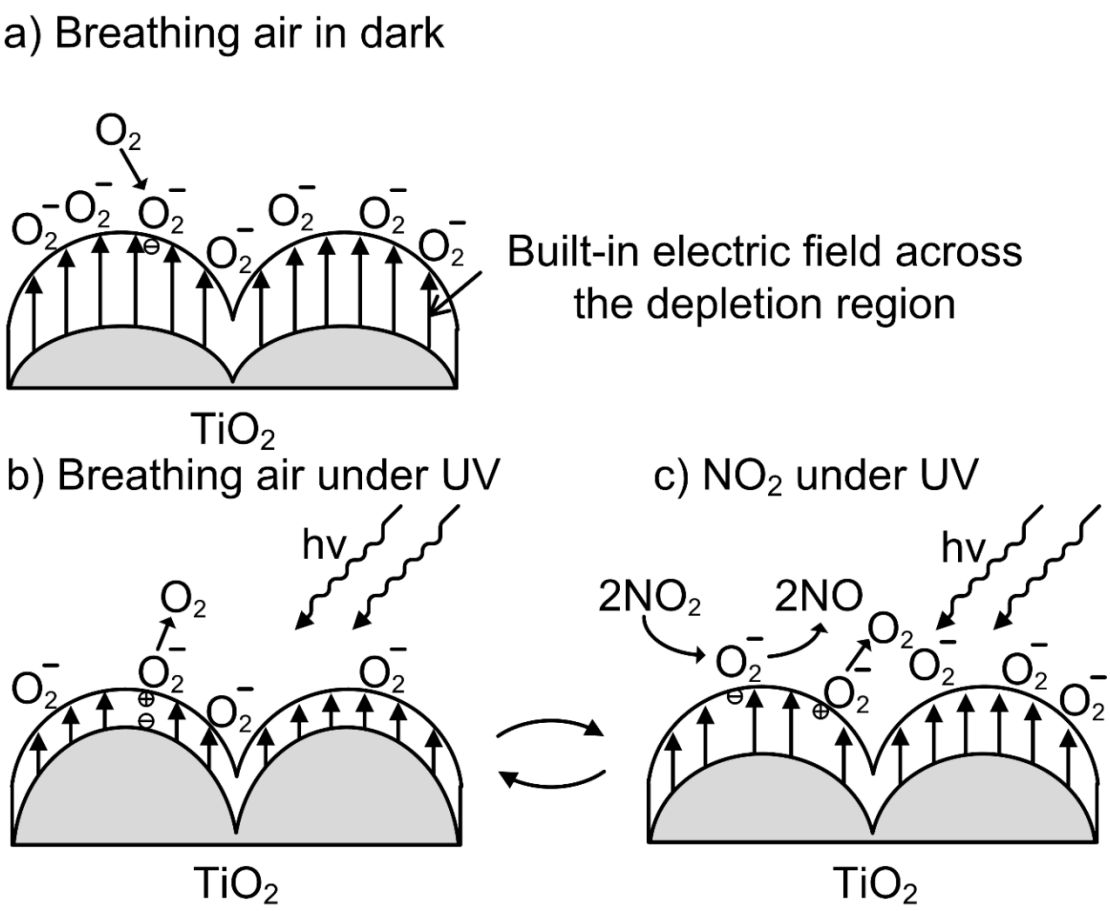

Figure 7.5 Schematic of proposed NO2 gas sensing mechanism of the TiO2 sensor under UV illumination: (a) In dark environment with breathing air in. (b) Under UV illumination in breathing air. (c) Under UV illumination with mixture of NO2 and breathing air.

C. Mechanism of NO_2 sensing under UV

A proposed possible gas sensing mechanism of the TiO_2 based sensor is illustrated in Figure 7.5. According to surface science experiment results, oxygen adsorbs on TiO_2 surface at a broad range of temperature from 105 K to 1000 K [227, 228]. The adsorbed oxygen are chemisorbed at oxygen vacancy sites, surrounded by Ti^{3+} pairs, forming oxygen anions on TiO_2 surface [229]. Meanwhile, reports have confirmed O_2^- as the dominant chemisorbed species on TiO_2 [228, 230]. Therefore, the adsorption of the oxygen is equivalent to the ionosorption of oxygen by taking nearby electrons near on TiO_2 surface as described by the following equation [61],

$$O_2(g) + e^- \rightarrow O_2^-(ad) \qquad (7\text{-}2)$$

The schematic shown in Fig. 5a describes such a condition where O_2^- is adsorbed on the polycrystalline TiO_2 surface in dark. The surface-adsorbed O_2^- induces the built-in electric field across the depletion region, resulting in high resistance in the dark. Upon UV illumination, photogenerated electron-hole pairs within the depletion region are separated by the electric filed. While photogenerated electrons are driven into the bulk, photogenerated holes migrate to the surface and recombine with the adsorbed O_2^-. Both processes decrease the depth of the depletion region, leading to the increase in current. Eventually, the surface adsorption and desorption processes of oxygen reach equilibrium as depicted in Figure 7.5b. When exposed to NO_2 as shown in Figure 7.5c, the resistance of the sensor increases due to the following reaction [48],

$$2NO_2(g) + e^-(hv) \rightarrow 2NO(g) + O_2^-(ad) \qquad (7\text{-}3)$$

NO_2 acts as a scavenger for photogenerated electron, resulting in decreasing the photo current. In addition, this reaction also restores surface adsorbed O_2^- concentration, which broadens the depletion region, resulting in further decrease of the current. Table

7.1 summarizes some of the proposed NO_2 sensors based on TiO_2 and their corresponding operating conditions.

Table 7.1 Operation conditions of TiO_2 based NO_2 sensors

Sensor materials (dopant)	Operation temperature (^{0}C)	Detection limits (ppm)
TiO_2-WO_3 [231]	350-800	20
ZnO-TiO_2 [53]	250	2-20
TiO_2 [58]	450-550	2-25
TiO_2(Cr) [217]	250	2-50
TiO_2(Al) [220]	400-800	50-200
Nano-tubular TiO_2 [219]	300-500	10-100
Nano-TiO_2(Nb) [218]	100-200	10
TiO_2 (this work)	**Room-temperature, UV**	**100-500**

D. Enhancement of responsivity with foreign receptors

As introduced in the earlier chapter, decorating certain noble metals on SCOs based sensors can sometimes improve their gas analyte responses [43]. This response enhancement due to loaded foreign receptors is also observed in our TiO_2-Au and TiO_2-Ag systems towards NO_2 sensing. We prepared the two kinds of surface decorated samples by DC sputtering Au and Ag onto TiO_2 thin films. TiO_2 thin films were fabricated with the above recipe, namely rf-sputtering of TiO_2 thin film, depositing electrodes, and annealing at 700 °C for 30 sec in Ar environment. Deposited metal layers were engineered to form well dispersed discontinuous Au and Ag nanoparticles (NPs) with high coverage areas. The morphologies of deposited NPs were characterized with AFM.

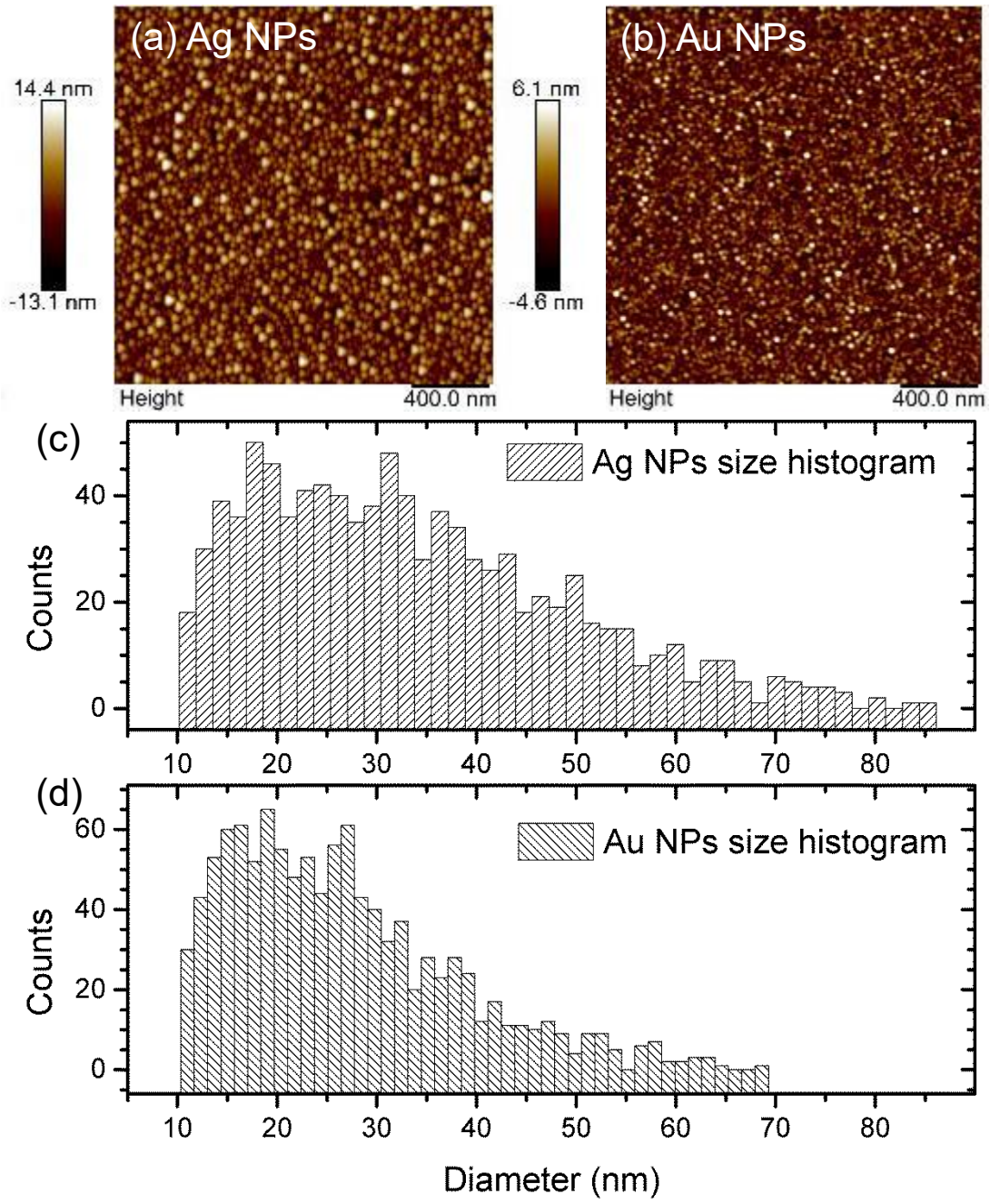

Figure 7.6 AFM images of deposited (a) Ag NPs and (b) Au NPs on TiO_2 based sensors. Insets: Histograms of particle sizes of the deposited metals.

Figure 7.6 shows the high resolution AFM images of sputtered Ag and Au NPs. All the quantitate analysis of the AFM images were performed with Nanoscope Analysis software. The estimated rms roughness of Ag and Au layers are 4.03 nm and 1.41 nm,

respectively. The average particle sizes of the deposited NPs are 33.4 nm and 27.7 nm for Ag and Au, respectively. More high resolution morphological images of Ag and Au NPs that were deposited with different process parameters are presented in the Appendix C.

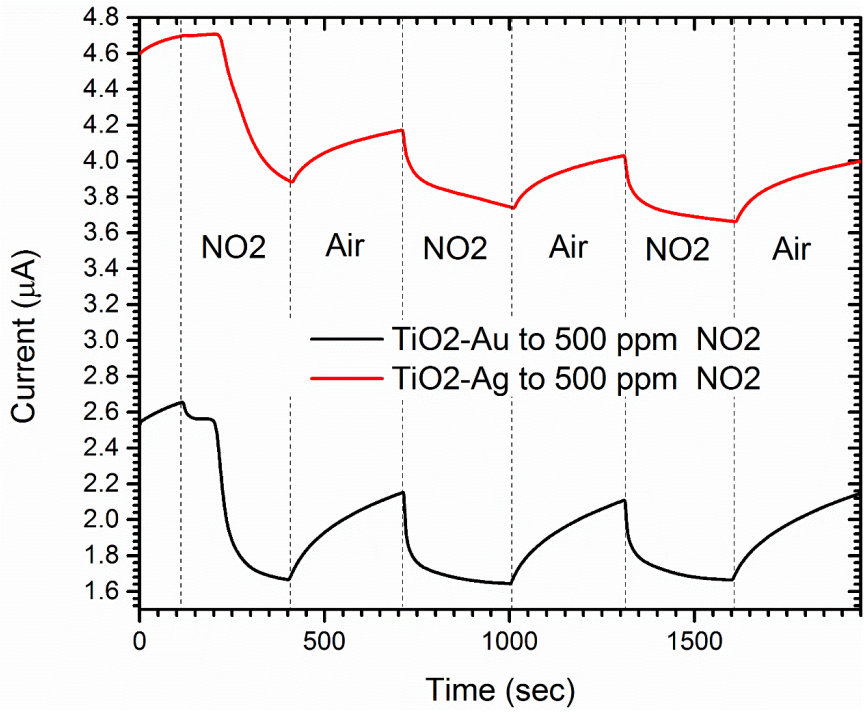

Figure 7.7 Dynamic responses of the TiO_2-Ag and TiO_2-Au based sensors exposed to: 500 ppm NO_2 mixed with breathing air under UV illumination.

Figure 7.7 shows three dynamic 500 ppm NO_2 on and off cycles of the TiO_2-Au and TiO_2-Ag based sensors under UV illumination. The sensors are exposed to an alternating flows of NO_2 and dry air for 300 sec. The responses of the sensors under first NO_2 on/off period exhibit differently from the others. At the beginning of the first NO_2 exposure cycle (at 110 sec), the monitored responses of both sensors remain relatively stable. This is due to the delay of the gas flowing through the long pipes. Later, currents of the biased TiO_2-Ag and TiO_2-Au sensors drop precipitous upon the

arrival of the analyte flow around 250 sec and 200 sec, respectively. On the contrary, both sensors respond to the exposure of NO_2 immediately in the following cycles. The sensors cannot fully recover within the exposure of 300 sec dry air, which is evident from the measured current at the end of each NO_2 cycle. However, the TiO_2-Au based sensor shows a very stable 500 ppm NO_2 detecting current baseline around 1.65 μA, which ensures a promising application of this sensor scheme for NO_2 leakage detection. A slightly drift of the current baseline is observed for the TiO_2-Ag film.

Figure 7.8 plots the calculated response (S) of TiO_2 and TiO_2-metals based sensors to the third NO_2 cycle under UV illumination. The sensors were exposed to 500 ppm NO_2 for 300 sec followed by 300 sec to breathing air. The value of S is 2.2 %, 9.1 %, and 23.7 % for TiO_2, TiO_2-Ag and TiO_2-Au systems, respectively. The results clearly indicate that the incorporation of Au and Ag NPs on TiO_2 surface enhances the analyte detection. The 500 ppm NO_2 response time (τ_{res}) is 56 sec, 86 sec and 40 sec for TiO_2, TiO_2-Ag and Au sensors, respectively. The corresponding recovery time (τ_{rec}) is 163 sec, 179 sec and 189 sec for TiO_2, TiO_2-Ag and Au sensors, respectively.

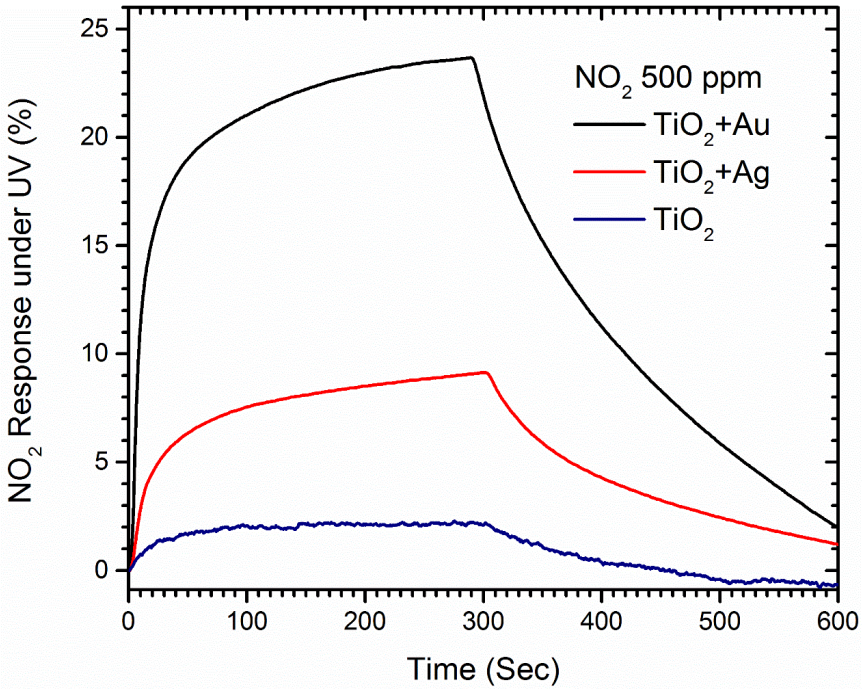

Figure 7.8 Comparison of 500 ppm NO2 response under UV for sensors fabricated with TiO2 thin film, TiO2 with Ag and TiO2 with Au bilayer films.

E. Enhancement of NO_2 sensitivity with optimized TiO_2 fabrication procedure

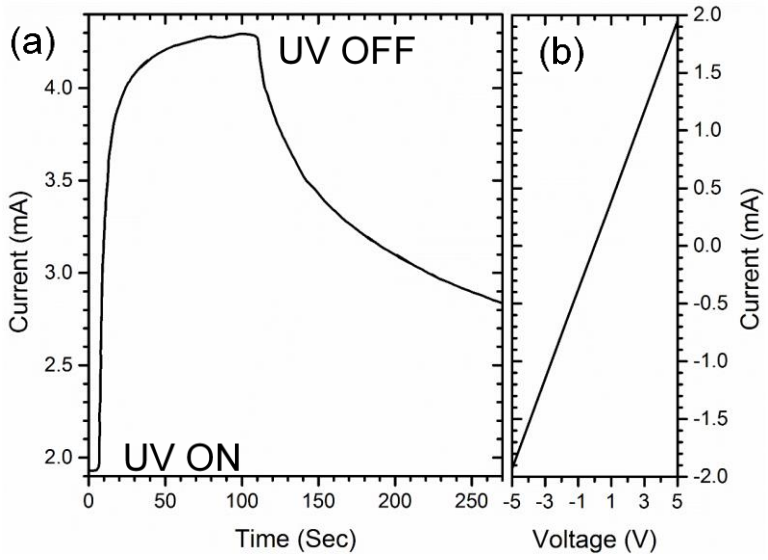

Figure 7.9 Measured current of TiO_2 based sensor of (a) dynamic UV ON/OFF response and (b) I-V sweep in dark from -5 V to 5 V.

I further optimized the fabrication procedure of TiO_2 thin films by annealing the sputtered films prior to the deposition of metal contacts to prevent electrodes from being damaged by the high annealing temperature. TiO_2 sensors built with this new recipe demonstrate a precipitous increase in NO_2 sensitivity. Figure 7.9a shows a typical dynamic UV response of the TiO_2 sensor based on new recipe with ~ 2.2 on/off ratio. From the dynamic response plot, we can estimate a roughly 100 second photocurrent stabilization time after UV illumination. Figure 7.9b shows the I-V sweep from –5 V to 5 V in the dark condition. The linear I-V curve indicates the formation of ohmic contacts between the deposited electrodes and TiO_2 thin film.

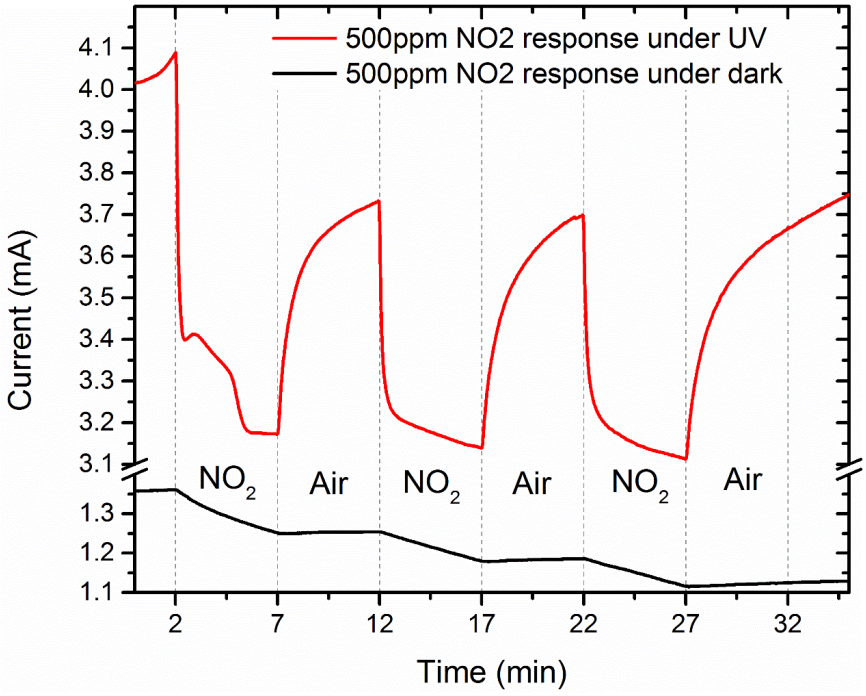

Figure 7.10 Dynamic responses of the TiO_2 based sensor exposed to 500 ppm NO_2 mixed with breathing air under UV illumination and dark.

Figure 7.10 shows the measured currents of the TiO_2 sensor to 500 ppm NO_2 under UV illumination and dark conditions. The carrier gas of the low concentration chemical

analyte is dry air. The film was repeatedly exposed to 500 ppm NO_2 for 300 sec followed by 300 sec dry air under both UV and dark conditions. Under UV illumination, the film exhibits reversible and intense NO_2 response compared to the the dark condition. Moreover, the response current to NO_2 in the two cycles remains constant under UV illumination, unlike the linear shifting of the current observed during the dark operation. These remarkable differences in the chemical responses clearly indicate that UV light facilitates the adsorbing and desorbing of NO_2 on TiO2 surface, as discussed elsewhere [54]. The increased baseline current under UV illumination is due to the generation of photon electron-hole pairs.

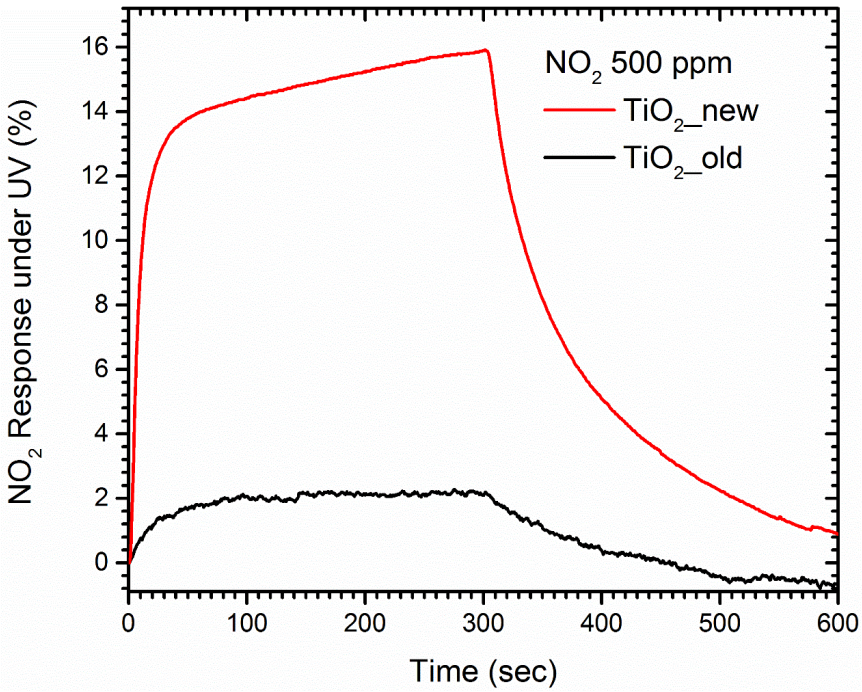

Figure 7.11 Comparison of 500 ppm NO_2 response under UV for sensors fabricated with old and new recipe of TiO_2 thin films.

Figure 7.11 shows the comparison of NO_2 responses under UV with the optimized and the initial recipes. Upon the exposure to 500 ppm NO_2 for 300 sec, the new TiO_2 sensor

exhibits a rapid response time (τ_{res}) of 26 sec and reaches a maximum of 15.9% current change. The sensor requires a 132 sec recovery time (τ_{rec}) in the breathing air to reset its photocurrent.

F. Investigation of surface contamination and morphology on the sensing performance

Thin film oxides have attract extensive attention owning to their use in memory devices, UV detectors, gas sensors, and many others. The numerous applications benefit from the unique properties of the thin film oxides including physical, optical, and chemical. These properties are known to be strongly dependent on the surface conditions of the thin films. However, it is not yet clear how surface properties of the thin film gas sensor affect its analyte sensing response. Here, I investigate the influence of surface carbon contamination and roughness on the NO_2 sensing properties of TiO_2 thin film sensors. The surface of the films were intentionally contaminated and damaged with organic polymers (photolithography resist) and microwave plasma, respectively. For the carbon contamination study, photolithography resist (PR) was firstly coated onto the annealed TiO_2 film. To eliminate the surface morphology change due to the addition of organic polymers, the PR coated TiO_2 was then mildly cleaned with Acetone, IPA, and DI water. XPS and AFM measurements of the film show detectable trace of carbon residues and resembling surface morphology to the as-is annealed TiO_2 films, respectively. For the surface roughness study, the TiO_2 films were coarsened by exposing the surface to the microwave plasma of O_2 at the power of 1000 W for 15 mins. AFM data manifests the damaged pristine surface. XPS data reveals the

close stoichiometry and chemical states of the blasted film to the as-is state. The interdigitated metal contacts were e-beam evaporated onto the distinctively prepared films for electrical measurements.

The surface morphology and roughness of the prepared TiO_2 thin films were obtained with atomic force microscopy (AFM) using a Bruker Dimension FastScan system. The stoichiometry of chemical state of prepared films were measured by X-ray photoelectron spectroscopy (XPS). XPS measurement was conducted in a Kratos Axis-165 system with a monochromated Al source and a 30 μm imaging spot. Survey scans were performed at 0^0 and 45^0 to the surface normal at a 1 eV step size. Additionally, high resolution scans with 0.1 eV step size were taken for Ti 2p, C 1s, and O 1s. XPS data analysis was performed using CasaXPS. The spectrum scale of the binding energy was calibrated towards the hydrocarbon peak at 284.8 eV.

Figure 7.12 shows the high resolution AFM images of the prepared samples. Gleaning from the first glance, the plasma damaged sample (Figure 7.12c) exhibits totally distinct morphology from the quite similar as-is annealed and carbon contaminated samples. Quantitatively, the root mean square (rms) surface roughness, listed in Figure 7.12d, doubles for the plasma damaged sample from the other cases. The values are 0.32 nm, 0.3 nm and 0.65 nm for the as-is annealed, contaminated, and microwave plasma damaged samples, respectively. These results clearly indicate the applied microwave plasma coarsens the surface of TiO_2 film, while the morphology remains identical after the carbon contamination treatment.

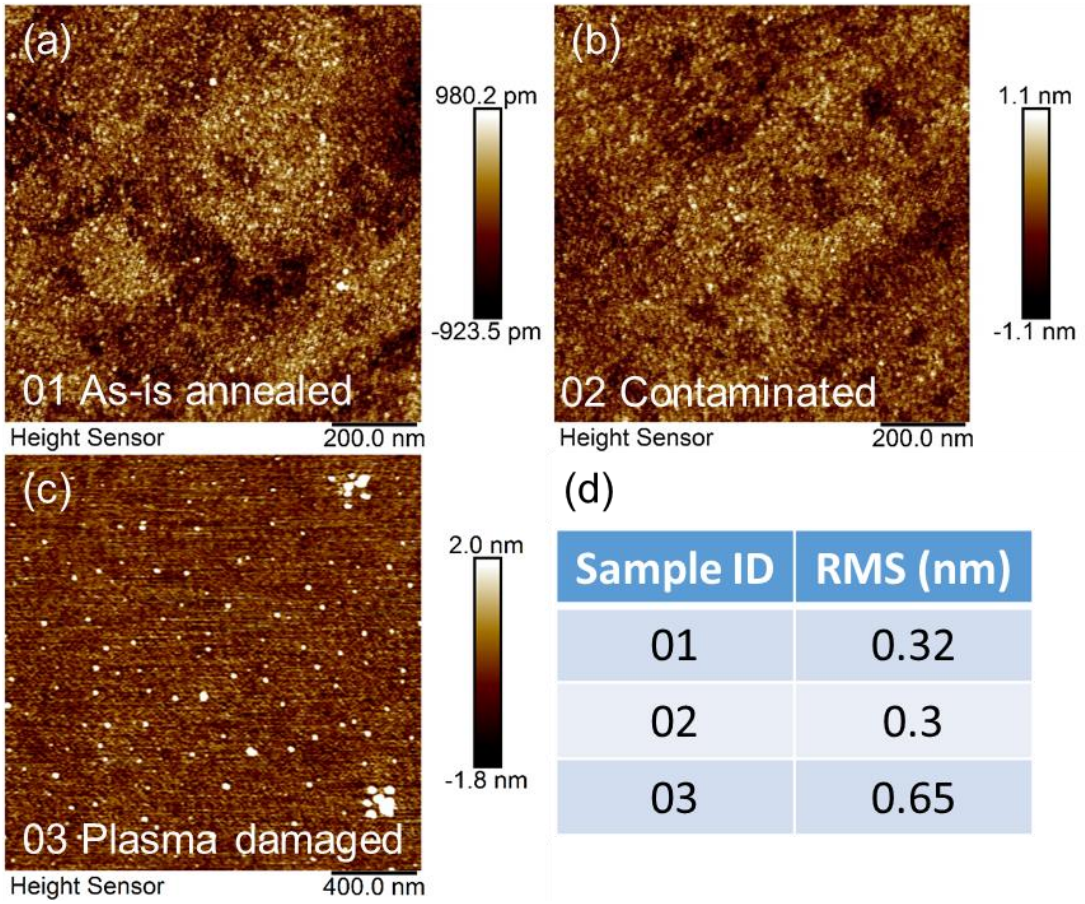

Sample ID	RMS (nm)
01	0.32
02	0.3
03	0.65

Figure 7.12 AFM images of (a) as-is annealed TiO_2, (b) contaminated TiO_2, and (c) plasma damaged TiO_2. (d) Table of estimated rms roughness for each sample.

Surface chemical information of the samples were obtained with XPS scans collected at both 0^o and 45^o to the surface normal. Figure 7.13a shows the collected XPS survey data of the 01 as-is annealed, 02 contaminated, and 03 plasma damaged TiO_2 films, at the 0^0 incident angle to the normal of samples. All the detected peaks can be assigned to the prepared films (Ti and O), the expected adventitious contamination (C), and the sapphire substrates (Al). The escaping electrons which transverse through the thin TiO_2 layer from the underlayer substrate attribute to the Al peaks. This collection of underlayer signal may be diminished with more surface sensitive analytic techniques,

such as Auger electron spectroscopy [147]. Figure 7.13b presents the ratios of the compositional concentration calculated from the XPS scan at 45 ^{0} over 0 ^{0}, for all the detected elements. Compare to the collection angle of 0 ^{0}, the excited electrons travel a longer distance through the overlayer at the 45 ^{0} and thus experience greater intensity attenuation. Therefore, those signals arising from elements beneath a super-surface layer will show a relative decrease (ratio < 1) with increased collection angle, as observed for O, Ti and Al. In contrast, the relative increase in atomic percentage of C in all samples at 45 ^{o} indicates that C arises from the surface contamination. In general, the estimated atomic concentrations of the detected elements vary within a narrow range for the examined TiO_2 films at 0 ^{0} incident angle, as shown in Figure 7.13c. The most notable difference is the increase of C from roughly 10 % in the as-is annealed and plasma damages samples to 17 % in the PR coated and removed TiO_2 sample. This additional C, along with the conclusion that C lays on surface, suggests that the implemented organic polymer cleaning process contaminates the surface with C residues. Figure 7.13d shows the almost identical Ti 2p peaks, with only slight variations in the signal intensities, of the examined TiO_2 films. These data are collected from high-resolution (0.1 eV) XPS scans at the incident angle of 0 ^{0}. The binding energies and shapes of the Ti peaks are in good agreement with the reported XPS measurements for TiO_2.

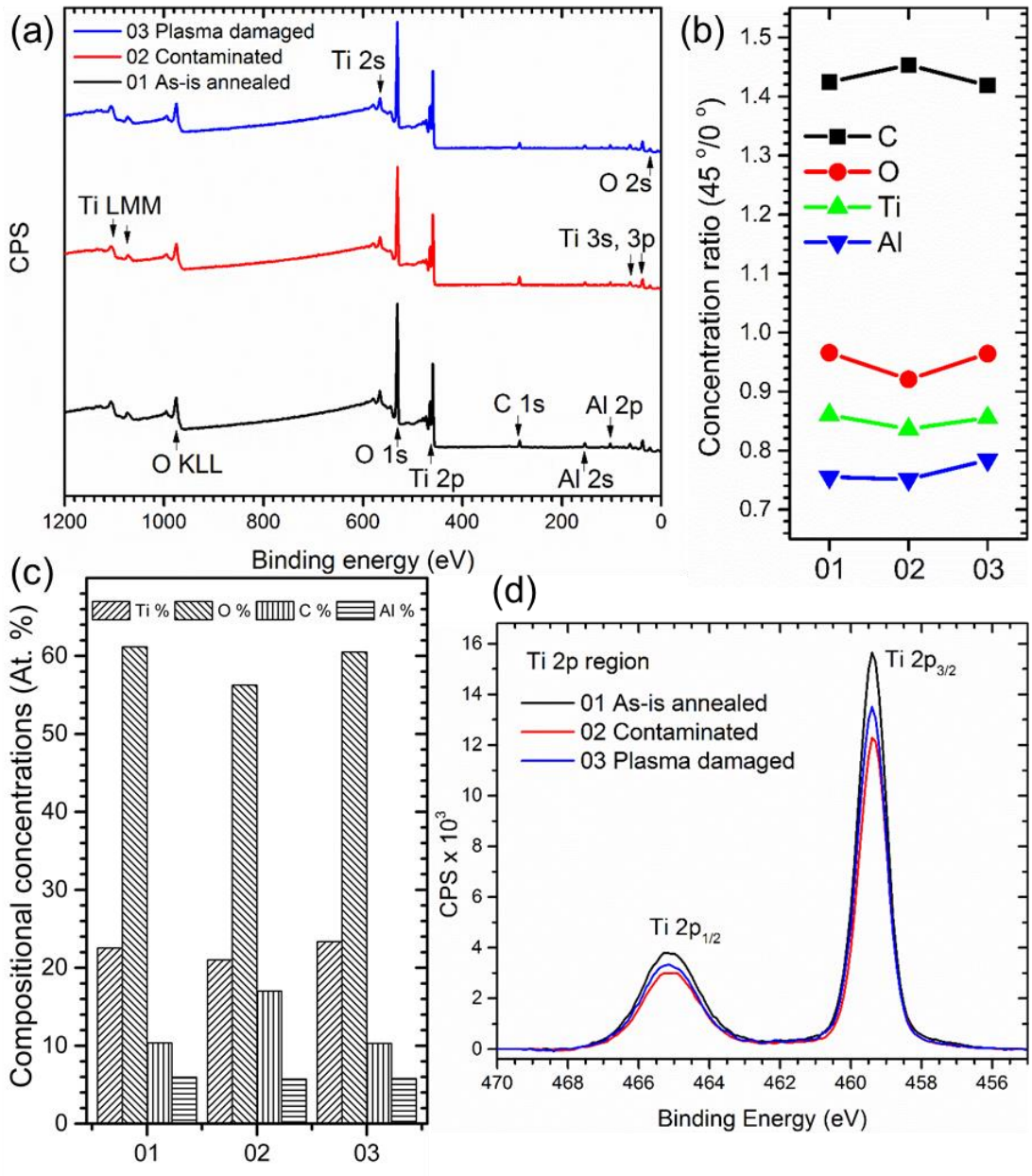

Figure 7.13 (a) XPS spectra of the prepared 01 as-is annealed, 02 contaminated, and 03 plasma damaged TiO_2 thin films. (b) Ratios of concentrations calculated from the XPS 45 ^{0} scan to 0 ^{0} scan. (c) Atomic concentrations of the detected compositions in the examined TiO_2 films at collection angle of 0 ^{0}. (d) High-resolution XPS spectra of Ti 2p regions of the TiO_2 films.

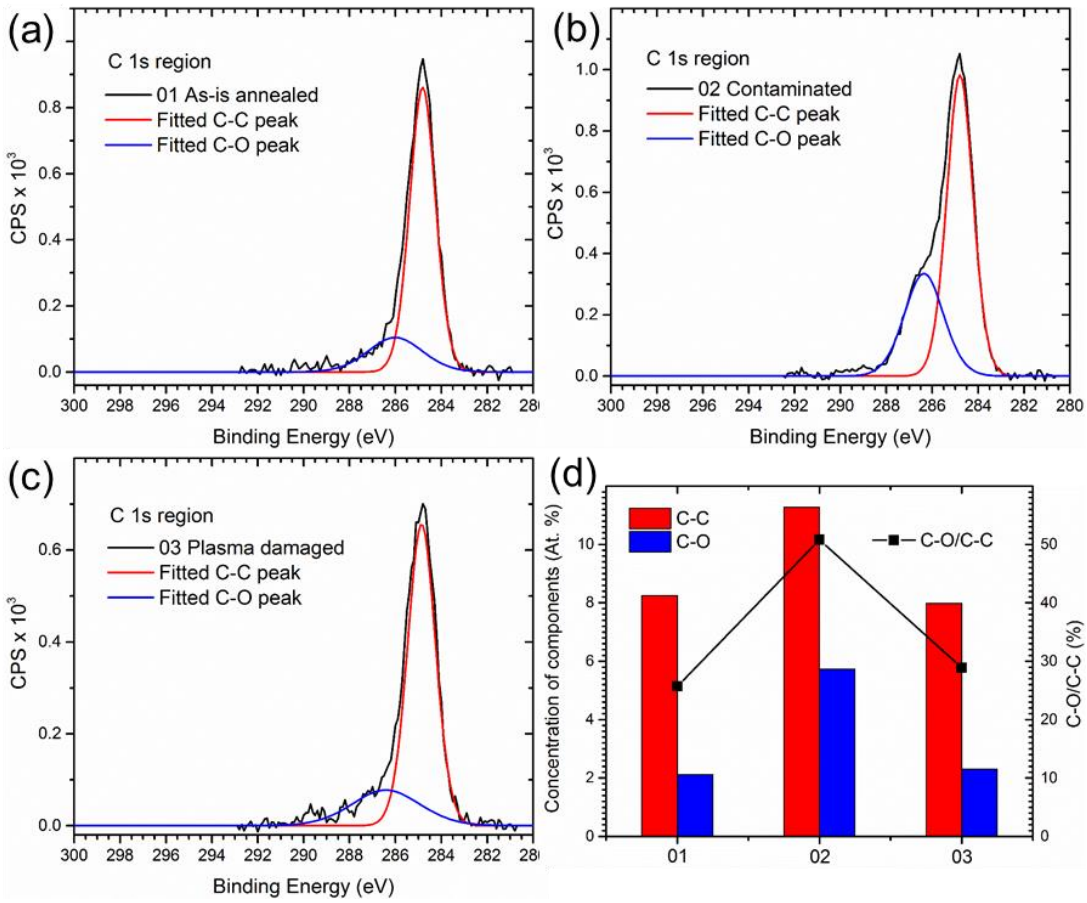

Figure 7.14 XPS spectra of C 1s region of (a) 01 as-is annealed, (b) 02 contaminated, and (c) 03 plasma damaged TiO_2 films. (d) Concentrations of the C-C, C-O components and the ratio of C-O to C-C in the TiO_2 films.

The components of C in the TiO_2 films are revealed by the high resolution XPS studies in the C 1s region. Figure 7.14a, b, and c show the obtained C 1s peaks from the 01 as-is annealed, 02 contaminated, and 03 plasma damaged TiO_2 films, respectively. All the C 1s peak are deconvoluted into C-C peaks at 284.8 eV and C-O peaks at 286.4 eV. While the carbon spectra of the as-is annealed and plasma damaged samples appear to be similar, a much higher C-O peak is noticed from the contaminated film at the first glance. The concentrations of the C components in the TiO_2 films are estimated by quantifying the areas of the fitted C-C and C-O curves, data shown in Figure 7.14d. An

additional 3 % of C-C and 3.6 % of C-O components appear on the surface of the contaminated TiO_2 film, which increases the ratio of C-O to C-C in the film significantly to 50.8 % as well.

Proper surface oxidization states of metal oxides are critical for high sensitivity and selectivity of the oxide-based gas sensors. The O 1s regions of the TiO_2 films are resolved in detail with high resolution XPS scans. Figure 7.15a, b, and c show the deconvoluted O 1s peaks, lattice oxide and hydroxide, of the 01 as-is annealed, 02 contaminated, and 03 plasma damaged TiO_2 films, respectively. The main O 1s peaks at 529.6 eV are assigned to lattice oxygen from TiO_2, and the side peaks with higher binding energy are attributed to the hydroxylation of the films [54]. No notable difference is observed from the spectra of the O 1s regions, which means the contaminated and plasma damaged films retain the oxidization information from the as-is annealed state. Figure 7.15d shows the concentration of O components and ratios of lattice oxide to hydroxide in the investigated films. The concentrations of components are normalized to the percentage of Ti in the corresponding film to eliminate the influence due to the C variation in the examined TiO_2 samples. Observed from the data, the normalized amounts of lattice O remain almost the same and the concentrations of hydroxide vary merely few percentages (within the error of the XPS tool) in the TiO_2 films. Therefore, we believe that the studied TiO_2 films share the same fingerprint of the oxidization states.

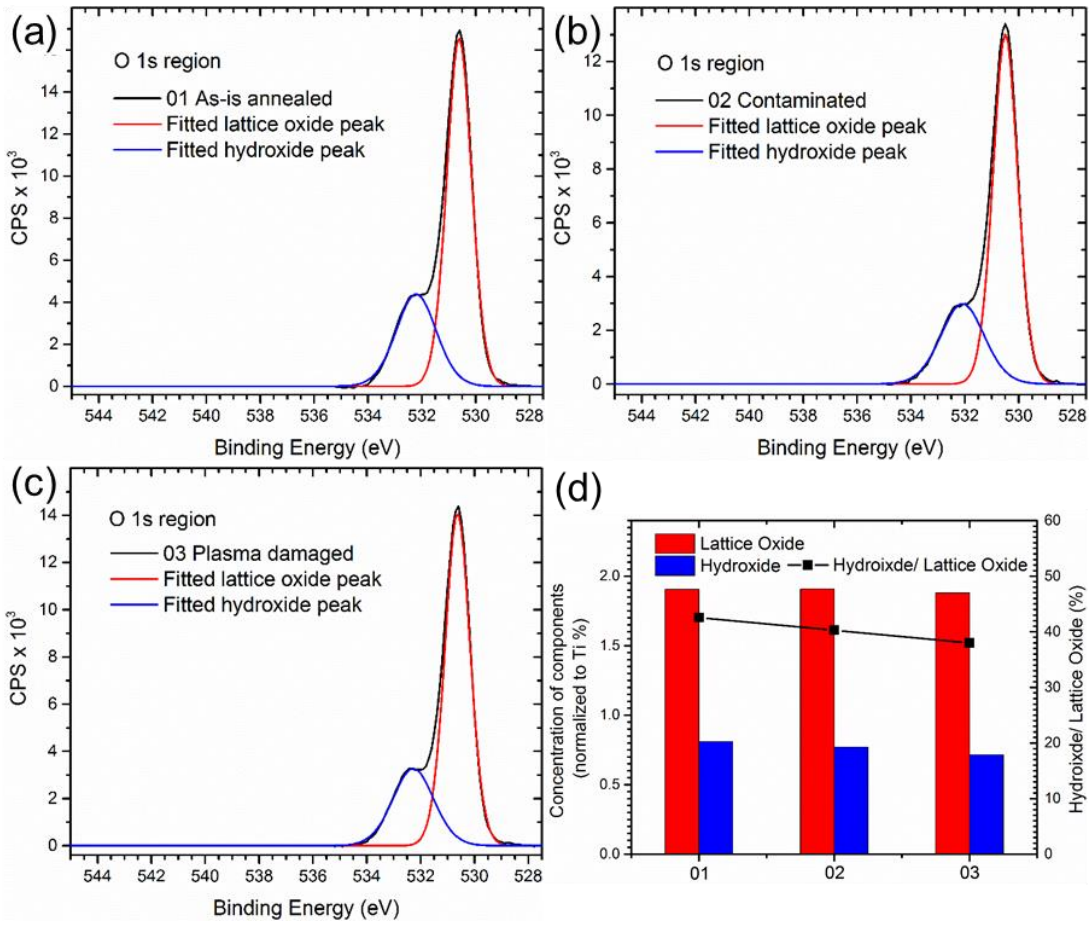

Figure 7.15 XPS spectra of O 1s region of (a) 01 as-is annealed, (b) 02 contaminated, and (c) 03 plasma damaged TiO_2 films. (d) Concentrations of the lattice oxide and hydroxide normalized to the concentrations of Ti in the films, and ratios of hydroxide to lattice oxide.

Having established the surface chemical information of TiO_2 thin films that were cleaned with different processes, we later fabricate NO_2 sensors with those thin films to investigate their gas sensing performance. The carrier gas for the measures is dry breathing air. The sensors fabrication process follows the optimized recipe as discussed in the last section. Figure 7.16 shows the monitored currents of the prepared sensors to 500 ppm NO_2 under UV illumination. The sensors were exposed to 500 ppm NO_2 for

300 sec followed by 300 sec dry air in one sensing cycle. The full measurement lasts 3 NO_2/Air cycles.

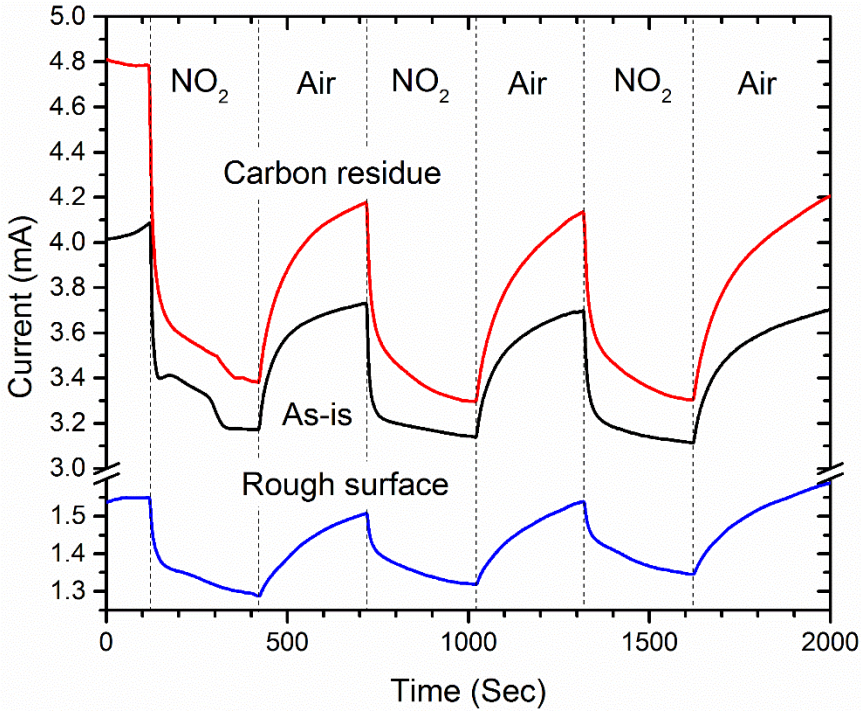

Figure 7.16 Dynamic responses of (a) S01 as-is annealed TiO_2, (b) contaminated TiO_2, and (c) S03 plasma damaged TiO_2 to 500 ppm NO_2 under UV illumination.

The UV photocurrents of S01 and S02 are about 3 times higher than S03. This difference implies that the thickness of S03 is reduced by the microwave plasma etching. The distinct 2-step current drop in all of the first NO_2 cycles is due to the built-up pressure at the microflow controller upon the delayed opening. At the end of the first NO_2/Air cycle, the observed currents of all sensors have not fully recovered to their initial baselines in the air. Therefore, the sensors lose a portion of their responses upon the first exposure to 500 ppm NO_2, which is due to the diffusion of the gas into the deep underlayer and the very slow desorption rate of these analytes. Evident from the smallest difference of the baseline current, S03 shows the fastest recovery rate than

the others. However, S01 and S02 exhibit very stable NO_2 responding currents while S03 shows a slight increase in the response and recovery current after cycles.

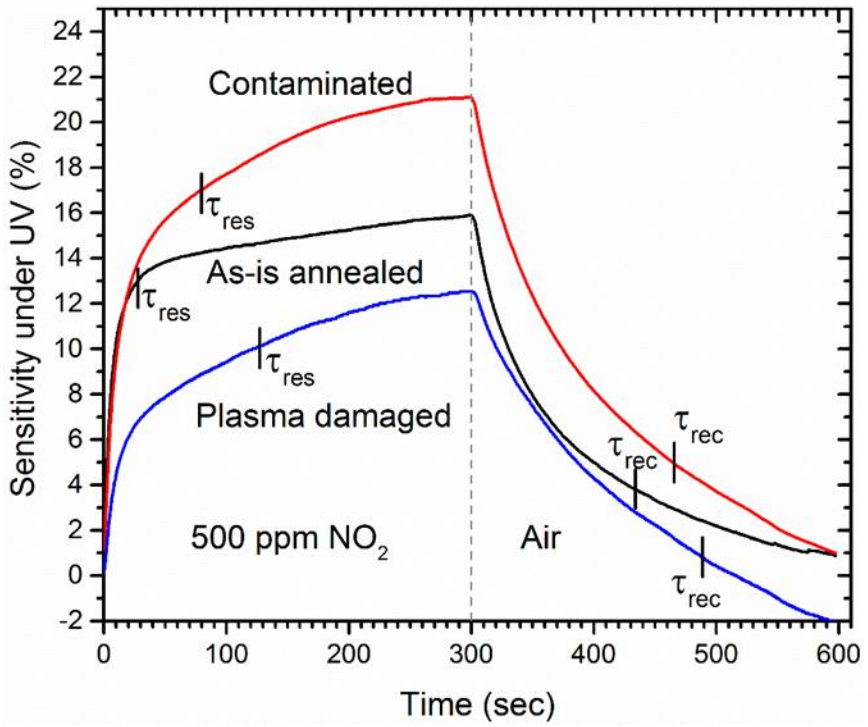

Figure 7.17 Comparison of the sensitivity of the as-is annealed, contaminated and plasma damaged TiO_2 films to 500 ppm NO_2. The time for 80% response and recovery was labeled.

Figure 7.17 shows the measured responses to 500 ppm NO_2 under UV illumination of the as-is annealed, contaminated, and plasma damaged TiO_2 films. The maximum sensitivity are observed at the end of the NO_2 exposure with the values 15.9 %, 21.1 % and 12.5 % for the as-is annealed, contaminated, and plasma damaged TiO_2 films, respectively. Therefore, the TiO_2 films are chemiresistively sensitive to the NO_2, regardless of the distinct surface conditions. The important figures of merits for the gas sensors, namely the response time (τ_{res}) and the recovery time (τ_{rec}) are defined as the time taken by the measured current to reach 80% of total current change in the presence of NO_2 (τ_{res}) and air (τ_{rec}), respectively. For the as-is annealed, contaminated, and

plasma damaged TiO_2 films, the observed response time are 26 sec, 78.6 sec, and 125.4 sec and the recovery time (τ_{rec}) are 132 sec, 166 sec, and 189 sec, respectively. Therefore, both the surface carbon contamination and roughness of the TiO_2 film suppress the response and recovery rate significantly. These results suggest that the adsorption and desorption rates of the gas analyte depend strongly on the surface conditions of the impurities and defects states.

G. Demonstrated semiconductor/metal systems for detecting various gas analytes

Table 7.2 summaries various manufactured semiconductor oxide/metal based gas sensors that respond to different gas analytes. The sensors are fabricated with similar procedures as the elaborated TiO_2 or TiO_2-Au/Ag thin films based NO_2 sensors. Appendix D details the parameters of these gas sensors.

Table 7.2 Database of semiconductor/metal thin films based gas sensors

Sensor materials	Detecting gases	Reference (Figure 7.18)
TiO_2-Pt	H_2	(a)
TiO_2-Cu	CO_2, CO	(b) and (c)
SnO_2-Cu	HCl, Cl_2	(d) and (e)
SnO_2-Fe	H_2S	(f)
SnO_2-Pd	H_2	(g)
CuO	HCN	(h)

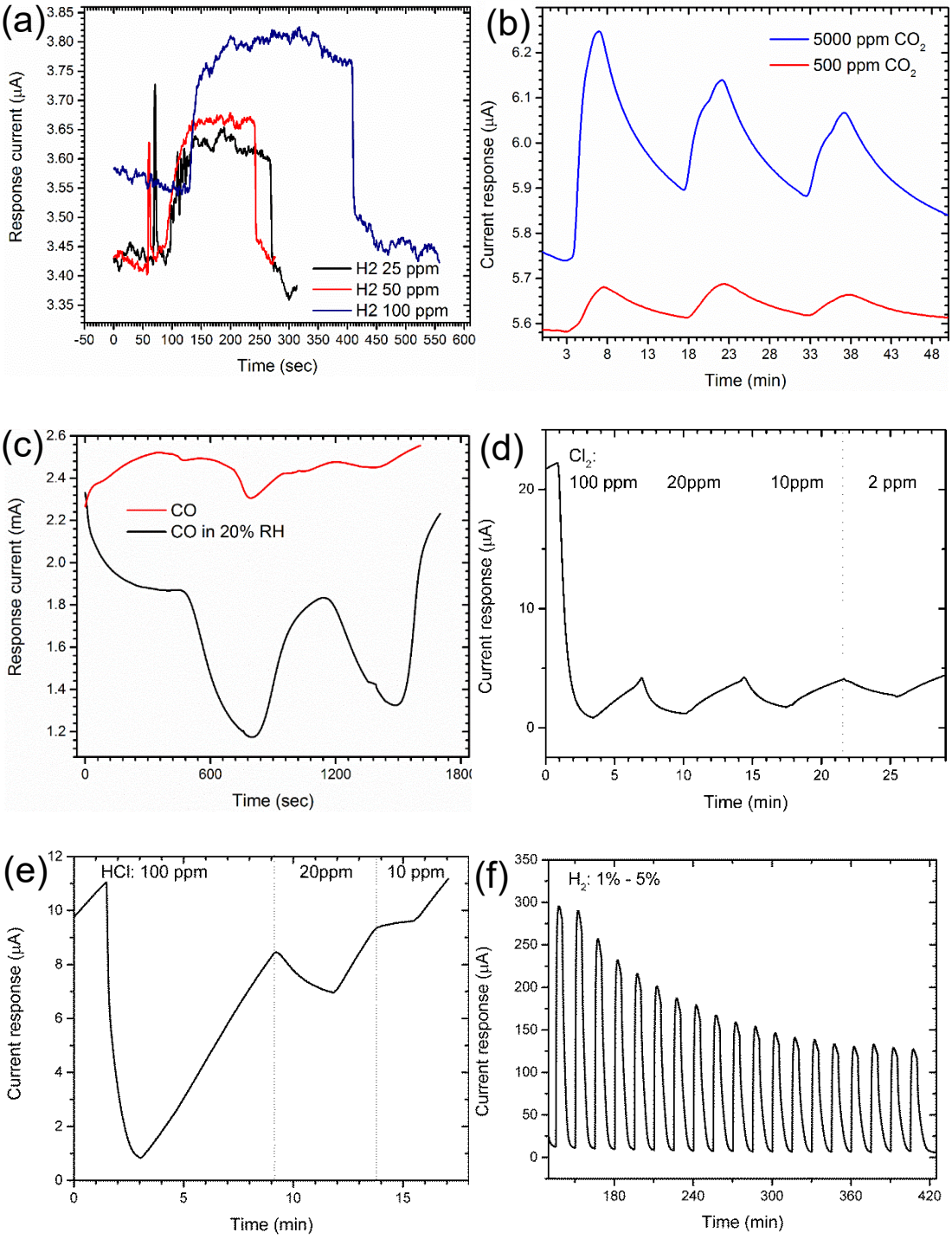
(a)
Response current (μA)
Time (sec)
H2 25 ppm
H2 50 ppm
H2 100 ppm
(b)
Current response (μA)
Time (min)
5000 ppm CO2
500 ppm CO2
(c)
Response current (mA)
Time (sec)
CO
CO in 20% RH
(d)
Current response (μA)
Time (min)
Cl2:
100 ppm
20ppm
10ppm
2 ppm
(e)
Current response (μA)
Time (min)
HCl: 100 ppm
20ppm
10 ppm
(f)
Current response (μA)
Time (min)
H2: 1% - 5%

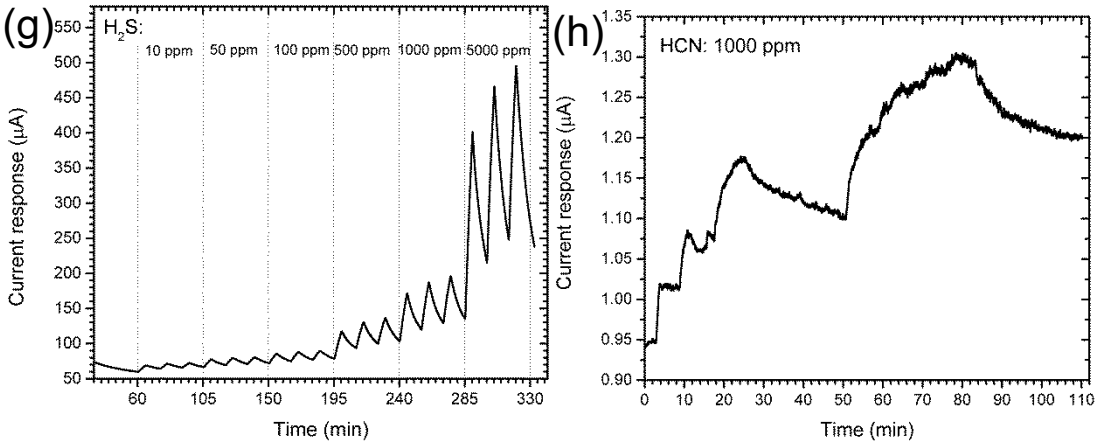

Figure 7.18 Demonstrated gas responses to various semiconductor/metal systems (a) TiO_2-Pt to H_2 at 25 ppm, 50 ppm and 100 ppm. TiO_2-Cu to (b) CO_2 at 500 ppm, 5000 ppm and (c) CO at 5000 ppm in 20% room humidity and dry air. SnO_2-Cu to (d) Cl_2 at 2 ppm, 10 ppm, 20 ppm and 100 ppm and (e) HCl at 100 ppm, 20 ppm and 10 ppm. (f) SnO_2-Pd to H_2 at 10000 ppm to 50000 ppm. (g) SnO_2-Fe to H_2S at 10 ppm to 5000 ppm. (h) CuO to HCN at 1000 ppm.

7.1.4. Conclusions

In this study, we have successfully fabricated selective TiO_2 based NO_2 sensors that work at room-temperature under UV illumination. The prepared anatase TiO_2 thin-film exhibits small grain size, smooth surface, and sharp UV absorbance. Assisted by UV illumination, the TiO_2 film shows a reversible and distinct NO_2 response with a relatively short response time at room-temperature. No response to the CO or CO_2 is measured with the TiO_2 based sensors. The measured responses to different NO_2 concentrations indicate a broad detecting range from 100 ppm to 500 ppm. The proposed gas sensing mechanism under UV relies on the modulation of the depletion region in TiO_2 due to the change in surface-adsorbed oxygen concentration. Furthermore, Au and Ag particles deposited on TiO_2 enhances the response of the TiO_2 base sensors. AFM and XPS examinations reveals that surficial carbon contamination

and increased surface roughness deteriorate the NO_2 sensing performance. Beyond the elaborated TiO_2 and TiO_2 with Ag and Au systems, various semiconductor oxides/metal systems were manufactured and tested with a list of target gases by employing the thin-film based sensor scheme. Many of those demonstrated material systems shows prominent sensing performance towards certain gases, which makes those systems potential candidates for gas sensing applications.

7.2. Semiconductor oxides/oxide-metals functionalized GaN nanowires for chemical gas sensing

7.2.1. Introduction

Gallium nitride (GaN) nanowires (NWs) functionalized with metal-oxides nanoparticles (NPs) have been explored extensively for gas sensing applications in the past few years. These sensors have several advantages such as miniature size, low-power consumption and fast response and recovery time over conventional schemes. The morphology of the oxide functionalization layer is critical for faster response and recovery time, with the target size distribution of NPs being in the range of 10 to 30 nm. However, morphological characterization of these NPs on GaN NWs can be challenging using commonly-used techniques such as scanning electron microscopy, transmission electron microscopy, and x-ray diffraction. Here, we demonstrate electrostatic force microscopy (EFM) in combination with atomic force microscopy (AFM) as a non-destructive technique for morphological characterization of the dispersed TiO_2 NPs on GaN NWs. We also discuss the applicability of this method to other material systems with a proposed tip-surface capacitor model. The gas sensing

performance of the fabricated TiO_2/GaN and TiO_2-Pt/GaN nanowires-based sensors have been demonstrated towards NO_2 and H_2, respectively.

7.2.2. Experimental details

High-quality GaN wafer was commercially available for the fabrication of GaN nanowires. The GaN layer was epitaxially grown on c-plane sapphire with an AlGaN buffer layer. The nanowire patterns were manufactured using inductively coupled plasma (ICP) etching in the gas environment of Cl/N2/Ar 25/5/1 sccm at 40°C. The ICP etching mask was consisted of a SiN passivation layer and a Ti/Ni mask layer that was patterned using deep-UV projection lithography. The nanowire fabrication process was precisely monitored by AFM measurement at each step to control the dimensions of the nanowires. The ICP etched GaN nanowires were later chemically polished in the mixed 10% wt. potassium hydroxide (KOH) with ethylene glycol solution at 80°C. The ohmic contacts (Ti/Al/Ti/Au) to GaN nanowires were deposited by e-beam evaporation. Please refer to the cited reference [232] for the detailed fabrication process of top-down etched GaN nanowires. The functionalization layer of TiO_2 was rf-sputtered on top of GaN nanowires with an estimated thickness of 2.5 nm. The deposition rate of TiO_2 was reduced by lowering the power from 300 W to 100 W. Post-annealing conditions of the sputtered TiO_2 were maintained at 700 °C for 30 sec in Ar environment. The annealed GaN nanowires with functionalization TiO_2 layer was examined by high-resolution electrostatic force microscopy (EFM) in combination with atomic force microscopy (AFM). The morphology of imaged TiO_2 nanoparticles was analyzed with Nanoscope Analysis software.

7.2.3. Results and discussion

Figure 7.19 shows the high-resolution AFM image obtained on GaN wafer. The image shows characteristic fringes of GaN lattice with threading dislocations, observed as dark spots in the image. The estimated rms roughness of the examined GaN surface is 0.312 nm.

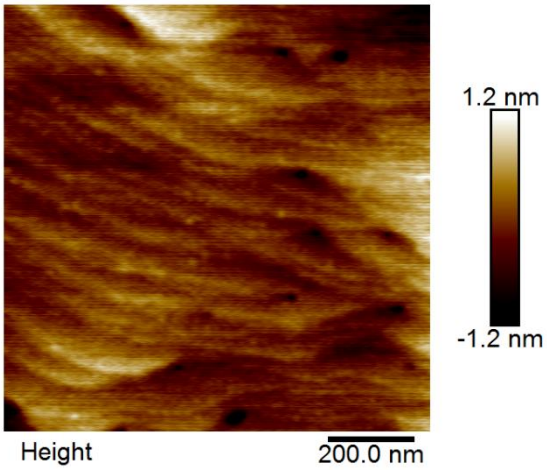

Figure 7.19 High-resolution AFM image on GaN surface.

Figure 7.20 shows the obtained AFM images during the dry etching process of GaN nanowires. Figure 7.20(a) shows the defined Ti/Ni mask for ICP etching. To pattern the nanowire structure, we firstly expose and develop the coated PR layer on the passivation SiN layer by deep-UV stepper photolithography. The metal mask results from the lift-off process of the e-beam evaporated metal layer on the patterned PR layer. Gleaned from the AFM measurement, the thickness of the metal layer is roughly 133 nm and the width of the mask at bottom is about 1 μm. The two 62 nm side peaks of the metal mask result from the shadowing effect of the e-beam evaporation. Figure 7.20(b) shows the ICP etched GaN nanowire structure using the above metal mask. The ICP etching stops at the AlGaN buffer layer, resulting a 665 nm high nanowire

structure. The cross-section of the nanowire shows a taped shape with 1 µm and 411 nm in width at the bottom and top, respectively. Figure 7.20(c) is the AFM image obtained after the etching of metal residual and SiN passivation layer. The height of the GaN nanowire is diminished to 614 nm, in good agreement with the thickness of the GaN layer. The width of the nanowire at the top increases to 460 nm while the bottom width remains at 1 µm.

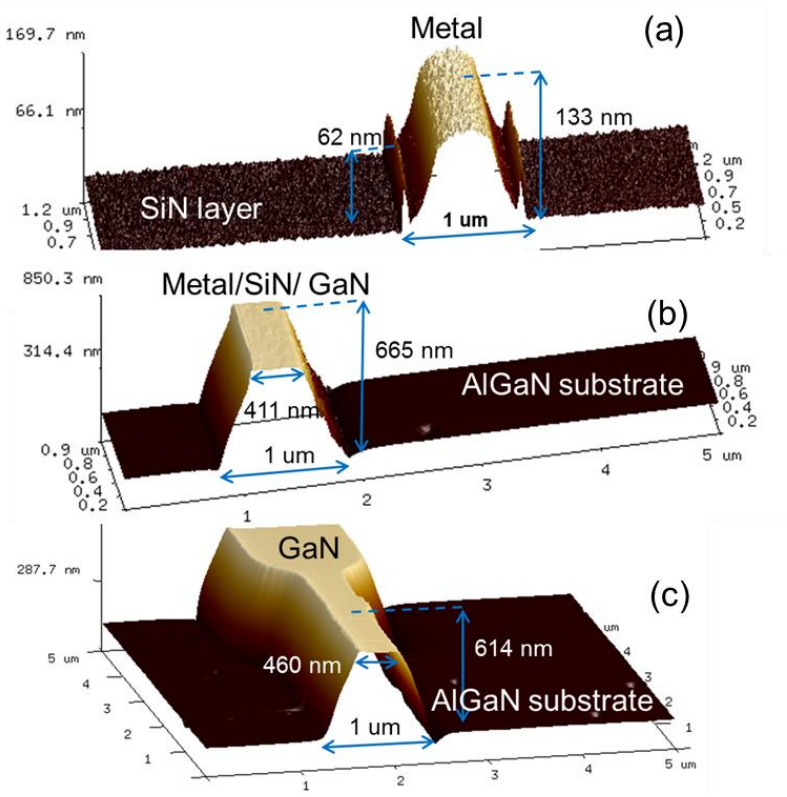

Figure 7.20 AFM images of nanowire in chronological order of (a) deposition of metal mask for ICP etching, (b) as-is ICP etched nanowire, and (c) residual mask and SiN passivation layer removed GaN nanowire.

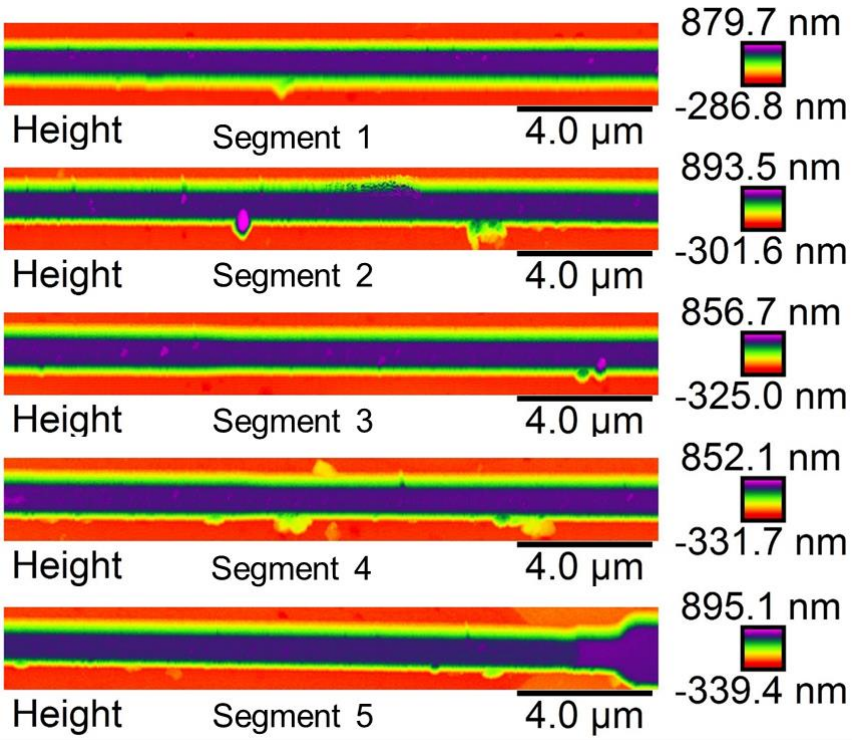

Figure 7.21 AFM images of a 100 μm long etched GaN nanowire.

Figure 7.21 shows the AFM images obtained from 5 consecutive segments of a 100 μm long nanowire. The results indicate a relative smooth side walls of the etched structure, despite occasional dirt. The uniformly controlled width along the nanowire is evident from the Figure as well.

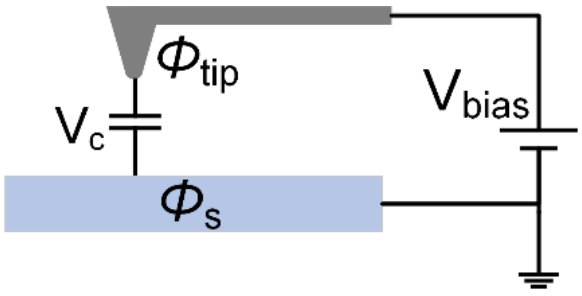

Figure 7.22 Schematic diagram of the tip-surface capacitor model for EFM.

Electrostatic Force Microscopy (EFM), like Magnetic Force Microscopy (MFM) shown in Figure 4.3, lifts up scan lines to the given height above the samples surface at the end of one AFM trace under tapping mode. Instead of probing the magnetic force, EFM measures the long-range electrostatic force between the conductive tip and the sample surface. The free space between the biased tip with *V* volt and sample forms a capacitor *C*. The energy stored in the capacitor is,

$$E = \frac{1}{2}C(V - V_{CPD})^2 \tag{7-4}$$

where the V_{CPD} is the difference in work function between the tip and sample. The negative gradient of the energy gives the expression of electrostatic force $\boldsymbol{F}$,

$$\vec{\boldsymbol{F}} = -\nabla E = -\frac{1}{2}\frac{\partial C}{\partial x}(V - V_{CPD})^2 \cdot \hat{\boldsymbol{x}} - \frac{1}{2}\frac{\partial C}{\partial y}(V - V_{CPD})^2 \cdot \hat{\boldsymbol{y}} - \frac{1}{2}\frac{\partial C}{\partial z}(V - V_{CPD})^2 \cdot \hat{\boldsymbol{z}} \tag{7-5}$$

The detected signal of EFM, phase shift P, is proportional to the gradient of $\boldsymbol{F}$ in z direction,

$$P = k\nabla\vec{\boldsymbol{F}} \cdot \hat{\boldsymbol{z}} = -k\frac{1}{2}\frac{\partial^2 C}{\partial z^2}(V - V_{CPD})^2 \tag{7-6}$$

where k is the system coefficient of the EFM measurement and V_{CPD} is the contact potential difference between the tip (Φ_{tip}) and sample (Φ_s).

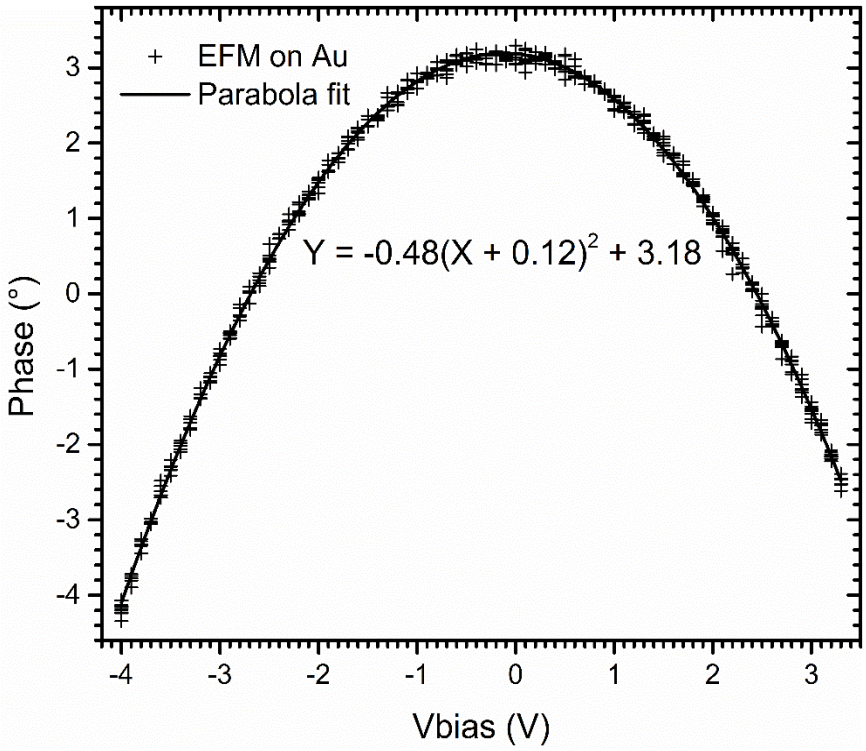

Figure 7.23 Plot of the phase signal as a function of applied bias with parabola fitting curve.

Figure 7.23 shows the detected phase signal with respect to the applied voltage, which convincingly verifies the parabolic dependence of P to V as predicted by Eq. 7-7. The best fitting parabola curve of the data can be analytically expressed as,

$$P_{Metal} = -0.48(V + 0.12)^2 + 3.18 \qquad (7\text{-}7)$$

The expression suggests a -0.12 eV difference in the work function of the metallic tip (Co) to the surface (Au). This result agrees well with the reported work functions for Co and Au, which is 5.0 eV and 5.1 eV respectively [233]. The constant term 3.18 is due to the offset in the EFM scan and 0.89 is proportional to the second derivative of the capacitance with respect to z.

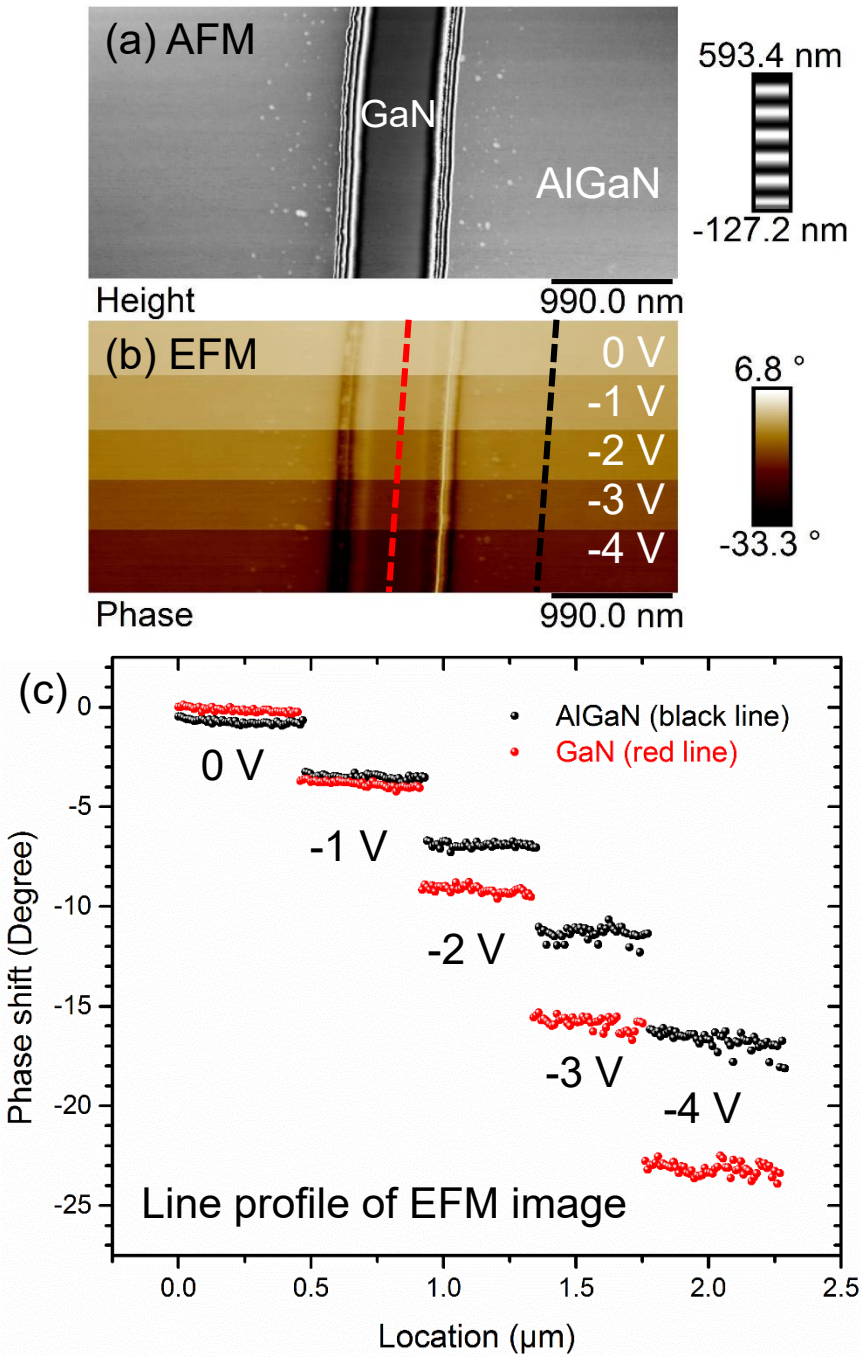

Figure 7.24 Images of the fabricated GaN nanowire (a) AFM image with zebra scale bar, (b) EFM image with 0 V to -4 V applied voltage. (c) Plot of phase signal of the selected lines (red and black) in (b).

Figure 7.24a and b show the AFM and EFM images obtained spontaneously from the etched GaN nanowire. The AFM image uses the zebra style scale bar, whose contrast

reflects the local variation in height. Evident from the AFM image, the surface of the fabricated GaN nanowire and AlGaN substrate is smooth with estimated rms roughness less than 0.7 nm. The corresponding EFM image is obtained at a constant tip height of 40 nm, with a progressive decrement of 1 V in bias voltage from 0 V. The detected phase signals of the two selected lines are shown in Figure 7.24c. The red and black lines correspond to the GaN and AlGaN regions, respectively. The phase contrast between the two materials deviate rapidly with the increased bias voltage, indicative of the feasibility of using EFM to differentiate low-conductive materials.

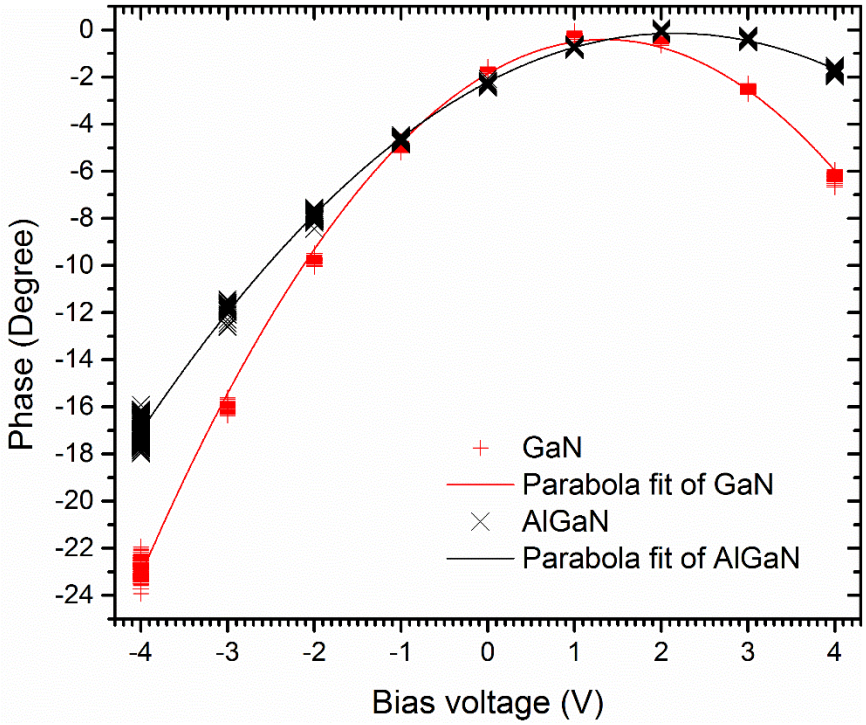

Figure 7.25 Plot of the phase signals obtained from GaN and AlGaN regions as a function of applied bias with parabola fitting curves.

Figure 7.25 is the plot of phase signals gleaned from GaN and AlGaN regions with respect to different bias voltages. The fits to quadratic functions of the two sets of data

confirms the $(V\text{-}V_{CDP})^2$ dependence as mentioned previously. The analytical expressions are,

$$P_{GaN} = -0.79(V - 1.35)^2 - 0.4 \quad (7\text{-}8)$$

$$P_{AlGaN} = -0.45(V - 2.15)^2 - 0.139 \quad (7\text{-}9)$$

The expressions indicate the difference between the work functions of the tip to the examined GaN and AlGaN are 1.35 eV and 2.15 eV, respectively. Given the condition that the tip has a work function close to 5.0 eV, the estimated electron affinities of the GaN and AlGaN are 3.65 eV and 2.85 eV, respectively, in good agreement with the reported data using ultraviolet photoemission spectroscopy measurements [234, 235].

Having demonstrated the applicability of EFM in characterizing low-conducting materials, Figure 7.26a and b show the captured AFM and EFM images on the TiO_2 functionalized GaN nanowire. The two images were acquired spontaneously under tapping mode. The scanning probe was held at the height of 40 nm above the surface to detect the phase contrast during the EFM measurement. The spatial variation of phase is proportional to second derivative of the electrostatic force with respect to z, as described in the Eq 7-7. The AFM data is scaled in the zebra style, which allows the depicting of wide-ranging height into a 2D image with detailed surface features. Clearly visible from the AFM image, the surface of the fabricated device, including the GaN nanowire, the AlGaN substrate and the passivation layer, is covered with granular TiO_2 nanoparticles (NPs). In corresponding EFM image, the phase contrast between the NPs and their surroundings convincingly indicates that the observed TiO_2 NPs adhere to the surface individually and are well dispersed. Figure 7.26c is the generated 3D rendering of the AFM images with the label for each region. The estimated rms roughness of the

GaN region, AlGaN region and passivation region is within a narrow range of 2 nm to 2.5 nm.

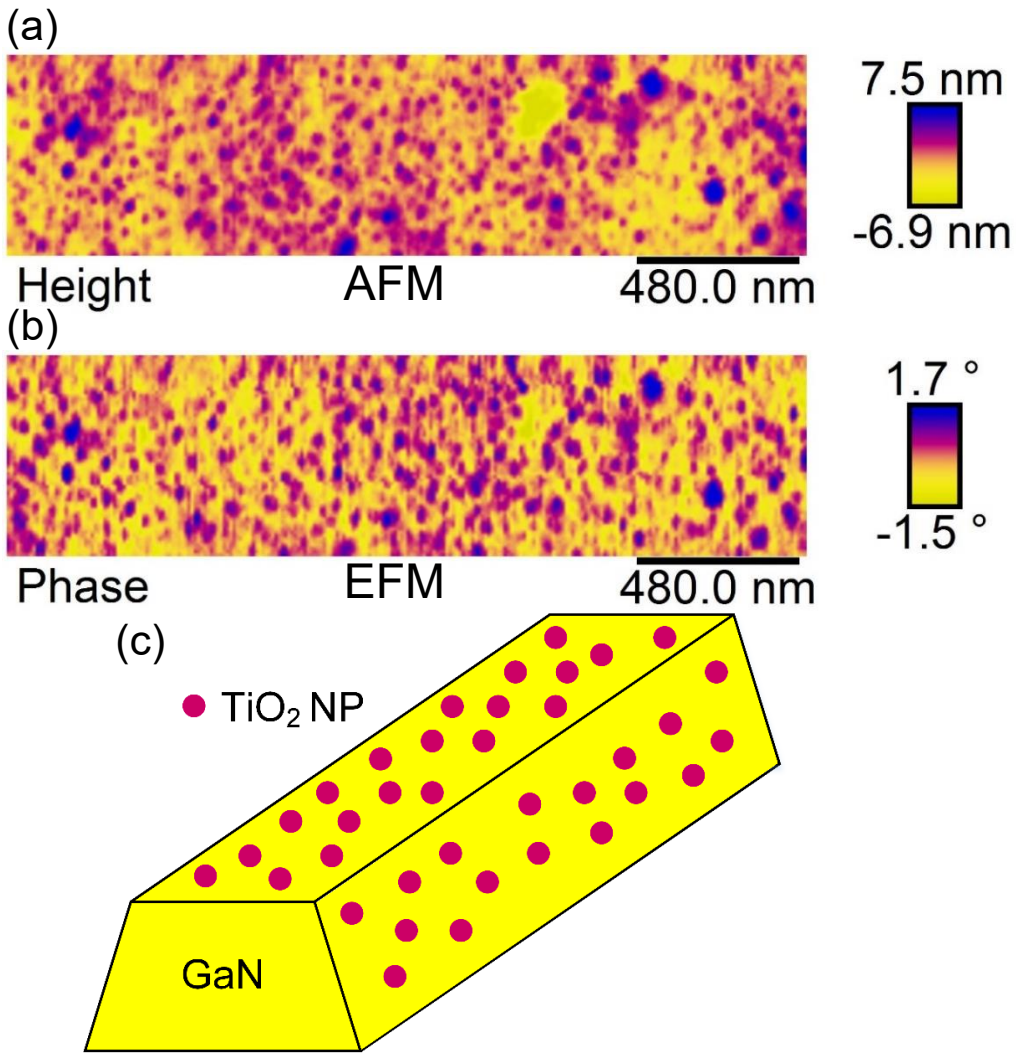

Figure 7.26 (a) AFM and (b) EFM images of functionalized TiO_2 nanoparticles on GaN nanowire. (c) Schematic diagram of the GaN nanowire with TiO_2 nanoparticles.

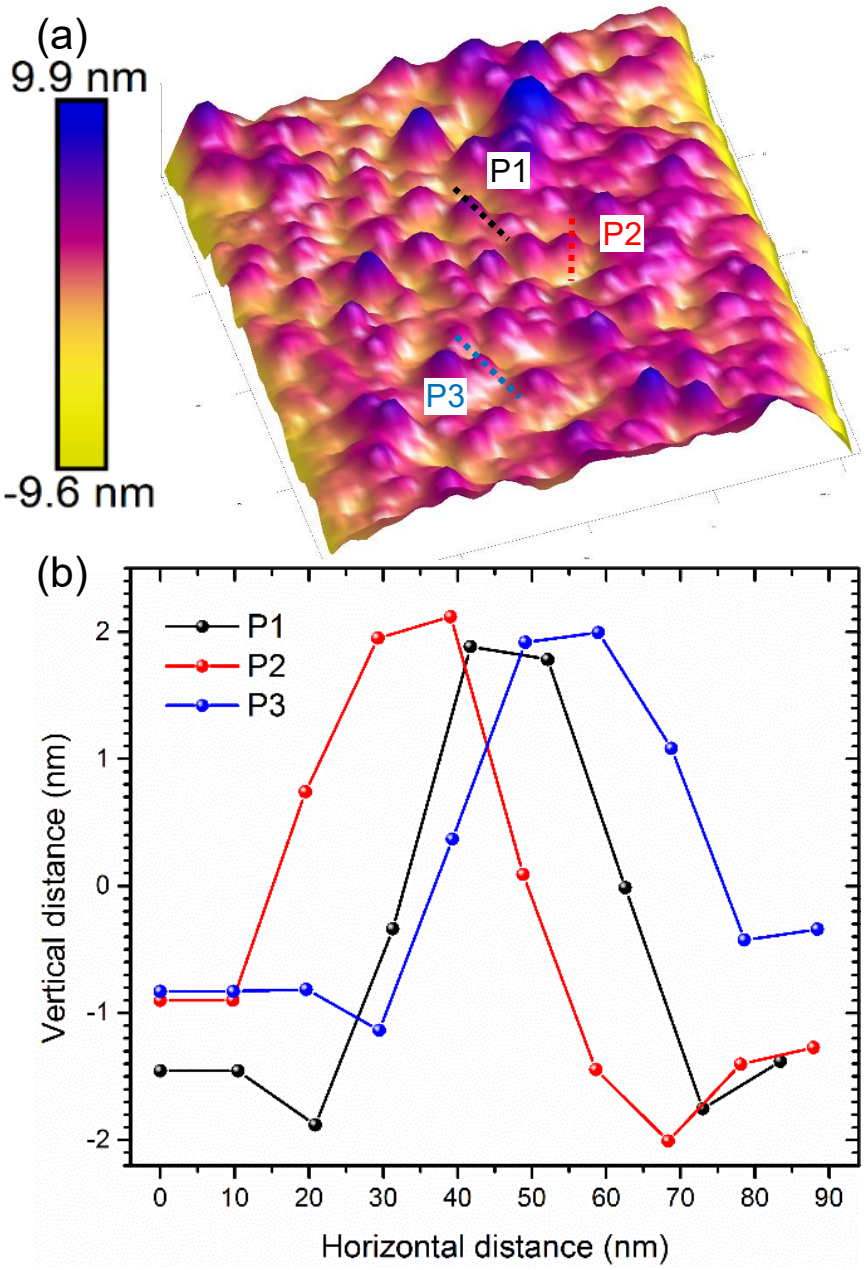

Figure 7.27 (a) AFM image on surface of TiO_2 NPs coated GaN nanowire. (b) Line profiles of three selected TiO_2 particles, indicated with P1 (black line), P2 (red line), P3 (blue line) in (a).

In addition to the confirmation of the formed TiO_2 NPs on surface, high resolution AFM image on the GaN nanowire is shown in Figure 7.27a. The estimated roughness of the region is about 2 nm. The image clearly manifests the granular of the dispersed

TiO_2 NPs on GaN surface. Three typical NPs, labeled as P1, P2 and P3 in Figure 7.27a, are selected to show their line profiles in Figure 7.27b. Gleaned from the plotted data, the heights of the particles ranges narrowly from 3 nm to 3.8 nm. The measured size in diameter of P1, P2 and P3 are roughly 53 nm, 57 nm and 50 nm, respectively.

Figure 7.28a shows the gas sensing performance of the TiO_2 functionalized GaN nanowire sensors at room-temperature. The sensors were exposed to 500 ppm NO_2 for 300 sec followed by 300 sec breathing air, under UV illumination. The monitored current decreases due to the presence of NO_2 analyte and recovers in the air. The results demonstrate the reversible and distinct gas response of the proposed sensor scheme which is comprised of the backbone GaN nanowire and the functionalized oxide layer. However, the sensitivity of the sensor to the gas analyte is merely 1.1 % to 1.7 % with the baseline shifting. To surmount the circumstances, foreign receptors were exploited and loaded onto the oxide functionalized sensors to promote their sensitivity to certain gas anelytes. Figure 7.28b shows the TiO_2-Pt functionalization multilayer enabled H_2 detection of the GaN nanowire based sensor at room-temperature. Under the UV illumination, the current of the TiO_2-Pt/GaN sensor increases to the exposure of 10% H_2 and decreases in the air. The estimated sensitivity of the sensor to the 10 % H_2 is about 20.6 %. In addition to the enhanced sensitivity, the sensor exhibits an instant temporal response as well. The estimated 80 % response time (τ_{res}) is less than 5 sec for the sensor. After recovering in the air for 300 sec, the current of the sensor resumes 90 % from the active H_2 detecting state to the initial state. These prominent sensing performance make the TiO_2-Pt/GaN based sensor suitable for H_2 concentration monitoring application.

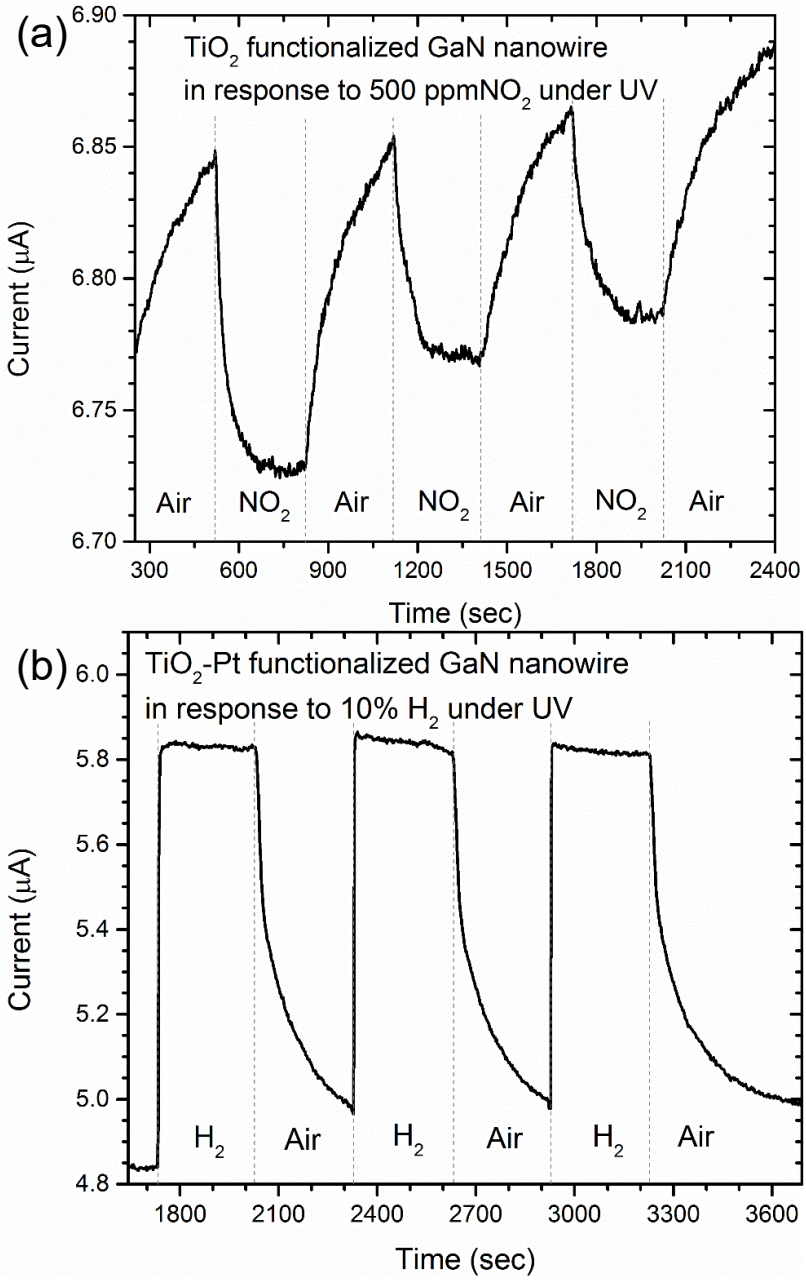

Figure 7.28 Dynamic gas responses of (a) TiO_2 functionalized GaN nanowire to three cycles of 500 ppm NO_2 under UV illumination. (b) TiO_2-Pt functionalized GaN nanowire to three cycles of 10 % H_2 under UV illumination.

7.2.4. Conclusions

In this study, we have successfully demonstrated the highly sensitive and selective gas sensors based on GaN nanowire with oxide/metal multilayers. The geometry of the

fabricated GaN nanowires can be precisely controlled with the ICP and KOH etching. The functionalization of the GaN nanowire for gas detection is realized by loading catalytic active TiO_2 NPs and TiO_2-Pt on the surface of nanowires. The characterization of the deposited TiO_2 using the combinatorial scanning probe tools, EFM and AFM, reveals the wide-spread distribution of the granular TiO_2 NPs on the surface. The functionalized GaN nanowires with TiO_2 and TiO_2-Pt responds to NO_2 and H_2, respectively.

7.3. Future challenges

Further investigation on the semiconductor oxide based gas sensors can be proceeded in the following aspects.

For the TiO_2 thin film based NO_2 sensors, the challenge of achieving a very-fast response and recovery rate remains. In addition to the proposed oxide nanoparticles functionalized GaN nanowires schemes, some other gas sensor structures are worth investigating as well. One promising candidate is the so called gate-refreshable structure. In this case, a metal gate is deposited on the backside of the TiO_2 thin film device, in contact with the sapphire substrates. This back gate is going to be used as a third terminal of the sensor to modulate the depth of the majority charge depletion region, with the biasing voltage. Notice again that the depletion region is induced by the surface adsorbed oxygen anions. Therefore, I would expect the modulation of the depletion region, which is equivalent to the change of the carrier concentration on the surface, to assist the adsorbing and the desorbing of the oxygen anions. In the way, the sensor can exhibit a faster response and recovery rate than the thin film based structure.

In fact, the enhancement in the recovery rate with the gate biasing voltage has been demonstrated in a similar gated ZnO nanowire structure [236]. To realize this back gated structure with the established TiO_2 thin film, we have to firstly reduce the thickness of the sapphire from 435 μm to the range of few hundred nm or even less. This is because a thick insulating sapphire layer would greatly increase the bias voltage to modulate the fermi energy of the TiO_2. The high quality gate sapphire layer can be deposited with the plasma enhanced chemical vapor deposition or the atomic layer deposition. Figure 7.29 shows the schematic diagram of the proposed gate-refreshable sensor structure.

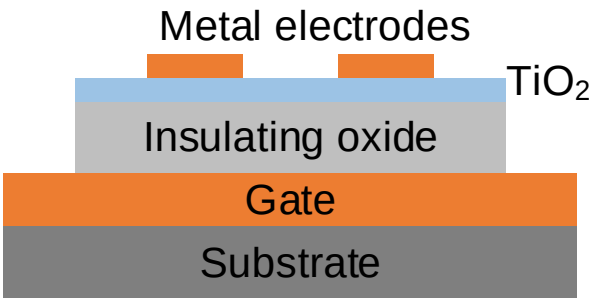

Figure 7.29 schematic diagram of the proposed gate-refreshable gas sensor.

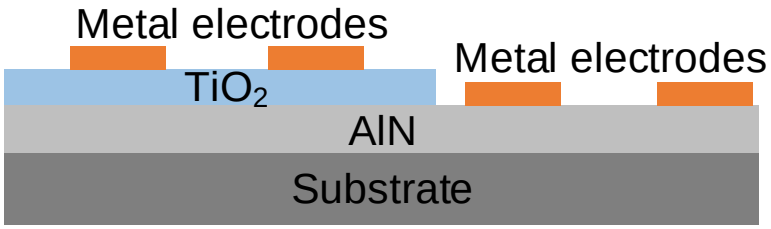

Figure 7.30 schematic diagram of the proposed acoustic wave assisted gas sensor.

Compared to the gate refreshable scheme, the concept of using acoustic wave to assist the chemical gas desorption has not been established yet and is thus more challenging

to be validated. The conceptual schematic diagram of the sensor scheme is proposed in Figure 7.30. The acoustic wave, especially ultrasonic, is frequently employed to fasten the physical and chemical dissolving process. Sparked from this typical application of the acoustic energy, I proposed to use the surface acoustic wave as an additional source of energy in facilitating the chemical desorbing process. The surface acoustic wave can be excited by applying biasing voltages on materials like AlN. AlN is also insulating. Under this condition, the structure is AlN on the substrate, TiO_2 as the functional layer on AlN, one pair of electrical contacts on the AlN layer for the excitation of surface acoustic wave, and one pair of electrical contacts on TiO_2 for the monitoring of the chemiresistive response towards analytes.

Regarding to the TiO_2 thin film sensor device, more efforts can be made to improve the energy efficiency. This can be achieved by scaling down the size of the sensor structure. With this approach, the active area of the TiO_2 film is reduced and thereby diminishes the amount of the dissipated energy. The proposal of minimizing the dimensions of the sensor will involve the nanoscale lithography and patterning steps. To prevent the damages due to the etching of the extra TiO_2, a lift-off process in the lithography is preferred. If the power consumption of the gas sensor is low enough to match the output power from energy harvesting systems [41], the gas sensors can then work sustainably and unattended without the external power [237-239].

The chapter 7.1 in the dissertation discusses the role of surface conditions of the TiO_2 thin film sensor on sensing performance. However, one question remain unsolved in that section is that how to restore the contaminated and rough surface of the TiO_2 films to enhance the sensing performance. Reactive ion etching, UV ozone, and aggressive

chemical solutions like Piranha can be candidates for the removal of carbon residues. However, more engineering studies have to be conducted to finalize the carbon cleaning recipe. In the case of rough surface, annealing seems to be the plausible method to cure the defects. But, again, it is not easy to find the right temperature and time to treat the defects while maintaining the high chemical response of the deposited TiO_2 film.

The current work on the topic of metal decorated oxides for gas detection applications can be extensively extended in the future. First of all, many other metals with good chemical catalysis, for example Ir, Ru, should be studied by incorporating them into oxides towards the gas detection. The gas sensing mechanism for a metal oxide system needs more exploration as well. The addition of metal, and the concomitant deposition of the oxide states of the metal, on the semiconductor oxides changes surface chemistry dramatically. While the surface chemistry affects the adsorption and desorption of gas analytes and the charge transfer strongly, the gas sensing mechanism may be dramatically different from the proposed mechanism for the TiO_2 sensor.

We have demonstrated that the TiO_2 nanoparticles functionalized GaN nanowires can improve the response time from the thin film case. However, the sensor scheme shows many remaining challenges. The first one is the shifting of the response and recovery baseline currents, towards the high current direction. This problem can be solved by reduce the defects in the etched GaN nanowires and the deposited TiO_2 layer. The GaN defects may come from the bulk or surface. The bulk defects should be addressed during the growth of the GaN layer. The surface defects, which may be induced in the dry etching process, can be removed with wet chemical etching. The optimization of

the fabrication of GaN nanowires will involve a number of characterization studies, like photoluminescence, Raman scattering spectroscopy, XPS, XRD, AFM, and etc. The defect associated with the deposited TiO_2 may be removed with elevated growth and annealing temperatures as well as the sputtering gas environment. But the implementation of these changes in the TiO_2 deposition conditions should be very cautious as the oxygen vacancy (defect) also governs the gas sensing performance. The relatively small sensitivity of the TiO_2 functionalized GaN nanowires sensor can be enhanced by increasing the surface-to-volume ratio of the device. In this path, the geometries of the GaN nanowire should be further scaled down.

Appendices

Appendix A.1

NiO and ZnMgO precursor solution

For NiO, nickel acetate tetrahydrate was dissolved in 2-methoxyethanol and monoethanolamine (MEA) in a glass vial. Similarly, $Zn_{1-x}Mg_xO$ precursor solution was prepared separately using zinc acetate tetrahydrate and magnesium acetate tetra hydrate in the same solvents. The molar ratio of $Ni^{2+}/(Zn^{2+}+Mg^{2+})$:MEA was maintained at 1:1 in the solution. The concentration of Mg^{2+} was adjusted to form $Zn_{1-x}Mg_xO$ thin films with x ranging from 0 to 0.1. Concentration of all metal ions was 0.4 M. The dissolved precursors were magnetically stirred at 60 °C for 2 hours in a water bath and then filtered with a 0.45 μm filter.

Appendix A.2

Procedure for ALD deposition of ZnMgO film

Thin films of magnesium-doped zinc-oxide ($Zn_{1-x}Mg_xO$) were deposited onto silicon using a Savannah 100 thermal atomic layer deposition (ALD) system from Cambridge Nanotech. ALD growth of $Zn_{1-x}Mg_xO$ was carried out at a substrate temperature of 150 $^{\circ}$C by alternating [ZnO] and [MgO] ALD cycles. A typical ALD cycle consisted of a series of [precursor – purge – oxidant – purge] pulse cycles. Diethylzinc (DEZ, $(C_2H_5)_2Zn$) and bis(ethylcyclopentadienyl)magnesium ($(EtCp)_2Mg$, $(C_2H_5C_5H_4)_2Mg$)

were used as the metal precursors for the deposition of the ZnO and MgO layers, respectively, and deionized water (DI) as the oxidant. For the [ZnO] ALD cycle, we used 0.015s for the DEZ and DI pulses with 30s purge time between pulses. For the [MgO] ALD cycle, we adopted 1s for the $(EtCp)_2Mg$ and 0.015s for the DI pulses with 30s purge time between pulses. As reported previously, self-limited ALD growth mode was achieved under these conditions.

Appendix B

Carrier gas: breathing air.

		Conditions			Specs		
Analyte	Conc.	UV	Temperature	Humidity	Sensitivity	T80	T20
xylenes	450ppm	ON	RT	>10%	NR		
methanol	400ppm	ON	RT	>10%	NR		
CO_2	1000ppm	ON	RT	>10%	NR		
CO	1000ppm	ON	RT	>10%	NR		
HCN	1000ppm	ON	RT	>10%	NR		
NO_2	100ppm	ON	RT	>10%	1.18%	215s	240s
NO_2	250ppm	ON	RT	>10%	1.58%	180s	240s
NO_2	500ppm	ON	RT	>10%	2.0%	180s	240s
NH_3	50ppm	ON	RT	>10%	NR		
NH_3	100ppm	ON	RT	>10%	0.45%		
NH_3	250ppm	ON	RT	>10%	0.5%	300s	300s
NH_3	500ppm	ON	RT	>10%	0.45%	300s	300s
NO_2	100ppm	OFF	RT	>10%	1.5%	300s	300s
NO_2	250ppm	OFF	RT	>10%	2.2%	300s	300s
NO_2	500ppm	OFF	RT	>10%	2.0%	300s	300s
NH_3	10ppm	OFF	RT	>10%	NR	300s	300s
NH_3	50ppm	OFF	RT	>10%	NR		
NH_3	100ppm	OFF	RT	>10%	NR		
NH_3	250ppm	OFF	RT	>10%	NR		
NH_3	500ppm	OFF	RT	>10%	NR		

The detailed list of analytes responses to TiO_2 thin film based gas sensor.

Appendix C

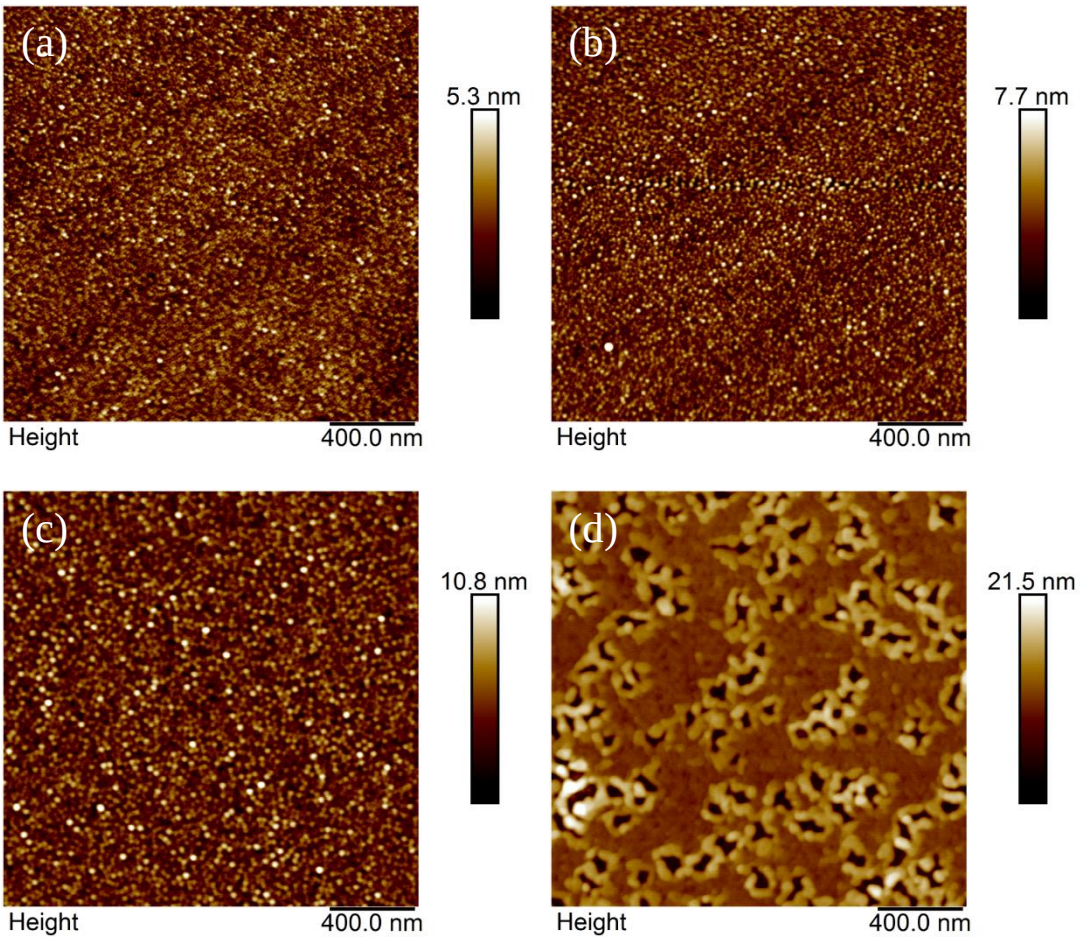

Figure C.1. AFM images reveal the transition of Au particles (a, b, and c) into film (d) on sapphire substrates with increased deposition time and power. The surface rms roughness of the deposited Au layer from a to d increases as well. The estimated numbers are 0.695 nm, 0.895 nm, 1.41 nm and 2.58 nm for a, b, c, and d, respectively.

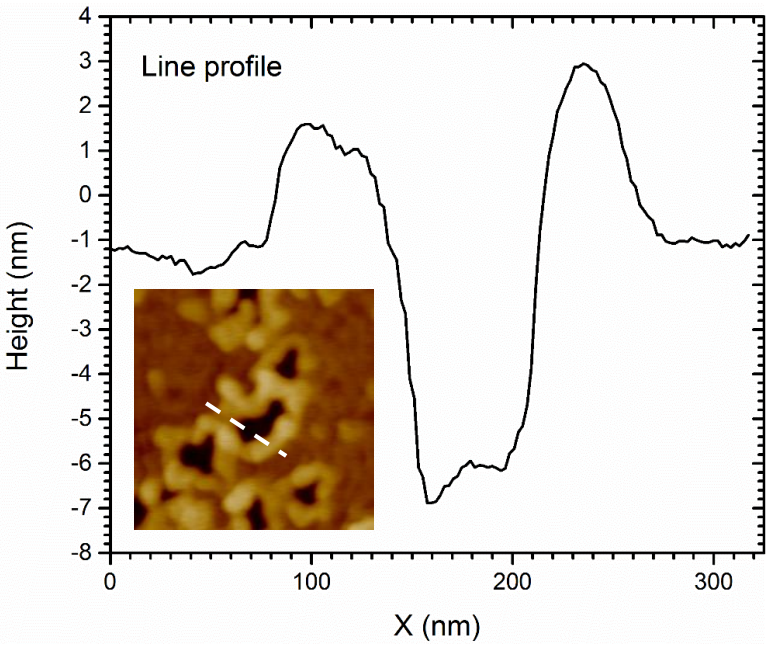

Figure C.2. Height profile of the selected line, indicated by the white dash line in the inset AFM image.

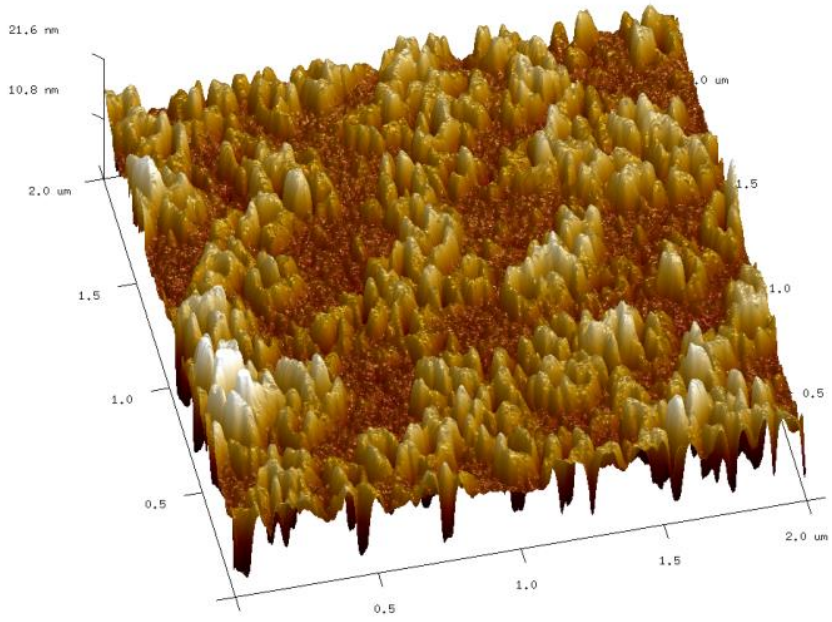

Figure C.3. 3D rendering of Figure C.1.d.

Appendix D

Fabrication details of the demonstrated semiconductor/metal systems for detecting various gas analytes.

Material system	Oxide thickness	Annealing condition	Metal thickness
TiO_2-Pt	11 nm	700 ^oC in Ar	2 nm
TiO_2-Cu	11 nm	700 ^oC in Ar	2 nm
SnO_2-Cu	96 nm	N.A.	10 nm
SnO_2-Pd	96 nm	N.A.	2 nm
SnO_2-Fe	96 nm	N.A.	2 nm
CuO	100 nm	700 ^oC in Ar	N.A.

Bibliography

[1] S. X. Huang, T. Y. Chen, and C. L. Chien, "Spin polarization of amorphous CoFeB determined by point-contact Andreev reflection," *Applied Physics Letters,* vol. 92, pp. 242509-3, 06/16/ 2008.

[2] R. D. Gomez, J. S. Ma, A. Arkilic, S. H. Chung, and C. Krafft, "Vortex-antivortex creation and annihilation on CoFeB crosstie patterns," *Journal of Applied Physics,* vol. 109, p. 07D310, Apr 1 2011.

[3] T. Xie and R. D. Gomez, "Formation of Magnetic Nanoparticles by Annealing Continuous CoFeB/Cu Bilayer Thin Films," *Magnetics, IEEE Transactions on,* vol. 51, pp. 1-4, 2015.

[4] S. H. Chen, M. H. Tang, Z. Z. Zhang, B. Ma, S. T. Lou, and Q. Y. Jin, "Interfacial effect on the ferromagnetic damping of CoFeB thin films with different under-layers," *Applied Physics Letters,* vol. 103, Jul 2013.

[5] D. D. Djayaprawira, K. Tsunekawa, M. Nagai, H. Maehara, S. Yamagata, N. Watanabe, *et al.*, "230% room-temperature magnetoresistance in CoFeB/MgO/CoFeB magnetic tunnel junctions," *Applied Physics Letters,* vol. 86, pp. 092502-3, 02/28/ 2005.

[6] S. Ikeda, R. Koizumi, H. Sato, M. Yamanouchi, K. Miura, K. Mizunuma, *et al.*, "Boron Composition Dependence of Magnetic Anisotropy and Tunnel Magnetoresistance in MgO/CoFe(B) Based Stack Structures," *Magnetics, IEEE Transactions on,* vol. 48, pp. 3829-3832, 2012.

[7] A. Fert, "Nobel Lecture: Origin, development, and future of spintronics," *Reviews of Modern Physics,* vol. 80, pp. 1517-1530, 12/17/ 2008.

[8] P. A. Grünberg, "Nobel Lecture: From spin waves to giant magnetoresistance and beyond," *Reviews of Modern Physics,* vol. 80, pp. 1531-1540, 12/17/ 2008.

[9] T. Miyazaki and N. Tezuka, "Giant magnetic tunneling effect in Fe/Al2O3/Fe junction," *Journal of Magnetism and Magnetic Materials,* vol. 139, pp. L231-L234, Jan 1995.

[10] J. S. Moodera, L. R. Kinder, T. M. Wong, and R. Meservey, "Large magnetoresistance at room temperature in ferromagnetic thin film tunnel junctions," *Physical Review Letters,* vol. 74, pp. 3273-3276, 04/17/ 1995.

[11] T. Tahmasebi, S. N. Piramanayagam, R. Sbiaa, and T. C. Chong, "CoFeB spin polarizer layer composition effect on magnetization and magneto-transport properties of Co/Pd-based multilayers in pseudo-spin valve structures," *Journal of Applied Physics,* vol. 113, pp. 023909-5, 01/14/ 2013.

[12] R. Law, R. Sbiaa, T. Liew, and T. C. Chong, "Magnetoresistance and Switching Properties of Co-Fe/Pd-Based Perpendicular Anisotropy Single- and Dual-Spin Valves," *Ieee Transactions on Magnetics,* vol. 44, pp. 2612-2615, Nov 2008.

[13] J. H. Chang, H. H. Chen, and C. R. Chang, "Instabilities of a spin-valve system with perpendicular polarizer and in-plane bias field," *Physical Review B,* vol. 83, Feb 22 2011.

[14] S. Ikeda, J. Hayakawa, Y. Ashizawa, Y. M. Lee, K. Miura, H. Hasegawa, *et al.*, "Tunnel magnetoresistance of 604% at 300 K by suppression of Ta diffusion in CoFeB/MgO/CoFeB pseudo-spin-valves annealed at high temperature," *Applied Physics Letters,* vol. 93, p. 3, Aug 2008.

[15] S. Ikeda, K. Miura, H. Yamamoto, K. Mizunuma, H. D. Gan, M. Endo, *et al.*, "A perpendicular-anisotropy CoFeB-MgO magnetic tunnel junction," *Nature Materials,* vol. 9, pp. 721-724, Sep 2010.

[16] L. Gan, S. H. Chung, K. H. Aschenbach, M. Dreyer, and R. D. Gomez, "Pulsed-current-induced domain wall propagation in permalloy patterns observed using magnetic force microscope," *Magnetics, IEEE Transactions on,* vol. 36, pp. 3047-3049, Sep 2000.

[17] S. H. Florez, C. Krafft, and R. D. Gomez, "Spin-current-induced magnetization reversal in magnetic nanowires with constrictions," *Journal of Applied Physics,* vol. 97, May 2005.

[18] S. S. P. Parkin, M. Hayashi, and L. Thomas, "Magnetic domain-wall racetrack memory," *Science,* vol. 320, pp. 190-194, Apr 2008.

[19] A. Ding, I. Will, and Y. B. Xu, "MFM Observation of Twin Pinning Sites on NiFe Nanowires," *Magnetics, IEEE Transactions on,* vol. 49, pp. 1334-1336, Apr 2013.

[20] J. C. Slonczewski, "Current-driven excitation of magnetic multilayers," *Journal of Magnetism and Magnetic Materials,* vol. 159, pp. L1-L7, Jun 1996.

[21] L. Berger, "LOW-FIELD MAGNETORESISTANCE AND DOMAIN DRAG IN FERROMAGNETS," *Journal of Applied Physics,* vol. 49, pp. 2156-2161, 1978 1978.

[22] S. D. Bader and S. S. P. Parkin, "Spintronics," in *Annual Review of Condensed Matter Physics, Vol 1*. vol. 1, J. S. Langer, Ed., ed Palo Alto: Annual Reviews, 2010, pp. 71-88.

[23] M. Hayashi, L. Thomas, R. Moriya, C. Rettner, and S. S. P. Parkin, "Current-controlled magnetic domain-wall nanowire shift register," *Science,* vol. 320, pp. 209-211, Apr 2008.

[24] V. Uhlíř, J. Vogel, N. Rougemaille, O. Fruchart, Z. Ishaque, V. Cros, *et al.*, "Current-induced domain wall motion and magnetization dynamics in CoFeB/Cu/Co nanostripes," *Journal of Physics: Condensed Matter,* vol. 24, p. 024213, 2012.

[25] S. Laribi, V. Cros, M. Munoz, J. Grollier, A. Hamzic, C. Deranlot, *et al.*, "Reversible and irreversible current induced domain wall motion in CoFeB based spin valves stripes (3 pages)," *APPLIED PHYSICS LETTERS,* vol. 90, p. 232505, 2007.

[26] G. Tatara and H. Kohno, "Theory of current-driven domain wall motion: spin transfer versus momentum transfer," *Physical review letters,* vol. 92, 2004.

[27] C. Bilzer, T. Devolder, J. V. Kim, G. Counil, C. Chappert, S. Cardoso, *et al.*, "Study of the dynamic magnetic properties of soft CoFeB films (4 pages)," *JOURNAL OF APPLIED PHYSICS,* vol. 100, p. 053903, 2006.

[28] S. Zhu, R. J. Gambino, M. H. Rafailovich, J. Sokolov, S. A. Schwarz, and R. D. Gomez, "Microscopic magnetic characterization of submicron cobalt islands prepared using self-assembled polymer masking technique," *IEEE Transactions on Magnetics,* vol. 33, pp. 3022-3024, Sep 1997.

[29] C. E. Morris and T. C. Skalak, "Acute exposure to a moderate strength static magnetic field reduces edema formation in rats," *American Journal of*

Physiology-Heart and Circulatory Physiology, vol. 294, pp. H50-H57, Jan 2008.

[30] C. E. Morris and T. C. Skalak, "Chronic static magnetic field exposure alters microvessel enlargement resulting from surgical intervention," *Journal of Applied Physiology,* vol. 103, pp. 629-636, Aug 2007.

[31] B. R. McLeod and E. L. Sandvik, "A Biofilm Growth Protocol and the Design of a Magnetic Field Exposure Setup to Be Used in the Study of Magnetic Fields as a Means of Controlling Bacterial Biofilms," *Bioelectromagnetics,* vol. 31, pp. 56-63, Jan 2010.

[32] L. Sang, M. Liao, and M. Sumiya, "A comprehensive review of semiconductor ultraviolet photodetectors: from thin film to one-dimensional nanostructures," *Sensors (Basel),* vol. 13, pp. 10482-518, 2013.

[33] F. Omnes, E. Monroy, E. Munoz, and J.-L. Reverchon, "Wide bandgap UV photodetectors: A short review of devices and applications," in *Gallium Nitride Materials and Devices Ii*. vol. 6473, H. Morkoc and C. W. Litton, Eds., ed, 2007.

[34] Y. N. Hou, Z. X. Mei, and X. L. Du, "Semiconductor ultraviolet photodetectors based on ZnO and MgxZn1-xO," *Journal of Physics D-Applied Physics,* vol. 47, Jul 2014.

[35] R. Debnath, T. Xie, B. Wen, W. Li, J.-Y. Ha, N. Sullivan, *et al.*, "A solution-processed high-efficiency p-NiO/n-ZnO heterojunction photodetector," *RSC Advances,* vol. 5, pp. 14646-14652, 2015.

[36] W. Zhang, J. Xu, W. Ye, Y. Li, Z. Qi, J. Dai, *et al.*, "High-performance AlGaN metal–semiconductor–metal solar-blind ultraviolet photodetectors by localized surface plasmon enhancement," *Applied Physics Letters,* vol. 106, p. 021112, 2015.

[37] J. Dai, C. X. Xu, X. Y. Xu, J. Y. Guo, J. T. Li, G. Y. Zhu, *et al.*, "Single ZnO Microrod Ultraviolet Photodetector with High Photocurrent Gain," *Acs Applied Materials & Interfaces,* vol. 5, pp. 9344-9348, Oct 2013.

[38] Y. Q. Bie, Z. M. Liao, H. Z. Zhang, G. R. Li, Y. Ye, Y. B. Zhou, *et al.*, "Self-powered, ultrafast, visible-blind UV detection and optical logical operation based on ZnO/GaN nanoscale p-n junctions," *Adv Mater,* vol. 23, pp. 649-53, Feb 1 2011.

[39] Y. Shen, X. Yan, Z. Bai, X. Zheng, Y. Sun, Y. Liu, *et al.*, "A self-powered ultraviolet photodetector based on solution-processed p-NiO/n-ZnO nanorod array heterojunction," *RSC Adv.,* vol. 5, pp. 5976-5981, 2015.

[40] X. Chen, H. Zhu, J. Cai, and Z. Wua, "High-performance 4H-SiC-based ultraviolet p-i-n photodetector," *Journal of Applied Physics,* vol. 102, Jul 15 2007.

[41] M. R. Hasan, T. Xie, S. C. Barron, G. Liu, N. V. Nguyen, A. Motayed, *et al.*, "Self-powered p-NiO/n-ZnO heterojunction ultraviolet photodetectors fabricated on plastic substrates," *APL Materials,* vol. 3, p. 106101, 2015.

[42] T. Xie, M. R. Hasan, B. Qiu, E. S. Arinze, N. V. Nguyen, A. Motayed, *et al.*, "High-performing visible-blind photodetectors based on SnO2/CuO nanoheterojunctions," *Applied Physics Letters,* vol. 107, p. 241108, 2015.

[43] D. K. Aswal and S. K. Gupta, *Science and technology of chemiresistor gas sensors*: Nova Publishers, 2007.
[44] G. Eranna, B. C. Joshi, D. P. Runthala, and R. P. Gupta, "Oxide materials for development of integrated gas sensors - A comprehensive review," *Critical Reviews in Solid State and Materials Sciences,* vol. 29, pp. 111-188, 2004.
[45] A. Kolmakov and M. Moskovits, "Chemical sensing and catalysis by one-dimensional metal-oxide nanostructures," *Annual Review of Materials Research,* vol. 34, pp. 151-180, 2004.
[46] H. J. Kim and J. H. Lee, "Highly sensitive and selective gas sensors using p-type oxide semiconductors: Overview," *Sensors and Actuators B-Chemical,* vol. 192, pp. 607-627, Mar 2014.
[47] I. Giebelhaus, E. Varechkina, T. Fischer, M. Rumyantseva, V. Ivanov, A. Gaskov, *et al.*, "One-dimensional CuO–SnO2 p–n heterojunctions for enhanced detection of H2S," *Journal of Materials Chemistry A,* vol. 1, p. 11261, 2013.
[48] G. Y. Lu, J. Xu, J. B. Sun, Y. S. Yu, Y. Q. Zhang, and F. M. Liu, "UV-enhanced room temperature NO2 sensor using ZnO nanorods modified with SnO2 nanoparticles," *Sensors and Actuators B-Chemical,* vol. 162, pp. 82-88, Feb 2012.
[49] M. Yang, J. He, X. Hu, C. Yan, and Z. Cheng, "Synthesis of nanostructured copper oxide via oxalate precursors and their sensing properties for hydrogen cyanide gas," *Analyst,* vol. 138, pp. 1758-1763, 2013 2013.
[50] X. W. Huang, X. B. Zou, J. Y. Shi, J. W. Zhao, Y. X. Li, L. M. Hao, *et al.*, "A new sensor for ammonia based on cyanidin-sensitized titanium dioxide film operating at room temperature," *Analytica Chimica Acta,* vol. 787, pp. 233-238, Jul 2013.
[51] I. A. Al-Homoudi, J. S. Thakur, R. Naik, G. W. Auner, and G. Newaz, "Anatase TiO2 films based CO gas sensor: Film thickness, substrate and temperature effects," *Applied Surface Science,* vol. 253, pp. 8607-8614, Aug 2007.
[52] G. S. Aluri, A. Motayed, A. V. Davydov, V. P. Oleshko, K. A. Bertness, N. A. Sanford, *et al.*, "Methanol, ethanol and hydrogen sensing using metal oxide and metal (TiO2–Pt) composite nanoclusters on GaN nanowires: a new route towards tailoring the selectivity of nanowire/nanocluster chemical sensors," *Nanotechnology,* vol. 23, p. 175501, 2012.
[53] R. Vyas, S. Sharma, P. Gupta, Y. K. Vijay, A. K. Prasad, A. K. Tyagi, *et al.*, "Enhanced NO2 sensing using ZnO-TiO2 nanocomposite thin films," *Journal of Alloys and Compounds,* vol. 554, pp. 59-63, Mar 2013.
[54] T. Xie, N. Sullivan, K. Steffens, B. Wen, G. Liu, R. Debnath, *et al.*, "UV-assisted room-temperature chemiresistive NO2 sensor based on TiO2 thin film," *Journal of Alloys and Compounds,* vol. 653, pp. 255-259, 2015.
[55] N. Ramgir, N. Datta, M. Kaur, S. Kailasaganapathi, A. K. Debnath, D. K. Aswal, *et al.*, "Metal oxide nanowires for chemiresistive gas sensors: Issues, challenges and prospects," *Colloids and Surfaces a-Physicochemical and Engineering Aspects,* vol. 439, pp. 101-116, Dec 2013.
[56] R. J. Lu, W. Zhou, K. Y. Shi, Y. Yang, L. Wang, K. Pan, *et al.*, "Alumina decorated TiO2 nanotubes with ordered mesoporous walls as high sensitivity NOx gas sensors at room temperature," *Nanoscale,* vol. 5, pp. 8569-8576, 2013.

[57] M. Yang, J. He, X. Hu, C. Yan, and Z. Cheng, "CuO Nanostructures As Quartz Crystal Microbalance Sensing Layers for Detection of Trace Hydrogen Cyanide Gas," *Environmental Science & Technology,* vol. 45, pp. 6088-6094, Jul 15 2011.

[58] J. Esmaeilzadeh, E. Marzbanrad, C. Zamani, and B. Raissi, "Fabrication of undoped-TiO2 nanostructure-based NO2 high temperature gas sensor using low frequency AC electrophoretic deposition method," *Sensors and Actuators B-Chemical,* vol. 161, pp. 401-405, Jan 2012.

[59] S.-W. Fan, A. K. Srivastava, and V. P. Dravid, "UV-activated room-temperature gas sensing mechanism of polycrystalline ZnO," *Applied Physics Letters,* vol. 95, p. 142106, 2009.

[60] G. Korotcenkov and B. K. Cho, "The role of grain size on the thermal instability of nanostructured metal oxides used in gas sensor applications and approaches for grain-size stabilization," *Progress in Crystal Growth and Characterization of Materials,* vol. 58, pp. 167-208, 2012.

[61] H. Chen, Y. Liu, C. S. Xie, J. Wu, D. W. Zeng, and Y. C. Liao, "A comparative study on UV light activated porous TiO2 and ZnO film sensors for gas sensing at room temperature," *Ceramics International,* vol. 38, pp. 503-509, Jan 2012.

[62] W. C. Tian, Y. H. Ho, and C. H. Chou, "Photoactivated TiO2 Gas Chromatograph Detector for Diverse Chemical Compounds Sensing at Room Temperature," *Ieee Sensors Journal,* vol. 13, pp. 1725-1729, May 2013.

[63] L. P. Liu, X. G. Li, P. K. Dutta, and J. Wang, "Room temperature impedance spectroscopy-based sensing of formaldehyde with porous TiO2 under UV illumination," *Sensors and Actuators B-Chemical,* vol. 185, pp. 1-9, Aug 2013.

[64] D. Haridas and V. Gupta, "Study of collective efforts of catalytic activity and photoactivation to enhance room temperature response of SnO2 thin film sensor for methane," *Sensors and Actuators B-Chemical,* vol. 182, pp. 741-746, Jun 2013.

[65] E. Comini, G. Faglia, and G. Sberveglieri, "UV light activation of tin oxide thin films for NO2 sensing at low temperatures," *Sensors and Actuators B-Chemical,* vol. 78, pp. 73-77, Aug 2001.

[66] J. B. Sun, J. Xu, Y. S. Yu, P. Sun, F. M. Liu, and G. Y. Lu, "UV-activated room temperature metal oxide based gas sensor attached with reflector," *Sensors and Actuators B-Chemical,* vol. 169, pp. 291-296, Jul 2012.

[67] P. Dhivya, A. K. Prasad, and M. Sridharan, "Nanostructured TiO2 films: Enhanced NH3 detection at room temperature," *Ceramics International,* vol. 40, pp. 409-415, Jan 2014.

[68] P. Weiss, "L'hypothèse du champ moléculaire et la propriété ferromagnétique," *J. Phys. Theor. Appl.,* vol. 6, pp. 661-690, 1907.

[69] J. S. Ma, "Investigation of magnetic domain configuration and vortex-antivortex creation and annihilation on CoFeB patterns," 2011.

[70] S. Florez, "Domain Wall Engineering of Nanoscale Ferromagnetic Elements and its Application for Memory Devices," Doctor of Philosophy, Department of Electrical and Computer Engineering, University of Maryland, College Park, 2006.

[71] T. Feng and J. Childress, "Fabrication of exchange-biased spin valves with CoFeB amorphous layers," *Journal of applied physics*, vol. 85, pp. 4937-4939, 1999.
[72] T. H. T. S. K. T. A. Y. Y. N. T. Osaka, "ChemInform Abstract: Co-Based Soft Magnetic Films Produced by Electroless Deposition," *ChemInform ChemInform*, vol. 23, pp. no-no, 2010.
[73] T. I. O. f. Standardization, "ISO 21348 definitions of solar irradiance spectral categories," vol. ISO 21348:2007(E), ed. Switzerland 2007.
[74] L. Peng, L. Hu, and X. Fang, "Low-Dimensional Nanostructure Ultraviolet Photodetectors," *Advanced Materials*, vol. 25, pp. 5321-5328, Oct 4 2013.
[75] E. Monroy, F. Omnes, and F. Calle, "Wide-bandgap semiconductor ultraviolet photodetectors," *Semiconductor Science and Technology*, vol. 18, pp. R33-R51, Apr 2003.
[76] Y. A. Goldberg, "Semiconductor near-ultraviolet photoelectronics," *Semiconductor Science and Technology*, vol. 14, pp. R41-R60, Jul 1999.
[77] M. Razeghi and A. Rogalski, "Semiconductor ultraviolet detectors," *Journal of Applied Physics*, vol. 79, pp. 7433-7473, May 15 1996.
[78] A. Tsukazaki, S. Akasaka, K. Nakahara, Y. Ohno, H. Ohno, D. Maryenko, *et al.*, "Observation of the fractional quantum Hall effect in an oxide," *Nature Materials*, vol. 9, pp. 889-893, Nov 2010.
[79] F. D. Auret, S. A. Goodman, M. Hayes, M. J. Legodi, H. A. van Laarhoven, and D. C. Look, "Electrical characterization of 1.8 MeV proton-bombarded ZnO," *Applied Physics Letters*, vol. 79, pp. 3074-3076, Nov 2001.
[80] S. Das, S. Chakrabarti, and S. Chaudhuri, "Optical transmission and photoluminescence studies of ZnO-MgO nanocomposite thin films," *Journal of Physics D-Applied Physics*, vol. 38, pp. 4021-4026, Nov 2005.
[81] M. Yang, J. He, X. Hu, C. Yan, Z. Cheng, Y. Zhao, *et al.*, "Copper oxide nanoparticle sensors for hydrogen cyanide detection: Unprecedented selectivity and sensitivity," *Sensors and Actuators B-Chemical*, vol. 155, pp. 692-698, Jul 20 2011.
[82] G. Heiland, "Zum Einfluss von Wasserstoff auf die elektrische Leitf¨ahigkeit von ZnO-Kristallen," *Zeit. Phys.*, pp. 459–464, 1954.
[83] J. D. A. Bielanski, J. Haber, "Electric conductivity and catalytic activity of semiconducting oxide catalysts," *Nature*, pp. 668-669, 1957.
[84] A. K. T. Seiyama, K. Fujiishi, M. Nagatani, "Anewdetector for gaseous components using semiconductive thin films," *Anal. Chem.*, p. 1502f, 1962.
[85] N. Taguchi, Published patent application in Japan Patent, 1962.
[86] N. Yamazoe, "Toward innovations of gas sensor technology," *Sensors and Actuators B-Chemical*, vol. 108, pp. 2-14, Jul 2005.
[87] N. Barsan and U. Weimar, "Conduction model of metal oxide gas sensors," *Journal of Electroceramics*, vol. 7, pp. 143-167, Dec 2001.
[88] N. Matsunaga, G. Sakai, K. Shimanoe, and N. Yamazoe, "Formulation of gas diffusion dynamics for thin film semiconductor gas sensor based on simple reaction-diffusion equation," *Sensors and Actuators B-Chemical*, vol. 96, pp. 226-233, Nov 15 2003.

[89] D. Szczuko, J. Werner, S. Oswald, G. Behr, and K. Wetzig, "XPS investigations of surface segregation of doping elements in SnO2," *Applied Surface Science*, vol. 179, pp. 301-306, Jul 2001.
[90] C. Kilic and A. Zunger, "Origins of coexistence of conductivity and transparency in SnO2," *Physical Review Letters*, vol. 88, Mar 2002.
[91] M. Iwamoto, Y. Yoda, N. Yamazoe, and T. Seiyama, "Study of metal oxide catalysts by temperature programmed desorption. 4. Oxygen adsorption on various metal oxides," *Journal of Physical Chemistry*, vol. 82, pp. 2564-2570, 1978 1978.
[92] P. Auger, "Sur l'effet photoélectrique composé," *J. Phys. Radium*, vol. 6, pp. 205-208, 1925.
[93] K. D. Childs, B. A. Carlson, L. A. LaVanier, J. F. Moulder, D. F. Paul, W. F. Stickle, *et al.*, *Handbook of Auger electron spectroscopy : a book of reference data for identification and interpretation in Auger electron spectroscopy*. Eden Prairie, Minn.: Physical Electronics Inc., 1995.
[94] G. Ertl and J. Küppers, *Low energy electrons and surface chemistry*. Weinheim, Federal Republic of Germany; Deerfield Beach, FL, USA: VCH, 1985.
[95] Y.-w. Chung, *Practical guide to surface science and spectroscopy*. San Diego: Academic Press, 2001.
[96] W. A. Coghlan and R. E. Clausing, "Auger catalog calculated transition energies listed by energy and element," *Atomic Data and Nuclear Data Tables*, vol. 5, pp. 317-469, // 1973.
[97] P. W. Palmberg, G. E. Riach, R. E. Weber, and N. C. MacDonald, *Handbook of Auger Electron Spectroscopy Data*: Physical Electronics Industries, 1972.
[98] S. Mroczkowski and D. Lichtman, "Calculated Auger yields and sensitivity factors for KLL–NOO transitions with 1–10 kV primary beams," *Journal of Vacuum Science & Technology A: Vacuum, Surfaces, and Films*, vol. 3, pp. 1860-1865, 1985.
[99] X. Z. Ding, B. K. Tay, X. Shi, M. F. Chiah, W. Y. Cheung, S. P. Wong, *et al.*, "Magnetic properties of Fe+-implanted silica films after post-implantation annealing," *Journal of Applied Physics*, vol. 88, pp. 2745-2749, Sep 1 2000.
[100] R. D. Gomez, A. O. Pak, A. J. Anderson, E. R. Burke, A. J. Leyendecker, and I. D. Mayergoyz, "Quantification of magnetic force microscopy images using combined electrostatic and magnetostatic imaging," *Journal of Applied Physics*, vol. 83, pp. 6226-6228, 1998.
[101] "Dimension 3000 Scanning Probe Microscope Instruction Manual," ed: Digital Instruments, Incorporated, 1996.
[102] P. Grütter, H. J. Mamin, and D. Rugar, "Magnetic Force Microscopy (MFM)," in *Scanning Tunneling Microscopy II*. vol. 28, R. Wiesendanger and H.-J. Güntherodt, Eds., ed: Springer Berlin Heidelberg, 1992, pp. 151-207.
[103] N. Fairley, *CasaXPS manual 2.3. 15*: Acolyte Science, 2009.
[104] J. Drenth, *X-Ray Crystallography*: Wiley Online Library, 2007.
[105] N. Laidani, R. Bartali, G. Gottardi, M. Anderle, and P. Cheyssac, "Optical absorption parameters of amorphous carbon films from Forouhi-Bloomer and Tauc-Lorentz models: a comparative study," *Journal of Physics-Condensed Matter*, vol. 20, p. 015216, Jan 9 2008.

[106] J. Tauc, Grigorov.R, and A. Vancu, "Optical properties and electronic structure of amorphous germanium," *Physica Status Solidi,* vol. 15, pp. 627-637, 1966.
[107] G. E. Jellison and F. A. Modine, "Parameterization of the optical functions of amorphous materials in the interband region," *Applied Physics Letters,* vol. 69, pp. 371-373, Jul 15 1996.
[108] A. R. Forouhi and I. Bloomer, "OPTICAL DISPERSION-RELATIONS FOR AMORPHOUS-SEMICONDUCTORS AND AMORPHOUS DIELECTRICS," *Physical Review B,* vol. 34, pp. 7018-7026, Nov 15 1986.
[109] F. Urbach, "The long-wavelength edge of photographic sensitivity and of the electronic absorption of solids " *Physical Review,* vol. 92, pp. 1324-1324, 1953 1953.
[110] S. Adachi, "At or Below the Fundamental Absorption Edge," in *Optical Properties of Crystalline and Amorphous Semiconductors*, 1st, Ed., ed: Springer US, 1999, pp. 179-250.
[111] K. Sedeek, E. A. Mahmoud, F. S. Terra, A. Said, and S. M. Eldin, "OPTICAL-PROPERTIES OF AMORPHOUS-CHALCOGENIDE THIN-FILMS - THE EFFECT OF TE ISOVALENCE SUBSTITUTION IN THE GE-S-SE SYSTEM," *Journal of Physics D-Applied Physics,* vol. 27, pp. 156-159, Jan 1994.
[112] C. Y. You, N. Tian, H. S. Goripati, and T. Furubayashi, "Current-perpendicular-to-the-plane giant magnetoresistance of an all-metal spin valve structure with Co40Fe40B20 magnetic layer," *Applied physics letters.,* vol. 96, p. 142503, 2010.
[113] C. Ahn, K.-H. Shin, and J. W. P. Pratt, "Magnetotransport properties of CoFeB and Co/Ru interfaces in the current-perpendicular-to-plane geometry," *Applied Physics Letters,* vol. 92, pp. 102509-3, 03/10/ 2008.
[114] G. A. Wang, S. Nakashima, S. Arai, T. Kato, and S. Iwata, "High sensitivity giant magnetoresistance magnetic sensor using oscillatory domain wall displacement," *Journal of Applied Physics,* vol. 107, pp. 09E709-09E709-3, 2010.
[115] N. Lei, T. Devolder, G. Agnus, P. Aubert, L. Daniel, J.-V. Kim, *et al.*, "Strain-controlled magnetic domain wall propagation in hybrid piezoelectric/ferromagnetic structures," *Nature Communications,* vol. 4, p. 1378, 2013.
[116] W. H. Rippard, M. R. Pufall, M. L. Schneider, K. Garello, and S. E. Russek, "Spin transfer precessional dynamics in Co[sub 60]Fe[sub 20]B[sub 20] nanocontacts," *Journal of Applied Physics,* vol. 103, pp. 053914-4, 03/01/ 2008.
[117] C. Y. You, H. S. Goripati, T. Furubayashi, Y. K. Takahashi, and K. Hono, "Exchange bias of spin valve structure with a top-pinned Co[sub 40]Fe[sub 40]B[sub 20]/IrMn," *Applied Physics Letters,* vol. 93, pp. 012501-3, 07/07/ 2008.
[118] G. Wang, Y. Masuda, T. Kato, and S. Iwata, "Design and performance of domain wall displacing-type field sensors using a magnetic tunnel junction and a giant magnetoresistive device," *Journal of Physics D: Applied Physics,* vol. 43, p. 455001, 2010.

[119] T. Tahmasebi, S. N. Piramanayagam, R. Sbiaa, H. K. Tan, and T. C. Chong, "Effect of different compositions of CoFeB spin polarizer on magnetoresistance and switching property of Co/Pd multilayers with perpendicular magnetic anisotropy," *Journal of Applied Physics*, vol. 111, p. 07D306, 2012.

[120] S. Li, H. S. Goripati, Y. K. Takahashi, T. Furubayashi, and K. Hono, "Current-Perpendicular-to-Plane Giant Magnetoresistance in Pseudo Spin Valves With $Co_2Fe(Ge_{0.5}Ga_{0.5})$ Heusler Alloy Ferromagnetic Layers and Cu/Ag Spacer," *Magnetics, IEEE Transactions on,* vol. 49, pp. 4413-4416, 2013.

[121] E. B. Svedberg, K. J. Howard, M. C. Bonsager, B. B. Pant, A. G. Roy, and D. E. Laughlin, "Interdiffusion in CoFe/Cu multilayers and its application to spin-valve structures for data storage," *Journal of Applied Physics,* vol. 94, pp. 1001-1006, Jul 15 2003.

[122] Y. H. Wang, W. C. Chen, S. Y. Yang, K. H. Shen, C. Park, M. J. Kao, *et al.*, "Interfacial and annealing effects on magnetic properties of CoFeB thin films," *Journal of applied physics,* vol. 99, pp. 08M307-08M307-3, 2006.

[123] S. Y. Jang, S. H. Lim, and S. R. Lee, "Magnetic dead layer in amorphous CoFeB layers with various top and bottom structures," *Journal of Applied Physics,* vol. 107, pp. 09C707-3, 05/01/ 2010.

[124] J. Hong, K. Aoshima, J. Kane, K. Noma, and H. Kanai, "Effect of thin oxide capping on interlayer coupling in spin valves," *Magnetics, IEEE Transactions on,* vol. 36, pp. 2629-2631, 2000.

[125] H. Sakakima, E. Hirota, and Y. Kawawake, "Enhanced GMR in [NiFe/Cu/Co] with specular reflective capping layers," *Journal of Magnetism and Magnetic Materials,* vol. 184, pp. 49-54, 4/7/ 1998.

[126] M. H. Li, J. W. Cai, G. H. Yu, H. W. Jiang, W. Y. Lai, and F. W. Zhu, "Effect of Cu surface segregation on properties of NiFe/FeMn bilayers," *Materials Science and Engineering: B,* vol. 90, pp. 296-300, 3/29/ 2002.

[127] H. W. Jiang, M. H. Li, G. H. Yu, F. W. Zhu, J. W. Cai, and W. Y. Lai, "Enhancement of exchange-coupling field in FeMn pinned spin valve by surfactant Bi," *Journal of Magnetism and Magnetic Materials,* vol. 264, pp. 1-6, 8// 2003.

[128] D. R. Baer, A. S. Lea, J. D. Geller, J. S. Hammond, L. Kover, C. J. Powell, *et al.*, "Approaches to analyzing insulators with Auger electron spectroscopy: Update and overview," *Journal of Electron Spectroscopy and Related Phenomena,* vol. 176, pp. 80-94, 2010.

[129] W. Laws Calley, J. D. Greenlee, W. E. Henderson, J. Lowder, M. W. Moseley, W. Alan Doolittle, *et al.*, "In situ Auger probe enabling epitaxy composition control of alloys by elemental surface analysis," *Journal of Vacuum Science & Technology B: Microelectronics and Nanometer Structures,* vol. 31, pp. 03C126-03C126-5, 2013.

[130] "Auger electron spectroscopy with four-grid spectaLEED," Version 2.1 ed: OMICRON Vakuumpgysik GmbH, 2000, p. 13.

[131] B. Singh, R. W. Vook, and E. A. Knabbe, "AES STUDY OF SULFUR SURFACE SEGREGATION ON POLYCRYSTALLINE COPPER," *Journal of Vacuum Science & Technology,* vol. 17, pp. 29-33, 1980.

[132] S. Ganesan, C. M. Park, K. Hattori, H. C. Park, R. L. White, H. Koo, *et al.*, "Properties of lithographically formed cobalt and cobalt alloy single crystal patterned media," *Ieee Transactions on Magnetics,* vol. 36, pp. 2987-2989, Sep 2000.
[133] J. I. Martin, J. Nogues, K. Liu, J. L. Vicent, and I. K. Schuller, "Ordered magnetic nanostructures: fabrication and properties," *Journal of Magnetism and Magnetic Materials,* vol. 256, pp. 449-501, Jan 2003.
[134] G. M. McClelland, M. W. Hart, C. T. Rettner, M. E. Best, K. R. Carter, and B. D. Terris, "Nanoscale patterning of magnetic islands by imprint lithography using a flexible mold," *Applied Physics Letters,* vol. 81, pp. 1483-1485, Aug 2002.
[135] K. Bessho, Y. Iwasaki, and S. Hashimoto, "Fabricating nanoscale magnetic mounds using a scanning probe microscope," *Journal of Applied Physics,* vol. 79, pp. 5057-5059, Apr 15 1996.
[136] J. Kennedy, J. Leveneur, G. V. M. Williams, D. R. G. Mitchell, and A. Markwitz, "Fabrication of surface magnetic nanoclusters using low energy ion implantation and electron beam annealing," *Nanotechnology,* vol. 22, p. 6, Mar 2011.
[137] S. S. Mukherjee, D. MacMahon, F. Bai, C.-L. Lee, and S. K. Kurinec, "Study of boron diffusion in MgO in CoFeB|MgO film stacks using parallel electron energy loss spectroscopy," *Applied Physics Letters,* vol. 94, p. 082110, 2009.
[138] C. Y. You, T. Ohkubo, Y. K. Takahashi, and K. Hono, "Boron segregation in crystallized MgO/amorphous-$Co_{40}Fe_{40}B_{20}$ thin films," *Journal of Applied Physics,* vol. 104, p. 033517, 2008.
[139] Y. Lu, B. Lépine, G. Jézéquel, S. Ababou, M. Alnot, J. Lambert, *et al.*, "Depth analysis of boron diffusion in MgO/CoFeB bilayer by x-ray photoelectron spectroscopy," *Journal of Applied Physics,* vol. 108, p. 043703, 2010.
[140] A. Ding, I. Will, C. Lu, and Y. B. Xu, "Vortex Domain Wall Formation in Nanowires With Twin Pinning Sites," *Ieee Transactions on Magnetics,* vol. 48, pp. 2304-2306, Aug 2012.
[141] X. Jiang, L. Thomas, R. Moriya, and S. S. P. Parkin, "Discrete Domain Wall Positioning Due to Pinning in Current Driven Motion along Nanowires," *Nano Letters,* vol. 11, pp. 96-100, Jan 2011.
[142] Y. Zhang, W. S. Zhao, J. O. Klein, D. Ravelsona, and C. Chappert, "Ultra-High Density Content Addressable Memory Based on Current Induced Domain Wall Motion in Magnetic Track," *Ieee Transactions on Magnetics,* vol. 48, pp. 3219-3222, Nov 2012.
[143] R. D. Gomez, E. R. Burke, and I. D. Mayergoyz, "Magnetic imaging in the presence of external fields: Technique and applications (invited)," *Journal of Applied Physics,* vol. 79, pp. 6441-6446, 1996.
[144] C. Fowley, N. Decorde, K. Oguz, K. Rode, H. Kurt, and J. M. D. Coey, "Perpendicular Magnetic Anisotropy in CoFeB/Pd Bilayers," *Magnetics, IEEE Transactions on,* vol. 46, pp. 2116-2118, 2010.
[145] K. Nomura, H. Ohta, K. Ueda, T. Kamiya, M. Hirano, and H. Hosono, "Thin-film transistor fabricated in single-crystalline transparent oxide semiconductor," *Science,* vol. 300, pp. 1269-1272, May 2003.

[146] K. Nomura, H. Ohta, A. Takagi, T. Kamiya, M. Hirano, and H. Hosono, "Room-temperature fabrication of transparent flexible thin-film transistors using amorphous oxide semiconductors," *Nature,* vol. 432, pp. 488-492, Nov 25 2004.
[147] T. Xie, D. Romero, and R. D. Gomez, "Surface compositions of atomic layer deposited Zn1−xMgxO thin films studied using Auger electron spectroscopy," *Journal of Vacuum Science & Technology A,* vol. 33, p. 05E110, 2015.
[148] L. Hu, J. Yan, M. Liao, L. Wu, and X. Fang, "Ultrahigh external quantum efficiency from thin SnO2 nanowire ultraviolet photodetectors," *Small,* vol. 7, pp. 1012-7, Apr 18 2011.
[149] Y. Chen, C. Zhu, M. Cao, and T. Wang, "Photoresponse of SnO2 nanobelts grown in situ on interdigital electrodes," *Nanotechnology,* vol. 18, p. 285502, 2007.
[150] S. Mathur, S. Barth, H. Shen, J. C. Pyun, and U. Werner, "Size-dependent photoconductance in SnO2 nanowires," *Small,* vol. 1, pp. 713-717, Jul 2005.
[151] H. Chen, L. Hu, X. Fang, and L. Wu, "General Fabrication of Monolayer SnO2 Nanonets for High-Performance Ultraviolet Photodetectors," *Advanced Functional Materials,* vol. 22, pp. 1229-1235, 2012.
[152] T. Oshima, T. Okuno, and S. Fujita, "UV-B sensor based on a SnO2 thin film," *Japanese Journal of Applied Physics,* vol. 48, p. 120207, 2009.
[153] K. Liu, M. Sakurai, M. Aono, and D. Shen, "Ultrahigh-Gain Single SnO2Microrod Photoconductor on Flexible Substrate with Fast Recovery Speed," *Advanced Functional Materials,* vol. 25, pp. 3157-3163, 2015.
[154] W. Tian, C. Zhang, T. Zhai, S. L. Li, X. Wang, M. Liao, *et al.*, "Flexible SnO(2) hollow nanosphere film based high-performance ultraviolet photodetector," *Chem Commun (Camb),* vol. 49, pp. 3739-41, May 8 2013.
[155] C.-H. Lin, R.-S. Chen, T.-T. Chen, H.-Y. Chen, Y.-F. Chen, K.-H. Chen, *et al.*, "High photocurrent gain in SnO[sub 2] nanowires," *Applied Physics Letters,* vol. 93, p. 112115, 2008.
[156] X. Xue, L. Xing, Y. Chen, S. Shi, Y. Wang, and T. Wang, "Synthesis and H2S sensing properties of CuO-SnO2 core/shell PN-junction nanorods," *Journal of Physical Chemistry C,* vol. 112, pp. 12157-12160, Aug 14 2008.
[157] L. Liu, M. An, P. Yang, and J. Zhang, "Superior cycle performance and high reversible capacity of SnO2/graphene composite as an anode material for lithium-ion batteries," *Scientific Reports,* vol. 5, p. 9055, 03/12/online 2015.
[158] R. P. Vasquez, "CuO by XPS," *Surface Science Spectra,* vol. 5, p. 262, 1998.
[159] D. Tahir and S. Tougaard, "Electronic and optical properties of Cu, CuO and Cu2O studied by electron spectroscopy," *J Phys Condens Matter,* vol. 24, p. 175002, May 2 2012.
[160] R. P. Vasquez, "Cu2O by XPS," *Surface Science Spectra,* vol. 5, p. 257, 1998.
[161] E. Palik, "Handbook of Optical Constants of Solids II Academic," *New York,* vol. 19912, 1991.
[162] I. Malitson and M. Dodge, "REFRACTIVE-INDEX AND BIREFRINGENCE OF SYNTHETIC SAPPHIRE," in *Journal Of The Optical Society Of America*, 1972, pp. 1405-1405.

[163] F. Koffyberg and F. Benko, "A photoelectrochemical determination of the position of the conduction and valence band edges of p-type CuO," *Journal of Applied Physics,* vol. 53, pp. 1173-1177, 1982.
[164] J. Robertson, K. Xiong, and S. Clark, "Band gaps and defect levels in functional oxides," *Thin Solid Films,* vol. 496, pp. 1-7, 2006.
[165] H. Ohta, M. Hirano, K. Nakahara, H. Maruta, T. Tanabe, M. Kamiya, *et al.*, "Fabrication and photoresponse of a pn-heterojunction diode composed of transparent oxide semiconductors, p-NiO and n-ZnO," *Applied Physics Letters,* vol. 83, pp. 1029-1031, Aug 2003.
[166] Y. Y. Xi, Y. F. Hsu, A. B. Djurisic, A. M. C. Ng, W. K. Chan, H. L. Tam, *et al.*, "NiO/ZnO light emitting diodes by solution-based growth," *Applied Physics Letters,* vol. 92, p. 113505, Mar 17 2008.
[167] D. Y. Kim, J. Ryu, J. Manders, J. Lee, and F. So, "Air-Stable, Solution-Processed Oxide p-n Heterojunction Ultraviolet Photodetector," *Acs Applied Materials & Interfaces,* vol. 6, pp. 1370-1374, Feb 2014.
[168] N. Park, K. Sun, Z. L. Sun, Y. Jing, and D. L. Wang, "High efficiency NiO/ZnO heterojunction UV photodiode by sol-gel processing," *Journal of Materials Chemistry C,* vol. 1, pp. 7333-7338, 2013.
[169] X. M. Chen, K. B. Ruan, G. H. Wu, and D. H. Bao, "Tuning electrical properties of transparent p-NiO/n-MgZnO heterojunctions with band gap engineering of MgZnO," *Applied Physics Letters,* vol. 93, p. 3, Sep 2008.
[170] P. Bhattacharya, R. R. Das, and R. S. Katiyar, "Comparative study of Mg doped ZnO and multilayer ZnO/MgO thin films," *Thin Solid Films,* vol. 447, pp. 564-567, Jan 2004.
[171] P. Bhattacharya, R. R. Das, and R. S. Katiyar, "Fabrication of stable wide-band-gap ZnO/MgO multilayer thin films," *Applied Physics Letters,* vol. 83, pp. 2010-2012, Sep 2003.
[172] A. Ohtomo, M. Kawasaki, T. Koida, K. Masubuchi, H. Koinuma, Y. Sakurai, *et al.*, "$Mg_xZn_{1-x}O$ as a II–VI widegap semiconductor alloy," *Applied Physics Letters,* vol. 72, pp. 2466-2468, 1998.
[173] Y. Sawai, K. Hazu, and S. F. Chichibu, "Surface stoichiometry and activity control for atomically smooth low dislocation density ZnO and pseudomorphic MgZnO epitaxy on a Zn-polar ZnO substrate by the helicon-wave-excited-plasma sputtering epitaxy method," *Journal of Applied Physics,* vol. 108, p. 063541, 2010.
[174] Z. Li, R. Yang, M. Yu, F. Bai, C. Li, and Z. L. Wang, "Cellular Level Biocompatibility and Biosafety of ZnO Nanowires," *Journal of Physical Chemistry C,* vol. 112, pp. 20114-20117, Dec 25 2008.
[175] J. Zhou, N. S. Xu, and Z. L. Wang, "Dissolving Behavior and Stability of ZnO Wires in Biofluids: A Study on Biodegradability and Biocompatibility of ZnO Nanostructures," *Advanced Materials,* vol. 18, pp. 2432-2435, 2006.
[176] W. Yang, R. D. Vispute, S. Choopun, R. P. Sharma, T. Venkatesan, and H. Shen, "Ultraviolet photoconductive detector based on epitaxial $Mg_{0.34}Zn_{0.66}O$ thin films," *Applied Physics Letters,* vol. 78, pp. 2787-2789, 2001.

[177] H. Endo, M. Sugibuchi, K. Takahashi, S. Goto, K. Hane, and Y. Kashiwaba, "Fabrication and characteristics of a Pt/$Mg_xZn_{1-x}O$ Schottky photodiode on a ZnO single crystal," *physica status solidi (c),* vol. 5, pp. 3119-3121, 2008.

[178] E. Haruyuki, K. Michiko, A. Masahumi, K. Yasuhiro, H. Kazuhiro, and K. Yasube, "High-Sensitivity Mid-Ultraviolet Pt/$Mg_{0.59}Zn_{0.41}O$ Schottky Photodiode on a ZnO Single Crystal Substrate," *Applied Physics Express,* vol. 1, p. 051201, 2008.

[179] A. K. Sharma, J. Narayan, J. F. Muth, C. W. Teng, C. Jin, A. Kvit, *et al.*, "Optical and structural properties of epitaxial $Mg_xZn_{1-x}O$ alloys," *Applied Physics Letters,* vol. 75, pp. 3327-3329, 1999.

[180] S. Choopun, R. D. Vispute, W. Yang, R. P. Sharma, T. Venkatesan, and H. Shen, "Realization of band gap above 5.0 eV in metastable cubic-phase MgxZn1-xO alloy films," *Applied Physics Letters,* vol. 80, pp. 1529-1531, Mar 2002.

[181] T. Maruyama and S. Arai, "The electrochromic properties of nickel oxide thin films prepared by chemical vapor deposition," *Solar Energy Materials and Solar Cells,* vol. 30, pp. 257-262, Aug 1993.

[182] T. Takagi, H. Tanaka, S. Fujita, and S. Fujita, "Molecular Beam Epitaxy of High Magnesium Content Single-Phase Wurzite $Mg_xZn_{1-x}O$ Alloys ($x \simeq 0.5$) and Their Application to Solar-Blind Region Photodetectors," *Japanese Journal of Applied Physics,* vol. 42, p. L401, 2003.

[183] A. Ohtomo, M. Kawasaki, Y. Sakurai, I. Ohkubo, R. Shiroki, Y. Yoshida, *et al.*, "Fabrication of alloys and superlattices based on ZnO towards ultraviolet laser," *Materials Science and Engineering: B,* vol. 56, pp. 263-266, 11/6/ 1998.

[184] Y. Vygranenko, K. Wang, and A. Nathan, "Low leakage p-NiO⁄i-ZnO⁄n-ITO heterostructure ultraviolet sensor," *Applied Physics Letters,* vol. 89, p. 172105, 2006.

[185] K. W. Liu, D. Z. Shen, C. X. Shan, J. Y. Zhang, B. Yao, D. X. Zhao, *et al.*, "$Zn_{0.76}Mg_{0.24}O$ homojunction photodiode for ultraviolet detection," *Applied Physics Letters,* vol. 91, p. 201106, 2007.

[186] G. Shukla, "$Zn_{1-x}Mg_xO$ Homojunction-Based Ultraviolet Photodetector," *Photonics Technology Letters, IEEE,* vol. 21, pp. 887-889, 2009.

[187] N. V. Nguyen, S. Sayan, I. Levin, J. R. Ehrstein, I. J. R. Baumvol, C. Driemeier, *et al.*, "Optical band gaps and composition dependence of hafnium–aluminate thin films grown by atomic layer chemical vapor deposition," *Journal of Vacuum Science & Technology A,* vol. 23, pp. 1706-1713, 2005.

[188] R. Shannon, "Revised effective ionic radii and systematic studies of interatomic distances in halides and chalcogenides," *Acta Crystallographica Section A,* vol. 32, pp. 751-767, 1976.

[189] J. F. Sarver, F. L. Katnack, and F. A. Hummel, "Phase Equilibria and Manganese-Activated Fluorescence in the System $Zn_3(PO_4)_2$ - $Mg_3(PO_4)_2$," *Journal of The Electrochemical Society,* vol. 106, pp. 960-963, November 1, 1959 1959.

[190] K. Koike, K. Hama, I. Nakashima, G.-y. Takada, K.-i. Ogata, S. Sasa, *et al.*, "Molecular beam epitaxial growth of wide bandgap ZnMgO alloy films on

(111)-oriented Si substrate toward UV-detector applications," *Journal of Crystal Growth*, vol. 278, pp. 288-292, 5/1/ 2005.
[191] R. Ghosh and D. Basak, "Composition dependent ultraviolet photoresponse in MgxZn1−xO thin films," *Journal of Applied Physics*, vol. 101, pp. -, 2007.
[192] R. Ghosh and D. Basak, "Composition dependence of electrical and optical properties in sol-gel MgxZn1−xO thin films," *Journal of Applied Physics*, vol. 101, pp. -, 2007.
[193] R. Ghosh and D. Basak, "Optical studies on Mg x Zn1−x O wide band gap semiconductor in the perspective of phase equilibrium," *Journal of Materials Science: Materials in Electronics*, vol. 18, pp. 141-144, 2007/10/01 2007.
[194] A. Singh, A. Vij, D. Kumar, P. K. Khanna, M. Kumar, S. Gautam, *et al.*, "Investigation of phase segregation in sol–gel derived ZnMgO thin films," *Semiconductor Science and Technology*, vol. 28, p. 025004, 2013.
[195] Z. Yin, Q. Zheng, S.-C. Chen, D. Cai, L. Zhou, and J. Zhang, "Bandgap Tunable Zn1-xMgxO Thin Films as Highly Transparent Cathode Buffer Layers for High-Performance Inverted Polymer Solar Cells," *Advanced Energy Materials*, vol. 4, pp. n/a-n/a, 2014.
[196] S. Fujihara, C. Sasaki, and T. Kimura, "Effects of Li and Mg doping on microstructure and properties of sol-gel ZnO thin films," *Journal of the European Ceramic Society*, vol. 21, pp. 2109-2112, // 2001.
[197] M. Ben Amor, A. Boukhachem, K. Boubaker, and M. Amlouk, "Structural, optical and electrical studies on Mg-doped NiO thin films for sensitivity applications," *Materials Science in Semiconductor Processing*, vol. 27, pp. 994-1006, 11// 2014.
[198] Y. Ishida, A. Fujimori, H. Ohta, M. Hirano, and H. Hosono, "Potential profiling of the nanometer-scale charge-depletion layer in n-ZnO⁄p-NiO junction using photoemission spectroscopy," *Applied Physics Letters*, vol. 89, pp. -, 2006.
[199] A. Soudi, P. Dhakal, and Y. Gu, "Diameter dependence of the minority carrier diffusion length in individual ZnO nanowires," *Applied Physics Letters*, vol. 96, pp. -, 2010.
[200] M. M. Fan, K. W. Liu, Z. Z. Zhang, B. H. Li, X. Chen, D. X. Zhao, *et al.*, "High-performance solar-blind ultraviolet photodetector based on mixed-phase ZnMgO thin film," *Applied Physics Letters*, vol. 105, p. 011117, 2014.
[201] Y. N. Hou, Z. X. Mei, H. L. Liang, D. Q. Ye, C. Z. Gu, and X. L. Du, "Dual-band MgZnO ultraviolet photodetector integrated with Si," *Applied Physics Letters*, vol. 102, p. 153510, 2013.
[202] Y. Zhao, J. Zhang, D. Jiang, C. Shan, Z. Zhang, B. Yao, *et al.*, "Ultraviolet Photodetector Based on a MgZnO Film Grown by Radio-Frequency Magnetron Sputtering," *ACS Applied Materials & Interfaces*, vol. 1, pp. 2428-2430, 2009/11/25 2009.
[203] K. W. Liu, J. Y. Zhang, J. G. Ma, D. Y. Jiang, Y. M. Lu, B. Yao, *et al.*, "$Zn_{0.8}Mg_{0.2}O$-based metal–semiconductor–metal photodiodes on quartz for visible-blind ultraviolet detection," *Journal of Physics D: Applied Physics*, vol. 40, p. 2765, 2007.

[204] G. Tabares, A. Hierro, J. M. Ulloa, A. Guzman, E. Muñoz, A. Nakamura, *et al.*, "High responsivity and internal gain mechanisms in Au-ZnMgO Schottky photodiodes," *Applied Physics Letters,* vol. 96, p. 101112, 2010.
[205] D. Y. Kim, J. Ryu, J. Manders, J. Lee, and F. So, "Air-Stable, Solution-Processed Oxide p–n Heterojunction Ultraviolet Photodetector," *ACS Applied Materials & Interfaces,* vol. 6, pp. 1370-1374, 2014/02/12 2014.
[206] J. Z. Chen, C. H. Li, and I. C. Cheng, "Phase transitions of room temperature RF-sputtered ZnO/Mg0.4Zn0.6O multilayer thin films after thermal annealing," *Thin Solid Films,* vol. 520, pp. 1918-1923, Jan 2012.
[207] A. Ohtomo, M. Kawasaki, T. Koida, K. Masubuchi, H. Koinuma, Y. Sakurai, *et al.*, "MgxZn1-xO as a II-VI widegap semiconductor alloy," *Applied Physics Letters,* vol. 72, pp. 2466-2468, May 1998.
[208] A. Kaushal and D. Kaur, "Pulsed laser deposition of transparent ZnO/MgO multilayers," *Journal of Alloys and Compounds,* vol. 509, pp. 200-205, Jan 2011.
[209] T. Xie, G. Liu, B. Wen, J. Y. Ha, N. V. Nguyen, A. Motayed, *et al.*, "Tunable Ultraviolet Photoresponse in Solution-Processed p–n Junction Photodiodes Based on Transition-Metal Oxides," *ACS Applied Materials & Interfaces,* vol. 7, pp. 9660-9667, 2015/05/13 2015.
[210] E. R. Segnit and A. E. Holland, "SYSTEM MGO-ZNO-SIO2," *Journal of the American Ceramic Society,* vol. 48, pp. 409-&, 1965.
[211] T. Torndahl, C. Platzer-Bjorkman, J. Kessler, and M. Edoff, "Atomic layer deposition of Zn1-xMgxO buffer layers for Cu(In,Ga)Se-2 solar cells," *Progress in Photovoltaics,* vol. 15, pp. 225-235, May 2007.
[212] J. S. Wrench, I. F. Brunell, P. R. Chalker, J. D. Jin, A. Shaw, I. Z. Mitrovic, *et al.*, "Compositional tuning of atomic layer deposited MgZnO for thin film transistors," *Applied Physics Letters,* vol. 105, Nov 2014.
[213] Z. Dai, C. S. Lee, Y. Tian, I. D. Kim, and J. H. Lee, "Highly reversible switching from P- to N-type NO2 sensing in a monolayer Fe2O3 inverse opal film and the associated P-N transition phase diagram," *Journal of Materials Chemistry A,* vol. 3, pp. 3372-3381, 2015.
[214] J. Yoo, H. Yoon, and E. D. Wachsman, "Sensing properties of MOx/YSZ/Pt (MOx = Cr2O3, SnO2, CeO2) potentiometric sensor for NO2 detection," *Journal of the Electrochemical Society,* vol. 153, pp. H217-H221, 2006.
[215] A. Das, R. Dost, T. Richardson, M. Grell, J. J. Morrison, and M. L. Turner, "A nitrogen dioxide sensor based on an organic transistor constructed from amorphous semiconducting polymers," *Advanced Materials,* vol. 19, pp. 4018-4023, Nov 2007.
[216] D. E. Williams, "Semiconducting oxides as gas-sensitive resistors," *Sensors and Actuators B-Chemical,* vol. 57, pp. 1-16, Sep 1999.
[217] A. M. Ruiz, G. Sakai, A. Cornet, K. Shimanoe, J. R. Morante, and N. Yamazoe, "Cr-doped TiO2 gas sensor for exhaust NO2 monitoring," *Sensors and Actuators B-Chemical,* vol. 93, pp. 509-518, Aug 2003.
[218] V. Galstyan, E. Comini, G. Faglia, A. Vomiero, L. Borgese, E. Bontempi, *et al.*, "Fabrication and investigation of gas sensing properties of Nb-doped TiO2 nanotubular arrays," *Nanotechnology,* vol. 23, p. 235706, Jun 2012.

[219] Y. Gonullu, G. C. M. Rodriguez, B. Saruhan, and M. Urgen, "Improvement of gas sensing performance of TiO2 towards NO2 by nano-tubular structuring," *Sensors and Actuators B-Chemical,* vol. 169, pp. 151-160, Jul 2012.
[220] B. Saruhan, A. Yuce, Y. Gonullu, and K. Kelm, "Effect of Al doping on NO2 gas sensing of TiO2 at elevated temperatures," *Sensors and Actuators B-Chemical,* vol. 187, pp. 586-597, Oct 2013.
[221] E. Comini, A. Cristalli, G. Faglia, and G. Sberveglieri, "Light enhanced gas sensing properties of indium oxide and tin dioxide sensors," *Sensors and Actuators B-Chemical,* vol. 65, pp. 260-263, Jun 2000.
[222] D. Mardare, M. Tasca, M. Delibas, and G. I. Rusu, "On the structural properties and optical transmittance of TiO2 r.f. sputtered thin films," *Applied Surface Science,* vol. 156, pp. 200-206, Feb 2000.
[223] E. McCafferty and J. P. Wightman, "Determination of the concentration of surface hydroxyl groups on metal oxide films by a quantitative XPS method," *Surface and Interface Analysis,* vol. 26, pp. 549-564, Jul 1998.
[224] J. Trimboli, M. Mottern, H. Verweij, and P. K. Dutta, "Interaction of water with titania: Implications for high-temperature gas sensing," *Journal of Physical Chemistry B,* vol. 110, pp. 5647-5654, Mar 23 2006.
[225] H. Tang, K. Prasad, R. Sanjines, P. E. Schmid, and F. Levy, "Electrical and optical properties of TiO2 anatase thin-films," *Journal of Applied Physics,* vol. 75, pp. 2042-2047, Feb 15 1994.
[226] Y. Q. Hou, D. M. Zhuang, G. Zhang, M. Zhao, and M. S. Wu, "Influence of annealing temperature on the properties of titanium oxide thin film," *Applied Surface Science,* vol. 218, pp. 97-105, Sep 2003.
[227] G. Q. Lu, A. Linsebigler, and J. T. Yates, "he adsorption and photodesorption of oxygen on the TiO2(110) surface," *Journal of Chemical Physics,* vol. 102, pp. 4657-4662, Mar 15 1995.
[228] W. Gopel, G. Rocker, and R. Feierabend, " Intrinsic defects of TiO2(110): Interaction with chemisorbed O2, H2, CO, and CO2, Physical Review B," *Physical Review B,* vol. 28, pp. 3427-3438, 1983.
[229] C. Shu, N. Sukumar, and C. P. Ursenbach, "Adsorption of O-2 on TiO2(110): A theoretical study," *Journal of Chemical Physics,* vol. 110, pp. 10539-10544, Jun 1999.
[230] C. Naccache, Meriaude.P, M. Che, and A. J. Tench, "Identification of oxygen species adsorbed on reduced titanium dioxide," *Transactions of the Faraday Society,* vol. 67, pp. 506-512, 1971 1971.
[231] V. Guidi, M. C. Carotta, M. Ferroni, G. Martinelli, L. Paglialonga, E. Comini, *et al.,* "Preparation of nanosized titania thick and thin films as gas-sensors," *Sensors and Actuators B-Chemical,* vol. 57, pp. 197-200, Sep 1999.
[232] G. Liu, B. Wen, T. Xie, A. Castillo, J.-Y. Ha, N. Sullivan, *et al.,* "Top-Down Fabrication of Horizontally-Aligned Gallium Nitride Nanowire Arrays for Sensor Development," *Microelectronic Engineering,* vol. 142, pp. 58-63, 2015.
[233] H. B. Michaelson, "The work function of the elements and its periodicity," *Journal of Applied Physics,* vol. 48, p. 4729, 1977.

[234] C. I. Wu, A. Kahn, N. Taskar, D. Dorman, and D. Gallagher, "GaN (0001)-(1×1) surfaces: Composition and electronic properties," *Journal of Applied Physics,* vol. 83, p. 4249, 1998.

[235] S. P. Grabowski, M. Schneider, H. Nienhaus, W. Mönch, R. Dimitrov, O. Ambacher, *et al.*, "Electron affinity of $Al_xGa_{1-x}N$(0001) surfaces," *Applied Physics Letters,* vol. 78, p. 2503, 2001.

[236] Z. Fan and J. G. Lu, "Gate-refreshable nanowire chemical sensors," *Applied Physics Letters,* vol. 86, p. 123510, 2005.

[237] W. Zhao, K. Choi, S. Bauman, Z. Dilli, T. Salter, and M. Peckerar, "A radio-frequency energy harvesting scheme for use in low-power ad hoc distributed networks," *Circuits and Systems II: Express Briefs, IEEE Transactions on,* vol. 59, pp. 573-577, 2012.

[238] W. Zhao, K. Choi, S. Bauman, T. Salter, D. A. Lowy, M. Peckerar, *et al.*, "An energy harvesting system surveyed for a variety of unattended electronic applications," *Solid-State Electronics,* vol. 79, pp. 233-237, 2013.

[239] M. Peckerar, W. Zhao, Z. Dilli, M. Dornajafi, D. Lowy, and S. Potbhare, "Supercapacitor/Battery Hybrids for Energy Harvesting Applications," *ECS Transactions,* vol. 41, pp. 31-35, 2011.